2019/02

Materialprüfungsanstalt
Universität Stuttgart

Technisch-
Wissenschaftlicher-
Bericht

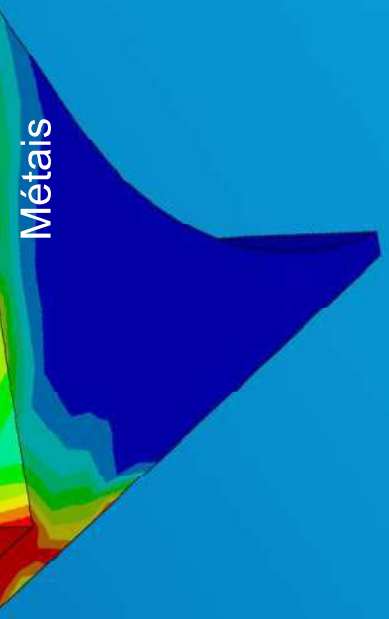

Benjamin Métais

Development of a Viscoplastic-Damage Model for Creep-Fatigue FE-Calculations of the Lead-free SnAgCu Solder Alloy for Automotive Applications

Métais

Materialprüfungsanstalt Universität Stuttgart

Development of a Viscoplastic-Damage Model for Creep-Fatigue FE-Calculations of the Lead-free SnAgCu Solder Alloy for Automotive Applications

Von der Fakultät Energie-, Verfahrens- und Biotechnik der Universität Stuttgart zur Erlangung der Würde eines Doktor-Ingenieurs (Dr.-Ing.) genehmigte Abhandlung

vorgelegt von
Dipl.-Ing. Benjamin Métais
aus Vendôme (Frankreich)

Hauptberichter:	Prof. Dr.-Ing. Stefan Weihe
Mitberichter:	Prof. Dr.-Ing. habil. Steffen Wiese
Tag der mündlichen Prüfung:	08.04.2019

2019
Institut für Materialprüfung, Werkstoffkunde und Festigkeitslehre (IMWF) Universität Stuttgart und
Materialprüfungsanstalt (MPA) Universität Stuttgart

Abstract

Automotive electronic devices are exposed to substantially harsher thermo-mechanical loads compared to commercial consumer electronic products. Inside an electronic device, there is a large number of solder joints, supporting the electrical as well as the mechanical interconnections. In terms of mechanical properties, solder joints are a weak point of the whole device assembly and can ultimately determine its reliability. In the past two decades, significant efforts have been made to set up methodologies for lifetime prediction of solder joints in automotive applications. Finite Element Analysis (FEA) is being increasingly employed with the aim to support product design and qualification process. However, constitutive FE models for solder alloys capable of describing their mechanical behavior at the relevant conditions of automotive applications are still not widely established. The currently employed state of the art material models applied in industry and research are based on uni-axial stationary creep. Thus, they naturally fail to describe properly the complex cyclic time-, strain rate, and temperature dependent behavior under the full temperature range of accelerated qualification lab tests and operation conditions. Furthermore, intrinsic degradation processes due to cyclic thermo-mechanical loading are not still completely investigated and are not taken into account within FE-calculations. Current FE-reliability prediction methodologies for solder joints are not possible without the usage of lifetime models (e.g. Coffin-Manson) and their calibration on a substantial set of experimental data. Due to the lack of models mapping intrinsic material degradation, the current prediction methods remain strongly constraint to a single solder type and loading conditions used within the lifetime experiments. More advanced techniques, originally proposed for steel alloys, employ viscoplastic constitutive models and damage mechanics and provide a powerful framework for predictive FE-based lifetime assessment. The goal of the present work is to build on these concepts and extend them for usage in solder joint simulations. An important part of the methodology development is the advanced experimental characterization necessary to obtain the material behavior, which extends the currently available research activities on solder alloys. The experimental investigations are focused on the intrinsic mechanical and aging properties of a Sn-based solder alloy and used for the formulation of a suitable FE-material model within the frame of damage mechanics. Within the thesis, a material testing procedure has been developed in order to perform mechan-

ical characterization on standardized specimens. The test program includes strain rate controlled cycling, stress relaxation phases, uniaxial and multiaxial Low Cycle Fatigue (LCF) as well as creep tests in the temperature range: -40°C up to 125°C. As a first step, the mechanical and microstructure properties of the material in the initial state prior degradation are investigated. A viscoplastic material model of two viscous functions originally proposed by Chaboche et al. has been numerically implemented for 3D simulations. The model maps the observed stress dependence on temperature, time and strain-rate of the alloy in both low and high strain rate regimes. A step by step procedure for calibration of the model parameters in the temperature range -40/125°C is detailed and discussed. As a second step, aging mechanisms are investigated by means of creep and fatigue tests. A lifetime concept based on creep-fatigue partitioning is worked out and applied for the lifetime assessment of a real Surface Mounted Device (SMD) chip resistor under temperature cycling. The method's predictions are correlated to reported experimental lifetime data within the project LiVe [1]. The proposed creep-fatigue partitioning approach provides means for fast estimation of solder joint reliability and might be used as a support of the design process of electronic devices. Finally, a full Continuum Damage Mechanics (CDM) model, which involves intrinsic damage propagation inside the material, has been developed and implemented for 3D simulations. Based on the observed aging properties, the damage model formulation takes into account local material softening due to creep-fatigue interaction. The CDM-simulation reveals the evolution of degradation in the solder joint component throughout its complete loading history. The main findings are discussed and put into perspective for future works dedicated to the implementation of the CDM approach for reliability prognosis and engineering lifetime concepts.

Zusammenfassung

Automobilelektronik-Steuergeräte werden im Vergleich zu kommerziellen Produkten der Unterhaltungselektronik wesentlich höheren thermomechanischen Belastungen im Betrieb ausgesetzt. Steuergeräte enthalten eine Vielzahl von Lötstellen, die die elektrischen und mechanischen Verbindungen zwischen den elektronischen Bauelementen gewährleisten. Das Lotmaterial wird im Betrieb stark beansprucht und kann sich als ausschlaggebend für die Langzeitstabilität eines Steuergeräts erweisen. In den letzten zwei Jahrzehnten wurden vermehrt Methoden zur Abschätzung der Lötstellenzuverlässigkeit für Kraftfahrzeuganwendungen entwickelt. Dabei wurden im Rahmen der Auslegung und Produktfreigabe numerische Finite Element (FE) Simulationen zur Lebensdauerprognose herangezogen. Allerdings stellt die Beschreibung des mechanischen Verhaltens von Loten in den relevanten Bedingungen der Automobilanwendungen immer noch eine Herausforderung dar. Die aktuell in Industrie und Forschung breit eingesetzten Materialmodelle für Lote dienen der Beschreibung von einachsigem stationärem Kriechen. Das komplexe zyklische Zeit-, Dehnraten- und temperaturabhängige Verhalten im gesamten Temperaturbereich von Labortests und Betriebsbedingungen kann mit diesen Modellen nicht vollständig abgebildet werden. Weiterhin, sind intrinsische Schädigungsprozesse aufgrund von zyklischen thermomechanischen Belastungen noch nicht vollständig untersucht und in FE-Berechnungen berücksichtigt. Aktuelle FE-basierende Vorhersagemethoden für Lötstellen sind ohne die Verwendung von Lebensdauermodellen (z.B. Coffin-Manson) und deren Kalibrierung anhand von experimentellen Daten nicht möglich. Die resultierende Lebensdauerprognosen sind auf die im Experiment verwendeten Lötstellengeometrie und Belastungsbedingung eingeschränkt. Erweiterte Ansätze zur Lebensdauerprognose, die diese Limitierungen zu überwinden versuchen, wurden im Bereich der Stahl- und Hochtemperaturlegierungen entwickelt. Sie basieren auf viskoplastischen FE-Materialmodellen erweitert durch Ansätze der Schädigungsmechanik. Ziel der vorliegenden Arbeit ist es, auf diesen Konzepten aufzubauen und sie für die Anwendung in Lötstellensimulationen zu erweitern. Ein wichtiger Teil der Methodenentwicklung ist die fortgeschrittene experimentelle Charakterisierung, erforderlich zur Ermittlung des Materialverhaltens. Die experimentelle Charakterisierung konzentriert sich auf die intrinsischen mechanischen und Alterungseigenschaften einer Zinnbasis Lotlegierung

und dient zur Formulierung eines geeigneten FE-Materialmodells. Im Rahmen der Arbeit wurde ein Testprogramm entwickelt, um standardisierte Proben mechanisch zu charakterisieren. Das in der vorliegenden Arbeit ertüchtigte Materialprüfverfahren umfasst dehnratengesteuerte zyklische Belastungen erweitert durch Spannungsrelaxationsphasen, einachsige und mehrachsige Ermüdung (LCF) sowie Kriechversuche im Temperaturbereich von -40 °C bis 125 °C. In einem ersten Schritt wurden die mechanischen und mikrostrukturellen Eigenschaften des Materials im Ausgangszustand vor der Alterung untersucht. Ein viskoplastisches Materialmodell mit zwei viskosen Funktionen, ursprünglich von Chaboche et al. erarbeitet, wurde numerisch für 3D-Simulationen implementiert. Das Modell bildet die experimentell beobachtete Spannungsabhängigkeit von Temperatur, Zeit und Dehnraten der Legierung sowohl im niedrigen als auch im hohen Dehnratenbereich ab. Eine schrittweise Methode zur Kalibrierung der Modellparameter im Temperaturbereich -40 bis 125 °C wird detailliert dargestellt und diskutiert. In einem zweiten Schritt wurden die Alterungsmechanismen mittels Kriech- und Ermüdungstests untersucht. Ein Lebensdauerkonzept basierend auf Kriechermüdungspartitionierung wurde ausgearbeitet und auf Lebensdauerbewertung eines realen SMD-Chipwiderstands unter Temperaturwechselbelastung angewandt. Die Vorhersagen der Methode werden mit den veröffentlichten experimentellen Lebensdauerdaten aus dem Projekt LiVe korreliert [1]. Der Kriechermüdungs-Partitionierungsansatz bietet die Möglichkeit zur schnellen Abschätzung der Lötverbindungszuverlässigkeit und kann als Unterstützung der Designentwicklung und elektronischen Bauteilfreigabe verwendet werden. Weiterhin, wurde ein vollständiges CDM-Modell (Continuum Damage Mechanics) mit lokalen Schädigungsfortschritt entwickelt und für 3D-Simulationen implementiert. Dadurch kann der Schädigungszustand der Lötstelle unter der lokalen Wechselwirkung zwischen Ermüdungs- und Kriechschädigung berechnet werden. Die CDM-Simulation zeigt die Entwicklung der Werkstoffdegradierung in der Lötstelle während der gesamten Belastungshistorie. Abschließend, werden die wesentlichen Erkenntnisse, künftiger Forschungsbedarf und Ansätze zur Weiterentwicklung und Industrialisierung des CDM-Ansatzes diskutiert. Der CDM-Ansatz kann künftig ein wichtiges Werkzeug im Rahmen des Designs für Zuverlässigkeit darstellen mit dem neue Aufbau-und Verbindungstechnik- Konzepte und Beanspruchungskollektive rein rechnerisch bewertet und optimiert werden können.

Acknowledgment

This work has been carried out in cooperation with the University of Stuttgart, (Materialprüfungsanstalt, MPA) and the company Robert Bosch GmbH, (research division for assembly technologies, department CR/APJ). I would like to thank Prof. Dr.-Ing. Stefan Weihe, director of the MPA-University of Stuttgart, for his supervision and guidance during this work as well as Prof. Dr.-Ing Steffen Wiese, from the University of Saarlandes, for his valuable advice and for reviewing this thesis. I am also grateful to Dr. Alexander Kabakchiev from the Robert Bosch GmbH, for his expertise, his scientific state of mind and the constant motivation and encouragements he gave me throughout the pursuit of this degree. I would like to acknowledge my fellow doctoral colleagues Mr. Youssef Maniar and Mrs. Marta Kuczynska for the fruitful and inspiring discussions we had on reliability and material modelling topics. I am thankful to the staff of the research department CR/APJ, Dr. Godehard Schmitz, Dr. Michael Guyenot and Dr. Roumen Ratchev, respectively department-, group- and team-leader of the research division for assembly technology of the Robert Bosch GmbH, for giving me the possibility to conduct my research and access the related resources needed during my thesis. I would like to express my appreciation to Dr. Mike Roellig and Mr. René Metasch, from the Fraunhoher Institute IKTS-Dresden, for their expertise inputs in the field of material testing and characterization of solder materials. Finally, I would like to thank my family and my friends for their continuous support and encouragement during my education and doctoral study.

Contents

List of symbols and abbreviations

List of symbols

β-Sn	Sn matrix phase of SnAgCu solder
ε^p	plastic strain
$\Delta\sigma$	stress amplitude
σ_{eq}	von Mises stress
σ_H	hydrostatic stress
ε_{III}	strain at tertiary creep stage
$\Delta\varepsilon$	strain amplitude
θ	twist angle for TT tests
T_h	homologous temperature
T_m	meting temperature
W^p	Dissipated plastic work
T_{mean}	mean temperature within a cycle
N_a	number of cycles at crack initiation
N_f	number of cycles to failure
t_r	time to rupture in creep test
P_{LM}	Larson-Miller creep damage parameter
t_{III}	time at tertiary creep stage
t_h	duration of dwell time periods
$S_k^{D(k)}$	sensitity of parameter D regrading var. k
D_c	creep damage parameter
D_f	fatigue damage parameter

List of mathematical variables related to the implementation of the ONERA2 model

variable	dimension	description
σ_{ij}	vector $[1 \times 6]$	true stress tensor
D	scalar	total damage variable
E_{ijkl}	fourth rank tensor $[6 \times 6]$	elastic stiffness matrix
ε_{kl}	vector $[1 \times 6]$	total strain
ε_{kl}^{p}	vector $[1 \times 6]$	plastic strain
ε_{kl}^{th}	vector $[1 \times 6]$	thermal strain
μ	scalar	shear modulus
λ	scalar	bulk modulus
δ_{ij}	scalar operator	Kroenecker operator
α_{CTE}	scalar	material constant: CTE
T	scalar	current temperature
T_{ref}	scalar	reference temperature for CTE
$\mathbb{1}$	vector $[1 \times 6]$	volumetric tensor [1 1 1 0 0 0]
$\tilde{\sigma}_{ij}$	vector $[1 \times 6]$	effective stress
$\tilde{S}_{ij}$	vector $[1 \times 6]$	effective deviatoric stress
Tr	operator	trace of vector
X_{ij}	vector $[1 \times 6]$	back stress
c_i	scalar $i = 1 \ldots 3$	material constant: Prager's term
γ_i	scalar $i = 1 \ldots 3$	material constant: dynamic recovery
d_i	scalar $i = 1 \ldots 3$	material constant: static recovery
ϕ	function	cyclic softening function
ϕ_∞	scalar	material constant: amplitude first softening
b_k	scalar	material constant: rate of softening saturation
ε_{acc}^{p}	scalar	accumulated plastic strain
R	scalar	isotropic hardening variable
σ_0	scalar	material constant: initial yield stress
Q	scalar	material constant: amplitude first hardening
b_q	scalar	material constant: rate of hardening saturation
σ_v	scalar	viscous stress
$\dot{\bar{\varepsilon}}^p$	scalar	equivalent plastic strain rate

K_2	scalar	material constant: drag stress in creep regime
m_2	scalar	material constant: Norton's exponent in creep regime
K_1	scalar	material constant: drag stress in viscoplastic regime
m_1	scalar	material constant: Norton's exponent in viscoplastic regime
D_1	scalar	fatigue damage variable
$\bar{\varepsilon}^p$	scalar	equivalent plastic strain
$\tilde{\sigma}_{eq}$	scalar	effective von Mises stress
a_1	scalar	material constant: linear fatigue damage
a_k	scalar	material constant: damage rate after crack initiation
δ	scalar	material constant: transition between a_1 and a_k
D_a	scalar	material constant: damage at crack initiation
b_1	scalar	material constant: fatigue damage, strain exponent
q	scalar	Clausmeyer quotient of multiaxiality
b_{qm}	scalar	material constant: multiaxiality exponent
D_2	scalar	creep damage variable
a_2	scalar	material constant: linear creep damage
b_2	scalar	material constant: creep damage, stress exponent
c_c	scalar	material constant: creep damage, strain exponent
c	scalar	material constant: ASME bilinear coefficient

List of abbreviations

AF	Acceleration Factor
ASME	American Society of Mechanical Engineers
BGA	Ball Grid Array
BSE	Backscattered Electron
CDM	Continuum Damage Mechanics
CNOW	Mat. model Chaboche-Nouailhas-Ohno-Wang
CR1206	Chip Resistor 12 in.×6 in.
DBC	Direct Bounded Copper
EBSD	Electron Backscatter Diffraction
ECU	Engine Control Unit
EDX	Energy Dispersive X-ray
FE	Finite Element
FEA	Finite Element Analysis
FEM	Finite Element Method
HCF	High Cycle Fatigue
LCF	Low Cycle Fatigue
IKTS	Institut für Keramische Technologien und Systeme (Fraunhofer Dresden)
LVDT	Linear Variable Differential Transformer
MPA	Materialprüfungsanstalt (Universität Stuttgart)
N-R	Newton-Raphson
ONERA	Office National d'Etudes et de Recherches Aérospatiales (national research center, Palaiseau, France)
PCB	Printed Circuit Board
RF	Relaxation Fatigue
RVE	Representative Volume Element
SAC	SnAgCu (tin-silver-copper) solder alloy
SEM	Scanning Electron Microscope
SMD	Surface Mounted Device
SVAR	State Variable
TMF	Thermo-Mechanical Fatigue
TT	Tension Torsion

1. Introduction

1.1. Motivation

The ongoing developments in the automotive industry follow the trend towards electric drives and autonomous driving in the long run. Especially in the context of electromobility, the demand for high performance electronic devices in cars is constantly increasing. As a consequence, a higher and more efficient integration of both logic and power components is needed [2]. In contrast to commercial consumer electronic products, automotive electronic devices must fulfill much higher requirements. On one hand, they are exposed to substantial thermo-mechanical loads. On the other hand, long term device reliability has to be guaranteed for a save operation estimated to 15 years or 300000 km [3], which is meanwhile well beyond the usage period of many consumer products.

In terms of durability, the solder joint has been identified as a potentially weak point of the electronic assembly [1], which can ultimately determine the lifetime of the electronic devices in long term operation. Solder joints ensure the interconnection between electronic components (e.g. chip resistors, capacitors, power chips or diodes) and the substrate, which can be for example an epoxy Printed Circuit Board (PCB) or a ceramic substrate like a DBC (Direct Bounded Copper), see Fig.1.1. In order to prevent a possible pre-damage of the components and substrates during the assembly, the soldering process has to be carried out at temperatures below 250 °C, which strongly restricts the choice of the materials used for soldering. Until 2006, tin-lead alloys have been the standard materials for soldering in electronic applications, as they were abandoned from production due to environmental reasons [4]. As substitutes for lead solder ternary alloys from the tin-silver-copper system were successfully introduced. Typical tin-based lead free solders for automotive electronics have a melting temperature of 220 °C and contain around 3 to 4% of silver and 0.5% of copper. However, lead-free solder materials show different microstructure properties and thermo-mechanical behavior compared to the typical lead-solder alloys [1]. As a consequence, failure mechanisms and methods for their modeling became necessary.

Despite significant efforts for characterizing lead-free solder alloys and establishing reliability guidelines for the solder material within automotive applications, the

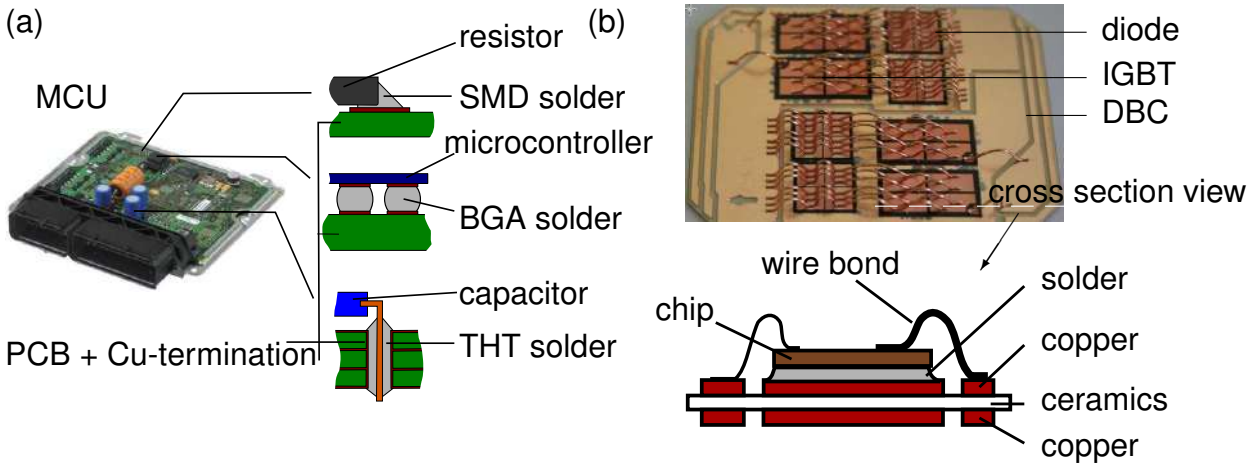

Fig. 1.1: (a) Engine Control Unit (ECU) composed of a large variety of assembled components on a PCB substrate, (b) power module assembled on a DBC substrate with mounted IGBTs and diodes connected with wire bonds, cross section view is depicted on the scheme, from [5]

state of the art methodology is still limited. It is not able to provide an accurate lifetime prediction for different solder geometries and various loading profiles without significant experimental effort on component level used for calibration of empirical lifetime equations. One of the reasons is the incompleteness of experimental investigations focused on the intrinsic deformation and damage behavior of the material in the complete temperature range of applications. Recent improvements in both experimental and simulation techniques propose better description of the viscoplastic deformation and damage properties of solder materials [6]. This work aims to extend the knowledge concerning the mechanical behavior and damage mechanisms of lead free solder alloys. This is achieved by performing an experimental characterization, extending the already available data. Based on modeling the deformation and damage behaviors, a new approach is proposed to calculate the degradation of solder joint materials under combined thermal-mechanical load cycles.

1.2. State of the art

Microstructure of SnAgCu (SAC) solder joints

A large number of components are usually assembled by SMD technology (Surface Mounted Device), which is currently the industrial process in use to fabricate electronic devices in serial production. For example, a chip resistor is connected to the

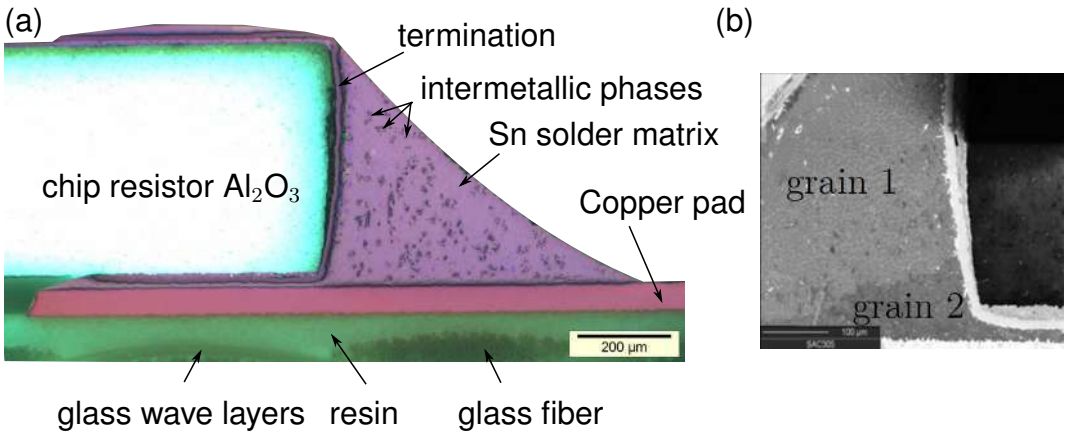

Fig. 1.2: (a) Granular microstructure in initial state: large grains from polarized light microscope after soldering process [7], (b) Microstructure of SMD-solder in its initial state from SEM picture [7]

PCB substrate via a solder joint material, as depicted in the cross section Fig.1.2(a). During reflow soldering, a solder paste containing dispersed solder particles is heated up above the melting temperature of the solder and cooled down in a controlled manner using optimized temperature profiles.

After solidification, the solder joint comprises a tin-rich matrix of the β-Sn phase, in which the intermetallic phases $AgSn_3$ and $CuSn_5$ are randomly distributed. The β-Sn phase exhibits a tetragonal centered crystal structure with anisotropic stiffness [8]. Moreover, the β-Sn matrix has birefringent properties which make visible the grain structure using polarized light microscopy [9]. After the soldering process, the joint has a structure with a rather homogeneous crystal orientation, see Fig.1.2(a). This observation is confirmed by a Scanning Electron Microscope (SEM) analysis Fig.1.2(b) where only two large grains are identified in the initial state prior to thermo-mechanical loading.

After 1000 temperature cycles -40℃/125℃, the microstructure of the solder joints changes and a large number of small grains are identified in the micrograph Fig.1.3(a). The occurring recrystallization process affects both standoff and meniscus region of the solder joint. On the Fig.1.3(a), the standoff region is cracked after 1000 cycles and the crack propagates further near the soft termination of the chip resistor but still through the bulk solder material, towards the meniscus region. The inter-granular crack propagates along the multiple grain boundaries which formed by a recrystallization process, see Fig.1.3(b).

The crack results from thermo-mechanical fatigue of the material due to the un-

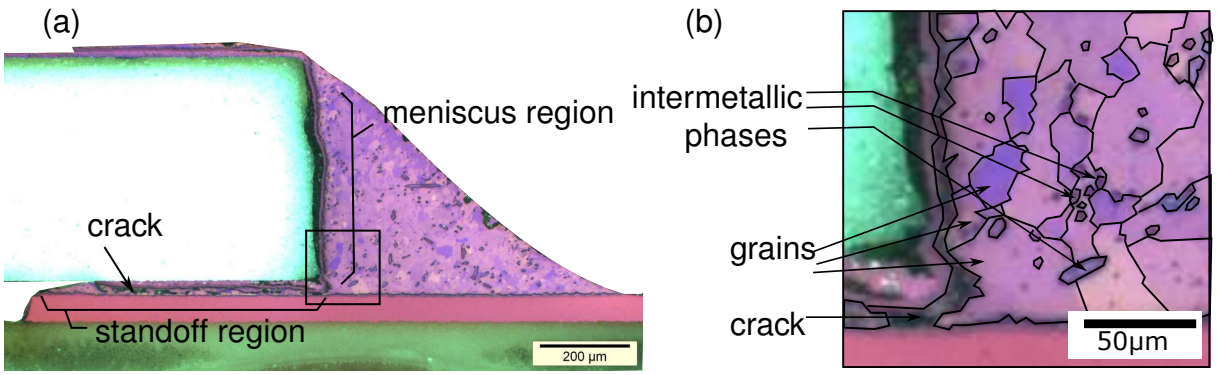

Fig. 1.3: (a) After 1000 temperature cycles -40℃/+125℃: grain size decreases. Light microscope polarized, from [7] (b) magnification: inter-granular crack propagation in the standoff region and at the bottom of the meniscus region

equal coefficients of thermal expansion of the joining partners, respectively PCB and Al_2O_3-chip resistor in this assembly. The solder joint, here the softer material, has to accommodate the thermal deformation driven by the neighboring materials which results in repetitive irreversible deformation occurring during each temperature change. Furthermore, at the homologous temperature of T_h=0.84, for T=125℃ (T_h=T/T_m, T_m is the melting temperature), plastic deformation accompanied by creep processes are expected for tin based alloys [10]. The influence of high homologous temperature on the mechanical properties of the lead free solder alloy has been widely studied, and microstructure evolution has been interpreted as a result of temperature activated creep mechanisms with a pronounced time dependency [11, 12]. Finally, in accordance with former investigations [1, 13, 14], the damage mechanisms for solder materials under passive temperature cycles can be considered as a complex interplay between creep and cyclic fatigue damages interacting under a wide range of homologous temperatures. The successive temperature cycles and thermally induced deformations continuously transform the microstructure of the material, indicating recrystallization of the β-Sn matrix. Starting from the initial state characterized by the presence of few large grains, a fine-grain polycrystalline structure and an inter-granular crack are observed after 1000 cycles indicating an ongoing degradation of the solder joint.

Current methods for reliability assessment of solder joints

Empirical models

Under field conditions, a potential solder joint degradation evolves over large periods of years. For this reason, an acceleration of aging mechanisms is necessary in order to study them. Basically, the quality and reliability of solder joints are investigated in laboratory using temperature controlled chambers. The devices are cycled between hot and cool temperature phases, with varying dwell time periods as well as temperature rates during the phase's transition. Due to the over-dimensioned thermal-loads applied, the failure occurs within a reasonable testing time. Thus, the challenging task for reliability engineers remains the lifetime extrapolations, from the accelerated lab loads towards field-like loading conditions using Acceleration Factors (AF). Acceleration factors are typically estimated empirically by using existing lifetime component data, for example following the approach proposed by Norris and Landzberg [15].

$$AK = \frac{N_{field}}{N_{test}} = \left(\frac{\Delta T_{test}}{\Delta T_{field}}\right)^{a} \left(\frac{f_{field}}{f_{test}}\right)^{b} \exp\left(c\left(\frac{1}{T_{field}} - \frac{1}{T_{test}}\right)\right) \tag{1.1}$$

However, in a recent publication, Dudek pointed out the discrepancy of AFs over field and labor testing condition for different components, which limits the application of Eq.(1.1) for lifetime prediction of various solder geometries [14].

Other methods focused on the deformation undergone by the solder material, stressed by its joining partner under temperature cycles. Engelmaier adapted the isothermal equation of Coffin-Manson and proposed a shear strain based lifetime equation [16].

$$N_f = \frac{1}{2}\left(\frac{\Delta\gamma}{\varepsilon_f}\right)^{-B}, \quad B = \frac{1}{0.442 + 6\times10^{-4}T_{mean} - 1.74\times10^{-2}\ln(1+f)} \tag{1.2}$$

f corresponds to the number of cycles per day and T_{mean} the mean temperature of a cycle. The fit parameters have been calibrated using lifetime data for tin lead solder components. The shear strain $\Delta\gamma$ in Eq.(1.2) can be estimated for example using the CTE difference of the joining partners. If only the standoff of the solder joint is considered, an approximation is given in Eq.(1.3) [17].

$$\Delta\gamma = \Delta CTE \times \Delta T \times \frac{l}{h} \tag{1.3}$$

where l and h are respectively length and thickness of the standoff region in case of a chip resistor solder joint. Nevertheless, Eq.(1.3) does not take into account either

the influence of the meniscus part nor the mechanical properties of the solder material. Therefore, numerical simulations supported by Finite Element Methods (FEM) are preferably used for lifetime estimation of solder joints. On one hand, they enable an accurate modeling of the solder joints geometries as well as complex thermal-load profiles. On the other hand, stresses and strains can be calculated on a local scale, and used as an indicator for the resulting local loads and a lifetime prognosis.

Physics-of-Failure approach supported by FE-simulation

FE based methods have been widely employed in the recent years, since the simulation techniques have been implemented and are available within commercial codes [18]. They enable reliability engineers to make fast variation of different design configurations, including geometrical variation and combination of various materials. Furthermore, the most loaded part of the product can be determined by simulation, giving crucial insight concerning the reliability and lifetime estimation of the product components. Actually, FE analysis have accelerated the development phases of electronic products, since in some cases, they can replace experimental reliability tests which are much more expensive and time consuming. Based on experimental characterization focused on secondary creep regime, phenomenological FE-material models were proposed assuming stationary creep as the main inelastic deformation mechanism for solder materials within the full temperature range of application [11, 19]. Garofalo proposed Eq.1.4 to model the secondary creep regime of metals and describe the time dependent plastic deformation using a single equation [20]. Metasch et al conducted series of incremental step creep tests on a lead free solder alloy and parametrized the Garofalo model for use in FE simulation [21].

$$\dot{\varepsilon}^p = c_1 \sinh\left(\frac{\sigma}{c_2}\right)^n \exp\left(-\frac{Q_c}{RT}\right) \tag{1.4}$$

However, creep models have been calibrated using creep experiments which are usually performed under a unidirectional load of a constant force magnitude [12] which strongly differs from typical automotive operating conditions. These imply cyclic thermal loads leading to varying strain rates, on one hand, and dwell time periods at a constant temperature where stress relaxation is expected, on the other hand. Thus, properties of the material under cyclic loads are expected to differ from those observed under uniaxial loads and high deformation amplitudes typical for secondary creep regime. Furthermore, secondary creep models neglect strain hardening properties as well as recovery processes being outside the stationary regime but more

pronounced during the primary creep regime in which actually the cyclic deformations are expected during typical automotive testing conditions.

In the state of the art methodology, damage-related parameters are derived from secondary creep models and used for lifetime prediction of solders joints under temperature cycles [1, 22]. These lifetime prediction methods combine results from FE simulations and existing lifetime components data. Damage-related quantities e.g. plastic strain $\bar{\varepsilon}^p$, plastic strain energy W^p, are evaluated using FE simulation and used in an Coffin-Manson-based lifetime equation, s. Eq.(1.5)-(1.6). The fit constants a_1, b_1, a_2, b_2 are then determined using existing lifetime components data [22].

$$N_f = a_1 \times \left(\bar{\varepsilon}^p\right)^{b_1} \tag{1.5}$$

$$N_f = a_2 \times \left(W^p\right)^{b_2} \tag{1.6}$$

Research works have demonstrated that empirical lifetime models like Eq.(1.5) are not universal and cannot be applicable to all the solder geometries [1, 14, 22]. For instance a BGA solder ball exhibits different a_i and b_i coefficients than a chip resistor solder joint [1]. Thus, when a new solder geometry differs too much compared to the geometry for which the a_i and b_i coefficients have been calibrated, a deviation from reality is expected and one has to perform the experimental reliability testing again for the new solder geometry. This discrepancy strongly limits the benefit of simulation techniques for lifetime prediction purposes since experimental reliability testing remains necessary for each new solder geometry. At least, state of the art methods may provide a relative comparison between two designs in term of reliability, but fails to predict absolute lifetime of new untested designs. On one hand, the material model used may be not accurate enough in the specific range of deformation corresponding to the mission profile. On the other hand, the damage-related parameters employed may not be sensitive enough to all relevant failure mechanisms and loading profiles considered.

Improvement of current methods

In the last decade new experimental techniques for material characterization of lead free solder alloys under cyclic loading have been reported [23, 24]. These works aimed to investigate solder mechanical behaviors under cyclic deformations, close to typical mission profiles of solder joints. Later, Yamamoto et al. carried out extended material testing on solder alloys with a focus on the interaction creep-fatigue, by vary-

ing strain rates and holding time periods [25] revealing a complex interplay of creep and fatigue damage mechanisms. Metasch et al. developed a customized experimental set-up for testing solder alloys in a wide temperature range, from -40℃ to 150℃. They pointed out a strong hardening behavior in the low temperature regime below 25℃ whereas moderate stress relaxation until a non-zero stress value were observed during holding time periods at 1% strain deformation for all the temperatures [26]. In fact, significant improvements in experimental characterization techniques including cyclic loads highlighted mechanical properties of solder materials like strain hardening in plastic domain, sensitivity to strain rate variation, stress relaxation under constant strain, cyclic stress softening etc. Thus, secondary creep models were not capable to map these mechanical properties and, in consequence, new material models for solder alloys become necessary.

Actually, similar mechanical properties are observed for steel- and Ni-based alloy above 0.5 homologous temperature, taking place in the area of gas turbine components [27, 28]. Such applications were the driving force for the development of unified viscoplastic material models capable of mapping the complex interplay of plastic deformation, hardening and creep. Furthermore, continuum viscoplastic models can be extended in the framework of continuum damage mechanics and therefore, enable lifetime prediction based on the simulation of the intrinsic damage evolution of the material [29, 30]. Recently, Kuna et al. adapted a viscoplastic Chaboche model with static recovery terms to address the strong viscous behavior of a lead free solder alloy observed during strain rate variation and relaxation tests and a Cock's pore evolution damage model for the description of the solder softening behavior [6, 31]. Yao et al. simulated solder alloy behavior using a phenomenological damage model of Lemaitre coupled with the viscoplastic equations of Chaboche [32]. Both authors postulated fatigue damage as predominant and calibrated their damage models with cyclic softening experiments. However, an application on creep damage observed experimentally within tertiary creep stage experiments [33] as well as enhanced softening after crack initiation [32] have not been reported. Moreover, a unified description of cyclic fatigue, stress relaxation behavior, unidirectional primary, secondary and tertiary creep within one material model has not been shown by now for solder alloys. Although creep damage was not taken into account, a damage mechanics approach for lifetime prediction of solder joints show very promising perspectives. Indeed, damage variables can be monitored over the cycles and provide the evolution of degradation, from its initial state up to significant degradation stage, as reported by Wippler et al. for a 2D simulation of chip resistor solder joint [33].

1.3. Outline of the thesis

As highlighted in recent research reports, lifetime of electronic components in automotive applications is often limited by solder joints reliability [1, 3]. The present work is focused on solder joints durability on the material level and, specifically, the modeling of the material behavior. The theoretical foundation concerning the phenomenological modeling of materials, and particularly the models employed on metals are presented in chapter 2. This theoretical part includes the basics of continuum mechanics in terms of nonlinear plasticity extended in the field of damage mechanics. Most of the concepts have been applied for steel based alloys loaded at high temperature. It will be shown within the thesis, that the viscoplastic and damage models originally formulated for steel alloys can be employed as well to model lead free solder material behavior in the temperature range corresponding to automotive applications. In chapter 3, the experimental setup exclusively developed to measure the mechanical properties of solder alloys is presented. The mechanical behavior is revealed through standardized tests: cyclic strain rate variation and stress relaxation tests characterize the deformation properties whereas cyclic fatigue and creep tests are carried out to investigate the damage properties. The resulting microstructure evolution during the measurements is analyzed by EBSD microscopy (Electron BackScatter Diffraction). The experimental evidence reported in chapter 3 constitute the basics for the new material model formulation presented in the following chapter. The mathematical framework for numerical integration into Finite Element (FE) code is briefly described in chapter 4 although the successful implementation has been a crucial step for enabling simulations of complex geometries using FE commercial packages. The second part of the chapter 4 deals with the procedure for model parameters identification, which has been worked out within the thesis and employed for the solder alloy studied here. In chapter 5, the lifetime prediction methods based on 3D FE-simulations is illustrated on a chip resistor example under thermal cyclic loads. Finally, the simulated lifetime is compared to existing lifetime component data for validation of the methodology. The last chapter summarizes the main findings of the work and proposes further developments to improve lifetime prediction based on damage simulation of solder joints.

2. Theory for the mechanical behavior of metals

Continuum mechanics builds the foundation for a phenomenological description of the macroscopic behavior of a material submitted to a mechanical load and subsequently undergoing deformation. During recent years, numerous advanced material models have been developed. One of them, which initiated numerous further works in both the scientific and industrial communities, dates back to the 1970's and the work of Chaboche [34]. The author proposed constitutive equations of nonlinear plasticity and viscoplasticity for a description of the mechanical behavior under cyclic repetitive loads of steel-alloys up to 600℃. This temperature corresponds roughly to T_h=0.5 in terms of the alloy's homologous temperature (Eq.(2.1)) with T_m as the melting temperature in K.

$$T_h = \frac{T}{T_m} \quad \text{(T in K)} \tag{2.1}$$

Later, the basic equations were extended to model other metals as copper, nickel, aluminum [35]. Finally, the Chaboche model has been adapted into the framework of damage mechanics. The constitutive equations provide not only the mechanical response but also the intrinsic damage of the material described at the macroscopic scale by internal state variables. [36]. Such a damage model is mainly employed in the reliability assessment of critical applications as, for example, high temperature alloy for turbine blades [27]. Besides, a modified Chaboche-damage model was recently employed for lifetime prediction of solder joints [6, 33].

2.1. Modeling deformation

2.1.1. Elastic-plastic deformation

Under small deformations, the material is assumed elastic: under loading, the material deforms proportionally to the tension (s. Eq.(2.2)). This linear rule (Hook's law) is applied particularly for metals in the elastic domain.

$$\sigma = E\varepsilon^{el} \tag{2.2}$$

Within the generalized linear equation Eq.(2.2), the stress σ and elastic strain ε^{el} are proportional to the coefficient E which is defined as the Young's modulus of the material. If the deformation is sufficiently large and the stress generated beyond the yield stress σ_0, the material can deform plastically. In continuum mechanics, the strain deformation comprises a sum of an elastic, plastic and a thermal part (s. Eq.(2.3)).

$$\varepsilon = \varepsilon^{el} + \varepsilon^{p} + \varepsilon^{th} \tag{2.3}$$

The elastic law is given in Eq.(2.2). An overview of the common plastic laws employed for metals is depicted in next section. The thermal strain ε^{th} refers to the volume expansion or contraction of the material in response to a change of temperature with respect to a reference temperature T_{ref}. At the temperature T_{ref} the material is assumed to be in its stress-free state.

$$\varepsilon^{th} = \alpha_{CTE} \times (T - T_{ref}) \tag{2.4}$$

The Coefficient of Thermal Expansion α_{CTE} (CTE) is often considered constant for small temperature ranges. For metals, the CTE is typically an increasing function of the temperature [37].

When the material deforms in the plastic domain, its resistance increases with increasing force load: in this case the material hardens. Hardening results as a consequence of inelastic deformation, which leads to an irreversible change in shape. The inelastic deformation can be separated into plastic and viscous part. The corresponding stress response is related to both, e.g. the hardening due to deformation (strain hardening) and hardening due to time (viscoplasticity). Some phenomenological models treat both in separate ways [18, 38, 39]. The class of viscoplastic models employed here formulate the inelastic strain within a unique plastic strain variable [40, 41]. Such models are usually referred to as unified. The fractions of time and strain hardening are strongly dependent on the material and the temperature. At the microscale level, the plastic deformation is interpreted in terms of microscopic processes. Ashby and Frost classified the different deformation mechanisms as a function of homologous temperature, the relative magnitude of shear load and the rate of deformation [10]. In this way, regions are formed, which correspond to the dominant mechanism, creating a so-called *deformation mechanism map*, as depicted in

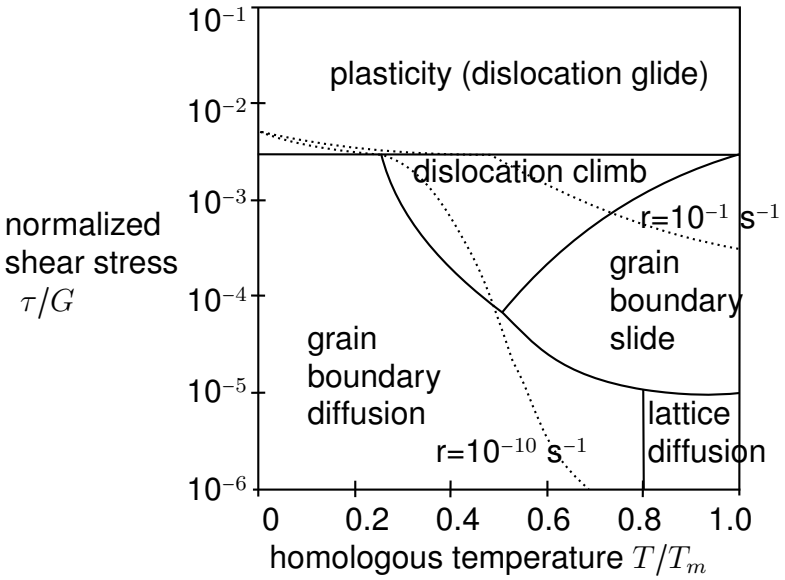

Fig. 2.1: Deformation mechanism map for metals adapted from Ashby and Frost [10]

Fig.2.1.

In automotive applications including laboratory and field-like loading conditions, solder joints can be exposed to temperatures between T_h = 0.47 (T=-40℃) and T_h=0.86 (T=+125℃). Under these conditions, strain rates in the range of about r=10^{-2}... 10^{-8} s^{-1} are expected during the phases of heating, dwell-times, as well as long-time cooling of the hardware assembly. Therefore, according to the Ashby map, dislocation climbing (at high rate, low temperature) and grain boundaries sliding (at low rate, high temperature) are expected to govern the deformation of the material at the atomic scale. Back to the macroscale level described by constitutive material models, the deformation mechanisms are mapped by strain- or time-hardening terms. On one hand, plasticity due to dislocation glide occurs at high strain rates, high stresses and low homologous temperatures. This mechanism can be associated with strain hardening and quasi-time-independent plasticity. On the other hand, viscous effects dominate at lower strain rates and high homologous temperatures. However, strain hardening cannot be completely neglected in this regime as reported by Chaboche [40] and Nouailhas [42] for steel alloys under intermediate temperatures. Thus, dislocation climb and grain boundary sliding processes at the microscale level are considered as a superposition of time and strain hardening effects at the macroscale level. Under high homologous temperatures time hardening properties are expected to dominate, whereas strain hardening is more pronounced in the low temperature regime.

2.1.2. Strain hardening

The hardening law is formulated by a plastic flow rule which describes the inelastic behavior and leads to nonlinear stress evolution in the plastic domain. For isotropic materials, as considered here, there are two types of hardening rules which can be combined, namely kinematic and isotropic hardening. The kinematic hardening rule assumes constant yield surface shape. The yield surface can be represented by a sphere in the principal deviatoric stress plane (see Fig.2.2). The radius of the sphere corresponds to the yield stress σ_0 so that elastic deformation occurs for stress states located inside the sphere. In order to fulfill the consistency condition under plastic deformation, $f = 0$ Eq.(2.5), the stress has to be located on the yield surface.

$$f = J_2(\sigma - X) - R - \sigma_0 \tag{2.5}$$

In order to maintain this condition true, the back stress variable X moves the yield sphere in the deviatoric stress plane as schematically shown in Fig.2.2. Finally, the evolution of X matches the nonlinear stress-strain flow after yielding, i.e. during plastic deformation. Widely used for modeling the mechanical behavior of metals under cyclic and monotonic loads, the integration of Eq.(2.6) takes into account the transient hardening behavior in each stress-strain loop.

$$\dot{X} = \frac{2}{3} c \dot{\varepsilon}^p - \gamma X \dot{\bar{\varepsilon}}^p \tag{2.6}$$

In this form, the equation Eq.(2.6) was initially proposed by Armstrong and Fredericks [43], as an improvement of the description of the Bauschinger effect. The first linear term (also called Prager's term [44]) describes the smooth hardening transition after yielding, where c is a material parameter. The second term is referred to as a recall term or dynamic recovery and is responsible for the nonlinear hardening evolution with the increase of plastic strain. The ratio c/γ matches the maximal value of X after large plastic deformation. The simplicity of Eq.(2.6) enables relatively easy calibration of the material parameter c and γ, for which only strain controlled cyclic or monotonic tests are necessary.

In contrast, isotropic hardening characterizes the growth of the yield surface with the accumulation of plastic strain. It describes the slow change of hardening with a monotonic increase of the isotropic variable R superposed to the yield stress of the material σ_0, as shown in Fig.2.2. The evolution law is given in Eq.(2.7)

$$R = Q\,(1 - \exp(-b\bar{\varepsilon}^p_{acc})) \tag{2.7}$$

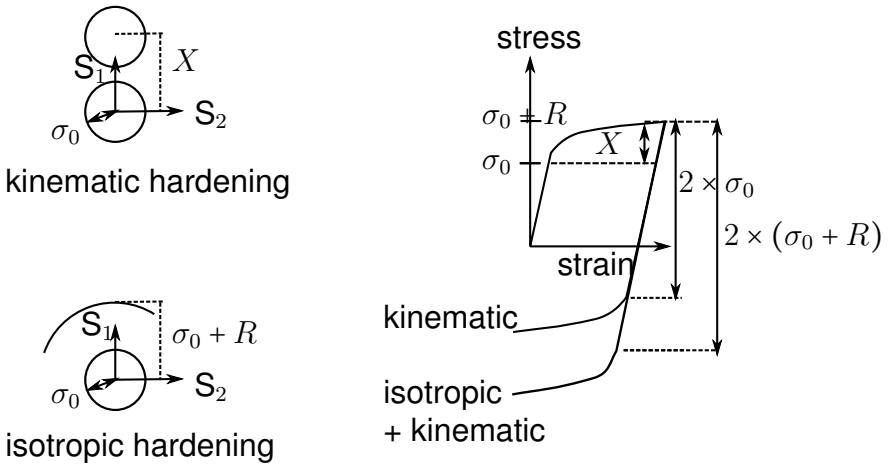

Fig. 2.2: Strain hardening modeled by kinematic and isotropic flow rules represented in deviatoric stress planes and stress-strain behavior under reversal loads

The effect is observed under strain controlled cyclic loads by an increase of the peaks of maximal stress after the first cycles. After sufficiently large number of cyclic loads, the relative increase of peak stress within subsequent cycles saturates, which leads to the stabilization of cyclic hardening. The material parameters Q and b describe respectively the asymptotic value of stress reached after stabilization and the speed of saturation, which is a function of the accumulated plastic strain $\bar{\varepsilon}^p_{acc}$. As mentioned above, strain hardening (pure kinematic or combined isotropic and kinematic) is related to the amount of stress generated in response to an applied deformation. Within the previous equations (2.6)-(2.7), time effects are omitted, i.e. the generated stress remains constant during a strain rate variation test, or a stress relaxation test. This model has been adapted for the description of the mechanical behavior of metals at a relatively low homologous temperatures [45]. At higher homologous temperatures, viscous properties become more pronounced. In this regime, a correct description of the stress-strain interaction requires the integration of time hardening effects.

2.1.3. Viscoplasticity

Solder materials are employed in industrial applications at high homologous temperatures of $T_h > 0.45$. As a consequence, the time hardening properties of the material cannot be neglected. Initially proposed to model stainless steels above 600°C, Chaboche et al. developed a new class of material model for the description of time hardening effects. The viscoplastic material model proposed is now often referred

to the author's name. The unified viscoplasticity framework of Chaboche makes use of both time independent strain hardening and rate dependent plasticity. Kinematic and isotropic hardening parts are both incorporated to describe the strain hardening effects of the primary creep domain. Moreover, the time effect is introduced by a thermodynamically consistent approach, defining a viscoplastic potential Ω Eq.(2.8) from which irreversible deformation can be derived Eq.(2.9) [36].

$$\Omega = \Omega(\varepsilon, \sigma, T, X, R) \tag{2.8}$$

$$\dot{\varepsilon}^p = \frac{\partial \Omega}{\partial \sigma} \tag{2.9}$$

The choice of the viscoplastic potential determines the plastic flow rule. Theoretical works have identified phenomenological potential function Ω, which is based on experimental observations like e.g. the strain rate dependency, steady state creep behavior and stress relaxation behavior. A detailed overview of the theory is given in a paper by Chaboche [46] where the interaction creep-viscoplasticity is discussed. In the viscoplastic theory of Chaboche the potential is based on the viscous stress σ_v which is a function of the internal state variables R (isotropic hardening) and X (back stress for kinematic hardening) in Eq.(2.10).

$$\sigma_v = J_2(\sigma - X) - R - \sigma_0 \tag{2.10}$$

In the following years, different potentials have been proposed in literature from which various rate dependent plastic flow rules have been derived. The simple power function Eq.(2.11), is often used as the rate dependent part of the Chaboche model. Combined with the strain hardening rules Eq.(2.6)-(2.7), the unified material model has been implemented in FE-commercial software ANSYS [18].

$$\Omega = \frac{K}{n+1} \langle \frac{\sigma_v}{K} \rangle^{n+1} \qquad \Rightarrow \qquad \dot{\bar{\varepsilon}}^p = \left(\frac{\sigma_v}{K} \right)^n \tag{2.11}$$

However, the flow rule in Eq.(2.11) shows limitations for the description of the rate dependency at high strain rate regime. Nouailhas observed a vanishing stress dependence on strain rate at rapid loading of stainless steels [42]. Thus, the authors proposed the potential function Eq.(2.12) incorporating the saturation of time hardening using an exponential term α.

$$\Omega = \frac{K}{n+1} \frac{1}{\alpha} \exp\left(\alpha \langle \frac{\sigma_v}{K} \rangle^{n+1} \right) \qquad \Rightarrow \qquad \dot{\bar{\varepsilon}}^p = \langle \frac{\sigma_v}{K} \rangle^n \exp\left(\alpha \langle \frac{\sigma_v}{K} \rangle^{n+1} \right) \tag{2.12}$$

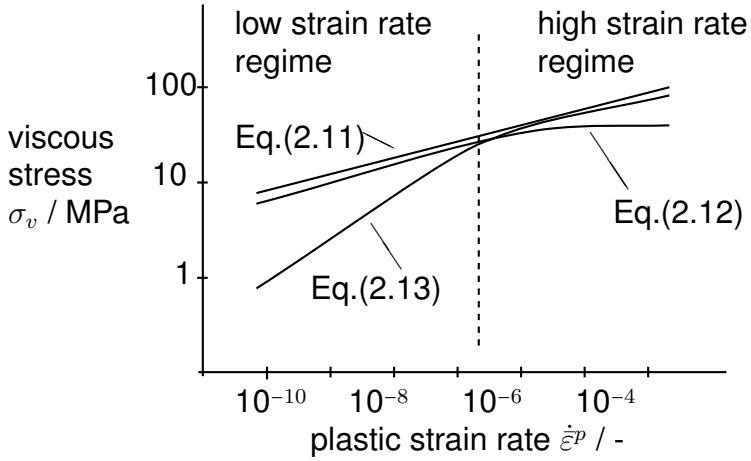

Fig. 2.3: Schematic representation of the visco-function Eq.(2.11)-(2.12)-(2.13) for description of time hardening in the low and high plastic strain rate regimes

Outside the saturation domain at high strain rate, the viscous stress remains a power function of the plastic strain rate, i.e only a logarithmic dependency stress vs. strain-rate covers the intermediate and low strain rate regimes. Finally, a potential function later proposed by Chaboche Eq.(2.13) describes two distinct strain rate regimes, for which the slope at high strain rate is not necessarily horizontal (see Fig.2.3), in contrast to the model from Eq.(2.12).

$$\Omega = \frac{K_1}{n_1+1}\langle\frac{\sigma_v}{K_1}\rangle^{n_1+1} + \frac{K_2}{n_2+1}\langle\frac{\sigma_v}{K_2}\rangle^{n_2+1} \qquad \Rightarrow \qquad \dot{\bar{\varepsilon}}^p = \langle\frac{\sigma_v}{K_1}\rangle^{n_1} + \langle\frac{\sigma_v}{K_2}\rangle^{n_2} \tag{2.13}$$

This plastic flow rule is referred to as *ONERA2* model, initially proposed by the author in 1989 [40]. In comparison to the other flow rule Eq.(2.11)-(2.12), the double exponential equation Eq.(2.13) is more flexible, capable to fit rate dependency for high and low strain rate when the slope of the curve varies over the strain rate decades as illustrated in Fig.2.3.

Until now, the Eq.(2.13) represents one of the most advanced viscoplastic potentials within the unified viscoplastic theories. The two slopes describe the rate dependency at high and intermediate strain rates. Experimentally, it can be investigated by cyclic loading tests under strain rates of moderate deformation speed. The low strain rate regime can be addressed using creep tests under loads, which naturally reside in the regime of low stresses. In order to describe both strain rate regimes, further non-unified models have been developed. Cailletaud proposed a two yield surfaces model which implies two dissociated plastic strains: one for quasi time independent plasticity and one for rate dependent creep deformation [38, 39]. Although the parti-

tioning of the inelastic strain into creep- and viscoplastic flows renders the calibration of the parameters easier, the consistent numerical integration of this class of models is more complex and the stress algorithms are less efficient compared to unified viscoplastic models as it has been evaluated in [41]. The main reason is related to the number of state variables, which have to be numerically calculated solving a nonlinear algebraic system of equations. The number of equations for non-unified models is higher than for the unified ones, thus increasing the computational effort. Nevertheless, a non-unified model has been successfully implemented into the commercial FE-software ABAQUS [47] with two yield surfaces. The model is available at the MPA University of Stuttgart. Some applications using the model can be found in [27, 28, 29, 30].

2.1.4. Time recovery effect (static recovery)

As mentioned in the previous section, the unified viscoplastic theory incorporates both strain and time hardening effects through a single plastic flow rule. However, a correct description of stress relaxation and steady state creep strain requires some modification of the basic strain hardening rules. A crucial improvement is the extension of the back stress terms by static recovery terms $d\left(J_2(X)\right)^{m-1}$ as in Eq.(2.14).

$$\dot{X} = \frac{2}{3} c\dot{\varepsilon}^p - \gamma X \dot{\bar{\varepsilon}}^p - d\left(J_2(X)\right)^{m-1} X \tag{2.14}$$

The viscous properties of materials can be measured using three types of tests: by variation of the strain rate, the strain rate dependency in the higher strain rate regime is obtained. In order to evaluate the share between time and strain hardening, a stress relaxation test can be performed. These two tests are schematically represented in Fig.2.4, associated with their state variables $X + R$ (strain hardening part) and the viscous variable σ_v. The stress state S does not follow the yield surface like in a pure strain hardening model (see Fig.2.2) but is located on the equipotential visco-surface. This surface is represented by a sphere of radius $\sigma_v + R$. When the strain rate increases, the equipotential visco-surface grows and the stress calculated increases whereas at the same time the quantities X and R remain constant (strain hardening), independently from the strain rate. During stress relaxation, the strain is maintained constant. If the material exhibits viscous properties, then the stress would relax. Typically, an exponential relaxation is observed as a function of time until a non-zero stress level is reached. As there is no explicit time influence in the formulation of X and R Eq.(2.6)-(2.7) (no static recovery), the quantity $X + R$ remains

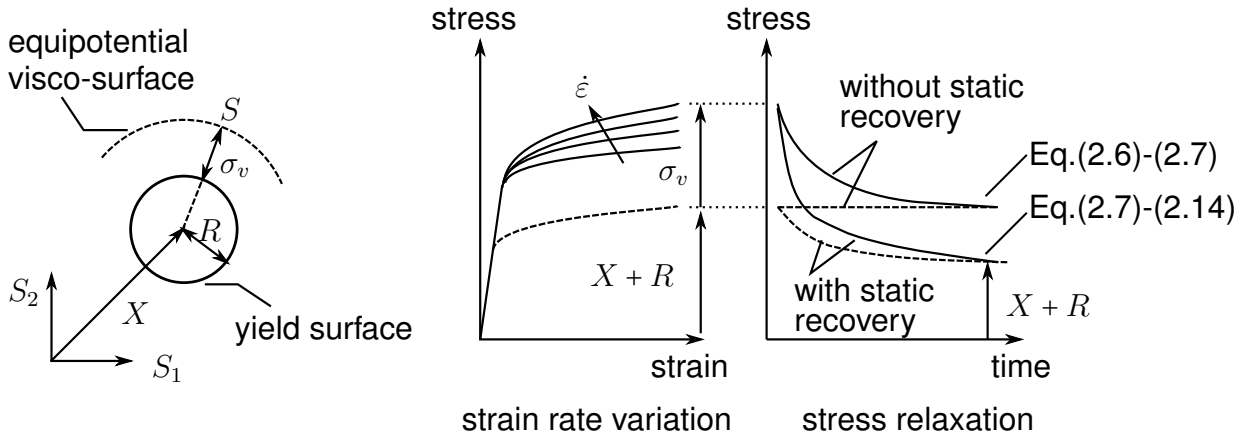

Fig. 2.4: Scheme of state variable evolution during strain rate variation tests and relaxation tests. Strain and time hardening properties are represented by the state variables $X + R$ and σ_v, respectively

constant. This value is equal to the one reached at the end of the loading phase. Therefore, the viscous stress can decrease down to this value. Wippler reported a high amplitude of stress relaxation for solder material above 65℃, which decreases beyond the theoretical strain hardening limit $X + R$ after two hours [6, 33]. In order to describe this behavior the authors implemented a static recovery term in the back stress similarly to the Eq.(2.14). Thus, the static recovery terms in the back stress amplify the stress relaxation by decreasing the strain hardening parts, which relax as a function of time (see Fig.2.4). The influence of static recovery during strain variation is negligible for the high strain rate (typically for $\dot{\epsilon} > 1 \times 10^{-5}$ s^{-1}), because the effect takes place only after a significant period of time, i.e. at very low strain rates or during several hours of stress relaxation periods.

The third possibility to investigate the viscous properties of the material is to perform creep tests. Under constant temperature and force load the deformation is measured over time until rupture. Typical creep strain curves are divided in three parts: primary creep and secondary creep stages are considered driven by viscous deformation. The tertiary creep state is related to creep damage development which will be discussed in the next section.

During primary creep, the strain hardening state variable $X + R$ increases and stabilizes. This stabilization characterizes the beginning of the secondary creep state where strain and time hardening are in an equilibrium state. Therefore, the strain

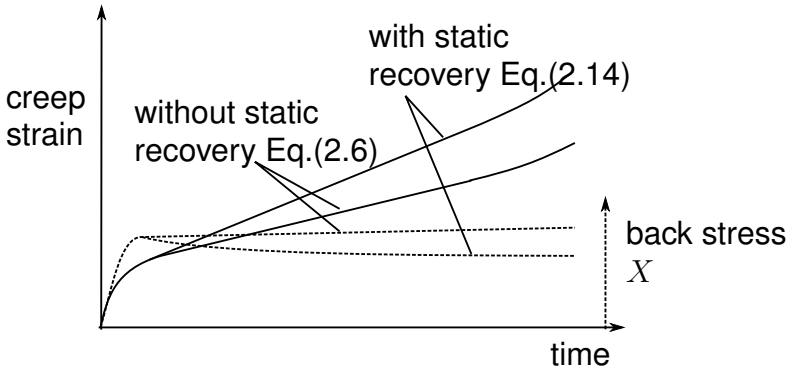

Fig. 2.5: Schematic representation of the back stress evolution (X) during primary and secondary stage of a creep test

rate develops in a stable manner within the secondary creep stage. As shown in Fig.2.5, the static recovery plays as well a role in the description of the steady state creep strain rate. The time recovery term reduces the back stress over time, which leads to a simultaneous increase of the time hardening part and consequently the corresponding strain rate. A correct description of the strain rate in the secondary creep state and the strain rate variation in the higher strain rate regime necessitates an extended viscous function Eq.(2.13), as well as time recovery terms in the strain hardening part (Eq.(2.14)).

Extensively investigated during recent years, solder materials reveal a pronounced time dependent mechanical behavior [1, 19], as well as strain hardening properties at lower temperatures, for instance when loaded by strain controlled cyclic loads [48]. Chaboche and co-workers developed a flexible material model from which the different terms can be adapted to map the mechanical behavior of various metals. However, the lack of sufficient material data for lead-free solder, combined with the complexity of the procedure to find the material parameters, have limited the use of Chaboche-based material model for description of the mechanical properties of solder materials. Recently, Wippler and Kuna simulated the behavior of a Sn-solder alloy using a Chaboche model with static recovery Eq.(2.14) and one power yield function Eq.(2.11). A good agreement was found for strain rate variation and stress relaxation behavior, however no investigation and modeling of the creep strain behavior at low stress was reported [6]. In the present work, a double power viscous function Eq.(2.13) combined with strain hardening and recovery terms Eq.(2.14) are implemented in order to model both the cyclic and creep deformation behavior of solder materials within an extended temperature range from -40°C to +125°C.

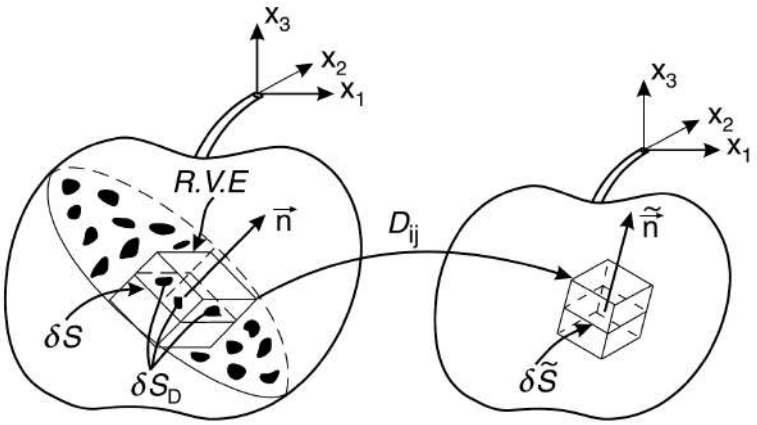

Fig. 2.6: Physical discontinuities and mathematical description on a continuum scale after discretization by a Representative Volume Element (RVE) from Lemaitre [55]

2.2. Modeling damage mechanisms

2.2.1. Continuum Damage Mechanics (CDM) approach

Advancements in measurement techniques for detecting and characterizing defects in materials and structures, established the basis for the development of phenomenological evolution laws mapping damage evolution for various material classes: metals, composite, ceramics, as well as concrete [49]. Numerous works shed light on the correlation between the mechanical response of a solid, its loading history as well as the type, quantity and distribution of defects in its structure. Dislocation movement, defects at grain boundaries as well as crack initiation due to local irreversible deformations have been observed at microstructure level [50, 51, 52, 53, 54]. Such inelastic processes leading to damage, are localized at the microscale. In order to take into account the collective influence of microscopic damage sources on the macroscopic scale, damage state variables have been introduced in the constitutive material models [36]. This lead to the development of the Continuum Damage Mechanics CDM framework (see Fig.2.6).

However, the influence of local damage cannot be easily accessed and quantified as it is the case for strains and stresses typically measured on standardized samples. The damage state variable D has been introduced by Kachanov as the local ratio between the density of micro-defects δS_D regarding the infinitesimal surface δS of a Representative Volume Element RVE where the defects are locally estimated by Eq.(2.15) [56].

$$D = \frac{\delta S_D}{\delta S} \tag{2.15}$$

After homogenization, the effective surface of the RVE δS becomes $\delta\tilde{S}$ in which the theory of continuum mechanics can be further applied. According to Kachanov's definition Eq.(2.15), $D = 0$ corresponds to virgin material in its initial state, whereas $D = 1$ occurs at the *breaking up* of the RVE which generally corresponds to a macroscopic crack initiation [51]. From an engineering point of view, the present damage theory and CDM approach turns promising for lifetime prediction of complex structures. Indeed, the main advantage provided by the CDM approach is that the induced progressive material deterioration through the decrease of strength, which can end up to crack initiation and propagation can be calculated on complex structures. The concept of effective stress Eq.(2.16) couples the mechanical properties and damage quantities. The elastic and hardening equations are continuously modified which enables the description of an intermediate damage state of the material $0 < D < 1$, occurring before crack initiation.

$$\tilde{\sigma} = \frac{\sigma}{1 - D} \tag{2.16}$$

The different damage mechanisms are separately formulated as a function of appropriate mechanical quantities, and are integrated into the D variable. From a practical point of view, the damage mechanisms can be identified and quantified within experimental tests using standardized samples. Fatigue and creep tests are used to assess damage development in the material under specific controlled loading conditions e.g. controlled strain-rate and strain amplitude, temperature or stress magnitude of the load. In the next sections, the formulation of equations governing the damage mechanisms relevant for the degradation of solder joints are discussed on the basis of results from different testing methods suitable to reveal and quantify the evolution of damage in the material.

2.2.2. Fatigue damage

A metallic material subjected to repetitive loads above the elastic limit can fail due to resulting stress levels much lower than that sufficient to cause fracture in an unidirectional static tensile test. The fracture occurring under cyclic condition is also called fatigue failure [55]. Failure investigations in metallic materials reveal that the fatigue process includes two domains. The first domain corresponds to high loads which cause high plastic strain deformation at each cycle. This domain is associated with low number of cycles to failure and is referred to as Low Cycle Fatigue (LCF). The second domain of cyclic loading is associated with small loads under which the material deforms mainly within the elastic domain. Under such condition, the material

can undergo a large number of cycles without failure and the corresponding domain is referred to as High Cycle Fatigue (HCF). Both domains are relevant for the design of electronic modules and reliability assessment of solder joints. For example, the failure caused due to mechanical vibration is located in the HCF domain. Pure thermal loading profiles on electronic components in an accelerated laboratory tests cause solder joints failure well below ten thousand cycles [14, 22]. Consequently, the fatigue domain of solder joints under laboratory thermal cycling is the Low Cycle Fatigue (LCF) as defined in [55] for cyclic failure occurring under 10000 cycles. The LCF domain is typically characterized by repeated cyclic strain controlled loads on a push-pull specimen.

The Coffin-Manson-Basquin approach

The Coffin-Manson-Basquin approach is employed to calculate analytically the number of cycles to crack initiation N_a. Initially developed to describe the fatigue behavior of steel alloys at a moderate homologous temperature [57, 58, 59], this simple empirical relation associates the number of cycles N_a to the strain amplitude $\Delta\varepsilon^{tot}$ which can be divided into elastic and plastic part $\Delta\varepsilon^{el}$ and $\Delta\varepsilon^{pl}$, respectively (s. Eq.(2.17)).

$$\Delta\varepsilon^{tot} = \Delta\varepsilon^{el} + \Delta\varepsilon^{pl} = \frac{\sigma_f^{'}}{E}\left(N_a\right)^b + \epsilon_f^{'}\left(N_a\right)^c \tag{2.17}$$

E is the Young's modulus of the material. $\sigma_f^{'}$ is the fatigue strength coefficient and b the fatigue strength exponent which corresponds to the slope of the curve in the HCF domain, where the elastic strain prevails. $\epsilon_f^{'}$ is the fatigue ductility exponent which is approximately equal to the true fracture strain in unidirectional tension. c is the fatigue ductility exponent, corresponding to the slope of the curve in the LCF domain where plastic strain prevails. Basically, elastic and plastic strain are evaluated on the stress-strain hysteresis as illustrated in Fig.2.7(a). Considering the deformation purely elastic after reversing the direction of deformation, the plastic strain amplitude can be calculated by $\Delta\varepsilon^{pl} = \Delta\varepsilon^{tot} - \Delta\sigma/E$, where $\Delta\sigma/E$ is identified as the elastic strain amplitude.

The double logarithmic scale is used to establish the Coffin-Manson-Basquin diagram where elastic and plastic strain define two notable domains in Fig.2.7(b). The empirical approach proposed by the authors is intended for a fit of the fatigue behavior of metal alloys. ASM (American Society for Metals) reported that the exponent b and c vary respectively between $-0.05 \cdots -0.12$ and $-0.5 \cdots -0.7$ [60], where a low value of b and c corresponds to a material with a long fatigue life. This approach is

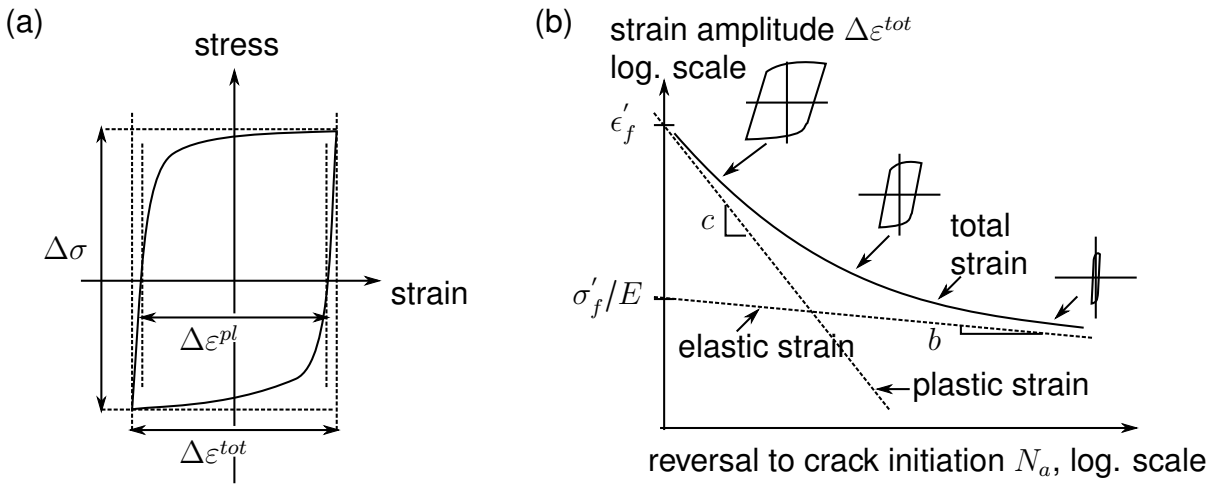

Fig. 2.7: Evaluation of fatigue damage using the Coffin-Manson-Basquin approach for strain controlled cyclic tests. (a) stress-strain hysteresis cycle, (b) Coffin-Manson-Basquin diagram

also widely used for estimation of lifetime of real components and is also mentioned in a standardized guideline for reliability calculation [61]. However, a direct application of Eq.(2.17) in case of non-isothermal loading conditions is not possible, because the parameters E, $\epsilon_f^{'}$, b, $\sigma_f^{'}$ and c are temperature dependent and only valid for isothermal cycles. Moreover, the Coffin-Manson approach takes the strain amplitude over one cycle as a damage-relevant parameter without taking into account cyclic softening specific for various alloys. Besides, the continuous evolution of damage modifies the mechanical properties, such as the distribution of elastic and plastic strain varies with the accumulation of cyclic loads. In fact, the Coffin-Manson-Basquin Eq.2.17 is appropriate to estimate the lifetime of a component only if the load and the mechanical properties remain unchanged over the cycles. Otherwise, the damage can only be properly modeled by a continuous description of the mechanical behavior, from the initial state of deformation, and towards the stage I, II and III of the cyclic fatigue up to the rupture of the sample (see Fig.2.8).

Modeling cyclic softening

Basically, the mechanical properties of a metal can change during its service-life which is the result of microstructure modifications and aging phenomena observable at the microstructure level. The environment temperature, and specific loading conditions are responsible for these modifications which affect the stiffness and strength of the material.

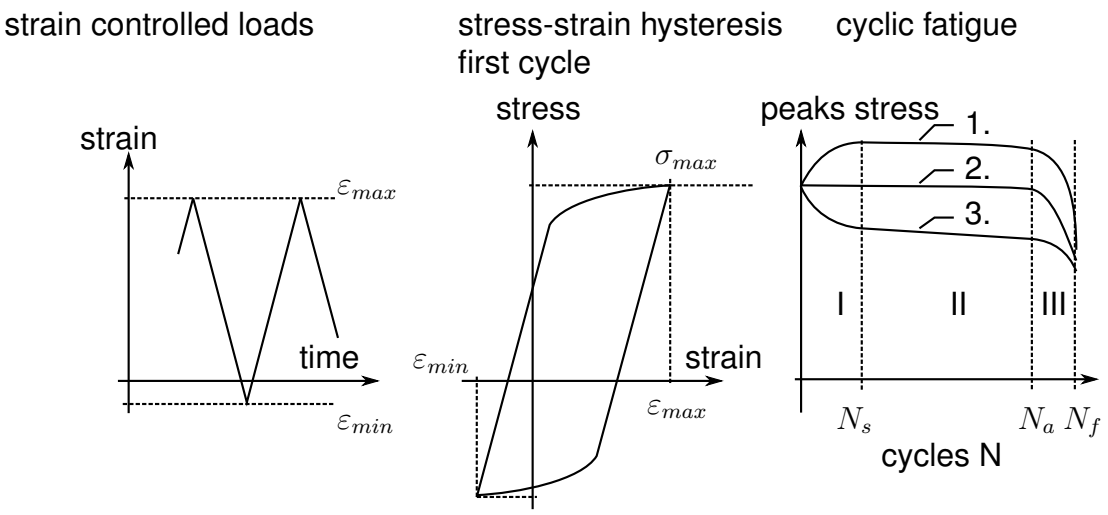

Fig. 2.8: Cyclic behavior of the material under strain controlled loading conditions during a LCF test

The mechanical response associated to cyclic fatigue can be divided in three stages throughout the life of the sample. In the first stage (I) $0 \dots N_s$, a fast cyclic hardening (type 1.) or softening (type 3.) can be observed. The damage development in this phase is considered low, and the cyclic hardening or softening is attributed to microstructural rearrangement with the accumulation of plastic strain [45]. The cyclic hardening or softening can be modelled by the isotropic hardening variable R Eq.(2.7), setting a positive or negative value of Q, respectively. Cyclic softening has been also modeled by a progressive increase of the dynamic recovery term in the kinematic back stress Eq.(2.6). Marquis proposes the Φ function in Eq.(2.18) for this purpose [45].

$$\phi(\bar{\varepsilon}^p_{acc}) = \phi_\infty + (1 - \phi_\infty) \exp(-b_k \bar{\varepsilon}^p_{acc}) \tag{2.18}$$

The stage (II) comprises the major part of the specimen life from the stabilized state N_s up to crack initiation at N_a cycles. During this phase, depending on the material and the temperature, the strength reduces resulting in a decrease of the peak stress with each repeated cycle. After N_a, the cyclic softening accelerates which corresponds to an initiation of a macroscopic crack in the sample. The decrease of the peak stresses follows in the phase (III) until the rupture of the sample at N_f. Typically, SAC based solders alloys show either type II or III, depending on the applied temperature, see Chap.3. Besides, the solder material tends to behave from a light cyclic hardening to a more pronounced cyclic softening by increasing the temperature

[33, 41]. Since the validity of damage mechanics beyond crack initiation is still under debate, most of the established damage models are only able to describe the stage I and II of the cyclic softening curve. Among them emerge two classes of models: those which are thermodynamically consistent, e.g. Lemaitre's model on one hand, and the phenomenological fatigue models, on the other hand.

Lemaitre's damage model

Lemaitre formulated the fatigue damage evolution as a function of the accumulated plastic strain and the current stress state. The equations are derived from the elastic energy release Y (Eq.(2.19)-(2.20)), and considered as thermodynamically consistent. Two material coefficients s and S are employed to adjust the model to experimental data. The damage rate is formulated (Eq.(2.19)) as a nonlinear function of stress (through the Y variable) multiplied by the linear accumulation of plastic strain. The popularity of this model is probably due the simplicity of these equations and consequently the calibration of the material coefficients S and s is possible within a moderate effort and a relatively small amount of experimental data [55]. Besides, the linear accumulation of plastic strain makes the linear extrapolation of D possible, for example under cyclic loading condition. In this way, one can considerably reduce the computational time by calculating a few cycles and then extrapolating the damage variable up to crack initiation where the evolution of D becomes nonlinear [54].

$$\dot{D} = \left(-\frac{Y}{S}\right)^s \dot{\bar{\varepsilon}}^p \tag{2.19}$$

$$-Y = \frac{1}{2(1-D)^2 E}\left(\frac{2}{3}(1+\nu)\sigma_{eq}^2 + 3(1-2\nu)\sigma_H^2\right) \tag{2.20}$$

However, only a linear dependency between the plastic strain and the damage development is given by Eq.(2.19)-(2.20). The non-linearity in these equations is with respect to the stress in which the damage rate follows a power function. For very ductile material, as a solder alloy at high homologous temperatures, the damage is much more sensible to the plastic strain than to the stress generated. Thus, the description of fatigue damage accumulation by Lemaitre's model is in this case limited, particularly at low strain amplitudes and high temperatures, where solder alloys show high ductility [41].

MPA phenomenological fatigue model

Alternative equations to model fatigue damage have been proposed, as for example at the MPA Stuttgart University. The goal was to find a suitable mathematical formulation to describe the damage evolution observed during cyclic loads at various strain amplitudes. A strong dependence of the accumulated plastic strain has been observed, which reveals a nonlinear evolution at different strain amplitudes [27, 29]. The damage Eq.(2.21) does not derive from an obvious thermodynamic potential or energy release like in the Lemaitre's model, however, this phenomenological equation provides a better description of the observed damage evolution.

$$D_1 = A_1 \times \bar{\varepsilon}^p_{acc,1} + B_1 \times \left(\bar{\varepsilon}^p_{acc,1}\right)^{C_1} \tag{2.21}$$

Eq.(2.21) is integrated in a complex viscoplastic-damage material model available at MPA (CNOW-model [28]). As the damage parameter D is coupled with the mechanical equations, the stages II and III depicted in the cyclic softening curve (see Fig.2.8) can be reproduced in the simulation. The first linear term accounts for the slow decrease of peak stresses observed during stage II. The second term (power function of $\bar{\varepsilon}^p_{acc,1}$) describes the progressive acceleration of damage-rate just before crack initiation. In principle, this model is capable to describe the fast stress fall after crack initiation (stage III in Fig.2.8). Nevertheless, the transition between the stage II and III can be very smooth for some materials, and in this case the damage-rate simulated with Eq.(2.21) can be too high after crack initiation as reported by [28]. In contrast, for the lower strain amplitudes, this formulation can lead to more conservative predictions compared to experimental data.

2.2.3. Creep damage

On one hand, fatigue damage can take place during the repetitive accumulation of plastic deformation under cyclic loads. On the other hand, creep damage has been typically attributed as the slow degradation of the material subjected to a tensile load over a long period of time. Creep damage is commonly investigated using uniaxial creep tests. Microstructure analysis performed by means of SEM on creep test samples reveals the formation of cavities and creep pores and reveal an inter-granular crack growth [41], commonly attributed to creep damage also in other metal alloys. Creep is experimentally assessed by tension creep tests, schematically shown in Fig.2.9.

During a creep test, sample-elongation is measured over time until rupture. The

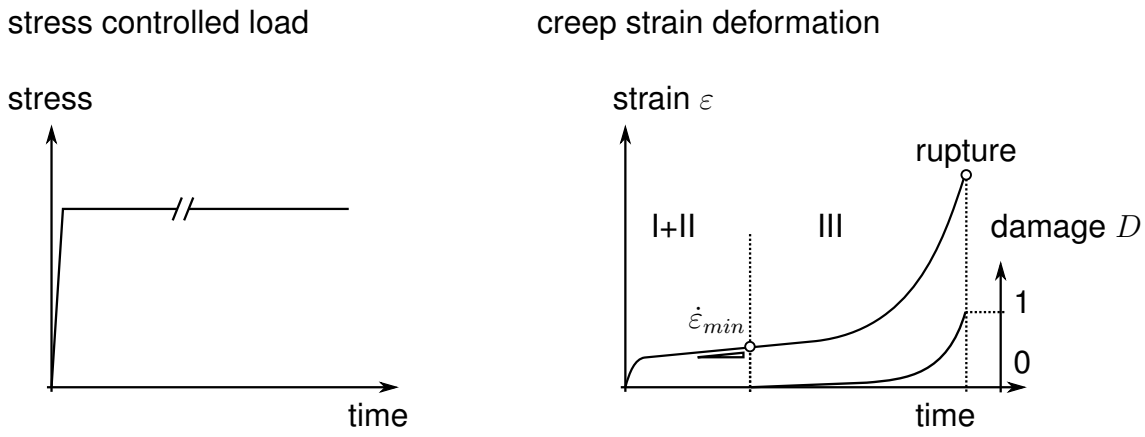

Fig. 2.9: Creep damage development during creep test where the testing sample is maintained under constant temperature and constant tensile force which results in creep strain deformation over time in three stages: primary I, secondary II and tertiary III creep stages, until rupture of the sample

first two stages of the curve (I+II) until the stabilization of the strain rate, are governed by deformation mechanisms [55]. Without considering damage development, the strain rate would follow the minimum strain rate ε_{min} reached in the steady state phase. In fact, the time at the minimum strain rate is considered as the beginning of damage [55]. After this time, the strain rate increases exponentially until the rupture of the sample.

The Larson-Miller's concept of master curve

The failure caused by creep damage processes is still under research, and remain a crucial issue in the design for reliability. Besides, many effects interact during creep damage development which also depends on the intrinsic nature of the metal. From a macroscopic point of view, the interplay between the applied stress and temperature and the observed rupture time of the sample has been first identified. The equation of Larson-Miller [62] associates the Larson-Miller Parameter P_{LM} as an empirical power function of the stress to describe the time to failure at different temperatures.

$$P_{LM} = (T + 273) \times (C + \log(t_r)) \quad T \text{ in } ℃ \tag{2.22}$$

$$f(\sigma) = \sigma^m \tag{2.23}$$

$$P_{LM} = B_1 + B_2 \times f(\sigma) + B_3 \times (f(\sigma))^2 \tag{2.24}$$

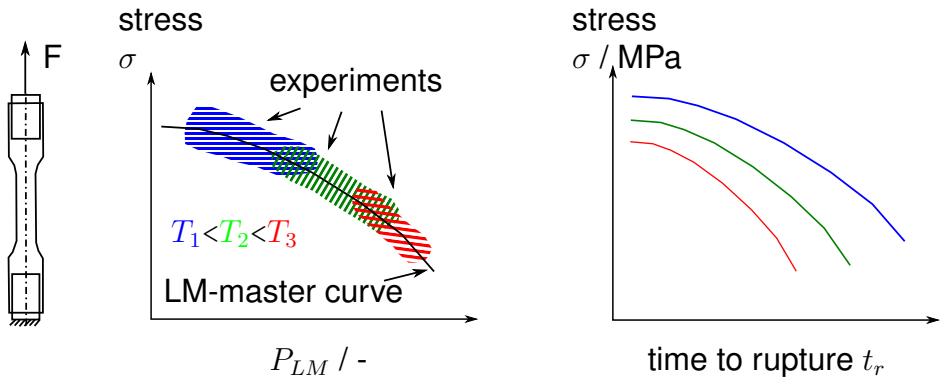

Fig. 2.10: Master-curve concept for creep rupture time after Larson and Miller [62]

The Larson-Miller parameter builds up the concept of master-curve for creep damage illustrated schematically in Fig.2.10. The four material specific parameters C, B_1, B_2, B_3 and m are calibrated to fit the applied stress σ and P_{LM}, which represents an equivalent creep damage parameter. A polynomial function of the stress often suits with the time to rupture t_r at different temperatures T [27, 29], see Eq.(2.23), Eq.(2.24).

The Larson-Miller approach is employed as standard method for estimation of creep rupture time for steel alloys [61]. The calculation of creep rupture by Larson-Miller is well adapted for components loaded repetitively within defined and constant stress state because the formulation excludes the other mechanical quantities e.g. strain or strain rate. For creep damage calculation within complex loading conditions, some assumptions have to be done particularly when the loading conditions are strain driven. In [27], the author used the median stress within the relaxation period to calculate the creep fraction of damage. Besides, the relation do not address the development of damage occurring within different strain stages, because only the stress is taken into account in Eq.(2.22) and Eq.(2.23).

Another empirical macroscopic relation for damage based on the strain rate variation during a creep test was proposed by Chaboche and Lemaitre [51].

$$D = 1 - \left(\frac{\dot{\varepsilon}_{min}}{\dot{\varepsilon}}\right)^{1/N} \tag{2.25}$$

The coefficient N is associated to the viscosity of the material, and therefore, strongly depends on the temperature and the stress magnitude applied during the creep test.

Kachanov model

Kachanov modeled creep damage using a scalar variable, later included into the damage mechanics framework. As a power relation associates strain rate and stress, and considering that the creep damage follows as well a power function of the strain rate (Eq.(2.25)), Kachanov integrates both relations to formulate the creep damage as a function of the input stress and temperature in Eq.(2.26) [56].

$$\dot{D} = \left(\frac{\sigma}{A_D(1-D)} \right)^{r_D} \tag{2.26}$$

A_D and r_D are temperature dependent material coefficients. A direct integration of Eq.(2.26) gives the time to rupture as a function of the applied stress. Thus, creep data can be analytically fitted and the material constants A_D and r_D are calibrated to match the time to rupture of experimental creep data [56]. The simplicity of the Kachanov's model and the good agreement of the power law to experimental creep rupture time of many metals enabled a wide usage of this approach to predict creep damage, usually for structures submitted to monotonic loads at high homologous temperatures (e.g. thin walled pipes under internal pressure) [55, 63] . However, Kachanov's equation is not adapted to describe the damage development under combined creep-fatigue loads, for instance, when the load switches from stress to strain driven situation. In fact, Eq.(2.26) is independent of the strain magnitude, which results to an over-prediction of creep damage at low strain and high strain rate, since stress in this regime is high due to the significant strain-rate dependence (viscosity) of the material.

MPA creep model

Phenomenological creep damage equations were developed at the MPA Stuttgart University and applied on steel alloys under creep-fatigue loading above 500℃ [28, 29]. As for the fatigue damage Eq.(2.21), the creep damage Eq.(2.27) is later integrated into the material routine CNOW for finite element simulations. The equivalent value of the creep strain $\bar{\varepsilon}_2^p$ is introduced in the Eq.(2.27) as an improvement of the creep damage model regarding the Kachanov's formulation Eq.(2.26). Thus, the creep damage follows a nonlinear evolution within a monotonic creep test, with low value in the first and second creep stages, until an exponential increase in the tertiary creep state.

$$\dot{D}_2 = (1 - D_2) \times 10^{-A_2} \left(\sigma_{eq}\right)^{B_2} \left(\bar{\varepsilon}_2^p\right)^{C_2} \tag{2.27}$$

This nonlinear evolution, as well as the sensibility of the creep damage development at different strain amplitudes can be fitted by the exponent C_2. Eq.(2.27) reveals good agreements to the damage evolution under combined creep-fatigue loading, by means of LCF-fatigue tests with incorporated dwell time relaxation periods [27, 29]. Besides, the Eq.(2.27) relates the creep damage rate and the equivalent von Mises stress with a power function. Although the MPA model fits most of the monotonic creep data, a first order power function of the stress overestimates the creep damage development for the lower stresses, as reported by [28]. To describe the creep behavior even in the low stress regime, Schemmel introduced a superposition of stress functions, which map descrete strain rate regimes.

Considering the physical meaning of creep damage, as a progressive growth of cavities and pores in the material, its intrinsic development should be enhanced under tension loads and rather limited under compression. Wippler and Kuna [6, 33] postulated this property for solder material and adapted their model to accumulate damage only within a tension stress state. The multiaxial character of loads and its influence on the creep damage development is still in research and a clear relation between the stress triaxiality and a generally valid damage development is not established for ductile materials at high homologous temperatures. One reason concerns the challenge to investigate experimentally the creep behavior under pure compression i.e. within a constant negative hydrostatic pressure. One possibility remains to perform combined strain controlled LCF tests with dwell time periods, where the strain during the dwell time period is maintained constant under compression. This experiment has been performed and reported by [25] for a Sn-based solder material at moderate temperature (40 °C). Yamamoto et al. reported on the fatigue-creep interaction within multiaxial load profiles and observed that successive positive stress relaxations affected the fatigue-life whereas comparable lifetimes were obtained for pure LCF and LCF combined with negative stress relaxation. This study argues with Kuna's postulate that creep damage can be neglected under negative hydrostatic pressure. This assumption is adopted in this work and implemented in the material model.

2.2.4. Interaction creep-fatigue

In practice, solder joint components are damaged due to both fatigue and creep phenomena. A first step consists in understanding separately each damage phenomenon. In a second step, the interaction between both damages shall be investigated and understood. Previous investigations on creep-fatigue defects were done for steel alloys or reinforced polymers [49, 51, 55, 64]. For these materials, a system-

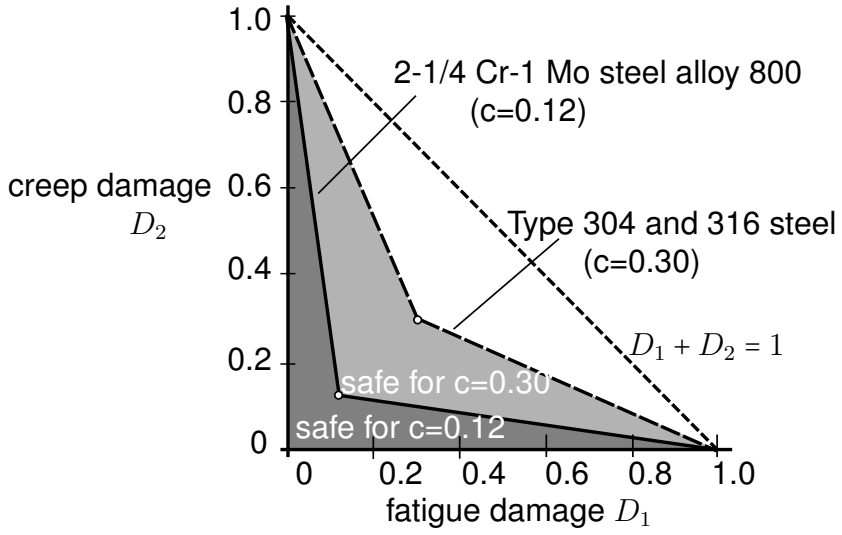

Fig. 2.11: Nonlinear accumulation rule of creep and fatigue damage after ASME standards [61] for steel alloys used for instance in power-plant turbines

atic decrease in fatigue life has been observed when creep damage accompanies fatigue dominated loads. From a microstructural point of view, it can be explained by the interaction between trans-granular (fatigue damage) and inter-granular (refered to creep damage) defects [49]. Creep induced cavities enhance crack propagation (fatigue damage) in the material which also increases the internal stress on the remaining effective surface (effective stress concept [56]). Thus, an increase of effective stress favors the nucleation and the coalescence of voids resulting in an increase of creep damage. Safety components integrated into critical applications as power plants are substantially submitted to both creep and fatigue, also within a high homologous temperature environment. Not considering the creep-fatigue interaction would lead to an under-estimation of damage and therefore to a non-conservative estimation of the component lifetime. For this reason, the simple linear accumulation of creep and fatigue damage was typically replaced by a nonlinear accumulation rule. Reliability engineers established analytical rules for this type of application and standardized the calculation of damage in a guideline design of components submitted to creep and fatigue damage at high homologous temperature [61], some applications can be found in the work of Schellenberg [64].

A symmetrical bilinear rule calculates the total damage respectively for creep and fatigue dominated loads in Eq.(2.28)-(2.29). The inflection point c (here $c = 0.3$ or $c = 0.12$) is a specific material parameter dependent on temperature. The diagonal in the diagram Fig.2.11 corresponds to the linear rule $D_1 + D_2 = D_{tot}$ whereas the

nonlinear rule is given by Eq.(2.28)-(2.29) for creep and fatigue dominated loads, respectively.

$$D_2 = 1 - \frac{1-c}{c} \times D_1 \qquad \text{for } D_1 \leq c \tag{2.28}$$

$$D_2 = \frac{c}{c-1} \times (D_1 - 1) \qquad \text{for } D_1 > c \tag{2.29}$$

The evaluation of creep and fatigue parts, D_2 and D_1, are based on the Miner-Palmgren's, Eq.(2.30) and Robinson's rule, Eq.(2.31), [65, 66, 67].

$$D_1 = \sum_i \frac{n_i}{N_{fi}} \tag{2.30}$$

n_i being the number of cycles at a given loading and temperature, corresponding to N_{fi} cycles to rupture (typically calculated using Coffin-Manson-Basquin Eq.(2.17)). If the stress varies during the dwell time period, which is the case for strain driven cyclic loads (a stress relaxation occurs), the creep damage should be integrated over time.

$$D_2 = \int \frac{dt}{t_r(t,\sigma)} \tag{2.31}$$

where $t_r(t,\sigma)$ is the creep rupture time corresponding to the stress level σ acting at time t which can be extracted from the Larson-Miller master curve Eq.(2.22). The method can be applied relatively easy in case of uniaxial loads, constant temperature and rapid cyclic loads between two dwell time periods.

However, if the material is cycled at a low frequency, creep may superimpose on fatigue during slow load variations. This interaction cannot be addressed by the Miner-Palmgren-Robinson's rules. For that, a continuous approach is needed. In the 70's, Chaboche and Lemaitre extended the CDM framework and integrated the nonlinear damage accumulation into the differential equations [53].

$$dD = dD_1(D) + dD_2(D) \tag{2.32}$$

The total damage increment results in the contribution of fatigue and creep damage rates (respectively dD_1 and dD_2), which are also dependent on the amount of the accumulated total damage D at this time.

$$dD_1 = \left[1 - (1-D)^{\beta+1}\right]^{\alpha(\sigma_{max},\bar{\sigma})} \times \left[\frac{\sigma_{max} - \bar{\sigma}}{M(\bar{\sigma}) \times (1-D)}\right]^{\beta} dN \tag{2.33}$$

$$dD_2 = \left(\frac{\sigma}{A}\right)^{r} \times (1-D)^{-K(\sigma)}\, dt \tag{2.34}$$

The equations Eq.(2.33) and (2.34) represent the nonlinear damage accumulation evolution which can be applied continuously to any loading histories without differentiating load variations and dwell time periods which is a prerequisite for applying the Miner-Palmgren-Robinson's rule.

The construction of nonlinear damage evolution laws requires material tests in which both creep and fatigue damage functions are activated. Typically, strain controlled cyclic loads with dwell time periods and low frequency cyclic loading are performed for this purpose. Whereas for steel and high temperature alloys such a database exists, a very small number of experiments on lead-free solder materials are available by now, for establishing a nonlinear accumulation rule like in Fig.2.11. Moreover, a detailed guideline for reliability of solder components based on creep and fatigue damage variables like in the ASME standards [61] for steel alloys is currently lacking.

2.2.5. Damage development under multiaxial-loads

The theoretical basis described above treats the damage development in a structure submitted to uniaxial loads. However, the durability of the material can be strongly influenced by the multiaxiality of the loads. For example, in pressure-vessels and pipes under inner-pressure at high temperature, the part of the structure submitted to a tensile-dominated stress state is much more affected compared to the part under compression, although both parts experience the same equivalent stress [28]. This observation indicates that the equivalent von Mises stress σ_{eq} is not sufficient to address accurately the damage development in structures submitted to multiaxial loads. Clausmeyer et al. proposed an evaluation of the multiaxiality using the ratio q defined in Eq.(2.35) [68]

$$q = \frac{1}{\sqrt{3}} \frac{\sigma_{eq}}{\sigma_H} \tag{2.35}$$

where σ_{eq} is the equivalent stress (after von Mises), and σ_H the hydrostatic pressure (equal to a third of the trace of the stress tensor). Following this definition, the stress state within multiaxial loads can be simplified using one representative volume element as schematically depicted in Fig.2.12

Here, the dominant loading direction is vertical and in case of unidirectional loads (case 1. and 2.), a constant q ratio is obtained $q = \pm\sqrt{3} \approx 1.73$. By applying an additional horizontal load, a multiaxial stress state is induced. In the different cases 4...6, the ratio between the deviatoric and volumetric part of the stress varies, which leads

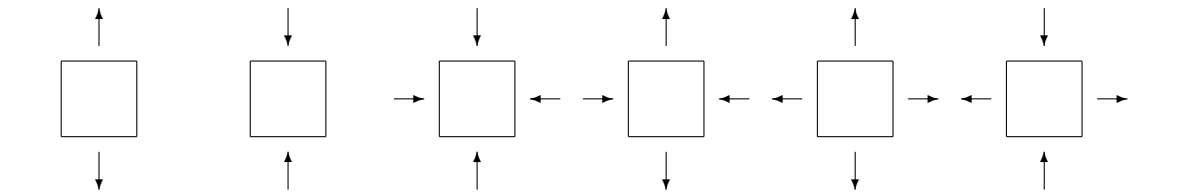

Fig. 2.12: Classification of multiaxial stress states using Clausmeyer's definition of q

to either a more shape-change dominated load (3. and 4.) or a volume-change dominated load (5. and 6.). Nevertheless, there is a limited number of experimental works reported, which show the influence of q such as the Fig.2.12 suggests. Experimental works are hampered by technical difficulties in the design of a sample with a homogeneous volume distribution of pre-defined q ratios. A common technique consists in modifying the geometry of the testing sample, such that a q ratio can be achieved in the critical zone where most of the damage is expected [69]. Typical variation of the geometries include

- notch specimens
- hole-cylinder (with and without notch)

Furthermore, by investigating these samples within tension-torsion conditions, one obtains the stress state corresponding to 3. and 4. In contrast, by applying hydrostatic pressure through the hole, the stress state represented in case 5 and 6 in Fig.2.12 can be obtained. Thus, creep and fatigue damage under multiaxial loads can be investigated by applying either unidirectional static or repetitive cyclic loads.

In [69], hollow cylinders of a steel alloy under axial force and inner-pressure at high temperature have been investigated on notched and not-notched samples. They obtained a q ratio near 1. As a result, substantial reduction of the creep time to rupture was observed in comparison to the uniaxial creep ruptures for equivalent stresses. The faster development of creep damage was attributed to the growth of cavities density which resulted from the positive hydrostatic stress state occurring during the inner-pressure load. In order to model this effect, they adapted the creep damage formulation of Graham-Walles [70] and integrated it in the constitutive equations of the material model.

$$\dot{D} = A_D \left[\left(\frac{\sqrt{3}}{q} \right)^{\alpha} \times \sigma_{eq} \right]^{n_D} \times \left(\dot{\bar{\varepsilon}}^{p} \right)^{m_D} \tag{2.36}$$

For uniaxial loads, a value of $q = \sqrt{3}$ results, and Eq.(2.36) follows the original form of the Graham-Walles relation. The coefficient α governs the sensitivity of the material regarding the value of $|q|$ and the substantial life reduction under high, positive hydrostatic loads ($|q| < 1.73$). However, in cases of a negative value of q, the equation (2.36) is not appropriate. It would predict a negative damage rate or, in other words, a healing effect. Negative values of q correspond to compression stress states which are expected to only reduce the development of creep damage. In accordance to the physical interpretation of creep damage, compression is expected to hamper the nucleation, growth and the convalescence of voids and cavities inside the material [71, 72].

The experimental results are presented in the next chapter (Chap.3), followed by the modeling of the mechanical and damage behavior (Chap.4) of the investigated solder material. The model developed in the present work comprises two flow rule functions, following the formulation in the ONERA2 model [40]. Kinematic and isotropic hardening are integrated in the model to describe the cyclic mechanical behavior. Two separate damage variables are employed for mapping the observed fatigue and creep damage development in the material. Finally, using the available experimental data, a nonlinear accumulation rule, similar to the one in ASME-standards [61], is proposed for the solder alloy.

3. Experimental investigation

3.1. Material characterization of solder joint materials

Within this work, extensive material characterization has been carried out on standardized samples, which reveals the properties of the material under controlled loading conditions. This builds the foundation for understanding the mechanical behavior in real situations where solder joints subsequently undergo complex thermo-mechanical loads. The different tests are performed within the relevant temperatures -40 °C, 25 °C, 75 °C and 125 °C according to the temperature loads used during lab qualification tests and real temperature profiles in service operation. During start and shut-down phases of the car engine, and/or internal heat generation in power components, the solder joints experience a repetitive cyclic thermo-mechanical loads due to the differences in thermal expansion between the assembly components. The governing damage mechanisms specific for the solder alloy resemble a complex interplay between plastic and creep deformation in the solder material. In order to separate thermal and mechanical effects, the different tests on standardized samples are performed under controlled isothermal conditions. The investigated mechanical loads correlate to the mechanical loads expected in real solder joints within typical electronic devices. For example, strain rate controlled cyclic loads represent the loading conditions during start and shut down phases. Combined creep and relaxation tests address the stationary loads during operation (higher temperature) and stand-by regime (lower temperature) of several hours. When the engine is turned off, the electronic components cool down to the environment temperature and the solder joint undergoes stress-relaxation during this period.

The experimental characterization of the material fulfills two goals. First, the database of standardized tests for lead-free solder material is extended and covers varying load profiles. This database includes information about the deformation and damage properties of the material in the temperature range of interest. For reliability prediction of real components, such experimental characterization is a crucial step. Indeed, most of guideline rules for lifetime estimation are based on phenomenological models which are derived from the characterization of the material using standardized bulk sample tests [61]. Such experiments reveal quantitative information on the behavior of the material which can be later described using constitutive models. The

different tests are designed on purpose to facilitate the formulation of the material model. The calibration of model parameters to match the real behavior in various loading conditions remains an issue, which is even more challenging when the complexity of the material model is high. Thus, a proper design of testing program, is an important prerequisite for understanding the properties of the material and for a formulation and calibration of a constitutive model.

3.2. Experimental setup

Because of the small size of the solder joint components and its complex geometries, a systematic local measurement of forces and deformations on the real component remains challenging. For this reason, the material characterization has been performed on bulk samples with test region diameter of 6 mm (see Fig.3.1) which have generally a larger size than the dimension of a common solder joint (<1 mm). Thus, it is important to verify that the bulk material is representative for the one in real solder joint components. In the following section, the microstructure of the of the bulk sample after fabrication is inspected using different microscopy techniques and compared to the microstructure of real solder joints after soldering, which is presented in Chapter 1.

3.2.1. Testing samples

The testing samples are produced by re-melting of the tin-based solder alloy and casting into a cylindrical form. Subsequently, the form is cooled down to ambient temperature. In a next step, the final geometry of the specimens is prepared by drilling of the raw solder cylinders (see Fig.3.1).

	(a)	(b)	(c)
sample	IKTS-Dresden [26]	produced within this work	produced within this work
diameter d	4 mm	6 mm	6 mm
length l	6 mm	12 mm	50 mm

Two kinds of sample geometries are machined for cyclic tests in tension and compression domains (a)-(b) and unidirectional creep tests (c), respectively. On both sample-sides, a thread is drilled ((b) and (c)), which is used to fix the sample in the material testing machine. The sample (a), produced by the Fraunhofer IKTS institute in Dresden, has a rectangular grip region to be clamped in their testing machine [26]. The resulting cyclic tests conducted with this samples are later utilized within this

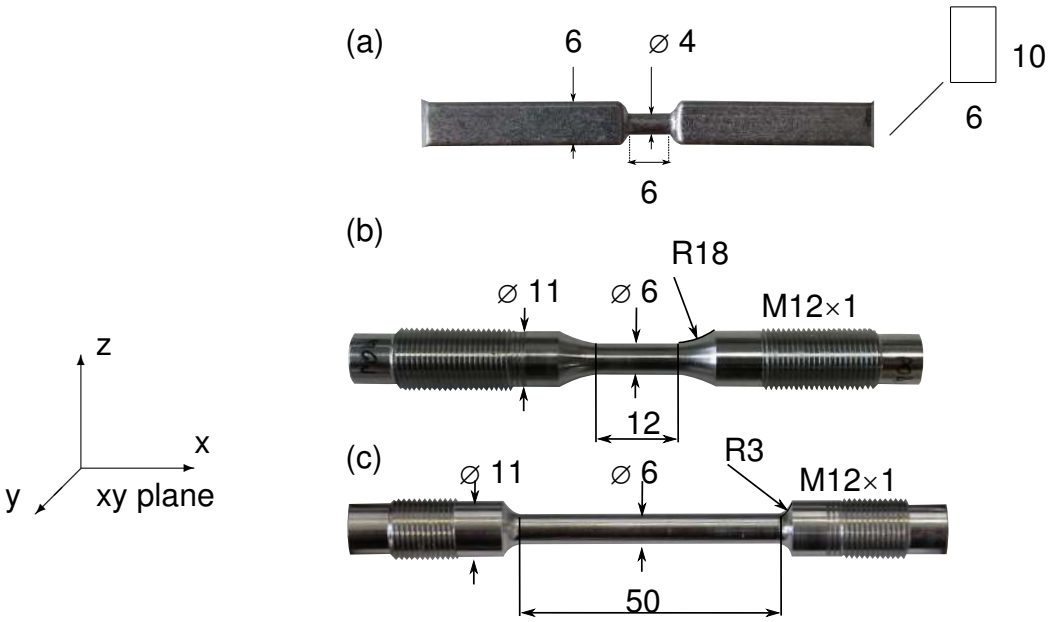

Fig. 3.1: Sample geometries:(a) as casted Fraunhofer IKTS push-pull sample [26, 48] ; (b) LCF sample and (c) creep sample produced during this work. Unit: mm

work and referred to the work of Metasch et al. [26]. Also for cyclic tests, the sample (b) has a test region of 12 mm length and 6 mm diameter. Thus, following the design rules for material testing in the tension-compression domain [73] the ratio diameter-to-length of the test region is $r = l/d = 2$. In contrast, the creep tests are exclusively performed in the tension domain where larger sample lengths are more appropriate. The test region of the creep sample tests has a length of 50 mm (Fig.3.1(c)). In order to decrease roughness and to avoid irreproducible surface crack initiation the samples have been polished, which is an important preparation step for obtaining high sample quality as described in [73].

3.2.2. Initial state of the material

Typical lead-free solder alloys comprise the elements tin (Sn), silver (Ag) and copper (Cu) as described in Chapter 1. Chemical analysis of the sample material has been performed using plasma optical emission spectrometry and show a similar composition compared to typical tin-based alloys employed in industrial applications [1]. After drilling the samples in their final shape, the microstructure of the material is analyzed on polished cross sections in the xy plane of the samples (see Fig.3.1). A Scanning Electron Microscope (SEM) with a sub-micrometer resolution reveals the microstructure in its initial state as depicted in Fig.3.2.

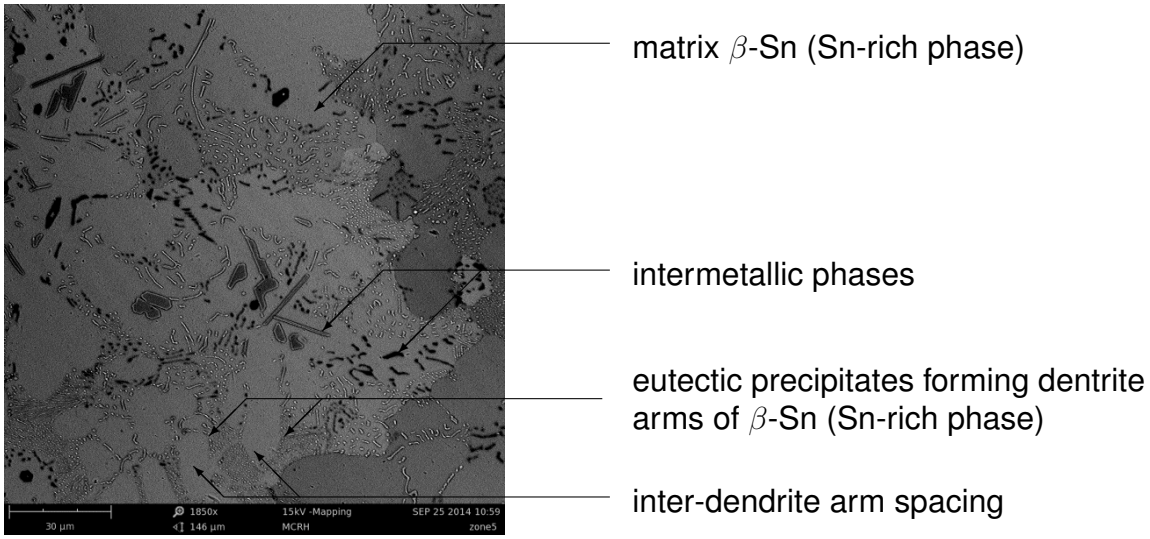

Fig. 3.2: SEM micrograph from Backscattered Electron (BSE). Solder material in its initial state after machining the sample

The microstructure of the solder material in its initial state is composed of a rich tin matrix (structure β-Sn) and intermetallic phases distributed throughout the material. Shape and size of the intermetallic phases vary from 1μm to 10μm. Small eutectic precipitations (<1μm) are visible throughout the Sn-matrix forming the tin-eutectic dendrite arms with approximately 10-20μm distance between dendrite arms. The observed size and distribution of intermetallic phases and eutectic dendrites correlate well to the microstructure of real solder joints after soldering process (see Chap.1).

The micrograph Fig.3.2 is processed by assembling the intensity of Backscattered Electron (BSE) being emitted from areas of the sample differing in atomic number (Z). Because the solder alloy is composed by different elements, a high contrast separates the tin-matrix from the binary intermetallic phases Ag_3Sn and Cu_6Sn_5. Besides, as $Z_{Cu} < Z_{Ag} < Z_{Sn}$, the silver-based intermetallic appears brighter than the copper-based intermetallic, since brightness is proportional to the atomic number Z for BSE images. In addition, the local element composition on the surface is verified by Energy Dispersive X-ray analysis (EDX) and the composition of the observed intermetallic phases are highlighted in Fig.3.3.

The corresponding EDX-spectra at the locations indicated in Fig.3.3 and provided in Appendix A.1, confirm the presence of the elements Sn, Ag and Cu. The spot (1) reveals mainly copper and tin and negligible amount of silver. In (2) mainly the element Sn is detected whereas in (3) tin and silver are observed with negligible amount of copper (see Appendix A.1). Finally, the composition is measured on a

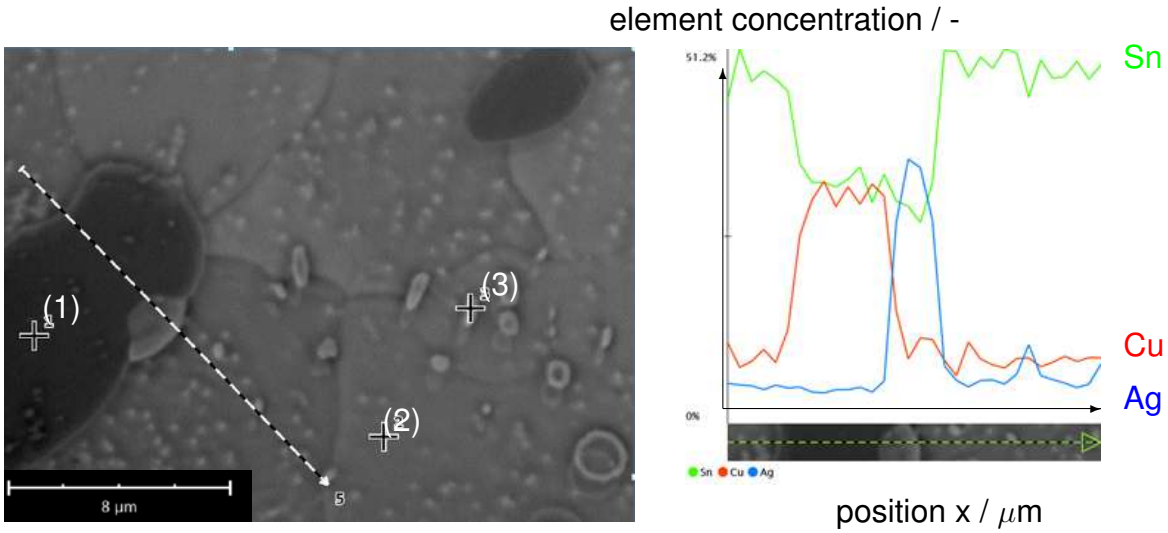

Fig. 3.3: EDX phase composition analysis along the dashed line in the SEM image. Single spots denoted (1), (2) and (3) indicate the positions of further EDX-analysis (the spectra are provided in Appendix A.1)

line-path crossing different phases. The concentration of the elements as a function of the position on this path is plotted in Fig.3.3. The matrix is composed by a rich Sn phase, which includes binary and tertiary eutectic elements of silver and copper in small concentrations. The Sn-matrix elements are present at the beginning and at the end of the line path. According to the thermodynamic phase equilibrium in the ternary system Sn-Ag-Cu, copper- and silver- rich intermetallic phases are expected [74]. The EDX- line profiles of the silver- and copper-concentrations strongly suggest the presence of the phase Cu_6Sn_5 (dark gray in Fig.3.3), as well as the phase Ag_3Sn in its vicinity (light gray). The Ag_3Sn phase and tin-rich matrix are expected to appear with similar contrast as observed in Fig.3.3, since the atomic number of silver and tin, being respectively 47 and 50, should produce similar contrast in the BSE-image. The SEM investigation suggests that the casted bulk samples and real solder joints after soldering process obtain a common phase composition. The size and morphology of the different phases of the alloy are comparable for the bulk sample and the solder joint. However, the SEM does not provide detailed information about the grain orientation and grain boundaries of the material. The different contrast of the tin-matrix in Fig.3.2 indicates several large grains extending over the dimension of the analyzed cross section (>150μm).

More detailed information on the grain structure has been gained by means of Electron Back-Scattered Diffraction techniques (EBSD). The EBSD technique is well suited for the analysis of polycrystalline micrographs, since it gives spatial information

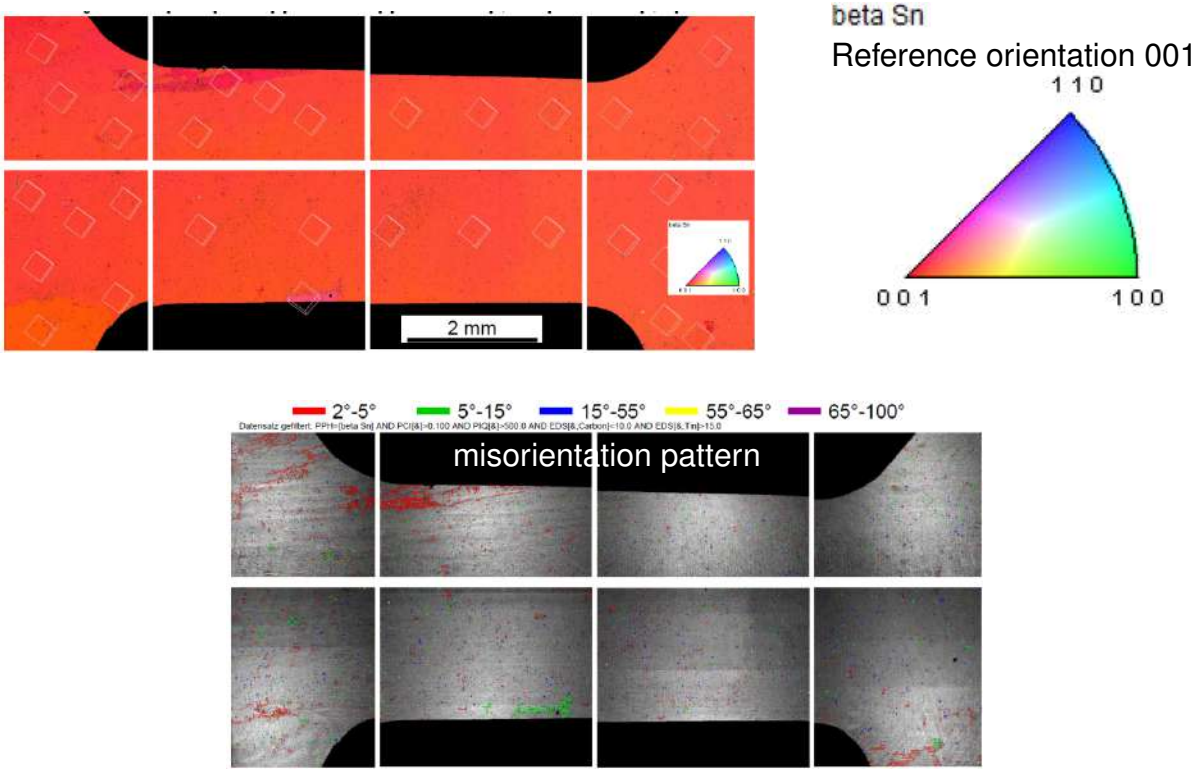

Fig. 3.4: EBSD micrograph of bulk sample in its initial state. Material: SAC after sample fabrication. The EBSD picture has been made in the TU-Dresden.

on the relative crystal orientation of individual grains. Fig.3.4 shows the results of a bulk sample EBSD-analysis in the initial state (prior to aging).

In its initial state, after casting, the bulk sample obtains a homogeneous crystal orientation (reference orientation 001), suggesting the presence of a large grain, which extends beyond the sample test region. Localized sites throughout the cross-section indicate regions of small relative misorientation (<15°) of crystal lattice. These results suggest local distortions of the grain lattice, suggesting the formation of a sub-grain structure. The micrograph does not indicate the presence of pores and other defects, which can be attributed to the casting process. These observations on the bulk sample are in accordance to the EBSD microstructure analysis in real solder joints where large grains with a sub-grain structure were reported (see Chap.1).

The microstructure analysis suggests that the material state obtained in the bulk sample correlates well to the one of a solder joint, despite the difference in absolute dimensions. Both show close similarities regarding the presence of intermetallic phases, morphology of the tin-matrix, as well as grain structure after casting/soldering. Thus, in the present work, we assume, that the mechanical properties of the solder alloy determined on bulk samples (see Fig.3.1) resemble the proper-

ties in solder joints in electronic components. In the following, the material testing equipment and results of the various tests obtained in this work will be described in detail.

3.2.3. Material testing equipment

Set-up for cyclic tension compression tests

Within this work, a new testing equipment was developed based on an existing commercial push-pull machine from Zwick und Roell in order to measure the material properties of the solder alloy necessary for the establishment of the material model.

Standardized characterization programs for metallic materials typically employ rotational symmetric samples (the same as in Fig.3.1) in order to realize a homogeneous stress state within the test-region (region of interest). A challenging task remains the local measurement of elongation as close as possible to the test-region. In addition, the measurements must be performed under strain rate controlled conditions with respect to the test-region elongation, as the viscous properties of the material are sensitive to the speed of deformation [73]. However, earlier works have shown, that commercially available sensors (contact-extensometers) were not suitable for measurements on soft, low-melting solder alloys. These devices are directly fixed on the surface applying local contact pressure, which cause substantial damage after few load cycles. The impact of the force applied by the extensometer increases with the temperature. Above 75 °C, and due to high stiffness decrease in comparison to the original stiffness at room temperature, the sample could not support the force introduced by the extensometer in addition to the input load. This lead to gradual bending of the test region with increasing cyclic loads (see Fig.3.5).

Thus, following the experience from earlier measurements (Fig.3.5) a sensor system design without contact in the measurement area becomes necessary. An alternative approach for solder material characterization was reported by Metasch et al. The authors designed a custom push-pull testing machine where the local deformation is measured by Linear Variable Differential Transformer (LVDT) fixed outside the test-region edges [26]. Using this type of instrumentation, the measurement region of the sample stays contact-free and undamaged.

Following the idea of Metasch et al, the testing machine used within this work is instrumented with two high temperature LVDTs (operation temperature up to 150 °C) [76]. The global deformation is measured outside the sample edges (see magnification in Fig.3.6). Moreover, the different components needed for the instrumentation

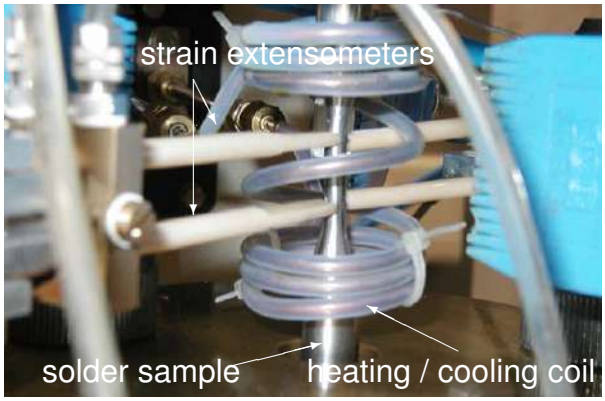

Push-pull machine set-up for cyclic tests with commercial extensometers

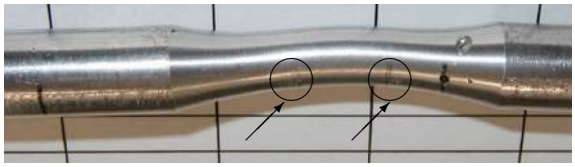

Damage on the surface caused by the contact of the extensometers

Sample bent in compression phase during push-pull deformation controlled test

Fig. 3.5: Cyclic measurement on solder sample using contact extensometer reported by MateCon GmbH, causing pre-damage on the surface of the sample [75]

are designed as small as possible, because the available volume is limited by the size of the temperature chamber. For this reason, the two LVDTs are positioned outside the temperature chamber and are connected to the sample by extensional stems as depicted in Fig.3.6.

The thermal chamber is equipped with a heat control system operating in the temperature range Room-Temperature (RT) up to 200℃. The local displacement of the test-region boundaries $\triangle$u (Fig.3.6) is measured by two LVDTs sensor signals. The two displacement signals are subtracted in real time by a multichannel digital amplifier [76], and transformed into an analog output in the range of 0...10V. The analog signal is connected to the input interface of the material testing machine electronics, which operates at a sampling rate of 500 Hz. The machine cross-head is driven in a closed feedback loop according to the external analog signal as a reference, which corresponds to the local elongation of the sample test-region (see Fig.3.6).

In this configuration strain-rate control with respect to the strain of the test region has been achieved during the load. Fig.3.7 gives a comparison between the displacement signals measured by the improved system using LVDTs on one hand, and the cross-head machine sensor displacement, on the other hand.

The measurement Fig.3.7 reveals a deviation of up to 25% between the sample displacement measured locally by the LVDTs and the displacement recorded by the machine cross-head sensor. This indicates the substantial inaccuracy, which would result if the cross-head signal would be used to describe the sample deformation. The strain-rate control using the LVDTs as a reference signal remains stable (note the linear profile of the black curve in Fig.3.7) over strain rates in the range of 1×10^{-3}

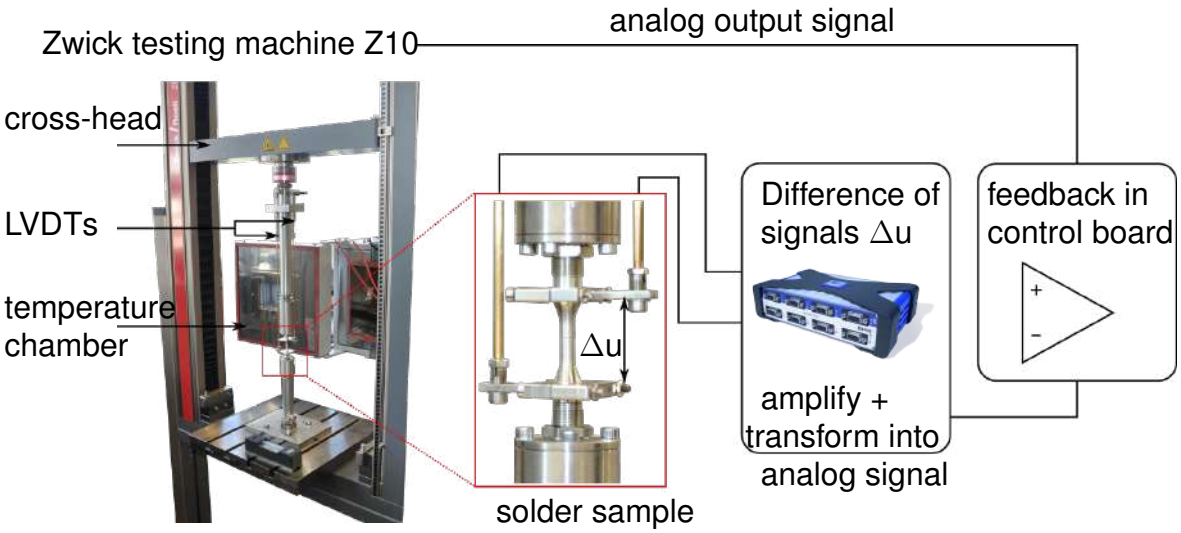

Fig. 3.6: Adapted Zwick Z10 machine for strain rate controlled tests regulated by a closed feedback system (HBM Quantum-X amplifier and numeric-analog converter) [76, 77]

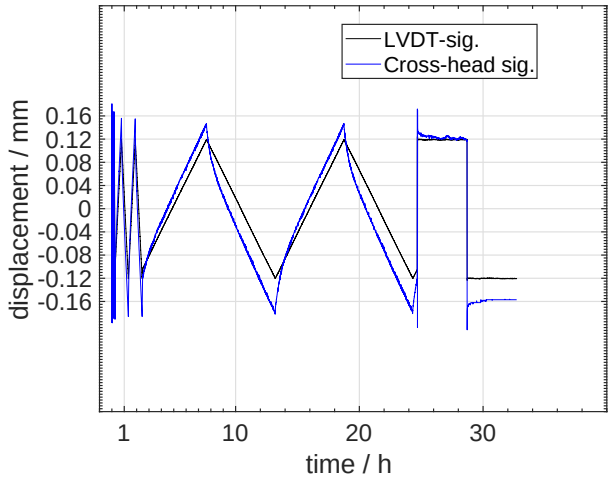

Fig. 3.7: Local deformation of the sample test region (LVDT-sig.) and corresponding displacement derived from the cross-head sensor of the machine (Cross-head sig.) during cycles of varying strain rates and relaxation periods. The signal from the LVDT sensors have been used for strain rate control in a closed feedback-loop, example of measurement at 25 ℃

to 1×10^{-6}. The improvement in the experimental characterization technique has been a crucial step towards accurate measurements of complex deformation profiles under temperatures up to 125℃. The testing equipment described above has been used for the characterization of the cyclic mechanical behavior of the solder alloy at different strain rates, stress relaxation phases, as well as Low Cycle Fatigue tests (LCF). Measurements at a temperature of -40℃ were performed on a similar setup elsewhere [26].

Specialized creep testing station

Creep measurements of metallic materials are typically scheduled over long time periods in the order of several months up to years. The evolution of time dependent deformation accompanied by creep damage is a thermally activated process enhanced by externally applied load. Despite their importance, creep measurements are by far not that challenging from technical point of view in comparison to deformation controlled measurements. During a creep test, the sample is loaded by a constant force at a constant temperature environment. At the same time, the elongation of the sample induced by the load is recorded. The force can be applied in a short amount of time without explicit strain rate regulation, since this initial loading period (several seconds) is negligible in comparison to the expected creep rupture time. In order to achieve several tests with creep rupture times in the order of months, a creep testing set-up has been developed within this work. The set-up comprises eight identical units, which enable the parallel measurement of samples under different forces. In each unit a single sample is mounted vertically and fixed on the upper side of the construction. The loads are applied by cylindrical steel weights of pre-defined masses, which correspond to the force magnitudes of the tests. The creep test units are placed in thermal chambers equipped with heat control system (see Fig.3.8), which maintains isothermal conditions at temperatures between 25℃ and 150℃.

The local absolute displacement of the sample test region boundaries is measured by LVDTs [76] following the same principle as in the set-up used for cyclic measurements described above. The signals are recorded via a QuantumX-HBM interface and saved on a computer disk. The final creep curve is obtained by taking the difference of the two LVDTs signals.

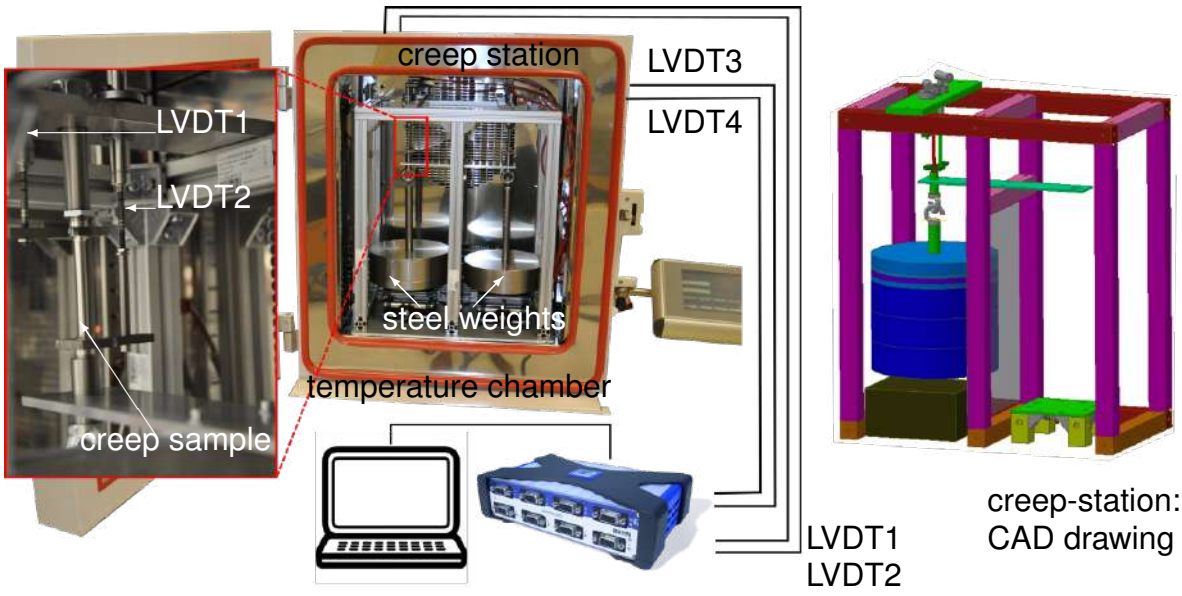

Fig. 3.8: Development of a creep station instrumented with HBM-LVDTs for the acquisition of creep data.

3.3. Experimental investigation of the deformation behavior

3.3.1. Characterization of the viscoplastic-creep behavior

In a first step, the mechanical behavior of the solder material is investigated by means of deformation controlled tests on bulk samples. Each sample is separately tested at isothermal temperatures e.g. -40℃, 25℃, 75℃ and 125℃. A complex deformation controlled program is applied during which the sample is successively cycled at different strain rates $1\times10^{-3}s^{-1}$, $1\times10^{-4}s^{-1}$, $1\times10^{-5}s^{-1}$ and $1\times10^{-6}s^{-1}$. Here, the reference length is taken as the length of the testing region of the sample: l_0= 12 mm (see Fig.3.1(a)). In this case, a strain rate of $1\times10^{-3}s^{-1}$ corresponds to a linear displacement of 0.012 mm/s. After the strain rate variation sequences, the sample is maintained at a constant strain amplitude for four hours in tension and compression, respectively. During these phases, the stress relaxation is recorded as depicted in Fig.3.9. The stress is calculated afterwards using the original section of the sample S_0=3×3×π=28.26 mm^2.

The mechanical behavior of the solder material in the domain of low stress levels and high strain amplitudes is measured by means of isothermal creep tests. As far as

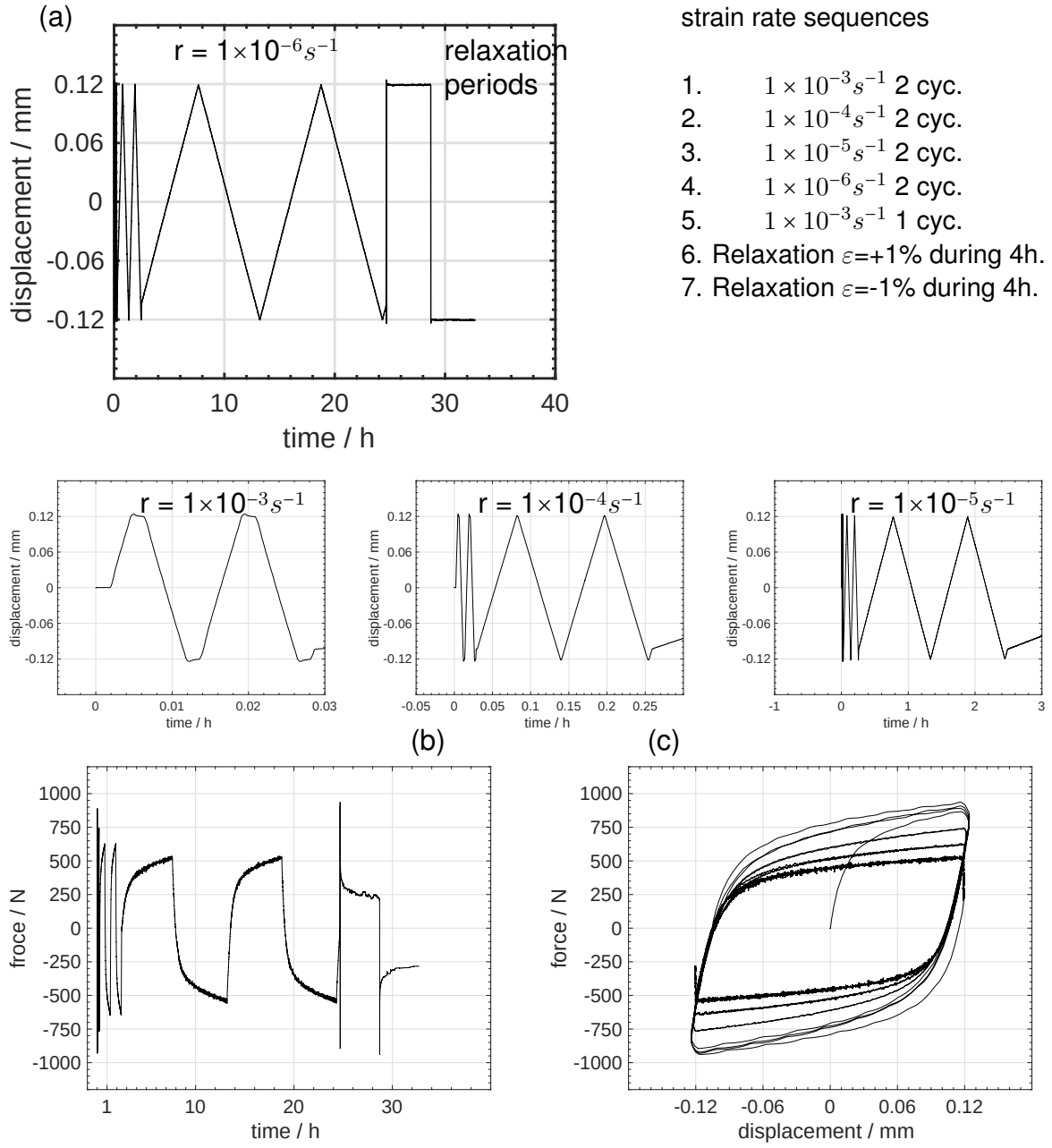

Fig. 3.9: Cyclic test comprising four levels of strain rate variation (2 cycles at each strain rate) followed by stress relaxation periods in tension and compression of 4 h. respectively. (a) displacement input profile. (b) force response recorded over time. (c) force-displacement hysteresis obtained. Alloy: SAC. Temperature: RT (sample P06)

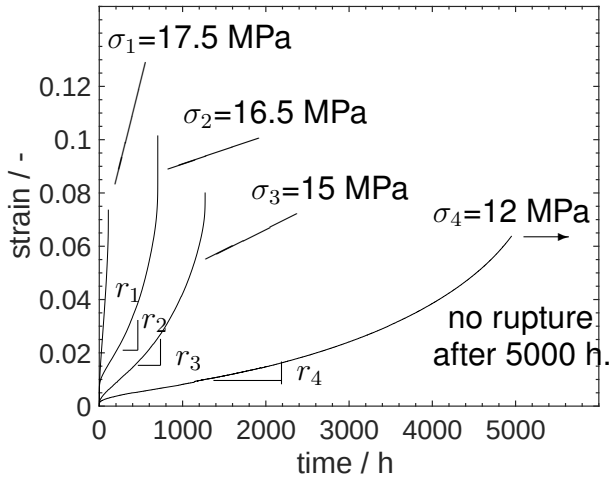

Fig. 3.10: Experimental creep tests at RT, SAC

the deformation is concerned, the purpose of the creep testing program is to investigate the thermally activated slow plastic deformation. Low stresses are applied (lower than the stress magnitude measured during the rate variation program) resulting in a very low rate of deformation. Here, three creep tests conducted at room temperature are given as an example and the corresponding curves are depicted in Fig.3.10.

3.3.2. Deformation properties at small strains and high strain rate

Substantial part of the observed cyclic deformation occurs in the plastic domain resulting in an elastic-plastic behavior as indicated by the stress-strain hysteresis Fig.3.9(c). The solder material shows even at room temperature a low yield strength (under 250N). After yielding, the strength-displacement evolution is highly nonlinear. The observed nonlinear hardening forms the shape of the measured force-displacement hysteresis. In the framework of constitutive modeling the hardening behavior of metal alloys is interpreted as a superposition of strain and time hardening (see Chap.4). In practice, the two effects are always activated and a clear separation between strain and time hardening is experimentally difficult to obtain.

However, under specific loading conditions, one of the effects can dominate over the other. A quantitative evaluation of both hardening effects is crucial for a proper selection of viscous function, which can adapted to the material behavior. This is one of the main goals in the design of the specific testing program presented in Fig.3.9(a).

As depicted in Fig.3.9(b)-(c), the stress magnitude increases with increasing strain rate, which indicates an increase of time hardening. Fig.3.9 shows that an increase over four decades of the speed of deformation gives rise to an increase of stress magnitude by a factor of two for the same strain amplitude (from 18MPa (500N) to 35MPa (975N) at strain rates of $1\times10^{-6}s^{-1}$ and $1\times10^{-3}s^{-1}$, respectively). At the limit of an infinitely low strain rate the time hardening part should be negligible, thus the corresponding stress can be mostly attributed to be build up by strain hardening. A strain rate of $1\times10^{-6}s^{-1}$ during cyclic loads corresponds to a time period of a single cycle higher than 10 hours. Even at such low strain rate, time hardening might not completely vanish as suggested by the measurement. If the strain rate could be reduced to $1\times10^{-7}s^{-1}$, the test program would have a duration higher than 2 weeks, which could not be realized due to technical issues.

In order to draw the distinction between the strain and the time hardening part, the stress relaxation behavior is used in the present work. The stress-reduction during the dwell time period results from the release of elastic strain and a transformation into plastic one. Consequently, the relaxation of stress is exclusively due to time dependent plastic flow which corresponds to the fraction of stress previously introduced by time hardening. Assuming that the previously introduced time hardening is being released after four hours of dwell time period, the remaining stress σ_r at the end of the relaxation test phase refers to the strain hardening part (250N corresponds to 9MPa in Fig.3.9(b)). This is supported by the observed stable stress level after approximately 3 hours in the dwell time period. The strain hardening part depends exclusively on the plastic strain per definition, thus it is independent on the strain rate applied in the loading phase. Furthermore, it remains nearly unmodified during relaxation periods, since the strain amplitude is kept constant during this test phase. Thus, we assume that strain hardening can be represented by means of the remaining stress at the end of a relaxation phase.

In this way, the evaluation of the deformation program (Fig.3.9(a)) gives the distribution of strain and time hardening parts in the range of small strains ($<$ 1%) and at relatively high strain rate ($1\times10^{-6}s^{-1}$...$1\times10^{-3}s^{-1}$). In this range, the ratio of time/strain hardening increases with strain rate from respectively 50%/50% to 71%/29% for the strain rates from $1\times10^{-6}s^{-1}$ to $1\times10^{-3}s^{-1}$. The interplay between time dependent and time independent plastic deformation gives rise to the viscoplastic behavior observed here for the solder alloy SAC at room temperature. The viscoplasticity is characterized by a sensitivity to strain rate variations as well as stress relaxation within dwell time periods at constant strain consistent with the experimental data obtained in the

present work. The deformation behavior in the domain of higher strain amplitudes and lower strain rates have been studied by means of creep tests, and is presented in the following.

3.3.3. Creep deformation at large strain and low strain rate

The creep curves depicted Fig.3.10 cover a large spectrum in terms of deformations and strain rates. The deformation over time follows typical stages classified in three categories: primary, secondary and tertiary creep. During the primary stage, the strain rate decreases continuously accompanied by increasing elongation of the specimen. The secondary creep phase is characterized by a nearly stable strain rate (linear increase of elongation with time), often referred to as stationary creep. During the tertiary creep the strain rate increases again leading to rupture of the sample. The different times to rupture range from 50 to 5000 hours and encompass almost 7 months of measurement duration.

During primary creep the competitive deformation processes discussed in the scope of cyclic tests, namely strain and time hardening are expected. This is supported by the fact, that the observed total strain in both cyclic tests and creep tests within the primary creep domain remain small <2%. With increasing stress in the creep tests, the amount of plastic deformation (quasi time-independent) accumulates in shorter periods of time resulting in an increasing sample elongation of primary creep strain. At lower stresses, less plastic strain can account for strain hardening, and thus, the strain and time hardening parts reach an equilibrium at longer times and lower strain amplitudes. In other words, the end of the primary creep stage (onset of stationary creep) in terms of time and corresponding sample elongation shows substantial dependency on stress.

During the steady state period the strain rate remains nearly constant, which is often interpreted as a regime in which hardening and softening processes compensate for each other. This period corresponds to more than 50% of the life of the sample and motivated numerous works which suggest secondary creep as the most important mechanism of deformation [19, 78] relevant in solder joint applications. Fig.3.10 shows that the secondary creep strain rate decreases with the applied stress and one has $r_1 > r_2 > r_3 > r_4$ (s Tab.3.1 and Fig.3.10). In the following section, it is interesting to compare the strain rate dependencies on stress between the creep tests Fig.3.10 and cyclic tests Fig.3.9(b)-(c).

3.3.4. Viscous stress towards viscoplastic-creep bounds

The viscous properties refer mainly to the time hardening part of the stress. As already mentioned, a direct measurement of the time hardening part is not possible for either cyclic or creep tests, since one can only measure the total stress σ. Thus, thanks to the stress relaxation, the strain hardening part may be quantified and attributed to the remaining stress σ_r (see previous section). By subtraction, the viscous stress σ_v can be evaluated by Eq.(3.1). σ_r is also referred in the literature as *threshold stress* or *hardening stress* H for the physical description of creep phenomenon [55, 79].

$$\sigma_v = \sigma - \sigma_r \tag{3.1}$$

However, the strain hardening part of the stress which accumulates within a creep test is still unknown, although its existence is revealed during the primary creep stage. In the following analysis, the evolution of strain hardening within a creep test is considered independent from the applied stress, and it reaches the same constant value at the onset of the steady state creep strain. This value is taken equal to the strain hardening quantity accumulated within cyclic tests and measured at the end of the relaxation and given the remaining stress σ_r=9 MPa at 25°C. Thus, for cyclic tests, the viscous stress is evaluated at the maximum peak stress corresponding to each strain rates evaluated in the secondary creep stage, and using Eq.(3.1). Moreover, the strain rates for the creep tests are evaluated in the linear part of each curves in Fig.3.10. As a result, the diagram Fig.3.11 illustrates the evolution of the viscous stress σ_v (time hardening part) as a function of the strain rate r in a large scale throughout creep and viscoplastic deformation.

The evolution of the viscous stress vs. strain rate suggests two regimes. In the high strain rate regime (viscoplasticity domain), roughly between 1×10^{-6} and $1\times10^{-3}s^{-1}$, the data points follow a constant slope in the double logarithmic plots which suggest a first order power dependence between viscous stress and strain rate in this regime. Here, the stress evolution is usually described by a power function of strain rate, also called Norton's relation of viscoplasticity (see Chap.2 eqv. to Eq.(2.11)) [80]. However, in the low strain rate regime (creep domain), the interdependency viscous stress vs. strain rate is much higher than in the high strain rate regime. The data points indicate a linear trend, but with a higher slope ($m_2 >> m_1$). In other words, the solder alloy exhibits a complex time hardening behavior, which depends on the strain rate regime. According to the Fig.3.11, a single power function (Nor-

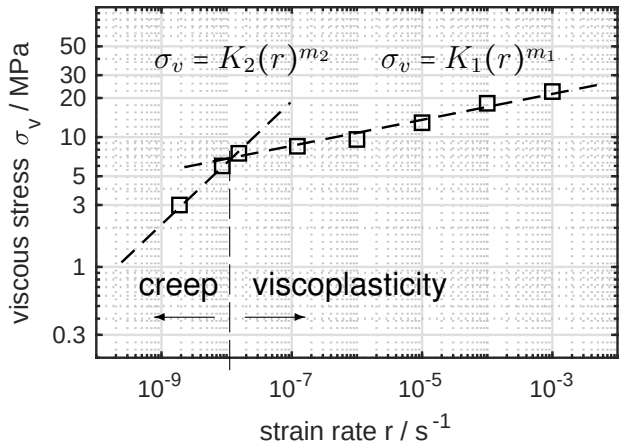

Fig. 3.11: Viscous stress evolution (time hardening) in function of the strain rate for SAC alloy at RT

test	σ_v / MPa	r / s^{-1}
	22.42	1×10^{-3}
cyclic	18.22	1×10^{-4}
test	12.9	1×10^{-5}
	9.59	1×10^{-6}
	8.5	1.22×10^{-7}
creep	7.5	1.54×10^{-8}
test	6	8.58×10^{-9}
	3	1.89×10^{-9}

Tab. 3.1: Viscous stress calculated with Eq.(3.1) from cyclic and creep measurement Fig.3.9-3.10

ton's rule Eq.(2.11)) is not able to describe the viscous behavior in the whole strain rate range including creep and viscoplasticity domains [80]. Furthermore, the viscous behavior suggests a double power relation, as each domain, respectively creep and viscoplasticity, could be described separately using one single power function. This observation builds the basis for a formulation of appropriated flow rule function in the material model (see Chapter 4), which will be able to describe the deformation behavior in the whole strain rate range.

From a microstructural point of view, the change in the stress-strain rate slope (see plot in Fig.3.11) suggests possible modifications of the deformation mechanisms. Particularly reported by Ashby [10], the deformation mechanisms are strain rate and temperature dependent (see Chap.2, Fig.2.1). The thermal condition 25°C tested here corresponds to T_h=0.60 in terms of the homologous temperature. Thus, according to Ashby deformation maps Fig.2.1 for pure tin (Sn) [78], the deformation mechanisms may change from grain boundaries slide to grain boundaries diffusion. This hypothesis is further motivated by the fact that the solder alloy exhibits a polycrystalline structure (see Fig.3.20) 3.22, and a strong time dependent plastic deformation throughout several orders of magnitudes from 1×10^{-9} to 1×10^{-3}.

In the high strain rate regime (viscoplasticity), the kinetics of deformation have been associated to grain boundaries sliding [10], caused by relatively high loads which are responsible for quasi-instantaneous plastic deformation. In the graph

Fig.3.11, this mechanism would be related to the Eq. $\sigma = K_1(r)^{m_1}$, corresponding to high strain rate, where the slope of the curve is low. In contrast, if the amount of load is too weak, the quasi-instantaneous plastic deformation is limited, and the mechanism of grain boundary sliding is not dominant any more. Nevertheless, if at sufficiently high homologous temperature (here T_h=0.6), plastic deformation may still occur but at a lower strain rate. The low strain rate is associated here with plastic flow over a large time scale (creep deformation). Thus, within this large time scale, the diffusion of grain boundaries may drive the kinetics of deformation which appears, in this domain, much more sensitive to the magnitude of the load. This higher sensitivity is suggested in Fig.3.11 by the higher slope of the curve $m_2 >> m_1$. In this regime (creep), the viscous stress is related to the strain rate by the Eq. $\sigma = K_2(r)^{m_2}$. Finally, the point of intersection between the two curves (at σ_v=7 MPa and r=1×10^{-8}) can be associated to the transition between the two mechanisms reported for pure Sn at 0.6 homologous temperature by Ashby [10].

The double linear trends observed in the experiments (in Fig.3.11) correlates to the transition between the mechanism which at this homologous temperature shows different sensitivities to the strain rate resulting in two different slopes m_2 and m_1, respectively for grain boundary sliding and grain boundary diffusion mechanism. Actually, the presence and fractions of the two mechanisms remain hypothetical, as a direct in-situ observation at the microstructure level is not available. The viscous behavior of the material could be explained by Ashby deformation mechanisms occurring at different strain rates and load levels, even if, at the moment, there is still no concrete observable evidences as e.g. micrographs depicting these mechanisms. Such an investigation may confirm the hypothesis of the two mechanisms, and prove the direct correlation between the observed two regimes of viscous behavior Fig.3.11 and the map of mechanism of deformations, based on Ashby's work (see Chap.2, Fig.2.1).

3.3.5. Influence of the temperature

In metallic materials, plastic deformation and hardening processes are temperature activated mechanisms. This common agreement is established for a large variety of metals [10], particularly at high homologous temperature where inelastic deformations may be accompanied by creep mechanisms, as discussed for the solder alloy in the previous section. Here, the influence of the temperature is present in the whole strain rate range, as even the lowest temperature of -40°C investigated here still corresponds to a high homologous temperature T_h >0.4. The two diagrams below

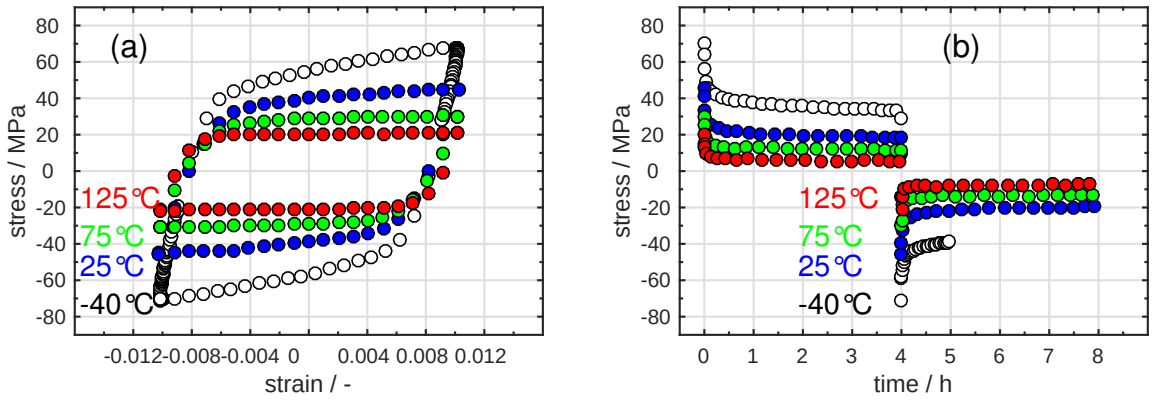

Fig. 3.12: (a) Cyclic stress-strain hysteresis for different temperatures -40 ℃...125 ℃ at constant strain rate r=1×10^{-3}s^{-1}. (b) Relaxation behavior within 4 hours for different temperatures -40 ℃...125 ℃. Rapid loading /unloading rate r=1×10^{-3}s^{-1}. Alloy: SAC

illustrate cyclic hysteresis (a) at a constant strain rate of 1×10^{-3}s^{-1} for different temperatures and the relaxation behaviors (b), respectively, for the same temperatures Fig.3.12.

Both strain and time hardening are affected by the temperature, as well as the elastic properties of the solder material. The elastic properties of the material manifest shortly after the reverse of the loading direction. In this domain, the Young's modulus can be determined graphically by the slope of the curve $|d\sigma/d\varepsilon|$. As it can be seen from Fig.3.12(a), the Young's modulus decreases with temperature. The hardening behavior is further modified by the temperature as the increase of stress after yielding tends to vanish with increasing temperature. For -40 ℃, the material exhibits hardening up to 1% of strain whereas for 125 ℃, the stress i.e. hardening processes saturate just after yielding. The substantial reduction of hardening modulus is linked to the stress relaxation behavior displayed Fig.3.12(b). The remaining stress at the end of the relaxation decreases when the temperature increases, which correlates with a decrease of hardening modulus observed in the stress-strain hysteresis Fig.3.12(a). Time hardening and viscous properties are also influenced by the temperature, as shown in (b), by the strong, and quasi-instantaneous stress relaxation in the first minutes of the dwell time period for the temperatures 75 ℃ and 125 ℃. As expected, the equilibrium strain vs. time hardening is modified with the temperature. The high amplitude of stress relaxation (>70%) as well as the low value of remaining stress after 4 hours relaxation for 125 ℃ (≈ 5 MPa), indicate that viscous effects (time hardening) over-balance strain hardening effects when the temperature

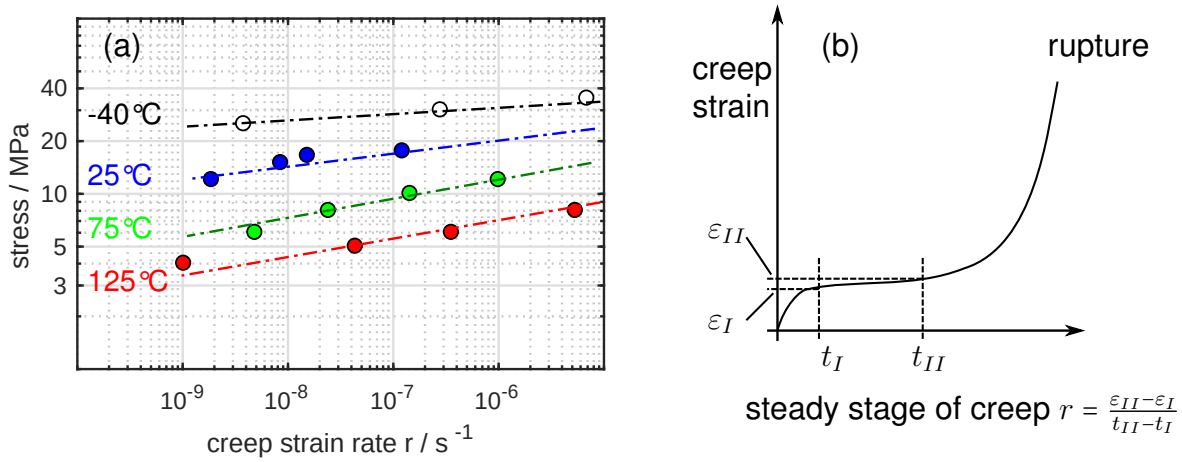

Fig. 3.13: (a) Strain rate r (in the steady state of creep) vs. applied stress for different temperatures. Alloy: SAC (b) Evaluation steady state creep strain r on a creep curve

increases. This high viscosity also manifests at higher strain within creep tests, where the steady state creep strain rate also shows a temperature dependency Fig.3.13.

The steady state creep strain rate, occurring typically at higher strain ($\varepsilon \approx 2\%$), depends on the applied stress and the temperature. For a same equivalent stress, the strain rate increases when the temperature increases. This effect correlates with the decrease of stiffness and hardening of the material with an increase of the temperature. Furthermore, the sensitivity of the stress regarding the strain rate modifies as well, as it is displayed on the graph Fig.3.13. The slope of the curves continuously increases with temperature which illustrate the increase of viscosity and, at the same time, a decrease of hardening mechanism and fall of the material stiffness. Once more, this observation within the steady state creep regime argues that viscous stresses (time hardening) over-balance strain hardening processes when the temperature increases. The effect is confirmed by cyclic and creep experiments, corresponding to small and large strain deformations respectively, in the temperature range between -40 °C and 125 °C.

According to Ashby's theory, the mechanisms of deformations are related to the homologous temperature, such as the decrease of stiffness and increase of strain rate are expected in response to a temperature increase for a constant load. In the map represented in Fig.2.1, a temperature change within a constant load may result in a change of mechanisms of deformation. Indeed, the homologous temperature, here between 0.4 and 0.85, overlaps several deformation mechanisms which also depends on the rate of plastic deformation and the magnitude of the load. For example, considering a normalized load in the range of 10^{-4}...10^{-3}, and at the same time a heating from 0.6 to 0.8 homologous temperature (T=130 °C to T=175 °C), the

resulting plastic deformation would be attributed to two overlapping mechanisms at the microstructure level, namely, dislocation climb and grain boundary sliding, the last being more pronounced at the higher temperature.

This situation may occur, for example, during rapid heating of a component from room temperature to 125°C, such as the thermal stresses induced in the solder joint remain high until recovery processes activate and provoke the stress relaxation. In contrast, during a slow cooling rate period, where the corresponding thermal stresses and deformation rates are both low, the mechanisms of deformation may shift from grain boundary sliding to grain boundary diffusion. Again, this situation is expected for soldered components, where solder joints are submitted to the low cooling rate after turning off the car engine.

Within the presented characterization program, the mechanical behavior of the solder material SAC reveals a complex interplay between time and strain hardening processes, which are also strongly dependent on temperature. Moreover, the different measurements realized (e.g. cyclic under small strain vs. unidirectional creep deformation at high strain) indicate that the viscous properties of the solder material prevail over the strain hardening processes (see Fig.3.12-3.13). Furthermore, this dominance is more pronounced with increasing the temperature and decreasing strain rate. Viscous effects are stronger activated within long time creep testing (for low strain rate) and relaxation periods, compared to rapid loading/unloading for example (see Fig.3.11). This non-uniformity of the material behavior over the whole strain and temperature ranges investigated here could be explained by concurring deformation mechanisms at microstructure level, in response to a thermal activation, a load or a strain rate change. The observed effects are analyzed and discussed in relation to the theoretical deformation mechanisms map for metals reported by Ashby [10] in Fig.2.1. Indeed, the measurements as in Fig.3.11 suggest a change in the deformation mechanism, which actually could correlate to the transition region between two mechanisms in the Ashby's map Fig.2.1. These complex mechanical properties are characteristic to the solder alloy in its initial state of deformation. Thus, the above-mentioned properties are related to an undamaged state of the material prior to degradation.

3.4. Experimental investigation of the damage behavior

As far as the experiments revealing the deformation properties are completed, the investigations are directed towards the characterization of the damage behavior of the material. As a common assumption for metals undergoing loads under high homologous temperature, creep damage has to be considered. Besides, electronic components undergo thermally induced cyclic loads, which means that damage in terms of both creep and thermo-mechanical fatigue has to be taken into account.

3.4.1. Damage evolution under creep loads

Microstructure transformation under creep loading conditions

The creep tests do not only characterize the deformation behavior at high strain and low strain rate, but also reveal the intrinsic degradation of the material. During these tests, the material is maintained at constant temperature under a constant load. Under these specific loading conditions, the degradation is mostly caused by creep damage development. Typical creep damage may be observed directly on the microstructure level of the material, as for example, by the substantial growth of pores and creep cavities, observed after failure of the sample [79]. The impact of creep on the solder material is shown in Fig.3.14 by EBSD microstructure micrographs after creep rupture time at 125℃ under 5 MPa.

Necking is observed in the region of creep fracture which indicates a high localization of inelastic deformation. Furthermore, the overview of the sample depicts smaller grains on both sides near the surface of fracture and correlates with a recrystallization process enhanced by high plastic deformation in this region. EBSD analysis is carried out on the two spots (1) near the fracture region, and (2) outside the fracture region. The EBSD analysis confirms that the grains size increases with the distance to the creep fracture zone. In addition, the insights (1) and (2) reveal the presence of cavities which can be identified by oval black flakes, elongated in the tensile direction of loading. These cavities were not present in the initial state (Fig.3.3), therefore they result from the applied stress and temperature and have developed during the 400 h. testing time until creep rupture. The cavities are distributed throughout the section of the sample (normal to the direction of loading). Besides, the density of cavities decreases with the distance to the fracture zone. The high density of cavities inside the grains (a) and at the crack-tip (c), near the fracture zone, suggest creep

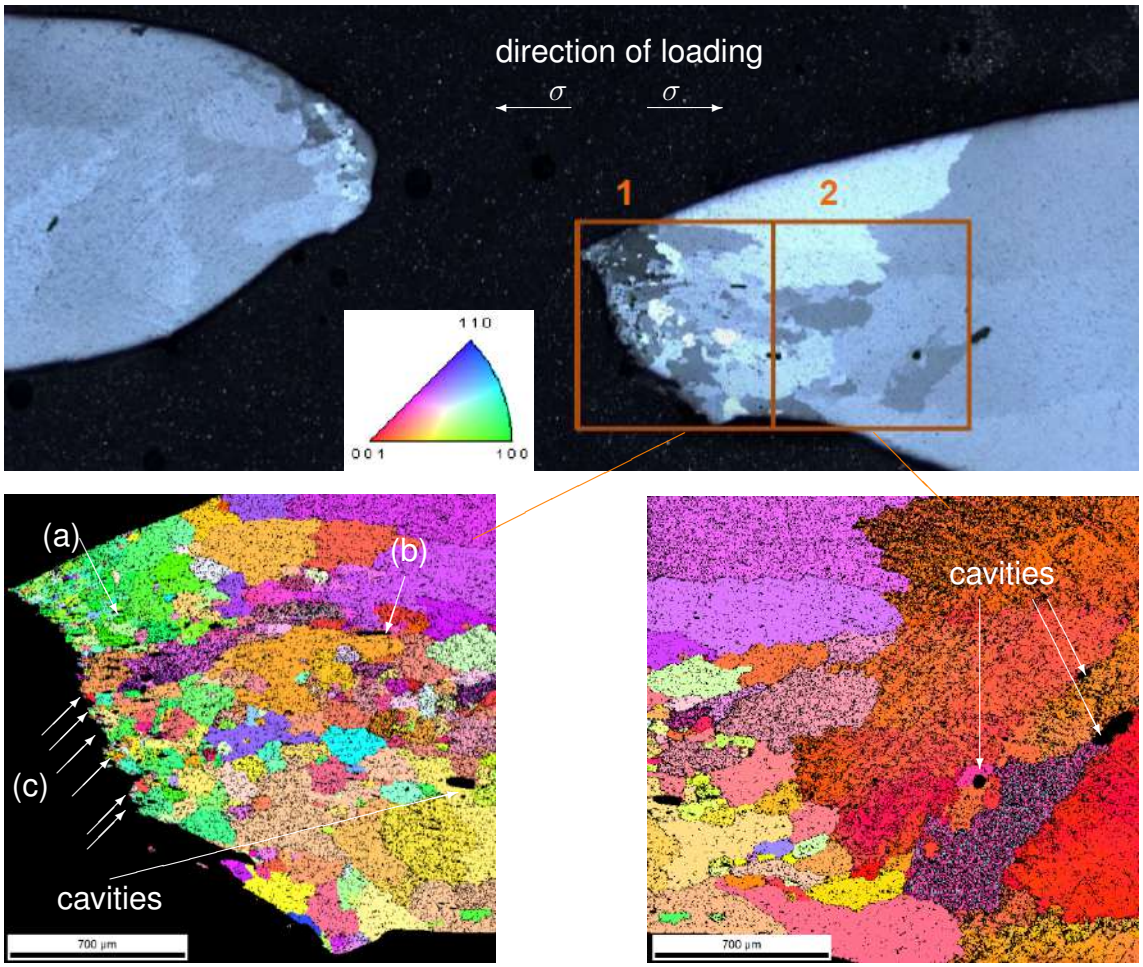

Fig. 3.14: Polarized light microcopy (picture overview) and EBSD micrographs after a creep test at T=125℃, stress σ=5 MPa. Cavities and voids are identified near the surface fracture (a), (b) and (c). EBSD picture made in TU-Dresden.

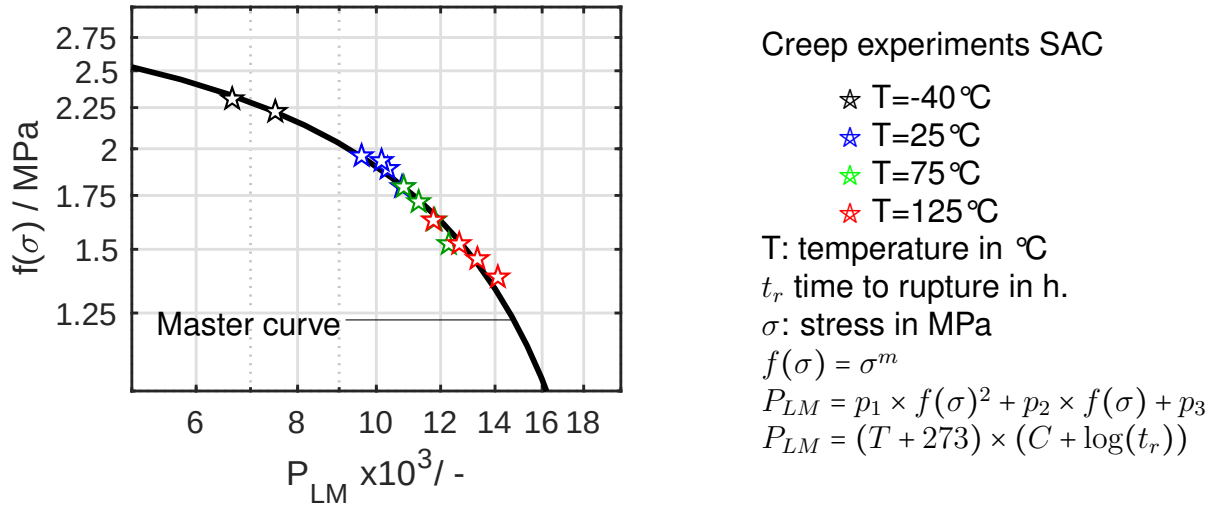

Fig. 3.15: Larson-Miller's master curve for solder alloy SAC

fracture enhanced by nucleation of voids. At the same time, the microstructure recrystallizes and many grain boundaries are thus delimited by cavities which appear at grain junctions, like in (b). This mechanism can be interpreted, at the grain level, as an inter-crystalline crack growth by interconnection of cavities and micro-defects which lead to a micro-crack which propagates along the grain boundaries.

In order to quantify the evolution of creep damage development we use the macroscopic deformation of the material, which is recorded from the beginning to the rupture of the samples. We assume that damage (i.e. general term including all microstructural processes like pores growth, cavity formation, dislocation accumulation, grain boundary sliding, micro-cracks, etc.) acts as a perturbation and leads to modification of the mechanical behavior. The impact of damage accumulation during the sample life can be correlated to the observed evolution of its mechanical properties (stress-strain-strain-rate and temperature) taking the initial mechanical properties of the material as a reference.

Larson-Miller's master curve

The corresponding creep time to rupture t_r can be evaluated after the concept of the Larson-Miller's master curve, see Fig.3.15 [62]. Here, t_r is included in the fit parameter P_{LM}. Thus, the stresses and their corresponding P_{LM} are fitted using a second order polynomial function. The fit-parameters are given in table 3.2.

Using a Larson-Miller's master curve, the time to rupture for arbitrary temperatures and stress levels can be calculated. It should be noted that only the samples which reached the creep failure are considered in the Larson-Miller fit. In Fig.3.16, the

C	m	p_1	p_2	p_3
28.0	0.24	-6.819×10^2	-4.746×10^3	2.184×10^4

Tab. 3.2: Larson-Miller parameters for SAC solder alloy

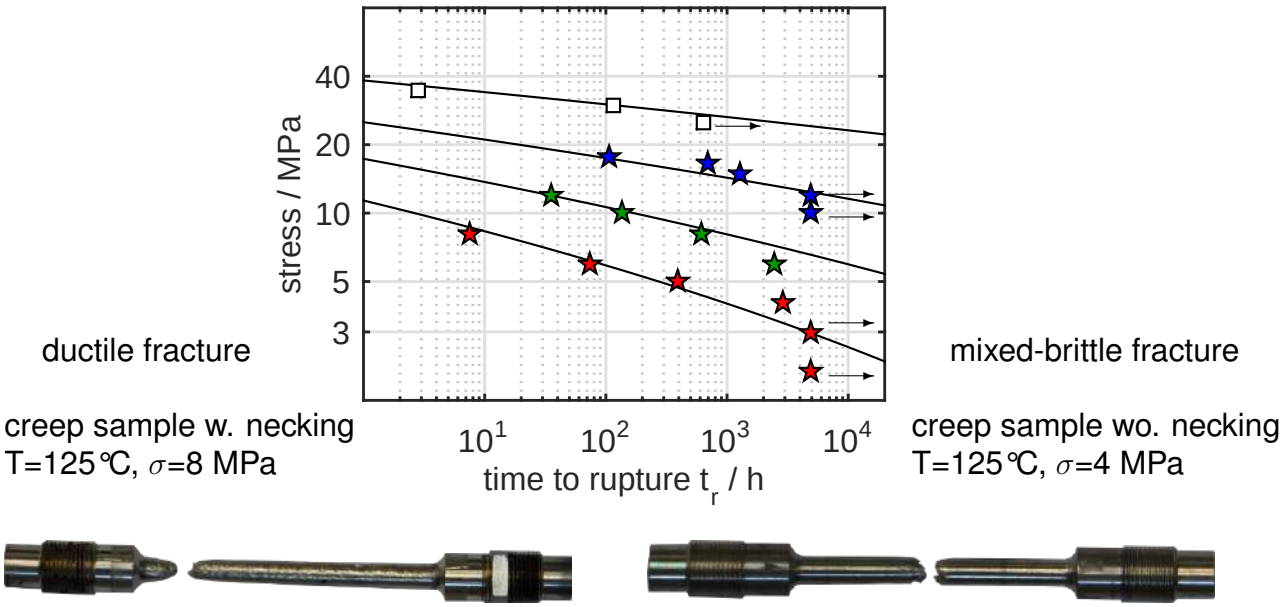

Fig. 3.16: Applied stress σ related to time to rupture t_r for creep tests in the range -40℃...125℃. Alloy: SAC

symbols marked by an arrow refer to creep tests which are still running, such that the times to rupture are expected higher than the diagram suggests. The diagram Fig.3.16 shows that the higher the temperature the lower the creep resistance. At 125℃ creep rupture occurs at extremely low stress level <5 MPa, which correlates to the low yield stress observed at this temperature (s. section 3.3.5).

Evaluation of creep damage

Similar to the Larson-Miller equation, a power function can be used to associate the times to rupture t_r, stresses σ, and temperatures T. This relation is often observed for other metals [79] and also basic phenomenological models were established to describe them. Looking at the creep curve Fig.3.17, the damage rate seems to increase continuously, and dramatically rises in the tertiary creep stage, causing the failure of the sample. Indeed, the strain rate seems to correlate to an equivalent creep damage parameter, which, after reaching an equilibrium state, increases until rupture of

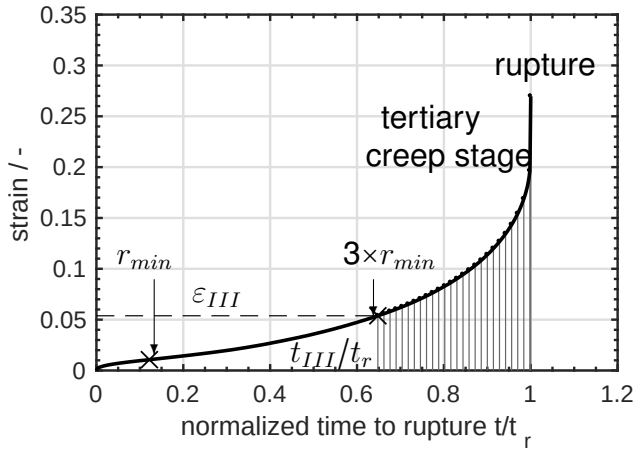

Fig. 3.17: Evaluation of the tertiary creep stage on an experimental creep curve, T=125℃, applied stress σ = 5 MPa. Alloy SAC

the sample. Chaboche and Lemaitre derive damage parameters from the strain rate (see Chap.2 Eq.(2.25)) [55]. Here, we employ a similar approach to evaluate creep damage for the solder alloy. The method requires the determination of the minimal strain rate r_{min}, which corresponds to the activation of creep damage [55]. Even if the theory divides the creep deformation in three stages, a perfectly constant minimal strain rate value over a large period, as assumed in the stationary creep phase, is rarely observed. The creep experiments show rather smooth transition in the evolution of the strain rate without a clear boundary between secondary and tertiary creep stages. Thus, we postulate an evaluation strategy in order to reproducibly quantify the beginning of the tertiary creep stage as follows: the time when the strain rate reaches a value by a factor of three higher than the minimal value r_{min}, then this marks the beginning of the tertiary stage. This point is characterized by the tertiary creep strain ε_{III} and by its specific time fraction t_{III}/t_r, shown as an example in Fig.3.17. This procedure is repeated for all creep experiments and the corresponding tertiary creep onset with coordinates (t_{III}, ε_{III}) are successively evaluated.

In fact, ε_{III} can be used as an indicator of the ductility under creep testing conditions because it correlates to the inelastic deformation accumulated in the material during the test. First, we observe that the ductility increases with temperature, which correlates to the pronounced viscous behavior discussed in the previous section.

The normalized quantity $1 - t_{III}/t_r$ is plotted as a function of stress in Fig.3.18(b). This quantity represents the amount of time (in %) that the material consumes in the tertiary creep stage. The diagram Fig.3.18(b) shows that the relative period of tertiary creep increases when the stress decreases. For instance, at 125℃, 80%

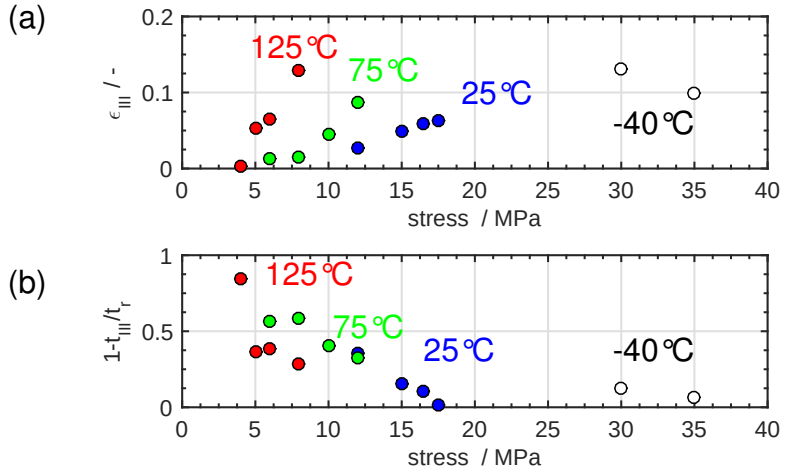

Fig. 3.18: (a) strain at the onset of the tertiary creep stage (ε_{III}) vs. the applied stress for creep experiments in the temperature range -40 °C...125 °C. (b) lifetime fraction from the beginning of the tertiary creep stage (t_{III}) to time to rupture t_r vs. the applied stress σ in creep experiments in the temperature range -40 °C...125 °C

of the lifetime is consumed in the tertiary creep at 4 MPa, whereas only 30% at 8 MPa at the same temperature. For low stresses, the tertiary stage occurs sooner ($t_{III}/t_r << 1$) but at a lower strain amplitude (as shown in Fig.3.18(a)). Afterwards, the damage rate remains relatively low, and a large part of the sample's life is located in the tertiary domain which mainly evolves under relatively low strain amplitudes. For these cases, a rather brittle fracture is observed. In contrast, when the material is put under higher stresses, it undergoes large deformations before it enters the tertiary creep stage. Then, as soon as the tertiary stage begins, the damage development becomes faster. Therefore, the relative fraction of life spent in the tertiary stage is low ($t_{III}/t_r \approx 1$). These tendencies suggest further that material ductility during creep depends on the applied stress. This is supported by the observation of substantial necking of the sample prior to rupture (Fig.3.16) at higher stresses in contrast to the rather brittle rupture at lower external loads .

Due to the significantly longer creep test times at low external loads, thermally induced slow deformation processes are expected to gain importance. Volume- and grain boundary diffusion and grain boundary sliding might be responsible for the formation of multiple microscopic defects like cavities and micro-cracks at grain boundaries. Such defects occur not at a single site, but at multiple locations throughout the microstructure. In the final stage, growth and coalescence of such localized defects can lead to macroscopic failure and sample rupture. In terms of damage mechanics,

damage due to creep at low stress is considered to evolve in a non-localized fashion, thus affecting the whole sample volume.

As a summary, material damage during creep tests reveal a significant dependence on temperature and stress level. Furthermore, total strain at creep rupture shows substantial increase with increasing stress levels.

3.4.2. Damage evolution under fatigue loading conditions

Material softening and microstructural transformations

The fatigue properties of the material are measured by means of standardized Low-Cycle Fatigue tests. The tests are conducted at constant temperatures of -40℃, 25℃, 75℃ and 125℃. The strain rate is maintained constant over all the tests at r=$1\times10^{-3}s^{-1}$ in the LCF regime. HCF measurements are performed at RT, with strain profiles following a sinus form at the frequency of 10 Hz. All cyclic tests have a symmetrical tension-compression ratio $R = -1$ ($R = \varepsilon_{min}/\varepsilon_{max}$) with respect to the minimal and maximal strain amplitudes ε_{min} and ε_{max}. As expected, the mechanical behavior of the material is affected by the repetition of cyclic loads. From a macroscopic point of view, the modifications of the mechanical properties are represented by a substantial decrease of the maximal stress obtained in each individual cycle. Microstructure analysis reveal significant modifications in terms of grain size evolution and relative grain orientation Fig.3.20-3.22. In the following, the impact of cyclic aging is highlighted by results of isothermal LCF test at temperatures of -40℃ and 125℃ under cyclic loads corresponding to ±0.50% strain amplitude (LCF-regime).

Between the first and up to the 500^{th} cycle, a slight increase of the maximum peak stress in each cycle is observed in Fig.3.19 at -40℃. Thus, until the middle-life $N_f/2$, stabilized cycles are depicted, such as the first and middle-life cycle appears identical. After N = N_f /2 = 1220 cycles, the maximum peak stress in each cycle decreases with a low rate (5 MPa in 1000 cycles) until N = 2200 cycles. The sudden fall of stress between N = 2100...2200 marks the presence of a macro-crack inside the sample, which propagates and causes a fast decrease of peak stresses in the last stage of the fatigue life. The non-symmetrical shape of the hysteresis within the last cycle is due to a localized macro-crack, because the compression domain offers more resistance than the tensile one, a higher stress results (-40 MPa in compression vs. 20 MPa in tension).

The micrographs reveal the absence of recrystallization mechanism during the LFC test at -40℃, see Fig.3.20. The sample test region has a homogeneous crystal

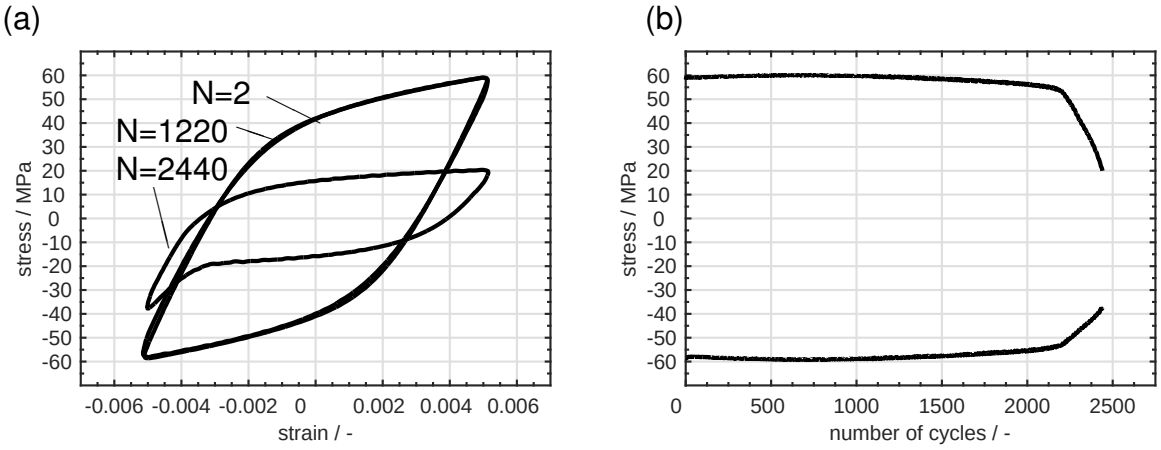

Fig. 3.19: (a) stress-strain hysteresis at initial state N = 2, middle life N = $N_f/2$ and end-of life N = N_f. (b) Peak stresses at each cycle within a LCF test at -40 °C. Alloy: SAC

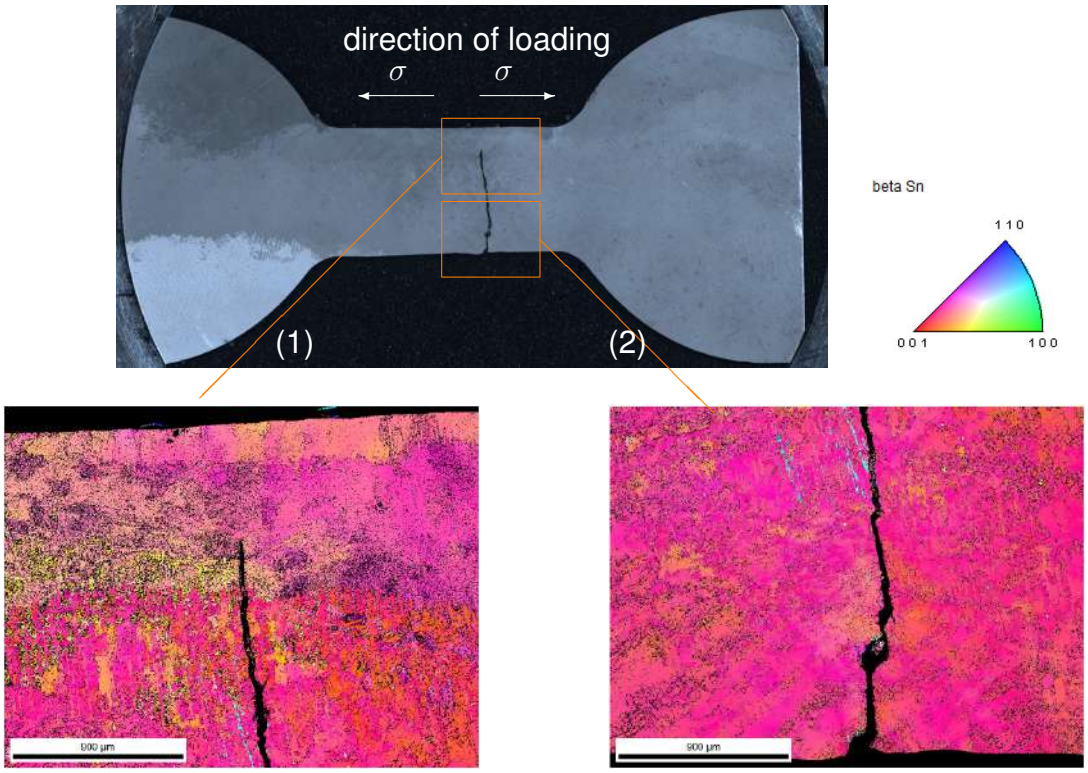

Fig. 3.20: Polarized light microscopy (overview of the sample) and EBSD micrographs after a LCF test, N=2440 cycles, $\Delta\varepsilon$=±0.5%, T=-40 °C. EBSD picture made in TU-Dresden.

orientation comparable to the microstructure observed at the initial state after casting the sample, see Fig.3.4. The crack initiates and propagates through a grain, perpendicular to the loading direction. Thus, a trans-crystalline crack propagation can be identified, as each side of the crack has the same crystal orientation [001]. Moreover the micrograph highlights a high localization of damage: outside the crack tip the microstructure remains unchanged and the material undamaged, as no other cracks have yet initiated at other positions within the sample test region. Voids and cavities are not detected.

In contrast, lower stresses are observed during cyclic loading at 125℃, see Fig.3.21(a) compared to -40℃ in Fig.3.19(a). Besides, cyclic isotropic hardening, observed during cyclic loading at -40℃ (see Fig.3.19(b)), is replaced by cyclic softening at 125℃ (see Fig.3.21(b)). Three phases could be identified on the curves Fig.3.21(b). A fast stress reduction is observed within the first 200 cycles and corresponds to the first phase of stress softening. The second phase is characterized by a slow stress decrease, which leads to the substantial reduction of the hysteresis surface (see Fig.3.21(a)) in the interval N = 200...1200 cycles. At about the 1200^{th} cycle, a smooth acceleration of stress reduction is depicted. This stage corresponds to crack initiation although it is not clearly remarkable at the temperature of 125℃, compared to the stress fall after crack initiation observed at -40℃. Nevertheless, the crack initiation is estimated in the range of the 1200...1500^{th} cycle according to Fig.3.21(b). After crack initiation, the stress reduction is more pronounced and follows its decrease until N = N_f (third phase of stress softening).

The fatigue test is stopped at N = N_f cycles, when 50% of stress reduction is obtained. The EBSD and microscopic analysis realized after N_f cycles reveal the fundamental transformation of the microstructure of the solder material under fatigue loads at 125℃. Originally composed by few large grains in its initial state (see Fig.3.4), the sample is now formed by a large number of small grains, particularly in the sample test region where most of the loads are concentrated. Two spots are investigated with EBSD-microscopy where macro-cracks have been already identified on polarized micrographs.

In contrast to -40℃, the damage is rather widely distributed, and macro cracks have started at several locations on the surface of the sample in (a), (d) and (e) in Fig.3.22. Initiation and propagation of the cracks do not follow the perpendicular direction of loading, as it is the case at -40℃, but follow an angle of about 45° with respect to the direction of loading. Small grains are identified along the crack and at the crack front in (f) and (c), and in the center of the sample in (b) which is at the

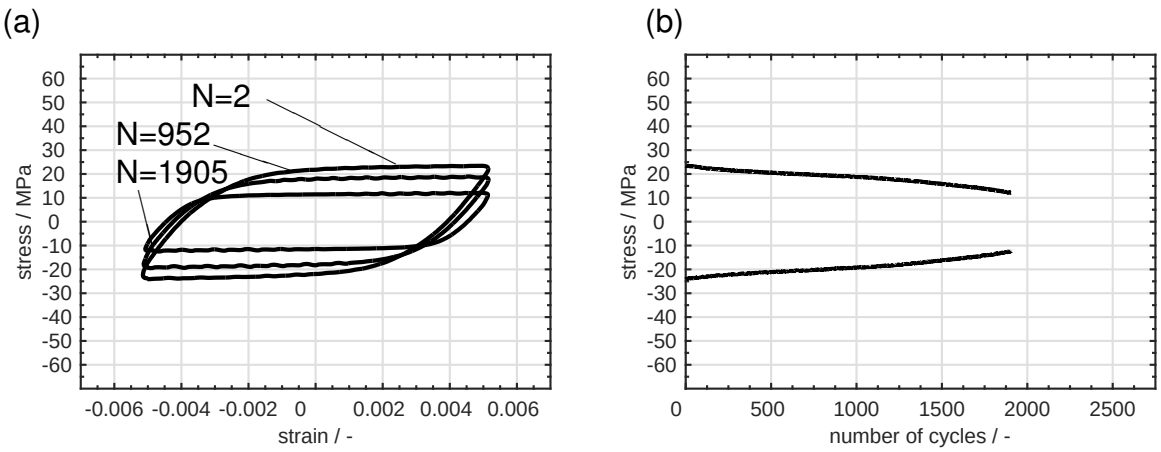

Fig. 3.21: (a) stress-strain hysteresis at initial state N = 2, middle life N = $N_f/2$ and end-of life N = N_f. (b) Peak stresses at each cycle within a LCF test at 125°C. Alloy: SAC

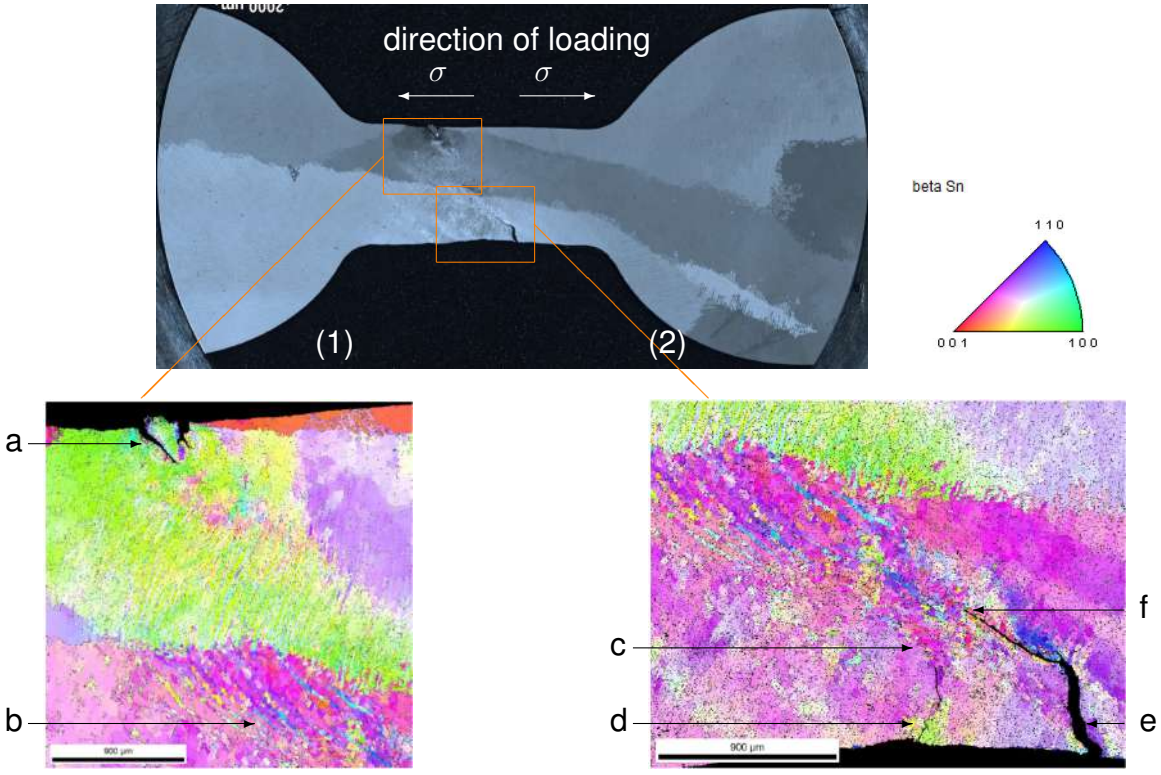

Fig. 3.22: Polarized light microscopy (overview of the sample) and EBSD micrographs after a LCF test, N=1905 cycles, $\Delta\varepsilon$=±0.5%, T=125°C. EBSD picture made in TU-Dresden

T / °C	E / MPa	$\sigma_f^{'}$	b	$\epsilon_f^{'}$	c
-40	57265	167.16	-0.0629	1.0478	-0.6817
25	45113	123.90	-0.0645	6.3824	-0.7950
75	35766	192.10	-0.1664	2.7115	-0.6822
125	26418	158.65	-0.1908	0.3993	-0.4675

Tab. 3.3: Coffin-Manson-Basquin fit parameters in Eq.(2.17)

moment still not cracked. All these observations argue for an intercrystalline crack propagation enhanced by recrystallization.

However, in the zones where the crack started, similar crystal orientations are measured within the zones near (a) and (e) and larger grains are identified in contrast to the crack front in (f) and (c). Besides, the hypothesis that the crack may start inside the grain is supported by the observation in (a), where a crack with a length of 300μm initiates and propagates through a grain with a homogeneous crystal orientation [100], see Fig.3.22(1)(a). Thus, the corresponding failure mechanism for fatigue loads at 125°C suggest a transcrystalline crack initiation in a first step. In parallel, due to the high homologous temperature and accumulated plastic deformation, the structure of the material recrystallizes, transforming the original monocrystalline structure into a polycrystalline one. Then, in a second step, the crack comes across recrystallized grains which are much more smaller and instead of going through these small grains, the crack propagates along the multiple grain boundaries depicting an intercrystalline crack growth.

Temperature dependent fatigue failure curves

The strain-based representation of Coffin-Manson-Basquin [57, 58, 59] is employed in Fig.3.23 to illustrate the cyclic fatigue resistance of the solder material at different temperatures. The tests presented in Fig.3.23 result from standardized LCF experiments performed at several institutes as well as the measurements carried out within the present work. Elastic and plastic strain amplitudes are calculated based on the total strain amplitude, the stress amplitude is measured during the test in the first cycle as well as the Young's modulus. Elastic and plastic strain amplitudes data are then reported in the diagrams Fig.3.23 with the corresponding number of cycles to failure N_f for the different tests, depicting two logarithmic asymptotes for LCF and HCF domains respectively.

The sum of the two asymptotes provides the Coffin-Mason-Basquin curves from which the four parameters are determined by linear regression, per temperature sep-

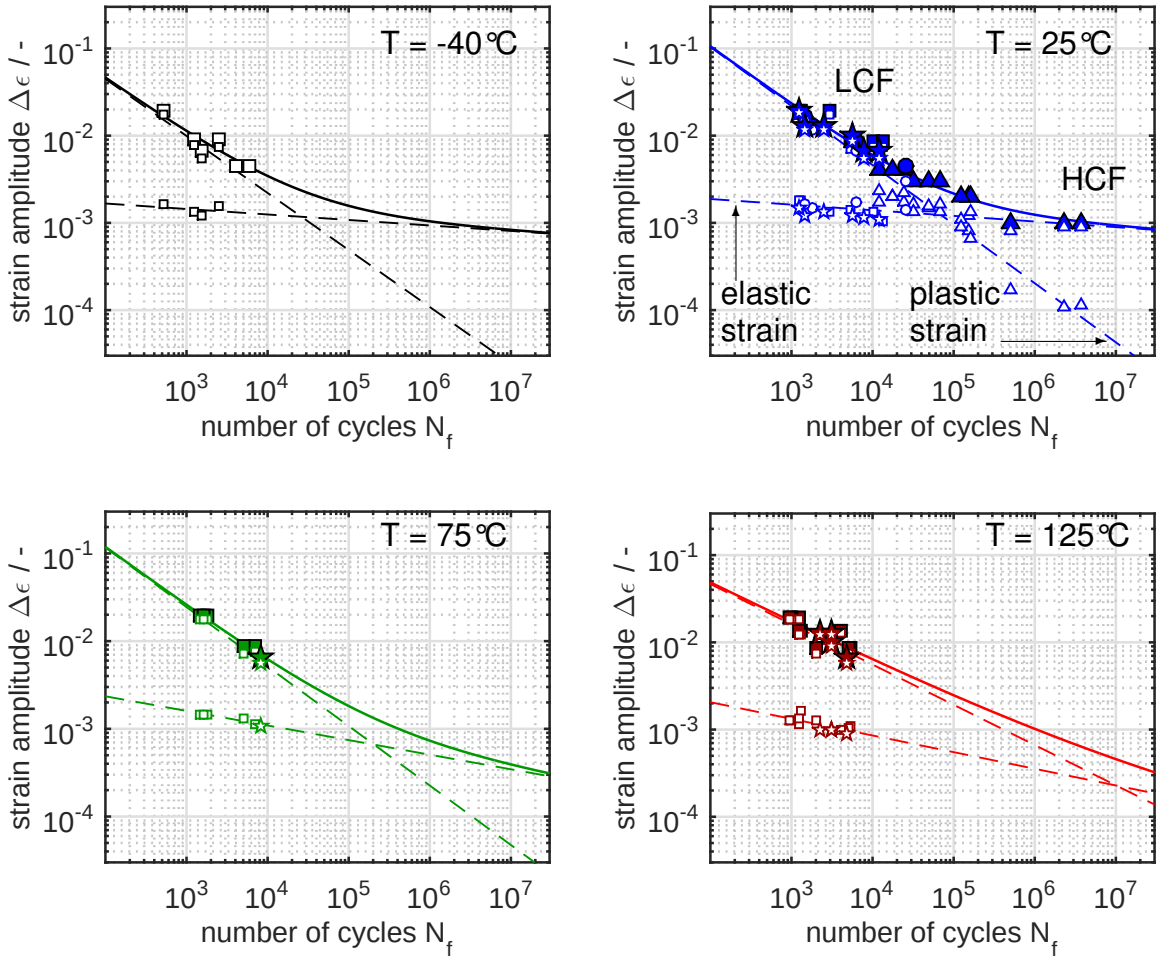

Fig. 3.23: Coffin-Manson-Basquin curves at -40 °C, 25 °C, 75 °C and 125 °C for the solder alloy SAC. Symbol coding regarding the origin of the tests: □: IKTS-Dresden, ◯: MPA-Stuttgart, △: CR/APM (Bosch), ☆: own measurements

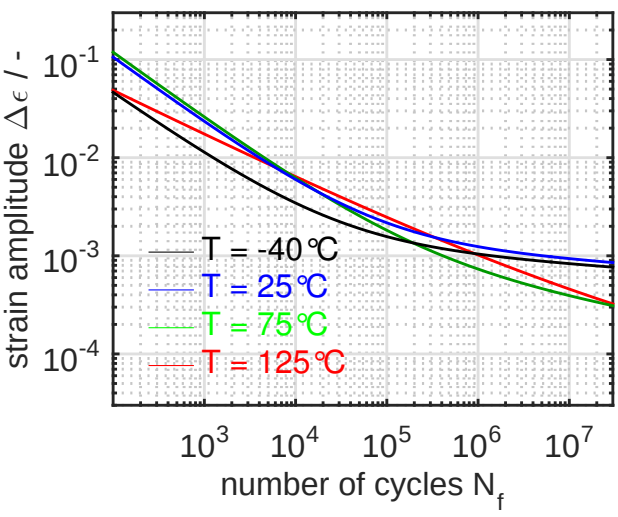

Coffin-Manson-Basquin eq.

$\Delta\varepsilon^{tot} = \frac{\sigma_f'}{E}(N_f)^b + \epsilon_f'(N_f)^c$

$\Delta\varepsilon$: strain amplitude

N_f: number of cycle to failure

Fig. 3.24: Fatigue life curves for the solder alloy SAC in the temperature range -40 °C...125 °C. Equation after Coffin-Manson-Basquin [57, 58, 59]

arately, see Tab3.3. The HCF regime have been investigated at room temperature. For the other temperatures, only a prediction can be provided by extrapolating respectively elastic and plastic part of the total strain from the LCF onto the HCF regime.

The influence of the temperature on the fatigue life is revealed by Fig.3.24. For a constant strain amplitude, different lifetimes are expected if the temperature varies. The variation is estimated by a half decade in the LCF regime whereas much higher in the HCF-regime, according to the extrapolated curves. In the LCF domain, within the temperature range -40 °C...75 °C, parallel asymptotes are depicted which correlate with a homogeneous ductility exponent $c \approx$ -0.70. However at 125 °C, the ductility exponent decreases in accordance with the high ductility of the material at $T_h \approx 0.8$, which allows larger deformation before crack initiation and fatigue failure. In contrast, the domain of fatigue resistance sinks with the increase of the temperature. For -40 °C and 25 °C, a safety region could be determined below the strain amplitude $\Delta\varepsilon$=1×10^{-3}, after which no fatigue failure is predicted for N $< 1\times10^7$ cycles. This region corresponds to predominantly elastic loading, which are less damaging for the solder material. For 75 °C and 125 °C, this safety region appears to reduce, illustrated by a higher b exponent in the HCF regime. Under these temperatures, the material exhibits a very low yield stress, such as any load engenders non negligible plastic deformation fraction and consequently damage in the sample.

test	T	$\Delta\varepsilon$	t_h	σ_{med}	N	N_{fa}	t_r
RF1	25℃	0.0133	10 min.	15.42 MPa	1570	2811	437 h.
RF2	25℃	0.0133	10 min.	15.41 MPa	1143	2811	437 h.
RF3	125℃	0.0133	3 min.	4.63 MPa	1887	1877	434 h.
RF4	125℃	0.0133	10 min.	2.82 MPa	1665	1877	6382 h.

Tab. 3.4: Relaxation-Fatigue tests (RF)

3.4.3. Combined relaxation-fatigue tests

Real thermo-mechanical loads on solder joints under operation result from repetitive heating- and cooling phases with time periods at nearly constant temperature in between. Therefore, strain controlled cyclic loads with dwell time periods are carried out on standardized samples in order to investigate the dwell time effect on the fatigue life. This type of test is referred to as Relaxation-Fatigue test (RF-test), in which the maximal strain reached within each cycle is maintained constant for a predefined time period. Tests are performed under temperatures of 25℃ and 125℃, with dwell times of t_h = 3 min and t_h = 10 min. The observed fatigue-life reduction in comparison to pure LCF-life without dwell time periods (t_h=0min) is represented in Fig.3.25.

The stress-reduction during the periods of fixed strain is monitored and the median relaxation stress during the 10th dwell time period is reported in Tab.3.4. N_{fa} represents the number of cycles to failure calculated from the LCF-life curves at $\Delta\varepsilon$ = 0.013, for pure cyclic loads. N corresponds to the number of cycles to failure for the RF tests presented in this section.

The dwell time periods of the RF-tests are located in the tensile domain where creep is expected to be more pronounced, in comparison to compression loads. Under compression, creep pores and cavities can be closed, thus limiting creep damage development. The observed reduction of lifetime varies up to 30%, which depends on the temperature applied and the duration of the time periods under fixed strain. The amount of creep damage during the RF experiments is evaluated using the Larson-Miller approach (see Chap.3). The median relaxation stress of the 10th cycle is defined as the equivalent stress responsible for creep damage development within the time t_h, [27], being repeatedly accumulated throughout the cycles. The resulting time to rupture t_r, corresponding to the median stress for temperature T, obtained by Eq.(3.2)-(3.3) is reported in Tab.3.4. The fatigue and creep life fraction are calculated using Miner-Palmgren and Robinson accumulation rules, Eq (3.4)-(3.5) , respectively.

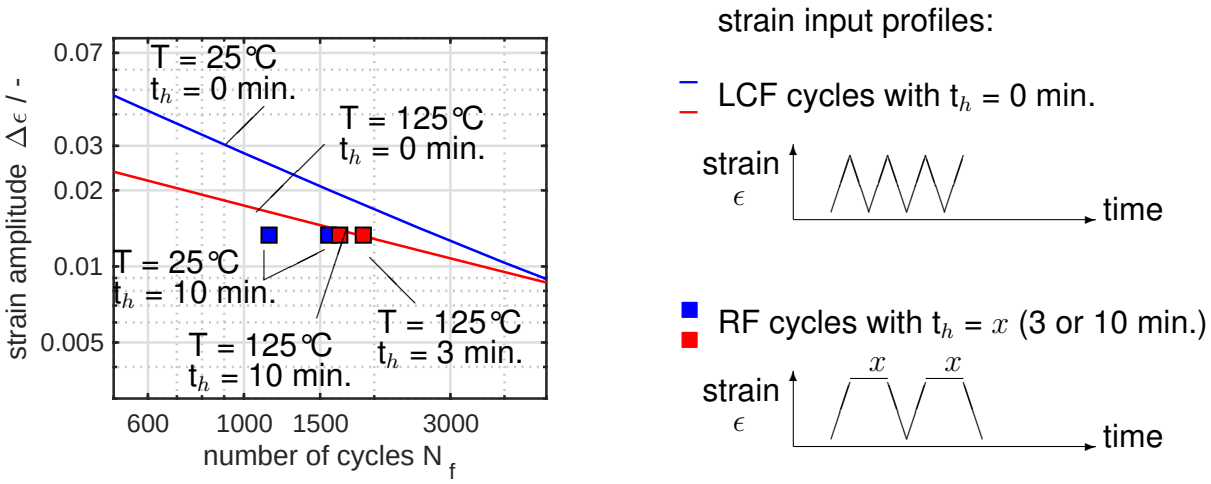

Fig. 3.25: Influence of the dwell time periods on the fatigue life of solder alloy SAC for 25 °C and 125 °C. Experiments: $\Delta\varepsilon$ = 0.013. A decrease of fatigue life is observed with increasing dwell time periods

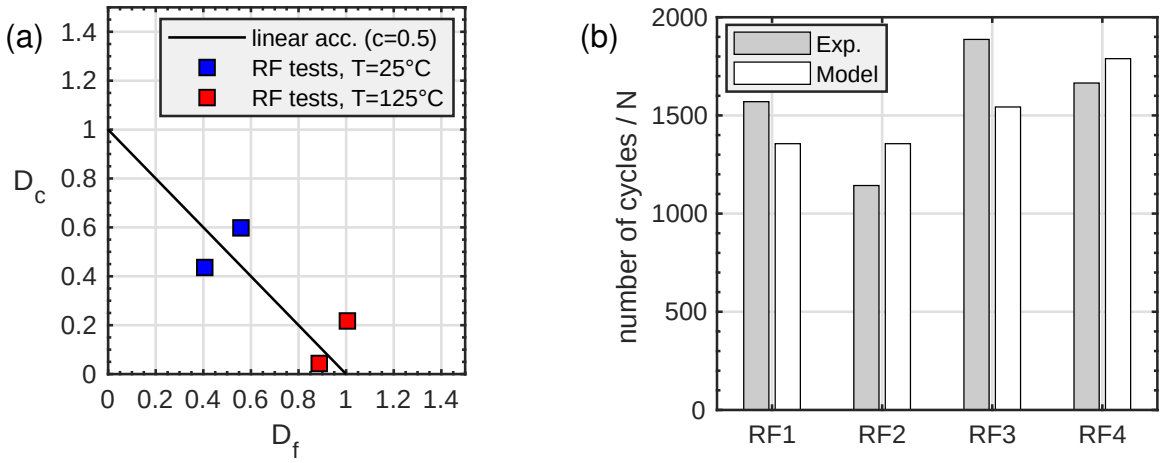

Fig. 3.26: (a) Creep-fatigue accumulation diagram evaluated using Coffin-Manson-Basquin and Larson-Miller damage parameters for the RF experiments and (b) Life-time prediction using a linear damage accumulation.

$$P_{LM} = f(\sigma_{med}) \tag{3.2}$$

$$P_{LM} = (T + 273) \times (C + \ln(t_r)) \tag{3.3}$$

$$D_f = \frac{N}{N_{fa}} \tag{3.4}$$

$$D_c = N\frac{t_h}{t_r} \tag{3.5}$$

The distribution of creep-fatigue damage fractions for the RF tests is presented in the Creep-Fatigue accumulation diagram Fig.3.26(a). The RF tests performed at 25℃ show a balanced damage distribution of creep and fatigue ratios ($D_c \approx D_f$) whereas the RF tests performed at 125℃ indicate dominant fatigue damage ($D_f > D_c$). Although creep damage is expected to be strongly activated at higher temperatures, the stress relaxation during holding time periods at 125℃ shows very low values (‘ 3 MPa). Effectively, this results in a relatively small contribution of creep to the total damage accumulation. In contrast, at 25℃, the stress reduces to 15 MPa, which leads to an increase of creep damage relative to fatigue development.

The RF tests suggest a linear accumulation rule for creep and fatigue damages, which is, at a first glance, independent of temperature. However, it should be noted, that the nature of the accumulation rule depends on the procedure used for evaluating the creep and fatigue damage parameters. As far as the RF tests are concerned, the ASME procedure has been employed in this work (ASME [61], section NH), using a combination of the Coffin-Manson-Basquin equation for the fatigue part and the Larson-Miller equation for the creep part. Using similar evaluation approach, a nonlinear accumulation rule was suggested for a Cr-steel alloy type 800 at comparable homologous temperature, (see Fig.2.11, Chap.2) with an inflection point at 0.12. The RF test results for the SAC solder alloy presented here are evaluated by a linear sum of creep and fatigue damage ratios. This results in a prediction quality for the number of cycles to failure N with a major deviation of 19% (for RF3), see Fig.3.26(b). The current results suggest a rather small interaction between creep and fatigue with linear accumulation of both damage contributions. However, in order to completely validate the impact of dwell time periods, and damage accumulation rule, further tests under varying strain amplitudes and temperatures would be necessary, which remains beyond the scope of the current work. Finally, the observed lifetime-reduction in the RF-tests compared to LCF-tests is attributed to the contribution of creep damage within the periods of fixed strain. During dwell times the stress relaxes

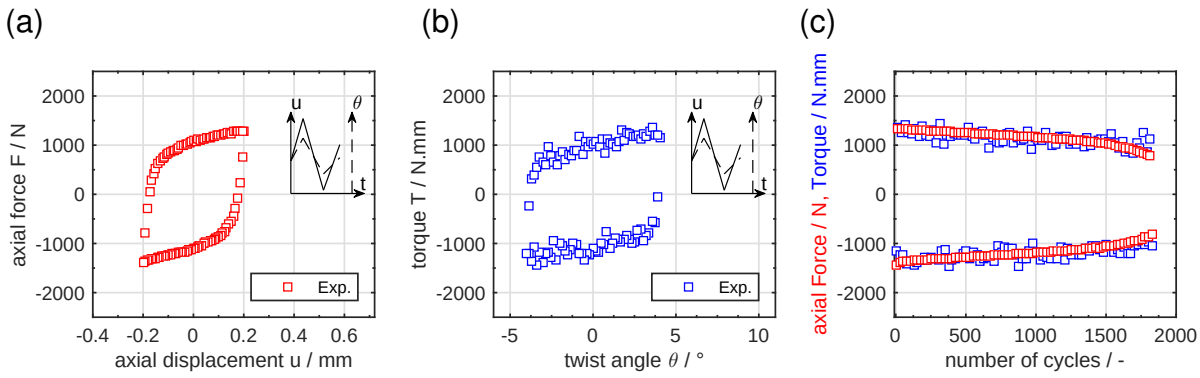

Fig. 3.27: (a) 10^{th} cycle, force vs. axial displacement. (b) 10^{th} cycle, torque vs twist angle. (c) cyclic softening of force and torque vs. cumulated number of cycles. experiment performaed at RT, alloy: SAC solder, u=± 20 mm, $\theta \pm 4^o$

to non-zero values, which leads to repetitive thermal activation of creep processes. Within each RF-cycle, creep damage is expected to add to fatigue damage, which leads to earlier failure of the sample compared to the pure LCF-cyclic lifetime.

3.4.4. Combined multiaxial tension-torsion fatigue tests

Until now, the material characterization was exclusively focused on uniaxial tests. Therefore, the correlation between varying multiaxial loads and cyclic damage evolution in solder alloys is still not understood. In order to address the shear mode of failure in terms of multiaxial fatigue conditions, tension-torsion tests have been conducted in this work. The experiments are carried out on full-bulk samples (without a hole or a notch). The geometry of the sample is adapted to the testing machine and to the strain sensor, which is able to measure axial and angular displacements (see appendix A.2). The sample is cycled -in phase- by angular and axial displacements controlled conditions, which are measured outside the gauges of the sample. The equivalent displacement rate is maintained constant by $1{\times}10^{-3}$ s^{-1}, the same as for the uniaxial LCF tests.

The applied multiaxial displacements lead to plastic deformation; therefore force-displacement and torque-twist angle hysteresis are observed during the cycles, here evaluated for the 10^{th} cycle in Fig.3.27(a)-(b). Under displacement controlled loading condition, one observes the substantial reduction of the maximal force and torque with the accumulation of cycles in Fig.3.27(c). The observable cyclic softening is comparable with than the one observed during the uniaxial cyclic tests. For this test, crack initiation is estimated at about 1600 cycles, for a total lifetime of 1850 cycles.

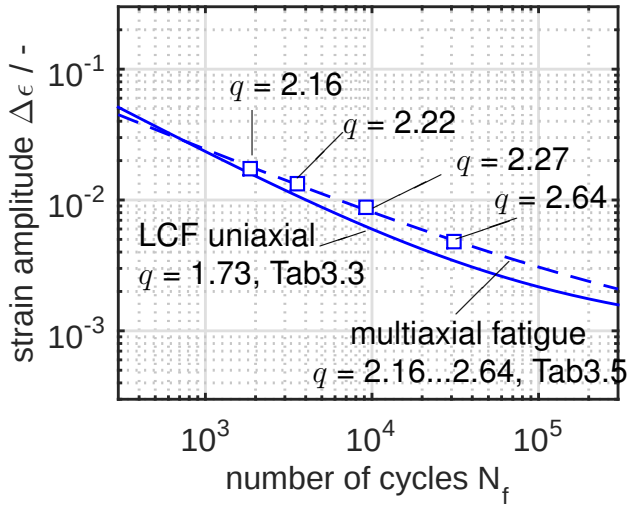

testing condition for tension-torsion tests

u / mm	θ / °	$\Delta\epsilon$ / -
0.20	4.00	1.74×10^{-2}
0.15	3.22	1.32×10^{-2}
0.10	2.39	8.92×10^{-3}
0.05	1.50	4.76×10^{-3}

$q = \frac{1}{\sqrt{3}}\frac{\sigma_{eq}}{\sigma_H}$, after Clausmeyer [68]

σ_{eq}: von Mises stress

σ_H: hydrostatic stress

Fig. 3.28: fatigue life curve under uniaxial and multiaxial loads obtained from tension-torsion cyclic tests at 25°C

E	$\sigma_f^{'}$	b	$\epsilon_f^{'}$	c
45113	174.35	-0.1021	0.9274	-0.5376

Tab. 3.5: fit parameters for Tension-Torsion cyclic loads (q = 2.2...2.6) in Coffin-Mason-Basquin Eq.(2.17)

Thus, axial displacements and twist angles are combined to obtain different equivalent strains which are a priori evaluated in the sample by FE-simulation. The combination of u and θ are systematically chosen to maintain the coefficient of multiaxiality q nearly constant. The samples are cycled until 50% of force reduction. A similar Coffin-Manson-Basquin curve can be constructed for tension-torsion loads where the equivalent strain amplitude can be associated to the number of cycle to failure. The tension-torsion life curve is displayed with the reference uniaxial cyclic curve in the Fig.3.28.

As a result, lifetimes of combined Tension Torsion (TT) tests (q = 2.2 ... 2.6) are slightly higher than the lifetimes of pure LCF tests (uniaxial q = 1.73) which are evaluated for an equivalent strain deformation within one cycle, see Fig.3.28. The four experiments performed under combined tension-torsion loads reveal an increase of about 25% of the number of cycles to failure in comparison with uniaxial cyclic loads. The four data points are fitted within a Coffin-Manson-Basquin equation and the fit parameters are summarized in the table below.

The interpretation of the results is still under debate, i.e. why cyclic torsional

loads damage less than cyclic uniaxial loads is not fully understood. The fatigue diagram Fig.3.28 suggests a systematically higher lifetime for the four different strain magnitudes.

In order to confirm or to reject this hypothesis, additional tests are required. Considering the relatively high experimental deviation of the fatigue life (in the order of 25%), the number of available LCF and TT-tests is not sufficient in order to quantify statistically the magnitude of the effect. Already mentioned before, the actual testing sample has a cylindrical test region. When submitted by torsional loads, the outer surface of the sample experiences much higher deformation compared to the middle regions where only the axial load contributes to the deformation. It results a high in-homogeneity in the strain distribution throughout the diameter and, as a consequence, a variation of the multiaxiality factor q. This in-homogeneity could be reduced by using hole-cylinder testing samples where the strain and q variations are constrained between the outer and inner wall of the sample, and are consequently lower compared to a bulk sample of the same outer diameter. Using such sample geometry, can confirm or reject the influence of multiaxial load on the fatigue life, and exclude any artifacts due to an in-homogeneities of the strain distribution.

Thus, future work is necessary to verify the influence of multiaxiality under lower strain amplitudes (near HCF regime) and varying q ratios. For instance, the development of fatigue damage under pure torsion loads can be of particular interest, since pure torsion loads correspond to a theoretical $q \to \infty$. Under such pure torsion loads the difference of fatigue life compared to a tension-compression or tension-torsion tests of same equivalent plastic deformation might be more pronounced, thus giving a clearer insight on the impact of multiaxial stress states.

4. Numerical modeling of the mechanical properties

4.1. Constitutive equations of the proposed model

The material model developed within this work is based on the viscoplastic theory by Chaboche and coworkers [34, 46]. The model has been adapted to describe the mechanical properties of a SAC solder alloy. An essential part of the formulation is the usage of a flow rule comprising two Norton's terms similar to the ONERA2 model proposed by Chaboche in [40]. Besides, as the ONERA2 model already incorporates kinematic and isotropic hardening with dynamic and static recovery terms, the formulation is further extended towards the framework of continuum damage mechanics for isotropic damage. Lemaitre et al introduced the concept of effective variables as the description of an intermediate damage state D, which takes a value between 0 and 1. 0 corresponds to an undamaged state whereas 1 to fracture. Following this, the internal variables are replaced by their effective value, which is consistent to the isotropic formulation of damage. In this work, two damage mechanisms are considered: fatigue and creep damage. Both are described by specific evolution laws and contribute to the total damage by a nonlinear accumulation rule. The nonlinear accumulation equation follows the bilinear rule proposed in the ASME standards, but differentiated and integrated into the constitutive equations. The subscripts ij, kl denote a tensor or a 6×6 matrix (fourth rank tensor). Other subscripts or no subscripts mark a scalar variable.

continuity
$$\sigma_{ij} = (1 - D) E_{ijkl} (\varepsilon_{kl} - \varepsilon^{p}_{kl} - \varepsilon^{th}_{kl}) \tag{4.1}$$

elasticity
$$E_{ijkl} = \mu(\delta_{ik}\delta_{jl} + \delta_{il}\delta_{jk}) + \lambda\delta_{ij}\delta_{kl} \tag{4.2}$$

Lamé constants
$$\mu = \frac{E}{2(1+\nu)} \quad \lambda = \frac{\nu E}{(1+\nu)(1+2\nu)} \tag{4.3}$$

thermal strain
$$\varepsilon^{th}_{kl} = \alpha_{CTE} \left(T - T_{ref}\right) \tag{4.4}$$

effective stress
$$\tilde{\sigma}_{ij} = \frac{\sigma_{ij}}{1 - D} \tag{4.5}$$

deviatoric stress
$$\tilde{S}_{ij} = \tilde{\sigma}_{ij} - \frac{1}{3} \operatorname{Tr}(\tilde{\sigma}) \tag{4.6}$$

back stress	$\dot{X}_{kl}^{(i)} = \frac{2}{3} c_i (1-D)\dot{\varepsilon}_{kl}^{p} - \gamma_i \phi \dot{\bar{\varepsilon}}^{p} X_{kl}^{(i)} - d_i \, \mathrm{J}_2(X_{kl}^{(i)}) X_{kl}^{(i)}$	(4.7)
superposition	$X_{kl} = \sum_{i=1}^{n=3} X_{kl}^{(i)}$	(4.8)
cyclic recovery	$\phi = \phi_\infty + (1-\phi_\infty)\exp(-b_k \varepsilon_{acc}^{p})$	(4.9)
over-stress	$\mathrm{J}_2(\tilde{\sigma} - X) = \sqrt{\frac{3}{2}(\tilde{S}_{ij} - X_{ij}) : (\tilde{S}_{ij} - X_{ij})}$	(4.10)
cyclic hardening	$R = \sigma_0 + Q(1 - \exp(-b_q \varepsilon_{acc}^{p}))$	(4.11)
viscous stress	$\sigma_v = \mathrm{J}_2(\tilde{\sigma} - X) - (1-D)R$	(4.12)
flow rule	$\dot{\bar{\varepsilon}}^{p} = \left(\frac{\sigma_v}{(1-D)K_1}\right)^{\frac{1}{m_1}} + \left(\frac{\sigma_v}{(1-D)K_2}\right)^{\frac{1}{m_2}}$	(4.13)
fatigue damage	$\dot{D}_1 = a_1 \dot{\bar{\varepsilon}}^{p} (\bar{\varepsilon}^{p})^{b_1} \left(\frac{\lvert q \rvert}{\sqrt{3}}\right)^{b_{qm}} \times a_f$	(4.14)
crack initiation	$a_f = 1 + \frac{a_k}{2}\left(1 + \tanh\left(\frac{D - D_a}{D_a/\delta}\right)\right)$	(4.15)
creep damage	$\dot{D}_2 = a_2 (\sigma_{eq})^{b_2} (\bar{\varepsilon}^{p})^{c_c}$	(4.16)
total damage	$\dot{D} = f_f(D_1, D_2)\dot{D}_1 + f_c(D_1, D_2)\dot{D}_2$	(4.17)

The model employs the concept of over-stress for associative viscoplasticity. The plastic, viscoplastic and creep deformation towards large time scale are unified within a single inelastic flow rule. An isotropic yield surface delimits the elastic domain using the von Mises theory of isotropic plasticity.

4.1.1. Numerical procedure in FE calculation

In order to calculate the mechanical deformations in complex geometries, the use of FE-supported simulation is necessary. Commercial FE-codes provide an interface for user-defined material models. In this way, a custom material model can be integrated as a FORTRAN subroutine which is called by the FE solver during the solution process. In this way, the commercial FE-solver can process the factorization and solution of the global assembly matrix whereas the user-subroutine supplies the material stiffness at integration point level. The global forces $[F]$, displacements $[U]$ and stiffness matrix $[K]$ are brought into equilibrium by an iterative Newton-Raphson solution of the quasi-static system of equations (acceleration and velocity terms are omitted in the equation of motion)

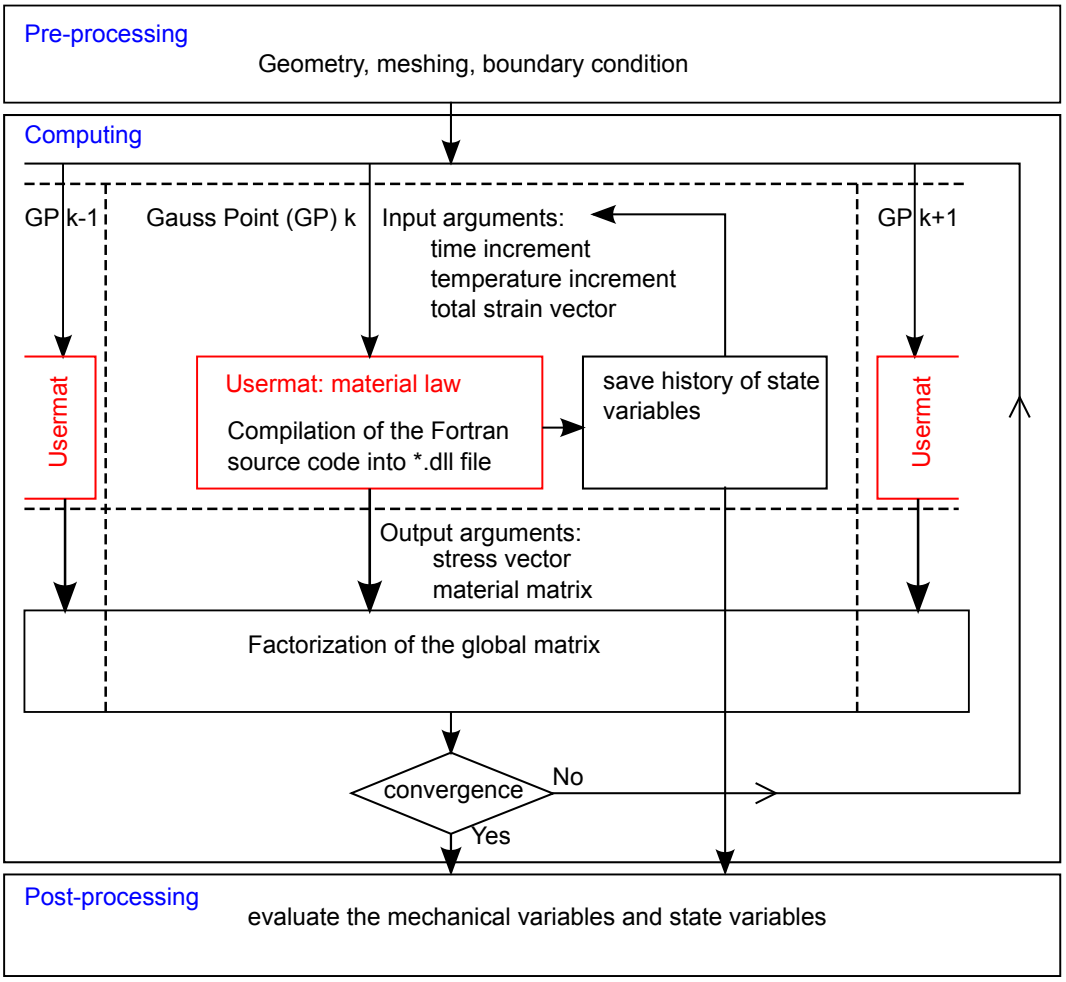

Fig. 4.1: Calculation procedure used in FE-simulation with a USER-defined material implemented as FORTRAN subroutine for the commercial software ANSYS [18]

$$[K] \times [U] = [F] \tag{4.18}$$

The global stiffness matrix $[K]$ maps the internal reaction of the material via its material matrix $[D]$, which is defined locally in every integration point (often referred to as Gauss point) of the structure (s. Eq.(4.19)). [B] refers to the element strain – displacement matrix.

$$[K] = \int_V [B]^T \times [D] \times [B] dV \tag{4.19}$$

The local calculation at each element Gauss point is dependent on the material law used which is included in the matrix $[\mathbb{C}^p]$.

During a solution step the user material subroutine is called by the solver, which

passes the

- time increment Δt
- temperature increment ΔT
- current total strain acting on this Gauss point

as input arguments. Using these arguments and the implementation of the material law Eq.(4.1)-(4.17) delivers the material matrix $[\mathbb{C}^p]$, also called consistent tangent operator and the resulted stress vector $[\sigma]$. In order to compute these quantities, state variables are saved into a dedicated data structure, which persists throughout all solution steps. By doing this, any previous loading history at any Gauss point can be accessed. This procedure is needed when the non-linearity of the constitutive equations does not allow a direct solution but necessitates a numerical iterative procedure to determine the tangent operator $[\mathbb{C}^p]$ and the resulted stress vector $[\sigma]$, see Fig.4.1.

4.1.2. Return mapping algorithm

In this section, the methodology employed to implement a numerically stable and robust material model are described. The main calculation steps and resulting equations are introduced in the current chapter. A detailed representation of the intermediate steps of calculation as well as the derivatives for the tangent operator and the Newton-Raphson algorithm can be found in appendix A.4.

Although the constitutive model contains a set of multiple differential equations, the implementation follows an established method proposed by Simo [81] for computational time-independent plasticity. In fact, the methodology proposed by the author can handle various mathematical formulations and model complexities [82, 83]. In three dimensions, the tensorial relations are discretized in an Euler backward schema. Then, based on a return mapping algorithm for over-stress viscoplasticity, all the internal state variables are determined. The return mapping scheme illustrated in Fig.4.2, considers in a first approximation the strain increment as an elastic one: it results the trial stress σ_{ij}^{tr} (calculated with the continuity Eq.(4.1)), from which the deviatorical trial stress S^{tr} is deduced (Eq.(4.6)). If trial equivalent stress overtakes the yield stress, then the increment generates plastic deformation and therefore a plastic correction has to be calculated.

The return mapping procedure is graphically represented in the principal deviatoric stress plane. This graphical representation helps to visualize the different

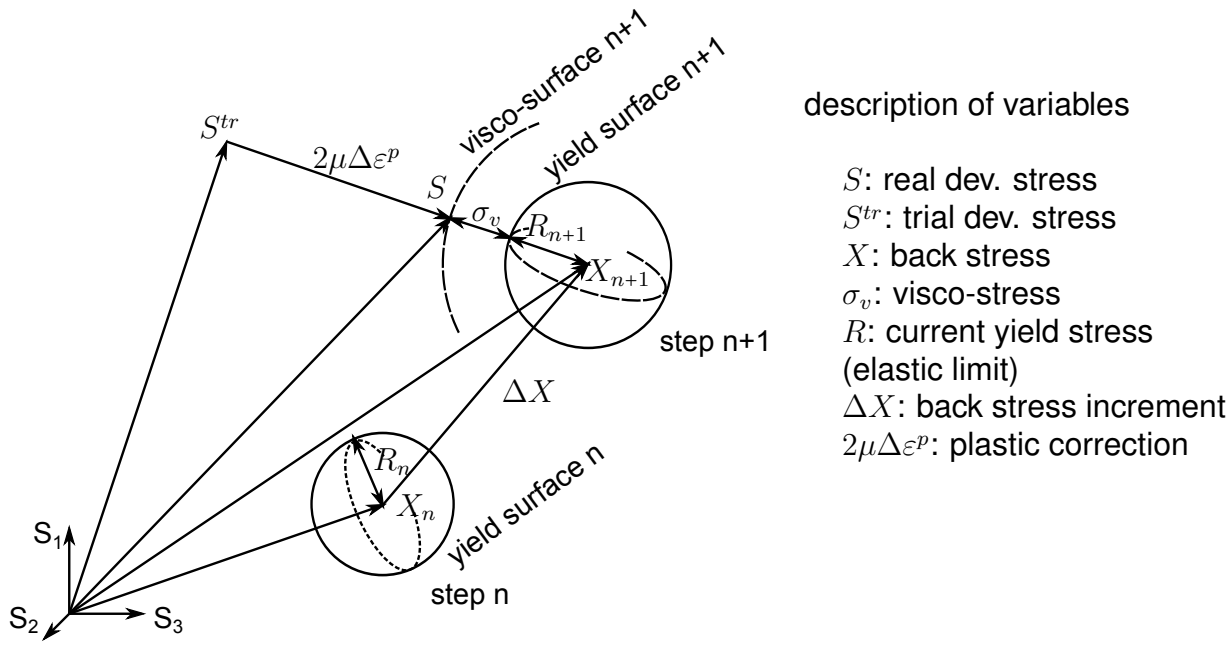

Fig. 4.2: Graphical representation of the return mapping schema in the deviatoric stress plane for an elasto-viscoplastic step calculation

equations which can be considered as vector operations. The equation of plastic correction Eq.(4.20) refers to the vector summation depicted on Fig.4.2.

$$\text{plastic corrector} \qquad S_{ij} = S_{ij}^{tr} - 2\mu\Delta\varepsilon_{ij}^{p} \tag{4.20}$$

Since the model incorporates kinematic and isotropic hardening terms, the yield surface can move (the coordinates of the center of the yield surface correspond to the back-stress vector X) and can grow (the radius R is depends on the plastic history). The yield condition is basically formulated like in Eq.(4.7) for combined isotropic-kinematic hardening models [31, 84, 85] using the J_2 operator according to von Mises plasticity (see appendix A.3). R_n is calculated with Eq.(4.11).

$$\text{yield condition} \qquad F = \mathrm{J}_2(\sigma^{tr} - X_n) - R_n \tag{4.21}$$

According to the yield criterion, the trial stress can be located outside ($F > 0$) or inside ($F < 0$) the yield envelope by assuming that no plastic deformation occurs within the trial step (elastic predictor). However, if static recovery terms are incorporated in the kinematic hardening, the back stress may relax during the time increment from n to $n + 1$, such that the value of X_n has to be updated according to this time increment,

based on its previous value taken during the last converged step $\hat{X}_n^{(i)}$.

$$X_n^{(i)} = \frac{1}{1 + d_i \Delta t \, \mathrm{J}_2(\hat{X}_n^{(i)})} \hat{X}_n^{(i)} \tag{4.22}$$

The real stress state S in $n+1$ is obtained when S returns to the visco-surface $n+1$. The visco-surface depicts a parallel envelop with respect to the yield surface, such as the gap between both spheres is defined by a state variable called *over stress* or *viscous stress* associated to the variable σ_v. This definition applies only for viscoplasticity and models based on associative over-stress theories [38, 39], which is the case for the model proposed in this work. When the stress returns to its visco-surface, the equilibrium is completed. Thus, the consistency conditions are met. The consistency can be graphically interpreted as a vector sum $S-X$ which is normed and therefore equal to the gap between the visco-and yield-surfaces, which is expressed by the visco-stress σ_v, see Fig.4.2

$$\text{consistency condition} \qquad \mathrm{J}_2(\sigma - X) = \sigma_v + R \tag{4.23}$$

For the current model, all the internal state variables R, X, σ_v depend on the plastic history and the current time increment (see resp. Eq.(4.11), (4.7) and (4.13). It means that the only unknown remains the plastic strain increment $\Delta\bar{\varepsilon}^p$ within the $n+1$ step, as the other quantities are either known in the step n or can be expressed in function of $\Delta\bar{\varepsilon}^p$. In other words, the strategy for numerically implementing the material law consists in reducing the number of coupled equations (4.1)-(4.17), using $\Delta\bar{\varepsilon}^p$ as solution-pivot variable. However, due to the nonlinearity of the J_2 operator, not all state variables can be separated. The 16 constitutive equations can still be reduced down to a system of 5 equations Eq.(4.24)-(4.28) with 5 unknowns $\Delta\bar{\varepsilon}^p$, h, $\mathrm{J}_2(X^{(1)})$, $\mathrm{J}_2(X^{(2)})$ and $\mathrm{J}_2(X^{(3)})$ which have to be solved numerically, where h is defined by $h = \mathrm{J}_2(\sigma - X)$.

$$f_1 = h - \alpha - Z_{eq} \tag{4.24}$$

$$f_2 = \left(\frac{h-R}{K_1(1-D)}\right)^{1/m_1} + \left(\frac{h-R}{K_2(1-D)}\right)^{1/m_2} - \frac{\Delta\bar{\varepsilon}^p}{\Delta t} \tag{4.25}$$

$$f_3 = \mathrm{J}_2(X^{(1)}) - w_1 M_1 \tag{4.26}$$

$$f_4 = \mathrm{J}_2(X^{(2)}) - w_2 M_2 \tag{4.27}$$

$$f_5 = \mathrm{J}_2(X^{(3)}) - w_3 M_3 \tag{4.28}$$

Because near the solution the equations are continuous and derivable, a Newton-

Raphson (N-R) iterative procedure is used to solve the system. For the first iteration ($k = 0$), the unknowns should take starting values as close as possible to the end values, which improve the convergence of the N-R algorithm Eq.(4.29)

$$\begin{bmatrix} \Delta\bar{\varepsilon}^p \\ h \\ \mathrm{J}_2(X^{(1)}) \\ \mathrm{J}_2(X^{(3)}) \\ \mathrm{J}_2(X^{(3)}) \end{bmatrix}^{k+1} = \begin{bmatrix} \Delta\bar{\varepsilon}^p \\ h \\ \mathrm{J}_2(X^{(1)}) \\ \mathrm{J}_2(X^{(3)}) \\ \mathrm{J}_2(X^{(3)}) \end{bmatrix}^{k} - \begin{bmatrix} \dfrac{\partial f_1}{\partial \Delta\bar{\epsilon}^p} & \cdots & \dfrac{\partial f_1}{\partial\, \mathrm{J}_2(X^{(3)})} \\ \vdots & \ddots & \vdots \\ \dfrac{\partial f_5}{\partial \Delta\bar{\epsilon}^p} & \cdots & \dfrac{\partial f_5}{\partial\, \mathrm{J}_2(X^{(3)})} \end{bmatrix}^{-1} \times \begin{bmatrix} f_1 \\ f_2 \\ f_3 \\ f_4 \\ f_5 \end{bmatrix}^{k} \tag{4.29}$$

The intermediate calculation for reduction of the number of equations as well as the expression of the derivatives are given in appendix A.4. For the unknowns $\mathrm{J}_2(X^{(1)})$, $\mathrm{J}_2(X^{(2)})$, $\mathrm{J}_2(X^{(3)})$, the starting point values are evaluated from the elastic predictor step (Eq.(4.22)). The value h represents the over-stress and is bounded between 0 and $\mathrm{J}_2(\sigma^{tr} - X_n)$ (trial effective stress) because the corrected stress and consequently the over stress should be at least smaller than the trial stress. $\Delta\bar{\varepsilon}^p$ ranges between 0 and the total equivalent strain increment per time increment (assuming that no elastic deformation occurs). In fact, f_1 depicts a discontinuity in 0, thus, the upper bound is chosen as starting point of the iterative procedure (s. Eq.(4.30)).

$$\Delta\bar{\varepsilon}^{p(0)} = \Delta t \left(\frac{\mathrm{J}_2(\sigma^{tr} - X_n)}{K_1(1-D)} \right)^{1/m_1} + \Delta t \left(\frac{\mathrm{J}_2(\sigma^{tr} - X_n)}{K_2(1-D)} \right)^{1/m_2} \tag{4.30}$$

$$h^{(0)} = \mathrm{J}_2(\sigma^{tr} - X_n) \tag{4.31}$$

$$\mathrm{J}_2(X^{(1)})^{(0)} = \mathrm{J}_2(X_n^{(1)}) \tag{4.32}$$

$$\mathrm{J}_2(X^{(2)})^{(0)} = \mathrm{J}_2(X_n^{(2)}) \tag{4.33}$$

$$\mathrm{J}_2(X^{(3)})^{(0)} = \mathrm{J}_2(X_n^{(3)}) \tag{4.34}$$

The convergence is achieved when the norm of the vector $[f_1 \quad f_2 \quad f_3 \quad f_4 \quad f_5]$ in Eq.4.29 is lower than 1×10^{-8} (user-defined criterion). When the convergence is not completed after 50 successive iterations, a subsection is initiated. After the subsection, time and strain increment are systematically reduced by a factor of 2. Once the convergence is obtained, the variables $\Delta\bar{\varepsilon}^p$, h, $\mathrm{J}_2(X^{(1)})$, $\mathrm{J}_2(X^{(2)})$ and $\mathrm{J}_2(X^{(3)})$ are determined and the return mapping is completed. Then, all the internal state variables are updated: accumulated plastic strain Eq.(4.35), current plastic strain Eq.(4.36),

back stress Eq.(4.37) and stress Eq.(4.38)

$$\bar{\varepsilon}^p_{acc} = \bar{\varepsilon}^p_{acc,n} + \Delta\bar{\varepsilon}^p \tag{4.35}$$

$$\varepsilon^p_{kl} = \varepsilon^p_{kl,n} + \frac{3}{2}\Delta\bar{\varepsilon}^p \frac{S_{kl} - X_{kl}}{\mathrm{J}_2(\sigma - X)} \tag{4.36}$$

$$X^{(i)}_{kl} = w_i \left(X^{(i)}_{kl,n} + (1-D) c_i \Delta\bar{\varepsilon}^p \frac{S_{kl} - X_{kl}}{\mathrm{J}_2(\sigma - X)} \right) \tag{4.37}$$

$$\sigma_{kl} = (1-D) \left(\sigma^{tr}_{kl} - 3\mu\Delta\bar{\varepsilon}^p \frac{S_{kl} - X_{kl}}{\mathrm{J}_2(\sigma - X)} \right) \tag{4.38}$$

4.1.3. Update of Damage variables

It should be noted that neither the fatigue nor the creep damage variables are involved in the return mapping procedure. The damage variables are coupled in a weak form to the internal variables previously mentioned. In other words, the damage variables are maintained constant during the return mapping procedure at $n+1$, and they take their previous value from the step n. Once the return mapping is finished and all the mechanical quantities are updated, the creep and fatigue damage variables are subsequently updated. This integration scheme is similar to an Euler-forward schema, also called *explicit* integration. q Eq.(2.35), is the ratio of multiaxiality which is calculated after updating the state variables. The discretized form of the fatigue and creep equation is given in Eq.(4.39) and Eq.(4.40) respectively.

$$\Delta D_1 = a_1 \Delta\bar{\varepsilon}^p (\bar{\varepsilon}^p)^{b_1} \left(\frac{|q|}{\sqrt{3}} \right)^{b_{qm}} \left(1 + \frac{a_k}{2} \left(1 + \tanh\left(\frac{D - D_a}{D_a/\delta} \right) \right) \right) \tag{4.39}$$

$$\Delta D_2 = a_2 \Delta t \left(\frac{\sigma_{eq}}{1-D} \right)^{b_2} (\bar{\varepsilon}^p)^{c_c} \text{ if } \mathrm{tr}(\sigma) > 0 \text{ else } \Delta D_2 = 0 \tag{4.40}$$

Because the damage equations are given in their differential form, the pre-integrated equation of ASME-standard [61] has to be adapted for a calculation of the nonlinear creep-fatigue accumulation. Thus, the total damage increment results from a nonlinear accumulation of the creep and fatigue damage increments (ΔD_2 and ΔD_1) and is accumulated after the solution step $n+1$.

$$\text{if} \quad \frac{\Delta D_2}{\Delta D_1 + \Delta D_2} < c \quad \text{then} \quad \Delta D = \Delta D_2 + \frac{1-c}{c}\Delta D_1 \tag{4.41}$$

$$\text{if} \quad \frac{\Delta D_2}{\Delta D_1 + \Delta D_2} > c \quad \text{then} \quad \Delta D = \Delta D_1 + \frac{1-c}{c}\Delta D_2 \tag{4.42}$$

$$D = D_n + \Delta D \tag{4.43}$$

The explicit integration of D_1 and D_2 enables the substantial reduction of the number of independent equations from 7 to 5 (Eq.(4.24)-(4.28)), which are solved using an N-R scheme. Furthermore, it reduces the number of unknowns and partial derivatives in the Jacobian matrix and thus, the computational effort to determine each partial derivative regarding each unknown. Besides, the damage equations Eq.(4.39)-(4.40) are formulated according to the behavior of the material observed during the experimental tests. Nevertheless, it cannot be excluded that other damage phenomena interact within the temperature and load ranges investigated.

With the explicit integration of D_1 and D_2, the equations can be easily modified by the user. Besides, if only the damage equations are modified, then the partial derivatives and the return-mapping schema remain unchanged, which enables the user to implement a new damage model with relatively low numerical integration efforts. However, a forward Euler integration is typically associated with a time-step dependence as well as numerical instability if too large time-temperature-deformation-increments are applied. In fact, the forward integration only concerns the damage evolution. In parallel, the other internal variables are implicitly integrated following Euler backward schema. The Euler backward schema ensures robustness and stability during the computation of the internal variables, which could handle fast evolution depending on the time-temperature and load increments. In contrast, the damage evolution is very slow in comparison to the other internal variables, which are related to rapid mechanical or load changes. For this reason, the explicit integration of damage does not affect the stability of the algorithm, considered here at the integration point level. Thus, the implicit computation during the return mapping scheme provides a relative low time step dependence of the internal variables.

However, by the explicit integration of damage, the time-step dependence might be higher, thus the damage variables become sensitive to the load-step size and its associated time increment. This is particularly the case for the creep damage D_2, which is directly proportional to the time increment and other internal variables. Nevertheless, the effect is expected to be moderate saturating if sufficiently low time increments are used. Besides, and due to the high complexity of the material model, too large time increment can lead to divergence of the local N-R, even if no damage development is considered. Therefore, it is advised to carefully define the solution time increments for this model according to the simulated specific structures, boundaries and loading conditions. In general, the time discretization shall always be adapted to ensure stability and correct computation at the integration point level, which later on assures a fast convergence during the global matrix assembly.

4.1.4. Consistent tangent operator

The user subroutine delivers the corresponding stress vector and material tangent matrix for each integration point as output-variables . The stress vector is determined after the return mapping and damage update procedures, as soon as the local N-R has converged. The calculation of the material tangent matrix is described in the following. If the material is considered linear elastic, the material matrix is equal to the elastic stiffness matrix E_{ijkl} (Eq.(4.2)). However, if plastic deformation is generated, the material matrix has to be determined by derivation of the output stress regarding the output strain increment. Besides, when the equations are implicitly derived with respect to continuum and derivable internal variables, the material matrix is called consistent operator. The use of a consistent tangent operator guarantees the quadratic convergence of the global Newton equilibrium iteration during the assembly procedure [31, 81, 82]. By derivation of Eq.(4.44) one obtains the general expression of the tangent operator $\mathbb{C}^p$ Eq.4.45

$$\mathbb{C}^p = \frac{d\sigma_{ij}}{d\varepsilon_{kl}} \tag{4.44}$$

$$\mathbb{C}^p = (1-D)\left(\frac{d\sigma_{ij}^{tr}}{d\varepsilon_{kl}} - \frac{d\Delta\bar{\varepsilon}^p}{d\varepsilon_{kl}}\vec{n}_{ij} - \Delta\bar{\varepsilon}^p\frac{d\vec{n}_{ij}}{d\varepsilon_{kl}}\right) \tag{4.45}$$

$$\frac{d\sigma_{ij}^{tr}}{d\varepsilon_{kl}} = E_{ijkl} \quad , \qquad \vec{n}_{ij} = \frac{S_{ij}-X_{ij}}{\mathrm{J}_2(\sigma - X)} \tag{4.46}$$

The first term is equal to the elastic stiffness. The vector $\vec{n}_{ij}$ corresponds to the plastic flow direction (see appendix A.4 for more details about their expression). $\mathbb{C}^p$ is determined by reformulation of the internal variables with respect to the input strain increment ε_{kl}. The derivatives are taken from the Jacobi matrix previously computed in Eq.(4.29). The method has been published by Kullig in [31], where 3 numerical variables are extracted and differentiated in order to form the consistent tangent operator. Here, the method is further adapted to compute the tangent operator from 5 numerical internal variables instead of 3 in [31]. The method starts with the system of equations $[f_1 \dots f_5]$, and implies that the quantities $\Delta\bar{\varepsilon}^p$, h, $\mathrm{J}_2(X^{(1)})$, $\mathrm{J}_2(X^{(2)})$, $\mathrm{J}_2(X^{(3)})$, h and S^{tr}, are influenced by a change of ε_{kl}. Then, the equations $[f_1 \dots f_5]$ are differentiated with respect to these variables. The remaining derivatives are then equal to 0. After rearrangement of the terms, one gets a system of equations where the pivot-matrix has been already determined during the return-mapping procedure. The intermediate steps are given in detail in appendix A.5.

$$\begin{bmatrix} \dfrac{\partial f_1}{\partial S_{kl}^{tr}} \dfrac{dS_{kl}^{tr}}{d\varepsilon_{kl}} \\ \vdots \\ \dfrac{\partial f_5}{\partial S_{kl}^{tr}} \dfrac{dS_{kl}^{tr}}{d\varepsilon_{kl}} \end{bmatrix} + \begin{bmatrix} \dfrac{\partial f_1}{\partial \Delta\bar{\epsilon}^p} & \cdots & \dfrac{\partial f_1}{\partial \mathrm{J}_2(X^{(3)})} \\ \vdots & \ddots & \vdots \\ \dfrac{\partial f_5}{\partial \Delta\bar{\epsilon}^p} & \cdots & \dfrac{\partial f_5}{\partial \mathrm{J}_2(X^{(3)})} \end{bmatrix} \times \begin{bmatrix} \dfrac{d\Delta\bar{\varepsilon}^p}{d\epsilon_{kl}} \\ \vdots \\ \dfrac{d\,\mathrm{J}_2(X^{(3)})}{d\varepsilon_{kl}} \end{bmatrix} = 0 \tag{4.47}$$

The derivatives form a linear system of 5 unknowns, with 5 vectors $[1 \times 6]$ as solution of the system. Each vector (e.g. $\dfrac{d\Delta\bar{\varepsilon}^p}{d\epsilon_{kl}}$) corresponds to the derivatives of $\Delta\bar{\varepsilon}^p$, h, $\mathrm{J}_2(X^{(1)})$, $\mathrm{J}_2(X^{(2)})$, $\mathrm{J}_2(X^{(3)})$, with respect to ε_{kl} respectively. The first term $\dfrac{d\Delta\bar{\varepsilon}^p}{d\varepsilon_{kl}}$ is obtained and needed in the formulation of the tangent operator Eq.(4.45). The derivatives of the plastic flow direction $\dfrac{d\vec{n}_{ij}}{d\varepsilon_{kl}}$ are obtained using the equivalent expression deduced after the return mapping procedure. The partial derivatives are expressed as functions of the 5 vectors $\dfrac{d\Delta\bar{\varepsilon}^p}{d\varepsilon_{kl}}$, $\dfrac{dh}{d\varepsilon_{kl}}$, $\dfrac{d\,\mathrm{J}_2(X^{(1)})}{d\varepsilon_{kl}}$, $\dfrac{d\,\mathrm{J}_2(X^{(2)})}{d\varepsilon_{kl}}$ and $\dfrac{d\,\mathrm{J}_2(X^{(3)})}{d\varepsilon_{kl}}$, determined from the system Eq.(4.47). After rearrangement the plastic flow direction derivative is obtained.

$$\frac{d\vec{n}_{ij}}{d\varepsilon_{kl}} = \frac{1}{Z_{eq}} \frac{dZ_{ij}}{d\varepsilon_{kl}} - \frac{1}{(Z_{eq})^2} Z_{ij} \frac{dZ_{eq}}{d\varepsilon_{kl}} \tag{4.48}$$

The intermediate expressions necessary to achieve this result are given in appendix A.5.

4.2. Calibration of the material parameters

The material model incorporates 32 material parameters which are separately calibrated at the temperatures of the isothermal tests.

- 16 parameters: E, ν, σ_0, c_1, γ_1, c_2, γ_2, c_3, γ_3, d_1, d_2, d_3, K_1, m_1, K_2, m_2 are related to the deformation mechanisms, describing the material properties at large and small strain, low and high strain rate, towards elastic, creep and visco-plastic deformation.
- 4 parameters b_k, ϕ_∞, b_q, Q describe the cyclic evolution of the material as a combination of cyclic hardening vs. cyclic softening depicting by the material
- 7 parameters a_1, b_1, a_k, δ, D_a, D_c, b_{qm} are used to describe the damage corresponding to pure fatigue, in uniaxial and multiaxial cyclic loads. It includes constant softening up to technical crack initiation and acceleration of the degradation afterwards, which leads to fatigue failure.

- 3 parameters a_2, b_2, c_c belong to creep damage, describing the slow creep damage mechanism at the onset of secondary and in the tertiary creep stage until creep rupture.
- 1 parameters c is dealing with the nonlinear accumulation of creep and fatigue damage into total damage. The nonlinear rule is expressed from ASME standards bilinear rule.
- The Coefficient of Thermal Expansion (CTE) α_{CTE} is taken from literature [33]

The large number of material constants renders the calibration task difficult. In order to facilitate the calibration, a basis of adapted experiments performed in defined and controlled loading conditions is of utmost importance. Although each parameter describes a specific property, their combination remains interdependent and some redundancy may exist between the different material constants. In order to avoid such redundancies, the parameters are successively calibrated step by step using the experimental tests. The different tests reveal specific material properties which can be described by a reduced set of parameters. Once a parameter (or more) are determined, they are kept fixed during the rest of the calibration procedure. In the following, the calibration procedure is described, which comprises both direct graphical determination method and analytical fit on functions which approximate the differential equations of the model. Other approaches for finding the parameters are based on optimization algorithms which basically minimize the mismatch between calculated and experimental values. Such algorithms have been employed for similar models in [33] and [86], where genetic optimization algorithm has been implemented. However, this algorithm requires a set of starting values, which should be as close as possible to the values of the final set of parameters for an efficient minimization. We experience that for the present model, the genetic algorithms were not efficient if the parameter-bounds are too large and the starting values too far from the end values. The gain of accuracy using such optimization algorithm renders rather low. Indeed, we found out that the starting values have substantial impact on the quality of the calibration. For these reasons, optimization algorithms are not employed in the following, but we focus our interest on the meaning of the different parameters and their impact on the mechanical properties of the material.

In a first step, the 16 parameters describing the deformation properties are determined. All the other parameters are set to zero or values that remove their influence. Poisson ratio and CTE parameters are taken from literature [33]. To begin, the experiments are approximated with an ideal uniaxial stress state and simulated with one

element loaded along one direction. This approximation allows very fast computation of various profiles and enables the user to perform a large number of simulations in a short time.

4.2.1. Elasto-plastic-creep parameters

Young's modulus

The Young's modulus is evaluated from the cyclic experiments. It corresponds to the first slope of the stress-strain hysteresis curve after changing the direction of loading. Due to the high viscosity of the material, the slope of the curve during initial loading renders dependent on the applied strain rate. Therefore, we use the stress-strain hysteresis produced with higher strain rate in order to minimize viscous deformations and creep effects. The Young's modulus is first calibrated by simulating a single finite element model. In order to verify the one element simulation the real sample geometry is designed and meshed in FE software. Because of the two-fold symmetry, only $1/8^{th}$ of the geometry is needed (see Fig.4.3). The same boundary conditions as in experiments are applied: controlled displacement on S_1 (where the LVDT's are in reality fixed to measure and control axial displacements) and fixed on the symmetry plane S_0. The stress is evaluated by the Reaction Forces $RF(nodes)$ of the nodes which belong to S_0, see Eq.(4.49).

$$\sigma = \frac{1}{S_0} \sum_{\text{nodes in } S_0} RF(\text{nodes}) \tag{4.49}$$

Then, taking this first determined Young's modulus and simulating the sample by FEA, a first hysteresis cycle is obtained which shows an underestimation of the elastic stiffness (doted line – – –), just after changing the loading direction (Fig.4.3(b)). Thus, this first determined Young's modulus is multiplied by a correction factor in order to match the stress-strain behavior measured within elastic domains, and the full line — are obtained giving better agreement with the experiments.

In fact, the correction is necessary due to geometrical effects since the displacement is measured outside the testing region of the sample. Thus, the stress in the sample is not homogeneous in the transition region where the diameter of the sample increases, thus inhomogeneous elastic deformation is expected to occur. The elastic deformation cannot be taken into account during the one element simulation which explain the underestimation of the Young's modulus. The correction factor is independent on the temperature and can be attributed to the specific geometry of the

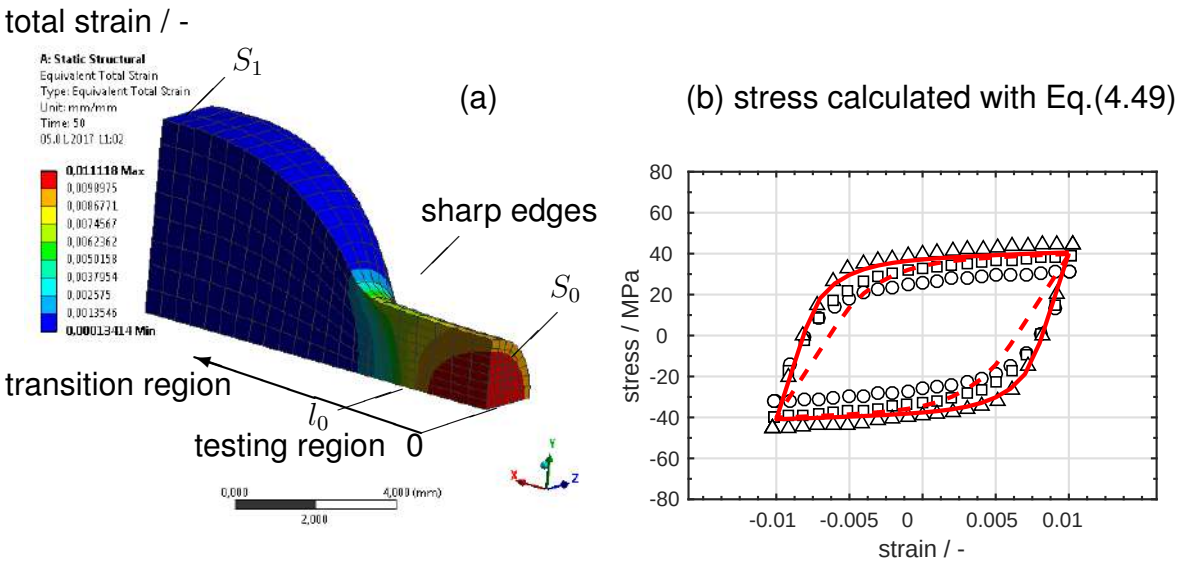

Fig. 4.3: (a) FE simulation of the real sample. Display: total strain in the testing region $[0 \dots l_0]$ and in the transition region. (b) FE simulation of a cycle of deformation at 25℃, rate: $1 \times 10^{-3} s^{-1}$. Results with first determined Young's modulus – – –, corrected Young's modulus —. Symbols △, □, ◯ represent 3 different experiments.

sample.

The Young's modulus evolution with the temperature is estimated by a linear function. However, it should be noted that the domain of validity is exclusively restricted to the domain of calibration. The melting temperature of the solder alloy is situated around 500 K. At this temperature, the material is no more in its solid form, and a Young's modulus close to zero may be assumed. The fit-equation in Fig.4.4 probably over-estimates the E modulus in the range 398...500 K. Similar Young's modulus values have been measured by Pang et al. [87] in the temperature range 25℃...125℃ which correlate well to our measurements considering the present experimental deviation of ± 5 GPa.

Hardening parameters

According to the model formulation, the stress results from three state variables which are dependent on the plastic strain (strain hardening) and time (time hardening). In uniaxial situation and for one dimension, the equations (4.1)...(4.17) are simplified in Eq.(4.50) and provide a function of stress σ.

$$\sigma = X + \sigma_v + \sigma_0 \tag{4.50}$$

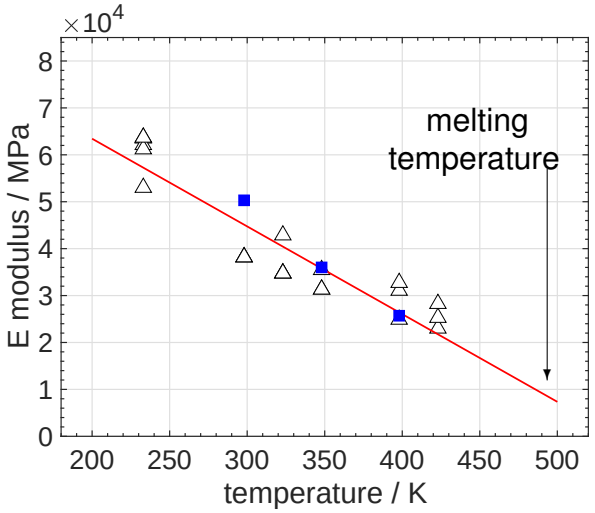

Fig. 4.4: E module as a function of the temperature, calibrated in the temperature range -40℃...125℃

where X represents the sum of back stress quantities, σ_v the viscous stress and σ_0 the initial yield stress. Because no cyclic isotropic hardening is observed for the material, the state variable R is simplified by its constant parameter σ_0. Strain hardening is expressed within the kinematic back stresses, where the back stress incorporates a time dependence by its static recovery term. Thus, time hardening is reflected by the double visco-function and in the static recovery term of the kinematic back stress. An exact separation of the different terms is not possible because time and plastic strain act in both parts. Nevertheless, under certain conditions, some terms are dominant and some can be neglected.

- At high strain rate, under small strain, only one part of the double visco-function is relevant. The static recovery terms can be in a first approximation ignored, even if the stress will be over-calculated in the relaxation period. Thus, linear and dynamic recovery terms can be estimated
- At low strain rate, at large strain, the equilibrium is established in the kinematic hardening part. Therefore, the back stress remains constant. Thus, the other part of the visco-function becomes dominant and can be determined.
- The static recovery terms are used to adjust the back-stress value in order to obtain the correct strain rate in creep tests and, finally, to match the rest-stress at the end of the relaxation period.

By doing this, a first set of hardening parameters can be found. The procedure needs three types of independent experiments: strain rates variation over several decades,

several creep tests, and a relaxation test. As an example, the procedure is depicted here to calibrate the hardening parameters of the solder material at 25℃. First, the following information has to be collected from the experimental test, which are related to the maximum stress obtained at different strain rates, the steady state creep strain rate during creep tests and the remaining stress at the end of the relaxation period, see Tab.3.1.

Kinematic hardening: linear and dynamic recovery terms

Without static recovery ($d_i = 0$), the back-stress equations can be integrated with respect to plastic strain. It results in an exponential function.

$$X = \sum_{i=1}^{3} \frac{c_i}{\gamma_i} \left(1 - \exp(-\gamma_i \times \bar{\varepsilon}^p)\right) \tag{4.51}$$

Considering that strain rate is kept constant during loading and unloading phases, the visco-stress σ_v remains constant due to the fact that the visco-stress only depends on the plastic strain rate. Moreover, the initial yield stress σ_0 is set to a low value, because of restricted pure elastic domain combined with large recovery during relaxation periods, observed as well by Wippler for similar solder alloy [33]. Since no static recovery is incorporated into the isotropic hardening state function R, the yield stress cannot relax and further constitutes an additional barrier to describe the remaining stress at the end of the relaxation. For this reason, we describe the non-linear monotonic hardening by kinematic back stresses. Therefore, any change of stress can be attributed to the back-stress-evolution. In other words, the back stress has to match the non-linearity of the stress-strain curve after yielding. Furthermore, by omitting static recovery, the equation becomes independent on time. In this case the quantity of back-stress that is accumulated during the loading phase remains constant during the relaxation period, because very low plastic deformation is generated during relaxation under fixed sample elongation. Thus, in a first approximation, the total equivalent amount of back stress $\mathrm{J}_2(X)$ after loading can be evaluated by the rest stress σ_r^{exp} at the end of the relaxation period.

$$\text{after relaxation} \qquad \mathrm{J}_2(X) \approx \sigma_r \tag{4.52}$$

By considering that X is a deviatoric quantity ($\mathrm{tr}(X) = 0$), and the load is uniaxial, the principal component X_{11} in the loading/unloading direction is related to its equivalent

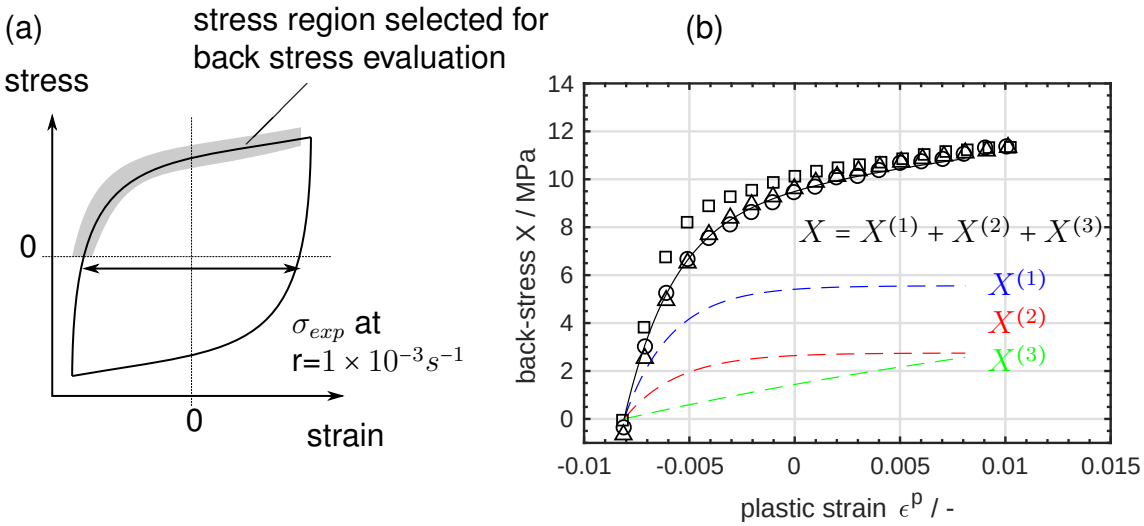

Fig. 4.5: (a) Evaluation of back stress in the experiments. (b) Fit of c_i and γ_i constants using Eq.(4.51) —. Experimental data at 25℃ X^{exp}: △, □, ◯

value $\mathrm{J}_2(X)$.

$$\mathrm{J}_2(X) = \sqrt{\frac{3}{2}\left((X_{11})^2 + (-\frac{X_{11}}{2})^2 + (-\frac{X_{11}}{2})^2\right)} \tag{4.53}$$

$$X_{11} = \frac{2}{3}\mathrm{J}_2(X) \tag{4.54}$$

Then, the back stress is obtained from the experimental stress-strain curve scaled with the stress level at the end of the relaxation period σ_r^{exp}.

$$X^{exp} = \frac{2}{3}\frac{\sigma_r^{exp}}{\sigma_{max}^{exp}}\sigma^{exp} \tag{4.55}$$

Under this assumption, the non-linearity of the stress-strain curve as well as the total amount of back stress generated in the loading phase are taken into account. In order to use the Eq.(4.51), the plastic strain has to be extracted from the total strain (measured) which is equivalent to an evaluation of the stress in the positive tensile domain (see Fig.4.5(a).

$$\varepsilon^p = \varepsilon - \frac{\sigma}{E} \tag{4.56}$$

Then, the c_i and γ_i parameters are found to match the hardening curve, as depicted in the Fig.4.5(b). $X^{(1)}$, $X^{(2)}$ and $X^{(3)}$ are calculated using the analytical expression of back stress in Eq.(4.51). The experimental data corresponds to a hysteresis cycle at the highest strain rate $1 \times 10^{-3} s^{-1}$. σ_{max}^{exp} is evaluated at this strain rate.

The superposition of three back-stress terms enables an accurate description of the nonlinear hardening in the small strain regime $[-1\% \ldots 1\%]$ and shows that the

Armstrong-Fredericks formulation [43] is appropriate to model the kinematic hardening behavior of the solder material . $X^{(1)}$ is used to describe the first part of hardening, just after that the material leaves its elastic domain in the strain range $[-0.01 \cdots -0.005]$. Outside this plastic strain range, $X^{(1)}$ saturates and takes the value c_1/γ_1. $X^{(3)}$ serves to match the last hardening slope, here in the range $[0.005 \ldots 0.01]$. A small value of γ_3 is set to obtain a quasi linear evolution of back-stress in this domain: $\Delta X = c_3 \times \Delta\varepsilon^p$, for ε^p which belongs to the interval $[0.005 \ldots 0.01]$. $X^{(2)}$ ensures a smooth transition between the two previous domains such as the c_i and γ_i parameters follow a defined order such as $c_1 > c_2 > c_3$ and $\gamma_1 > \gamma_2 > \gamma_3$.

Visco-hardening at high strain rate

The viscoplastic hardening behavior of the material is highlighted within the strain rate variation tests. At a defined strain amplitude, a higher stress is obtained when a higher strain rate is applied during the loading phases. The stress variation is called visco-stress (or over-stress) and is defined in the material model by the status variable σ_v. Thus, according to the formulation proposed by Chaboche [40], a double power function is chosen to relate visco-stress and plastic strain rate (ONERA2 model) in Eq.(4.57).

$$\dot{\varepsilon}^p = \left(\frac{\sigma_v}{K_1}\right)^{1/m_1} + \left(\frac{\sigma_v}{K_2}\right)^{1/m_2} \tag{4.57}$$

$$\dot{\varepsilon}^p \approx \left(\frac{\sigma_v}{K_1}\right)^{1/m_1} \quad \text{if} \quad K_2 >> K_1 \quad \text{and} \quad m_2 > m_1 \tag{4.58}$$

The first visco-function (with the parameters m_1 and K_1) is dedicated to the visco-hardening behavior at high strain rate. The second visco-function can be deactivated by setting $K_2 >> K_1$ (e.g. $K_2 = 1 \times 10^5$ and $m_2 = 2 \times m_1$, Eq.(4.58)) and will be determined in a subsequent step. In this way, visco-stress and plastic strain rate are extracted from the experimental tests using following assumptions. First, plastic strain rates are approximated by total strain rates, considering a low elastic strain evolution at 1% strain deformation, Eq.(4.59)-(4.60)-(4.61). This assumption is justified by the fact that the hardening behavior saturates after 1% strain deformation and a low stress evolution is observed beyond this strain.

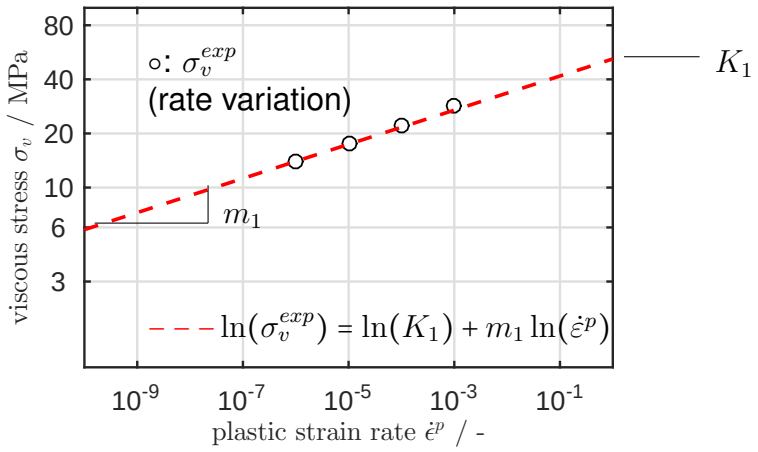

Fig. 4.6: Graphical determination of viscous parameters m_1 and K_1 using a logarithm-based over-stress diagram. The experimental data are evaluated with Eq.(4.62)

$$\dot{\varepsilon} = \dot{\varepsilon}^e + \dot{\varepsilon}^p \tag{4.59}$$

$$\dot{\varepsilon} = \frac{\dot{\sigma}}{E} + \dot{\varepsilon}^p \tag{4.60}$$

$$\dot{\varepsilon} \approx \dot{\varepsilon}^p \tag{4.61}$$

Then, the experimental values of σ_v are determined using Eq.(4.62). The total stress σ is read after 1% strain deformation at a defined strain rate. By neglecting static recovery terms, the back stress X is approximated by Eq.(4.51) using the c_i and γ_i parameters found previously.

$$\sigma_v^{exp}(\dot{\varepsilon}^p) = \sigma_{max}^{exp}(\dot{\varepsilon}^p, \varepsilon = 1\%) - X(\varepsilon = 1\%) - \sigma_0 \tag{4.62}$$

Finally, the visco-diagram can be constructed Fig.4.6, where experimental viscous stress and plastic strain rate are plotted both in logarithmic scales. The viscous parameters are determined graphically: m_1 corresponds to the slope of the curve and K_1 represents the viscous-stress generated at a strain rate of $1 \times 10^0 s^{-1}$.

After determining the elastic constants, the kinematic hardening parameters and the first visco-function, the model is capable to describe the deformation behavior at small strain and high strain rates. This is illustrated within cyclic loads in Fig.4.7, in strain rate controlled situation, where the strain amplitude varies from -1% to +1% and the strain rate from $1 \times 10^{-3} s^{-1}$ and $1 \times 10^{-6} s^{-1}$.

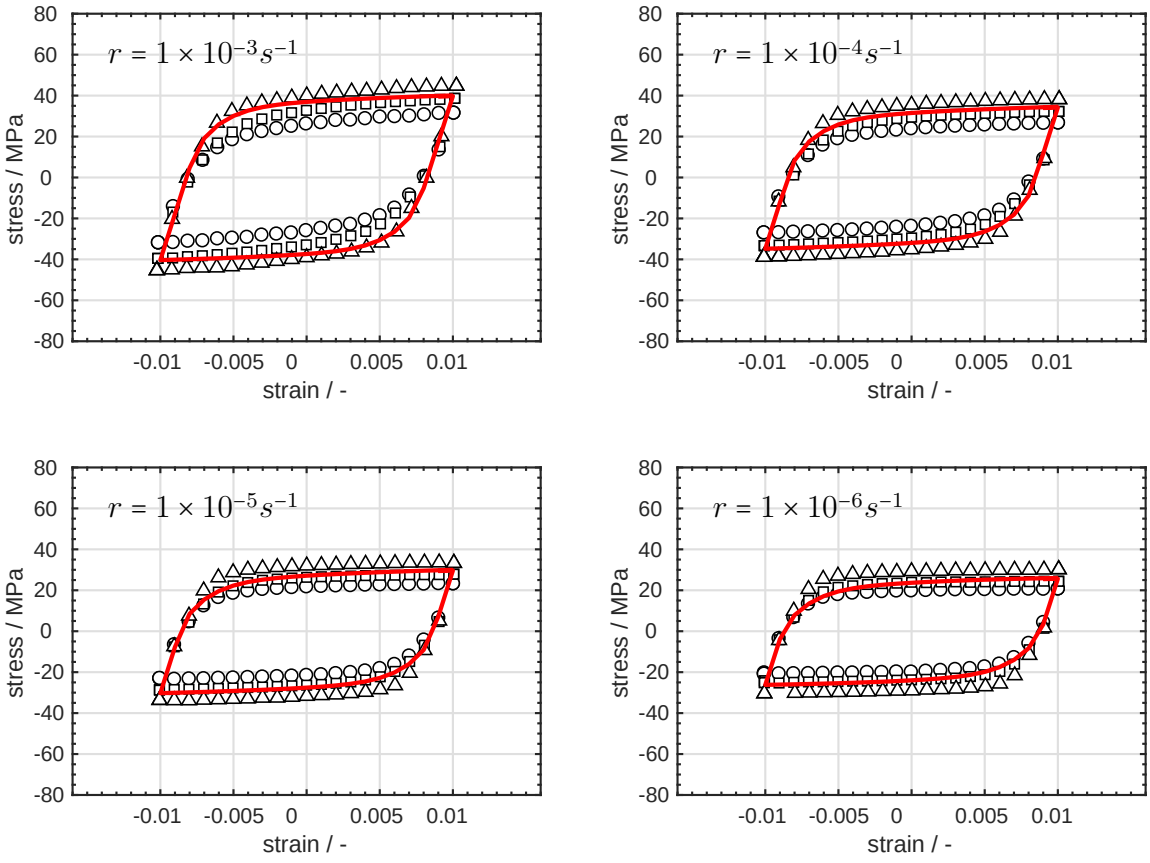

Fig. 4.7: Experiments □, △, ∘ and model prediction — at different strain rates r for T=25℃ after parametrization of elastic constants, kinematic hardening and first visco-function, influence of the strain rate on the stress-strain hysteresis

Visco-hardening at low strain rate and static recovery terms

At low strain rate, the static recovery terms included in the back stress become relevant. Therefore, the time hardening processes developing in this strain rate regime result as a mixture between visco-hardening (which increases stress with increasing strain rates) and recovery processes (which tends to decrease stresses over a period of time). This low strain rate regime occurs during relaxation periods and steady state creep (secondary creep stage). Under these conditions, the back stress cannot be approximated by Eq.(4.51) but the full differential equations Eq.(4.7) have to be considered. Indeed, the equations (4.7)-(4.8) have no integral form due to the presence of static recovery terms. For this reason, the only way to access the back-stress evolution is to employ the discrete differential equations, as they are implemented in the material model. Thus, one has to calculate the mechanical response with the material model, and during the computation, to store the back-stress values after each time iteration.

In practice, the back stress X is saved into a status variable and re-read after calculation (post-processing operation). Then, these values are used to evaluate the experimental viscous stress σ_v^{exp} as the difference between the applied stress σ^{exp} in the creep experiments and its corresponding back stress X obtained after simulation of steady state creep under the same applied stress, Eq.(4.63).

$$\sigma_v^{exp} = \sigma^{exp} - X - \sigma_0 \tag{4.63}$$

In parallel, the secondary creep strain rates $\dot{\varepsilon}^p$ are evaluated in the creep experiments. Thus, the visco-diagram Fig.4.6 is further extended into Fig.4.9 with strain rate and viscous stress points obtained in the creep experiments. The experimental data point are represented by □ in Fig.4.9. In a similar way, the parameters K_2 and m_2 of the second visco-function are used to fit the creep data points in the low strain rate regime where Eq.(4.57) can be approximated by its asymptotic behavior.

$$\dot{\bar{\varepsilon}}^p \approx \left(\frac{\sigma_v}{K_2}\right)^{1/m_2} \tag{4.64}$$

At a first glance, the determination of the material parameters appears straightforward, but in fact, a strong interplay exists between X and σ_v^{exp} because of the static recovery terms. Indeed, the experimental viscous stress σ_v^{exp} is not directly derived from the experiments but also depends on X which is obtained by simulation. Furthermore, X also depends on the static recovery constants, more pronounced during

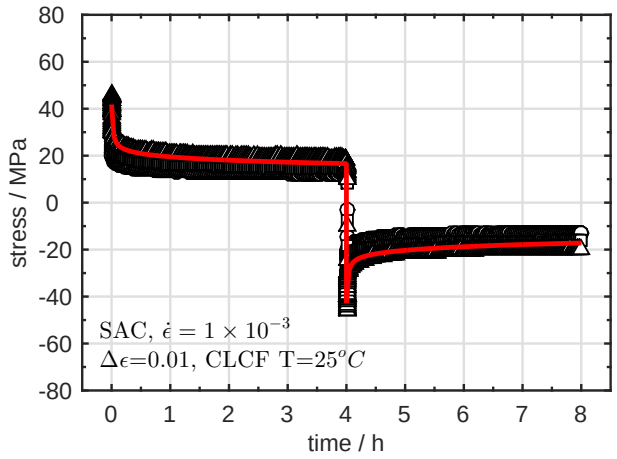

Fig. 4.8: Stress relaxation obtained with the final set of parameters. — Model prediction. △, □, ∘: 3 independent experiments

low plastic strain rate loads.

Static recovery terms d_i are used to match both stress relaxations and smooth transition between the lower viscous stress level obtained during the lower strain rate variation tests and the higher steady state creep rate obtained during the creep test with the higher applied stress. In fact, increasing the d_i decrease the corresponding back stress X and subsequently increase the viscous stress σ_v. This would be illustrated by a vertical translation of the data points plotted in Fig.4.9.

Then, one adjusts the constants K_2 and m_2, in order to match the the creep data points with asymptotic Eq.(4.63), Fig.4.9. Thus, the double visco-function (Eq.(4.57)) matches correctly the corresponding creep and viscoplastic data points, revealing a satisfying equilibrium in the status variables X and σ_v, respectively related to recovery processes and hardening in the whole strain rate regime. Besides, an accurate prediction of stress relaxation is simulated as shown in Fig.4.8.

In order to calibrate the second visco-function and the static recovery parameters, creep and relaxation experiments are necessary. Moreover, due to a strong coupling between viscous stresses and back stresses at low strain rate regime, a direct determination of the constants is not possible. That's why they are determined step by step, using both simulation and graphical methods to evaluate respectively the back stress X and viscous stress σ_v , and approaching an ideal match like in Fig.4.8-4.9. The existing coupling effects, however, lead to a complex interplay between static recovery and creep strain rate. Both the back stress X and the viscous stress σ_v cannot be directly measured in the creep experiments, which makes these variables dependent on the simulation and therefore on the material constants used.

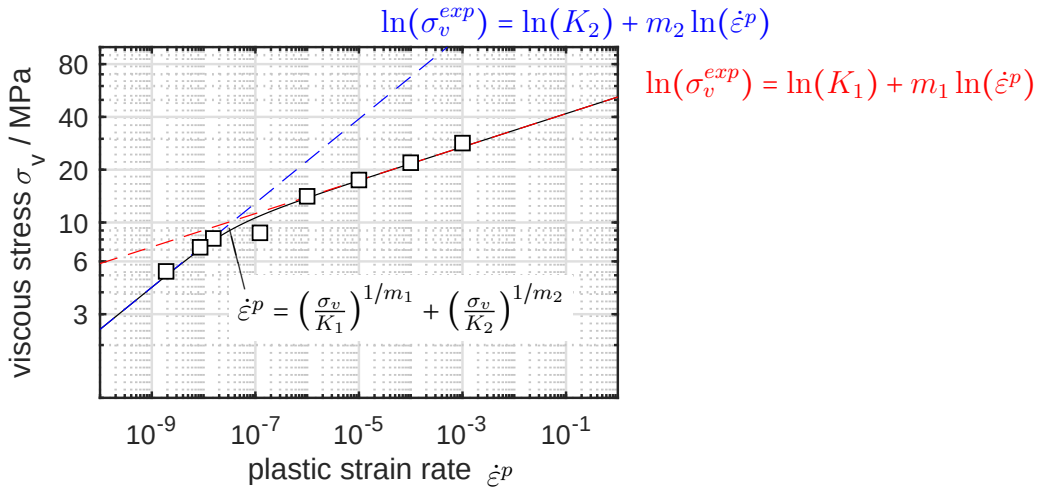

Fig. 4.9: Over-stress diagram in creep and viscoplastic strain rate regimes and calibration of the two visco-functions with the asymptotic functions Eq.(4.58) – – – and Eq.(4.64) – – – and ONERA2-visco function Eq.(4.57) ––. □: viscous-stress σ_v from creep and strain rate variation experiments calculated with Eq.(4.63)

Nevertheless, the model is capable to describe primary and secondary creep stage for various stress magnitudes, as depicted in Fig.4.10, for stresses varying between 17.5 and 12 MPa. This constitutes the main advantage of the double visco-function of the ONERA2 model. On one hand, the first visco-function is used to describe the high strain rate regime (Fig.4.7) but remains insufficient for a description of the low strain rate regime. On the other hand, the second visco-function, enhanced with static recovery, is able to describe the low strain rate regime. Thus, a correct description of primary and secondary creep stages Fig.4.10, and relaxation behavior (Fig.4.8) is obtained with the ONERA2-model which would not be achieved using a single visco-function and without static recovery.

From here, the material parameters which describe the mechanical behavior of the material prior to degradation are determined. In summary, the model is capable to describe strain-stress hysteresis at different strain rates, stress relaxation in dwell time period, and the secondary creep strain rate for low stress within the low strain rate regime. This mechanical behavior is driven only by deformation mechanisms and corresponds to an undamaged state, prior to any damage processes. In the following, the material parameters used to describe the damage behavior are determined.

4.2.2. Fatigue damage description

Under cyclic strain controlled conditions, the solder material shows a substantial decrease of its strength with the accumulation of cycles. The observed cyclic stress

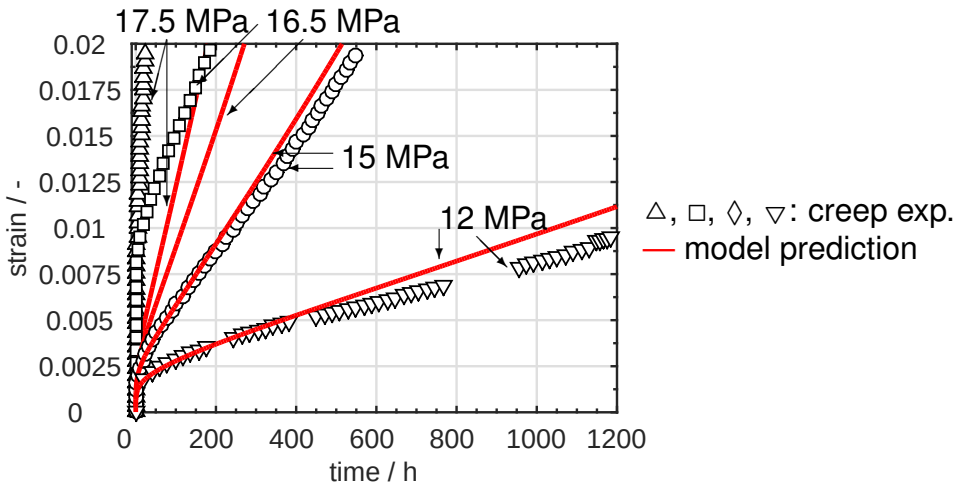

Fig. 4.10: Description of primary and secondary creep stage with the ONERA2-model in the strain range $0\ldots2\%$

$\pm\Delta\varepsilon$	σ_0	N_l	σ_l	N_a	σ_a	N_f	σ_f
0.01	43.82	200	34.00	924	26.91	1266	21.91
0.0066	32.97	456	31.82	2245	28.20	2531	16.48
0.0038	42.67	700	39.71	5394	33.91	6274	21.33
0.0025	34.18	3575	31.78	21000	26.87	25184	17.09

Tab. 4.1: Experimental fatigue data at 25°C as referred in Fig.4.11

softening is further correlated to an internal degradation and typically attributed to fatigue damage processes. In fact, the SAC alloy shows no evidences of cyclic hardening but rather a cyclic softening which can be divided in three phases as highlighted in Fig.4.11.

As far as fatigue modeling is concerned, the calibration procedure is exclusively based on the cyclic softening curves which are obtained under strain controlled cyclic tests at constant temperature. Distinct tests have to be conducted for different strain amplitudes until end-of-life of the sample, here defined by 50% stress reduction regarding the maximum stress measured in the first cycle. At least, a minimum of three different strain amplitudes is required. As an example, we parametrized the proposed fatigue model for 25°C. In a first step, the following information have to be collected from the cyclic softening curve which corresponds to specific points defined in Fig.4.11. They are reported in Tab4.1 for different strain amplitudes $\pm\Delta\varepsilon$.

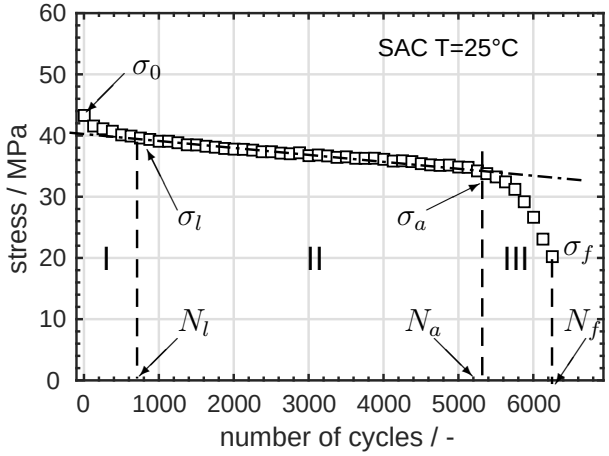

Fig. 4.11: Substantial decrease of the maximum stress in each cycle under cyclic strain controlled condition. □: example of cyclic experiment $\Delta\varepsilon = \pm 0.0038$ where the I, II and III stages of cyclic softening are identified

First stage of cyclic softening: ϕ function within $[0 \dots N_l]$

During the first stage of softening, within the interval $[0 \dots N_l]$, a fast exponential stress decrease is observed. Thus, this effect can be modeled by increasing the dynamic recovery term in the kinematic back-stresses using an exponential function ϕ which depends on the accumulated plastic strain. By increasing the dynamic recovery term, one decreases the total amount of back stress generated, and therefore, it decreases in the same amount the resulting stress, and results in the first softening stage of the interval $[0 \dots N_l]$. The effect of the ϕ function vanishes for high values of accumulated plastic strain such as ϕ saturates to ϕ_∞ after N_l number of cycles. However, the damage D increases as well within this interval $[0 \dots N_l]$ and also participates to the cyclic softening. In order to separate the two effects, the stress at the stabilized cycle σ_l is extrapolated to σ_{0l} which corresponds to the stress reduction only due to the contribution of the ϕ function, Eq.(4.65).

$$\sigma_{0l} = \sigma_l - \frac{\sigma_l - \sigma_a}{N_l - N_a} N_l \tag{4.65}$$

Thus, one defines $\Delta\sigma_\infty$: the amplitude of stress which decreases only due to the ϕ function.

$$\Delta\sigma_\infty = \sigma_0 - \sigma_{0l} \tag{4.66}$$

Then, the back stress quantity $\mathrm{J}_2(X)$ generated for a defined strain amplitude $\Delta\varepsilon$ is calculated either using the approximated Eq.(4.51) or directly by simulation using the

$\pm\Delta\varepsilon$	0.01	0.0066	0.0038	0.0025
$\mathrm{J}_2(X)$	10.55	9.72	8.61	4.21
$\Delta\varepsilon^p$	0.0076	0.0047	2.40×10^{-3}	6.58×10^{-4}

Tab. 4.2: Calculated inelastic variables corresponding to the fatigue tests of Tab4.1

material model. In this case, $\mathrm{J}_2(X)$ is read from the status variables of the material model. Similarly, the plastic strain accumulated within one cycle can be approximated using Eq.(4.56) or obtained after simulation.

Thus, using the boundary conditions $\phi(N = 0) = 1$, and $\phi(N = Nl) = \phi_\infty$, and considering the back stress contribution $\mathrm{J}_2(X)$ in the first cycle, the stress softening in the first stage is given by

$$\Delta\sigma_\infty = \mathrm{J}_2(X) - \frac{\mathrm{J}_2(X)}{\phi_\infty} \tag{4.67}$$

Finally, ϕ_∞ is calculated using Eq.(4.66) for different strain amplitudes $\Delta\varepsilon$ and averaged by its mean value. ϕ_∞ is related to the amplitude of the stress softening in the interval $[0 \dots N_l]$. In a second step, we determined the parameter b_k. For this, the diagram Fig.4.12 is constructed, using the experimental softening curve in the interval $[0 \dots N_l]$, respectively for different strain amplitudes. The accumulated plastic strain $\bar{\varepsilon}^p_{acc}$ is plotted on the x-axis, which is approximated by

$$\bar{\varepsilon}^p_{acc} = 2 \times N \times \Delta\varepsilon^p \tag{4.68}$$

where N is the number of cycle in the interval $[0 \dots N_l]$. Besides, the relative stress decrease is normalized for each strain amplitude and plotted on the y-axis.

Above $\bar{\varepsilon}^p_{acc} = 10$, all the experiments have reached their saturation levels. Thus, the depicted behavior Fig.4.12 can be modeled by an exponential function with a saturation rate. This saturation rate corresponds to the material parameter b_k. The softening behavior in the first stage $[0 \dots N_l]$ reveals a low dependency to the strain amplitude such as all the experiments can be modeled as a function of the accumulated plastic strain only.

Second stage of cyclic softening: evolution of the fatigue damage variable D_1 within the interval $[N_l \dots N_a]$

After N_l number of cycles, the effects of the ϕ function vanishes, and the stress softening occurring within the interval $[N_l \dots N_a]$ is attributed to fatigue damage de-

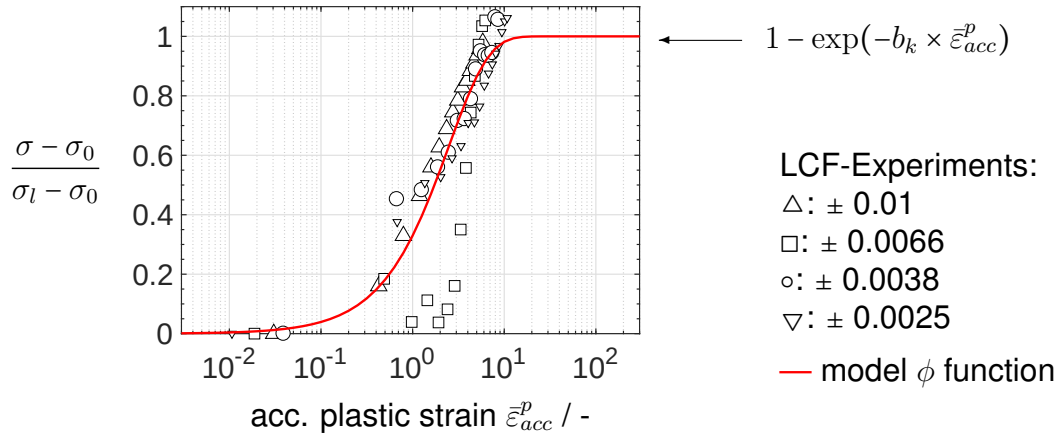

Fig. 4.12: Modeling first cyclic softening by change of recovery term in the back-stress part. Calibration of ϕ function using experimental data

velopment D_1. Within this interval, the stress softening is considered linear. Then, a linear damage development is set up to model the behavior. Without considering the $\tanh$ term, and multiaxial effects (which are treated separately later), the damage rate D_1 depends on two material parameters a_1 and b_1, as well as the plastic strain rate $\dot{\bar{\varepsilon}}^p$ and the absolute plastic strain $\bar{\varepsilon}^p$, see Eq.(4.69).

$$\dot{D}_1 = a_1 \times \dot{\bar{\varepsilon}}^p \times \left(\bar{\varepsilon}^p\right)^{b_1} \tag{4.69}$$

This linear development of D_1 occurs in the interval $[N_l \dots N_a]$, such as D_1 reaches the value D_a in N_a. D_a is a material parameter and corresponds to the amount of damage accumulated in the material to initiate a crack. D_a is averaged over all the temperatures to describe the stress reduction until N_a for all the experiments. Thus, Eq.(4.69) is integrated with respect to the number of cycles and considering the plastic strain $\bar{\varepsilon}^p$ constant within a cycle. The approximated integral is obtained Eq.4.70, where $2 \times \Delta\varepsilon^p$ is the resulted plastic strain after one cycle of deformation.

$$D_1 = a_1 \times 2 \times \Delta\varepsilon^p \times N \times \left(\Delta\varepsilon^p\right)^{b_1} \tag{4.70}$$

Thus, by setting $D_1(N_a) = Da$, it results a power function of plastic strain where the two material parameters a_1 and b_1 could be determined by linear regression using the experimental data Tab4.1 and 4.2.

$$\frac{D_a}{2 \times \Delta\varepsilon^p \times N_a} = a_1 \times \left(\Delta\varepsilon^p\right)^{b_1} \tag{4.71}$$

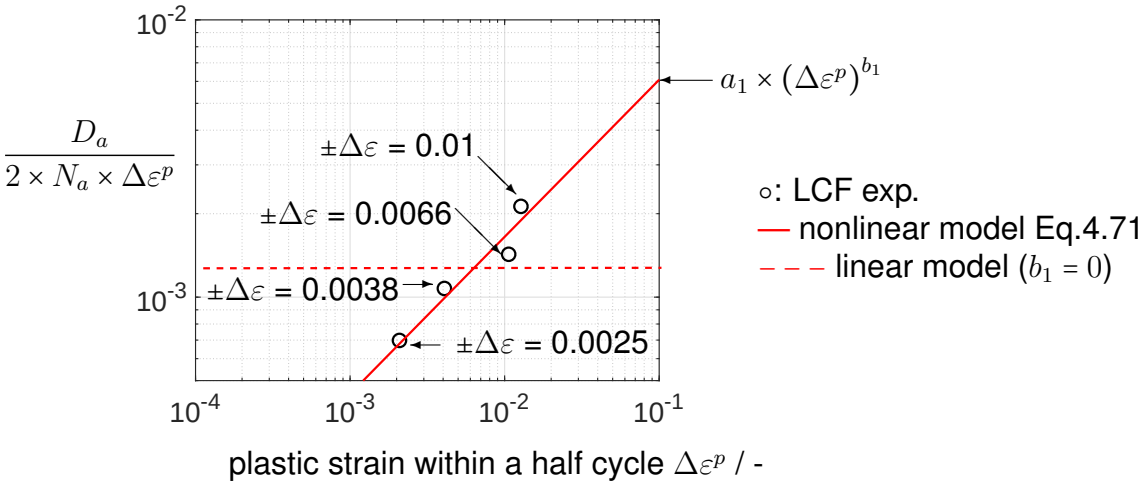

Fig. 4.13: Fitting the material constants for fatigue damage D_1 with a nonlinear power function —

The diagram Fig.4.13 particularly shows the existence of a nonlinear dependence between plastic strain and fatigue damage development, enhanced here by the number of cycles to crack initiation N_a for an accumulated damage D_a. If we would have considered a linear function in the model (– – –), such as D_1 is a linear function of the accumulated plastic strain $2 \times \Delta\varepsilon^p \times N$, we would obtain a horizontal red curve, not capable to capture the nonlinear behavior observed at different strain amplitudes.

This nonlinear function constitutes an improvement of the damage equation typically found in literature [28, 30, 55], which allows more flexibility to describe the fatigue damage development for various strain amplitudes and is specific to the material model proposed in the present work. It should be noted that the law of evolution is independent on stress. Due to the high ductility of the material, the stress generated for different strain amplitudes in the range $\Delta\varepsilon = 0.0025 \ldots 0.01$ does not vary significantly, and a correlation between damage development and stress magnitude could not be found here. For this reason, the stress term is excluded from the damage equation which only depends on derived plastic strain variables.

Third stage of cyclic softening: damage development after crack initiation within $[N_a \ldots N_f]$

After a constant stress softening within the interval $[N_l \ldots N_a]$, an acceleration of the softening is observed after N_a which further evolves up to the sample life-time at N_f cycles. The acceleration of softening is attributed to macroscopic crack which initi-

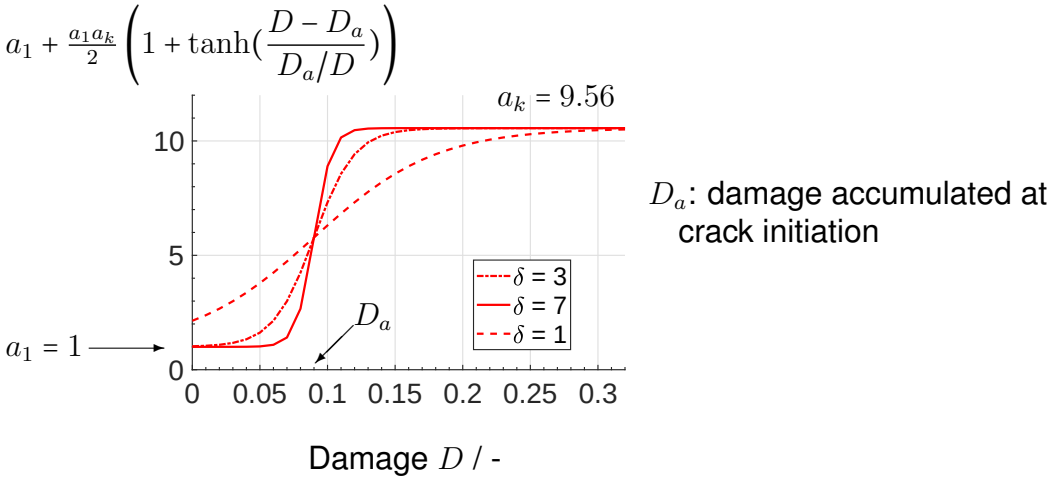

Fig. 4.14: Tangent hyperbolic function $\tanh$ models the smooth transition near crack initiation D_a and change the fatigue damage rate for $D >> D_a$ from a_1 to a_k

ates and then propagates through the sample. From a macroscopic point of view, this results in higher damage rates after N_a cycles. In the present model, the fatigue damage equation is split to describe the second and the third stages of cyclic softening. For this, a $\tanh$ function is introduced to assure the transition from the second to the third stage and to describe the material behavior until its end-of-life. When $D = D_a$, the damage rate is scaled by a factor a_k to model the acceleration of degradation. The material parameter a_k is determined as the ratio of the softening rate respectively between the second and the third stage.

$$a_k = \frac{\frac{\sigma_f - \sigma_a}{N_f - N_a}}{\frac{\sigma_a - \sigma_l}{N_a - N_l}} \tag{4.72}$$

Then, a_k is averaged by applying Eq.(4.72) for the different strain amplitudes investigated. Besides, the material parameter δ ensures a smooth transition between the two slopes and makes a correct description of the softening curve within the inflection region near $N = N_a$. The influence of the parameter δ is depicted in Fig.4.14.

The calibration procedure for the fatigue damage model is now completed. In order to verify that the model describes the experimental curves, the 4 LCF tests are successively simulated using one element. In each cycle, the maximum and minimum stresses are reported in Fig.4.15 and compared to the experimental data. Furthermore, the experimental end-of-life criterion has been chosen as 50% stress reduction. Using the material model calibrated as described above results in a damage variable value of $D = 0.30$ achieved for 50% stress reduction. Thus, the critical damage is

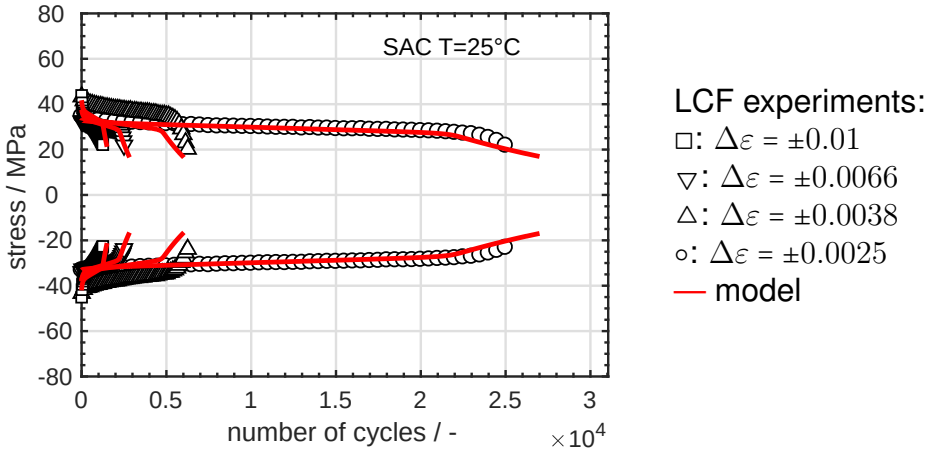

Fig. 4.15: Simulation of stress softening using a fatigue damage model for 4 LCF tests with varied strain amplitudes until samples end-of-life

defined and set by $D_c = 0.30$ corresponding to the local macroscopic degradation observed in the measurements.

Finally, the proposed damage model delivers a good description of the stress softening observed during LCF tests for various strain amplitudes. For this, the model uses a ϕ function to modify the recovery processes in the back stress, a modified non-linear damage equation of plastic strain and a $\tanh$ function to describe the transition after crack initiation and further to end-of-life of the material. The proposed equation (4.14)-(4.15) shows a good correspondence to the observed fatigue damage on the macroscopic sample scale mapping the interaction between plastic strain, damage and stress softening.

4.2.3. Creep damage description

Creep damage is observed during dedicated creep tests. It can be quantified by using the resulted time-strain curve measured until creep rupture. During primary and secondary creep stages, the deformation results from time dependent irreversible microscopic processes, but the amount of damage is still considered low within the two first stages. These stages have been modeled in the previous sections by using a double visco-function for the low creep strain rates. Creep damage evolves mainly in the tertiary creep stage after a certain amount of strain deformation has been accumulated. For this reason, creep damage is expected to be dependent on stress, time but also plastic strain, in order to model correctly both the onset and evolution of the tertiary creep stage. In uniaxial tensile deformation, the creep damage rate is

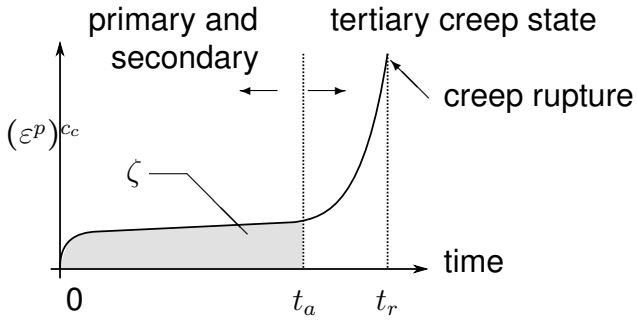

Fig. 4.16: Evaluation of creep damage at crack initiation time: integral of strain over time from 0 until t_a, time at the onset of tertiary creep defined as an equivalent time to crack initiation under creep condition

stress / MPa	t_a / h	ζ
16.5	577.1	1261
15	967.9	1629
12	3964	5234

Tab. 4.3: creep data points used for calibration of the creep damage model

given by

$$\dot{D}_2 = a_2 \left(\tilde{\sigma}_{eq}\right)^{b_2} \left(\bar{\varepsilon}^p\right)^{c_c} \tag{4.73}$$

The parameter c_c provides means to control the calculation of creep damage at small strains. In particular, during relaxation periods, where stress is relatively high but the strain remains low, the development of creep damage is expected to be rather low. The small strain regime further governs the loading/unloading ramps during cyclic fatigue tests, where small strains ($< 1\%$) are applied. In order to integrate the influence of strain in the creep damage development, we define and calculate the area under the strain curve ζ over time t

$$\zeta = \int_{t=0}^{t=t_a} \left(\bar{\varepsilon}^p\right)^{c_c} dt \tag{4.74}$$

ζ is calculated numerically using the material model. Then, the parameters a_2 and b_2 are determined using the time-strain creep curves for various stress levels. The specific strain-time points are reported in table 4.3 and illustrated in Fig.4.16 where ζ has been calculated.

By assuming a nearly constant stress, Eq.(4.73) can be integrated over time. We consider that a damage D_a has been accumulated at the onset of tertiary creep occurring at the time t_a. Then, the following equality from Eq.(4.73)-(4.74) results

$$D_a = \zeta \times a_2 \times (\sigma)^{b_2} \tag{4.75}$$

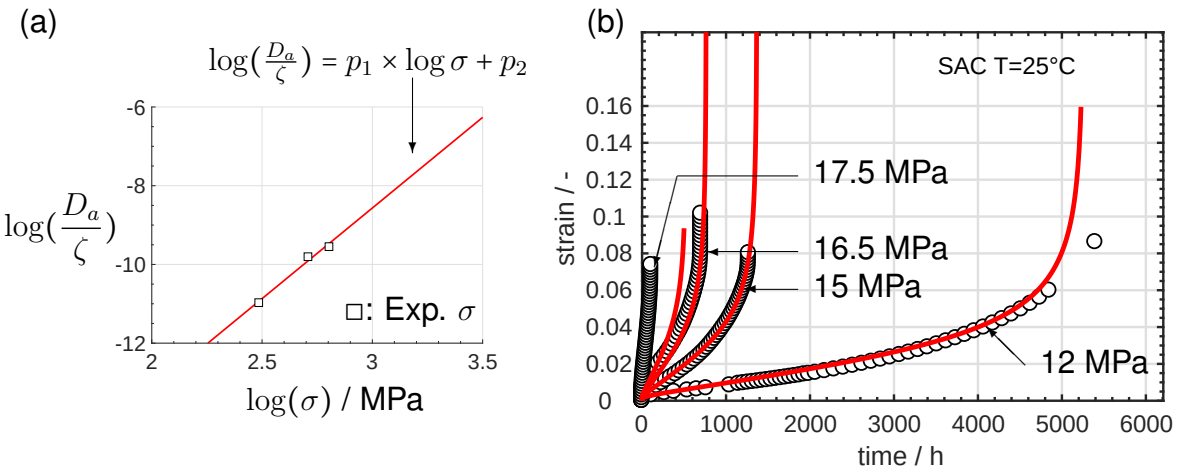

Fig. 4.17: (a) Fit of stress parameters in the creep damage equation.(b) Modeling tertiary creep stage until creep rupture for various stress magnitude using the creep damage model Eq.(4.73). —, creep exp. ∘

which serves to describe the correlation between D_a and the stress using a logarithmic fit, Fig.4.17(a). By analogy with Eq.(4.75), we find $a_2 = \exp(p_2)$ and $b_2 = \exp(p_1)$. These are the material parameters governing the creep damage evolution for the SAC solder material at 25 °C.

It should be noted that the same damage approach is employed for creep damage development as for fatigue damage development depicted in the previous section. The material parameter D_a fulfills the role of damage threshold necessary to initiate a crack. The crack initiation manifests either by an acceleration of stress softening within LCF condition or by an acceleration of strain rate at the onset of the tertiary creep stage within creep testing condition. A unique damage threshold for crack initiation, for both creep and fatigue damage mechanisms, has many advantages. For instance, it facilitates the damage accumulation in case of combined fatigue-creep tests, where both damage processes act simultaneously and cause a crack. Thus, the creep tests at 25 °C can be simulated with the damage model, where the results are plotted in Fig.4.17(b).

After calibration of the material constants for creep damage, the model is able to describe the smooth transition between secondary and tertiary creep stages, and to predict within a reasonable accuracy the time to rupture for various stress level within creep testing conditions. The good correspondence to experimental data shows that the creep damage evolution has been correctly modeled with the phenomenological Eq.(4.73), such that the interplay between time, strain and stress are appropriately taken into account. The creep damage is in Fig.4.17(b) indirectly depicted, because

test	R behavior	strain amplitude	dwell time period	N_a
RF1	$R = -1$	$\Delta\varepsilon = \pm 0.0066$	10 min.	1460
RF2	$R = 0$	$\Delta\varepsilon = 0 \ldots 0.0132$	10 min.	1000

Tab. 4.4: Relaxation-Fatigue (RF) experimental lifetime at 25°C

the strain-time curve reveals the development of damage by the acceleration of strain rate at the onset of tertiary creep stage. It is modeled in the simulation by a large increase of creep damage as soon as $D = D_a$, occurring at $t = t_a$, the onset of tertiary creep, leading to creep rupture (see Fig.4.17(b)).

4.2.4. Modeling creep-fatigue nonlinear damage accumulation

In the previous sections, creep and fatigue damage have been treated separately. However, their respective damage evolution is not independent. Typically, one of the damage processes develops faster if the other one also develops simultaneously, such as the total damage cumulated is greater than the sum of both Eq.(4.16), [49]. This effect is often referred to as nonlinear creep-fatigue damage accumulation. It can be modeled, from an empirical point of view, by ASME nonlinear rule [61]. Here, we adapt the ASME bilinear equations and integrate them into the present damage model. It results a nonlinear sum of fatigue and creep damage rates, such as the bilinear rule adopts a differential form within the material model, instead of an integral form, like it has been originally formulated in the ASME standard rules.

Indeed, the rule is called bilinear because the same nonlinearity is attributed for fatigue as for creep dominated damage loads. The material parameter c governs the nonlinearity producing a higher total damage than the sum of both. For determination of c, combined creep-fatigue tests are used, as for example a LCF test with dwell-time periods. In such tests (called RF test for Relaxation-Fatigue), creep damage is accumulated during the successive stress relaxation periods within the dwell times in addition to cyclic fatigue. It should be noted that $c = 0.5$ gives a linear accumulation rule. Two RF tests, see Tab4.4, are carried out at 25°C and are used to calibrate the material parameter c.

As a first step, the simulation of the tests RF1 and RF2 is performed using a linear damage accumulation by setting $c = 0.5$. The accumulated creep and fatigue damage under these conditions are calculated by simulation until $N = N_a$ cycles. The fatigue and creep fraction of life, respectively $\bar{D}_1$ and $\bar{D}_2$ are calculated as the ratio between their values at N_a and D_a: damage threshold for initiating a crack. The simulation

test	D_a	$D_1(N = N_a)$	$D_2(N = N_a)$	$\bar{D}_1$	$\bar{D}_2$
RF1	0.09	0.06368	0.0020	0.7075	0.0222
RF2	0.09	0.05250	0.0065	0.5833	0.0722

Tab. 4.5: Relaxation – Fatigue (RF) simulation results with linear accumulation rule

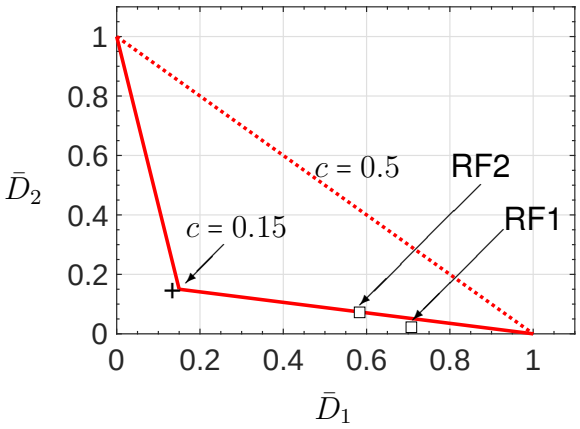

Fig. 4.18: Bilinear damage accumulation rule adapted from ASME standards for use within the present damage material model. In Eq.(4.41)-(4.42), the material parameter c is calibrated with RF tests at 25°C

results of the tests RF1 and RF2 are listed in the table 4.5.

$$\bar{D}_1 = \frac{D_1(N = N_a)}{D_a} \qquad \bar{D}_2 = \frac{D_2(N = N_a)}{D_a} \tag{4.76}$$

Finally, the bilinear damage accumulation diagram can be constructed using the fraction of life consumed by creep $\bar{D}_2$ and fatigue damage $\bar{D}_1$, see Fig.4.18. The parameter c is determined graphically at the intersection of the two bilinear functions which represents the two slopes formulated in Eq.(4.41)-(4.42).

A value of $c = 0.15$ gives a good match to the two RF tests carried out at 25°C. In the present case, it means that under fatigue dominated loads, the total damage will be the sum of the fatigue damage D_1 and 5.66 $((1 - c)/c)$ times the creep damage D_2. The model correlates well with the experimental observations, where the number of cycle to crack initiation occurs sooner for RF tests than for pure LCF test (with a same strain amplitude). If only linear damage accumulation would be considered in the damage model, a significant over-estimation of the number of cycles to crack initiation N_a would result. Thus, a nonlinear damage accumulation is necessary to prevent non-conservative lifetime estimation for combined fatigue and creep loads. This is of utmost importance for handling real thermo-mechanical loads on solder

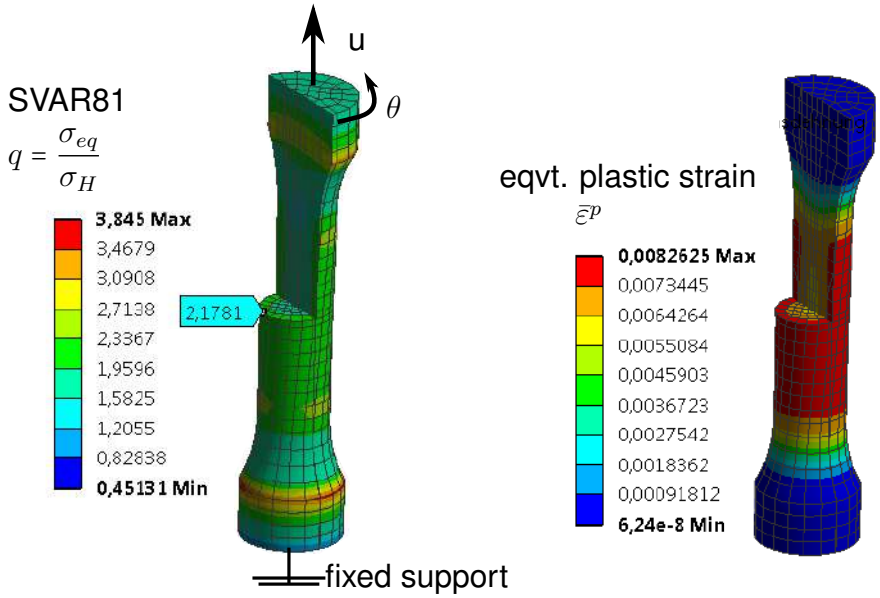

Fig. 4.19: q distribution in the sample, plastic strain $\bar{\varepsilon}^p$ definition after 100 cycles. FE-simulation of the testing sample by using the material model as a user subroutine. Loading conditions: u=± 0.20 mm, $\theta = \pm 4^o$

joint components, as the observed solder degradation results from both fatigue and creep damage.

4.2.5. Multiaxial fatigue parameters

Multiaxial fatigue damage development is investigated by means of cyclic combined Tension Torsion tests (TT). These tests are conducted until end-of-life which is defined as the number of cycles corresponding to 50% of force and moment reduction compared to the initial cycle. TT tests are performed within controlled multiaxial conditions, as the Clausmeyer ratio q is defined and fixed over the cycles [68]. In the previous sections, the parameters of the material model have been found by performing simulations of a single FE-element, thus assuming a homogeneous stress distribution. However, in case of TT loading conditions, the stress state cannot be simplified to a loading configuration applicable on one element, thus the whole testing sample has to be considered. The testing sample has been modeled and simulated using the commercial FE-software ANSYS in combination with the material model implemented as a user subroutine. The Clausmeyer ratio q and the equivalent plastic strain distributions are evaluated and shown in Fig.4.19 for the loading conditions: $u = +0.20$ mm, $\theta = +4^o$.

Due to the rotation, a higher local plastic deformation occurs at the edge of the sample, which also correlates with a higher local q ratio. Related multiaxial fatigue

test	load profile	q	N_a	$\Delta D_{exp,100}$	$\Delta D_{simu,100}$
TT1	u =± 0.20 mm, θ = $\pm 4^o$	2.17	1565	0.0058	0.0075
TT2	u =± 0.15 mm, θ = $\pm 3.22^o$	2.22	3093	0.0029	0.0044
TT3	u =± 0.10 mm, θ = $\pm 2.39^o$	2.34	7966	0.0011	0.0021
TT4	u =± 0.05 mm, θ = $\pm 1.50^o$	2.69	26820	0.000335	0.000565

Tab. 4.6: Tension Torsion tests (TT), experimental and simulation results after 100 cycles

damage is taken into account in the model by introducing the q coefficient in the fatigue damage rate equation before crack initiation Eq.4.77. The material parameter b_{qm} accounts for its influence regarding the damage evolution and acts as an exponent. In case of uniaxial deformation, one has $q = \sqrt{(3)} \approx 1.73$, which cancels the effect of the q term within uniaxial conditions.

$$\Delta D_1 = a_1 \Delta \bar{\varepsilon}^p \left(\bar{\varepsilon}^p\right)^{b1} \left(\frac{|q|}{\sqrt{3}}\right)^{b_{qm}} \tag{4.77}$$

The parameter b_{qm} is determined using the 4 TT tests listed in Tab4.6 (see also Chap.3) and by simulating the test sample under the experimental loads. First, the value of $b_{qm} = 0$ is set to 0 and the accumulated damage $\Delta D_{simu,100}$ is evaluated after 100 cycles using the FE simulation. The results are reported in the table 4.6. In a second step, $\Delta D_{exp,100}$ is calculated which corresponds to the experimental damage after 100 cycles in Eq.(4.78).

$$\Delta D_{exp,100} = \frac{D_a}{N_a} \times 100 \tag{4.78}$$

This damage value is based on the assumption that the damage develops linear from 0 to crack initiation which occurs after N_a cycles. Besides, the damage quantity needed to initiate a crack is defined by D_a, such as D follows a linear evolution between 0 and N_a cycles. D_a has been previously determined ($D_a = 0.09$) as a material parameter for all the temperatures.

Without multiaxial corrections (by setting $b_{qm} = 0$, see Tab4.6), the simulation overestimates the damage accumulation such as $\Delta D_{simu,100} >> \Delta D_{exp,100}$. This can be explained by the large amount of plastic deformation occurring at the edge of the sample where the multiaxial ratio $|q|$ is also higher than in its center. Indeed, the gap between experimental and simulative damage increases with the multiaxial ratio $|q|$, as depicted in Fig.4.20 for the different TT experiments performed. In order to overcome this gap, which is observed in case of multiaxial loads, a power function of q is

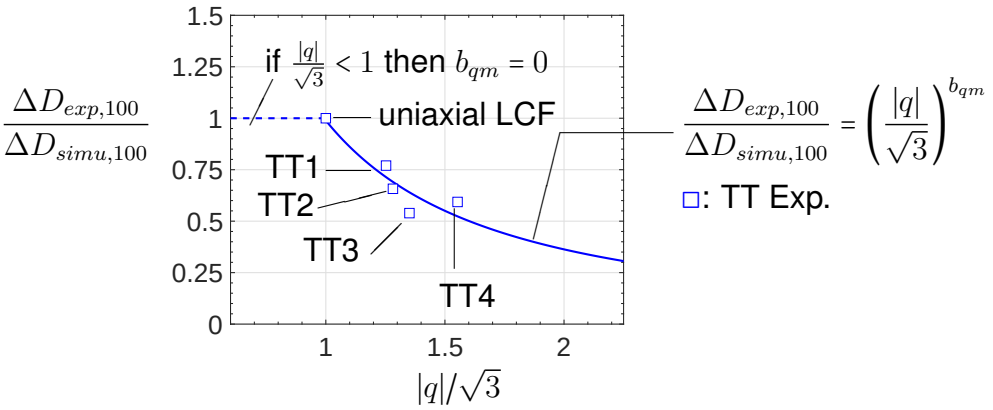

Fig. 4.20: Determination of the exponent b_{qm} using the Tension-Torsion tests for various multiaxial ratio $q = [1.73 \dots 2.69]$

introduced in the fatigue equation Eq.(4.77). This function of $|q|$ acts as a correction in the fatigue damage equation and enables the description of uniaxial and multiaxial fatigue damage evolution. Thus, the exponent parameter b_{qm} can be directly determined from the fit curve for the different TT tests realized and plotted Fig.4.20.

However, $|q|$ values below 1.73 have not been yet investigated experimentally. The introduced equation would predict a higher damage than for uniaxial loads but the real increase remains unknown. In order to prevent extrapolation failure in this uninvestigated domain, a threshold criterion sets $b_{qm} = 0$ for $q < 1.73$. By doing this, the damage rate in the range $|q| \in [0 \dots 1.73]$ is equivalent to the damage rate for $q = 1.73$, corresponding to uniaxial loads. A detailed study on the FE simulation of the testing sample until end-of-life using a usermat-subroutine for Ansys can be found in [88], where the fatigue damage evolution under multiaxial loads are discussed.

4.3. Sensitivity analysis

4.3.1. Thermo-mechanical material parameters

The present material model can be used after the calibration of its 32 parameters. The calibration has to be repeated for the other temperatures. Experimental tests are conducted at -40°C, 75°C and 125°C and the procedure to find out the material constants is systematically repeated, see appendix A.6. It results the following temperature dependent material parameters set listed Tab4.7. In ideal case, the temperature dependency of the parameters has to be defined continuously, particularly if thermo-mechanical simulation is considered. In practice, the material parameters are

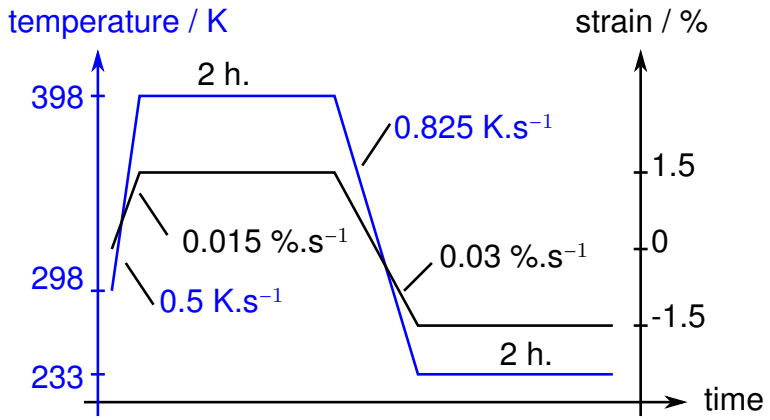

Fig. 4.21: Thermo-mechanical loading profile used on one element simulation for the sensitivity analysis

linearly interpolated in between their respective value at the four temperatures investigated. Outside the temperature range $[-40^oC \dots 125^oC]$, the material parameters keep a constant value equal to the one taken at either -40°C or 125°C.

4.3.2. Sensitivity analysis of the material parameters

The large amount of material parameters, raises the question about their respective influence and their sensitivity onto the mechanical response of the material. Thus, a numerical sensitivity analysis has been carried out. The total damage D is chosen as the variable of comparison and the 32 material parameters are successively varied.

For this, one thermo-mechanical cycle is applied on one element, as depicted Fig.4.21. This particular loading profile refers to a coupled thermo-mechanical load. Simultaneously, the material is strained and heated up to 125°C and 1.5% tensile strain, then kept under these conditions for a dwell time period of 2 hours, then cooled down to -40°C and compressed to -1.5% for 2 additional hours of dwell time period. Such a cycle is representative of real loading profile applied on solder joints tested in laboratory. Per definition, the sensitivity S of D regarding the parameter k can be approximated by Eq.(4.79), where k is related to a material parameter in our case.

$$S_k^{D(k)} = \frac{dD}{dk}|_k \approx \frac{|D(k) - D(k + \Delta k)|}{D(k)} \tag{4.79}$$

For all the material parameters defined for the 4 temperatures, we applied a variation of +10% with respect to their original values, such as $\Delta k = 0.1 \times k$. Then, a thermo-mechanical simulation is run for each parameter variation and the relative

parameter	-40℃	25℃	75℃	125℃
E / MPa	57265	45113	35766	26418
ν / -	0.36	0.36	0.36	0.36
σ_0 / MPa	0.5	0.5	0.25	0.15
c_1 / MPa	9600	5000	2500	4000
γ_1 / -	2200	900	900	2000
c_2 / MPa	5000	2200	1500	1300
γ_2 / -	1700	800	800	900
c_3 / MPa	1500	400	600	300
γ_3 / -	40	60	100	170
ϕ_∞ / -	1.00	1.95	1.29	1.87
b_k / -	0.13158	0.4	0.35	0.42
a_1 / -	0.003876	0.0060	0.0058	0.0229
δ / -	6	7	7	7
D_c / -	0.30	0.30	0.30	0.30
b_2 / -	4.303×10^{8}	82.02	1366	10905
a_2 / -	1.036×10^{-33}	1.8149×10^{-10}	3.2819×10^{-11}	6.5602×10^{-12}
D_a / -	0.09	0.09	0.09	0.09
d_1 / s^{-1}	1×10^{-9}	1×10^{-9}	1×10^{-9}	1×10^{-9}
d_2 / s^{-1}	1×10^{-7}	1×10^{-6}	1×10^{-6}	1×10^{-6}
d_3 / s^{-1}	1×10^{-6}	1×10^{-5}	1×10^{-5}	1×10^{-5}
K_1 / MPa.s^{-m_1}	75	55	35	28
m_1 / -	0.08	0.095	0.08	0.075
K_2 / MPa.s^{-m_2}	1200	560	280	120
m_2 / -	0.28	0.24	0.27	0.28
a_k / -	11	9.56	10	10
b_1 / -	0.009472	0.241	0.2755	0.4425
c_c / -	2	2	1.8	1.5
b_q / -	300	272	272	272
Q / MPa	7	0	0	0
α_{CTE} / K^{-1}	20×10^{-6}	20×10^{-6}	20×10^{-6}	20×10^{-6}
c / -	0.15	0.15	0.50	0.50
b_{qm} / -	-1.45	-1.45	-1.45	-1.45

Tab. 4.7: Temperature dependent mechanical material parameters for SAC alloy for use in the developed viscoplastic-damage model ONERA2

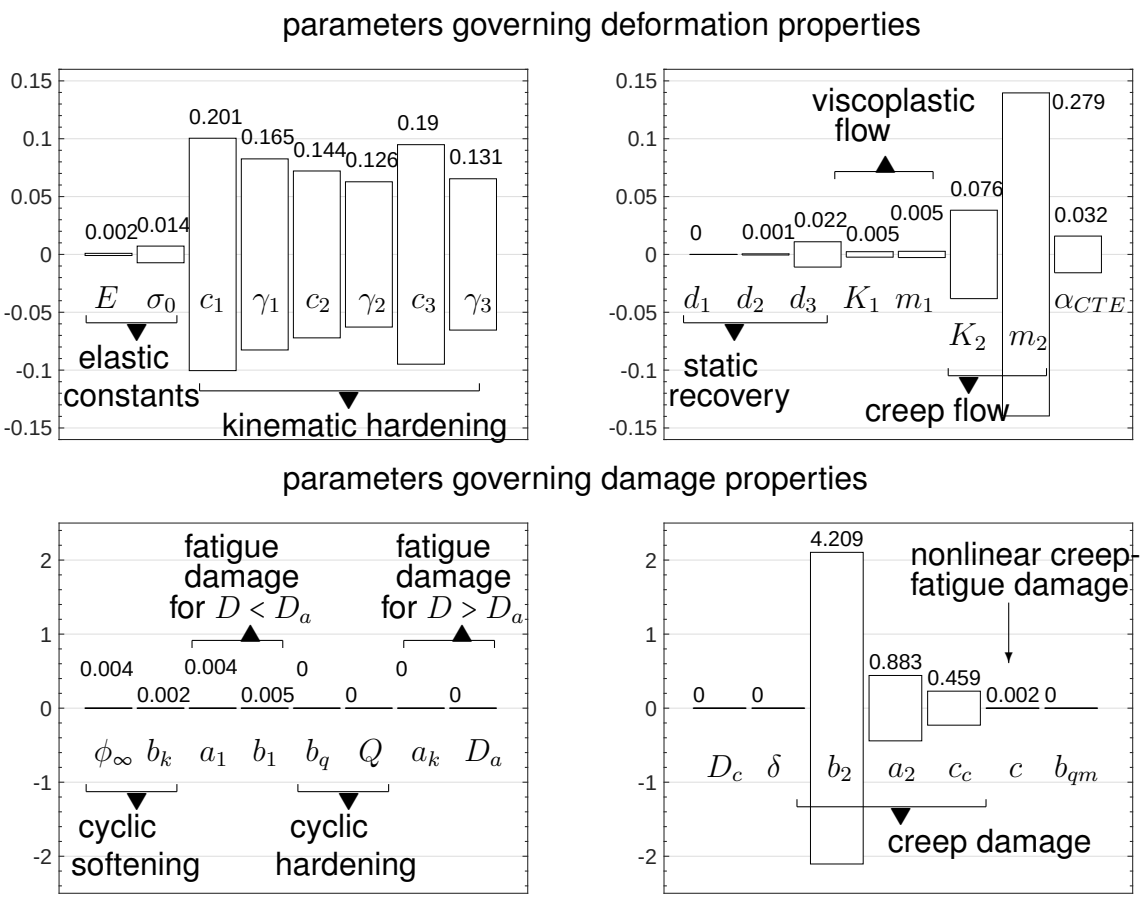

Fig. 4.22: Relative importance of each material parameter regarding the damage development D

variation of the total damage D is illustrated in Fig.4.22.

As far as the deformation properties are considered, the relative sensitivity of each deformation parameter on the total damage varies from 0 to 28%. The influence of the elastic parameters is low, under 2% (Young's modulus E, yield stress σ_0) in contrast to the influence of the kinematic and visco-creep-hardening parameters which govern the inelastic deformation of the material after yielding. The highest influence is observed for the creep strain rate exponent m_2, for which a variation of 10% results in a variation of 28% of damage for the given loading profile Fig.4.22.

As expected, the damage related parameters show the highest sensitivity. The creep damage parameters a_2, b_2, c_c reveal a significant impact on the calculation of damage. b_2 is related to the stress exponent in the creep damage equation. The high sensitivity is explained by the creep rupture behavior at high temperature. At high temperature, for a low variation of applied stress a large variation of creep time to rupture results, governed by the stress factor in the creep damage equation. Besides,

the chosen loading profile Fig.4.22 enables the development of creep higher than fatigue damage, particularly because tensile stress is combined with high temperature, which also demonstrates the high importance of the creep damage parameters for combined thermo-mechanical loads.

The sensitivity analysis reveals the relative importance of each material parameter. Even if the deformation related parameters are not directly associated with damage development, their influence remains significant. In fact, the damage is exclusively calculated using deformation state variables like e.g. stress and plastic strain which are directly associated with the deformation related variables. The most important parameter regarding its sensitivity is the creep damage exponent b_2. Creep damage development needs to be carefully described and its parameters calibrated accordingly. This is only possible with sufficient amount of experimental data which include, among others, creep rupture curves within a large stress range resulting in a wide interval of creep time to rupture. Such experimental data is needed as well for the different temperatures. Because the parameters are interpolated in the simulation of varying temperature loads, it is important to map the temperature range accordingly in order to prevent numerical issues due to linear interpolation function over large temperature intervals.

The large number of material parameters renders not only the calibration more complex, but also questions their interdependence. The 32 parameters are calibrated using less than 32 independent experiments, therefore an interplay between some of them is expected. During the calibration procedure, the interplay between the parameters describing the viscous properties of the material has been pointed out. It concerns the parameters K_1, m_1, K_2, m_2 which have a direct influence on the strain rate dependence within the viscoplastic-creep regimes, and d_1, d_2 and d_3, static recovery parameters governing the stress relaxation. However, it has been shown during the calibration that the d_i parameters not only influence the relaxation behavior but the strain rate dependence in the low strain rate regime as well, such as a strong interplay exists between the parameters K_2-m_2, and the d_i. A distinct separation is difficult to obtain from an experimental point of view. It would require e.g. several creep tests at low stresses, providing strain rates in the range of 1×10^{-10} s^{-1} and below, which should be outside the region of influence of the static recovery parameters. Thus K_2, and m_2, would be determined using those tests, independently of the static recovery influence.

The parameters are determined step by step, one temperature after another. The procedure proposed in this work employs principally graphical methods and numeri-

cal function to approximate and isolate specific part of the model and then determine the material parameters accordingly. In some cases, numerical simulation is employed to calculate state variables which would not be accessed otherwise, as for example the back stress X and viscous stress σ_v. Following this procedure, the physical meaning of each parameter is identified and can be referred to a physical property of the material measured during the experiments.

The calibrated material parameters show substantial temperature dependence, which is not explicitly addressed in the present work. Some parameters reveal unsteady evolution over the temperature (e.g. b_2, ϕ_∞), which is, from a physical point of view, questionable. The unsteady evolution may be the consequence of the parameters interdependence, as mentioned above, or the result of an intrinsic temperature dependence: This could not be resolved on the basis of experimental data gathered within the current work. Provided sufficient experimental data including non-isotherm tests, the calibration procedure could be extended for mapping the temperature evolution of the parameters. However, a step-by-step procedure focused on a single temperature, as proposed here, would no longer be suitable. For this, a global optimization routine might be a better solution, using boundary conditions which guarantee a steady temperature evolution of the parameters. The calibration procedure proposed in this work can be still used to determine the initial sets of parameters. In a second step, the parameters can be further optimized by a global routine over the total temperature range of the experiments.

5. Finite Element simulation

5.1. Simulation of LCF testing samples

In the following, a Finite Element (FE) simulation is presented, which makes use of the material model described in the previous chapter. The aim of this numerical analysis consists in the application and verification of the material model on more complex structures compared to a single element. In this way, FE simulations of the realistic experimental conditions are realized for the different temperatures of the Low Cycle Fatigue (LCF) experiments. The selected experiments Fig.5.1 correspond to LCF measurements with the same strain amplitude ±1%, giving cyclic deformations of ±0.06 mm related to the sample test region. Because of geometrical symmetry only 1/8 of the sample is modeled and meshed, as illustrated Fig.5.2. Cyclic displacement controlled conditions u = ±0.03 mm are successively applied on the outer surface, which corresponds to the position where the displacements are controlled in the LCF experiments (position of LVDTs, see Chap.3). For the 4 temperatures tested, the model is able to predict the reaction forces in the initial state, where the sample is considered nearly undamaged within the first few cycles. At higher cycle numbers intrinsic development of fatigue damage leads to cyclic stress softening, which is modeled by the evolution of the damage variable D, representing the degradation of the material. Because D is coupled with the mechanical equations, the increase of D results in a decrease of stiffness representing the cyclic softening (see Fig.5.1). Above 25°C, the model maps the force decrease, crack initiation as well as acceleration of softening until end-of-life, which has been defined in the tests at 50% of initial force reduction. For a temperature of -40°C, experiment and simulation correlate well up to crack initiation which is shown by a change in the softening slope. After crack initiation, the simulation deviates and predicts slower force reduction with the accumulation of cycles than the same forces measured in experiment.

Damage simulations appear challenging for calculating the accelerated stress fall beyond crack initiation. With progressing evolution of damage, a localization of the variable D is detected in the center of the sample testing region, where crack initiation have been observed during LCF experiments (see Fig.5.2). At sample level, several damaged elements are necessary to decrease the global reaction forces. In other words, the damage D has to propagate throughout several elements within the

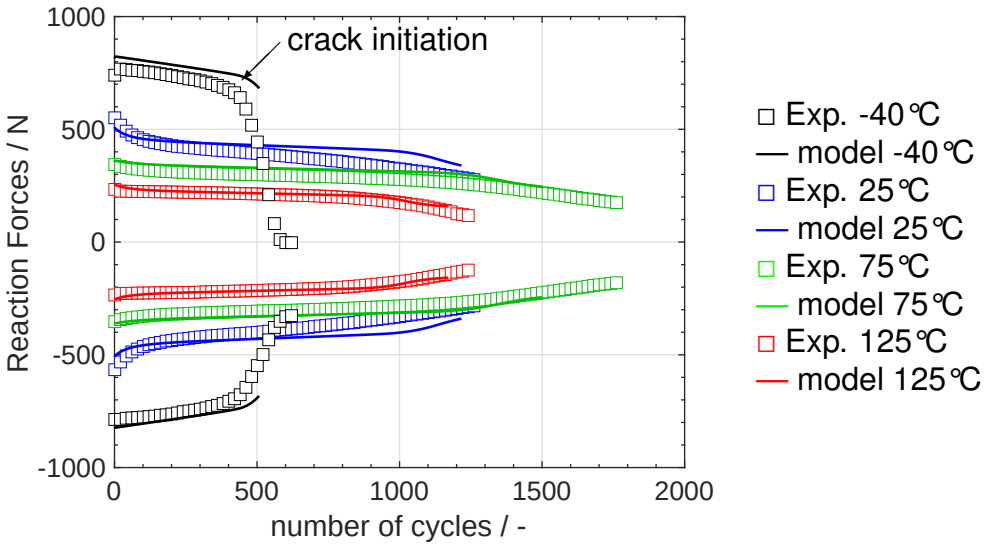

Fig. 5.1: Experiments and model prediction pf fatigue behavior during LCF tests in the temperature range -40 °C ... 125 °C: the decrease of Reaction Forces describes the observed cyclic stress softening

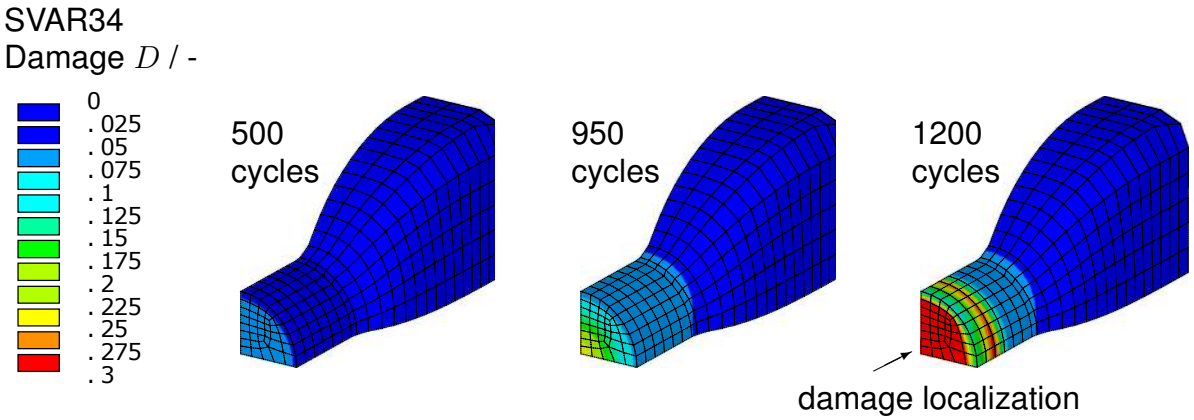

Fig. 5.2: Damage evolution and distribution within the testing sample: from $0 \ldots D_c$. $D_c = 0.3$ represents the damage value at failure. Example of simulation at 25 °C

test	T_{min}	T_{max}	T_{mean}	t_{rampe} heat/cool	t_h at T_{min}/T_{max}	$N_{f50,exp}$
TS1	-40℃	150℃	55℃	10s/10s	30min/30min	231
TS2	-40℃	125℃	42.5℃	10s/10s	30min/30min	454
TS3	-40℃	90℃	35℃	10s/10s	30min/30min	3018

Tab. 5.1: Experimental lifetime data of CR1206 solder joints from LiVe [1]

sample testing region. At -40℃, the force reduction is too fast to enable stress fall by damage propagation. Thus, instead of propagating, damage localizes within a small number of elements and barely affects the global reaction forces which results in a slower force decrease after crack initiation in the simulation. The effect can be visualized on Fig.5.2, where the damage localizes in the center of the sample instead of propagating throughout the testing region. Nevertheless, the FE simulation demonstrates the ability of the model to calculate stress softening in larger structure by using internal damage variables coupled into the material model. Despite the localization of damage which limits the transition of stress softening after crack initiation, a good correspondence is found between the distribution of damage Fig.5.2 and the aged microstructure after LCF testing, see Fig.3.20-3.22 in Chap.3 The adequate match in the stress softening curves Fig.5.1, and the damage distribution Fig.5.2 gives confidence that the damage properties are correctly described by the material model.

5.2. Chip resistor component CR1206

5.2.1. Lifetime assessment within creep-fatigue loads and temperature changes

As a next step, a simulation of reported experimental lifetime data of CR1206 chip resistor mounted on a free PCB substrate is presented [1]. After soldering, the samples have been submitted to temperature cycles using an oven equipped by two chambers system (Shock Test TS). The degradation of solder joints is evaluated using shear-tests. An end-of-life criterion has been defined by 50% of shear force reduction compared to the initial force needed to pull the resistor after fabrication [1]. The number of cycles at which the criterion is reached is defined as $N_{f50,exp}$ and reported in Table 5.1.

The thermo-mechanical loads on chip resistor solder joints are simulated by means of a 3D FE-simulation using a simplified geometry of the assembled chip component. In Fig.5.3 a 1/4 model of a CR1206 soldered to a FR4 board is depicted.

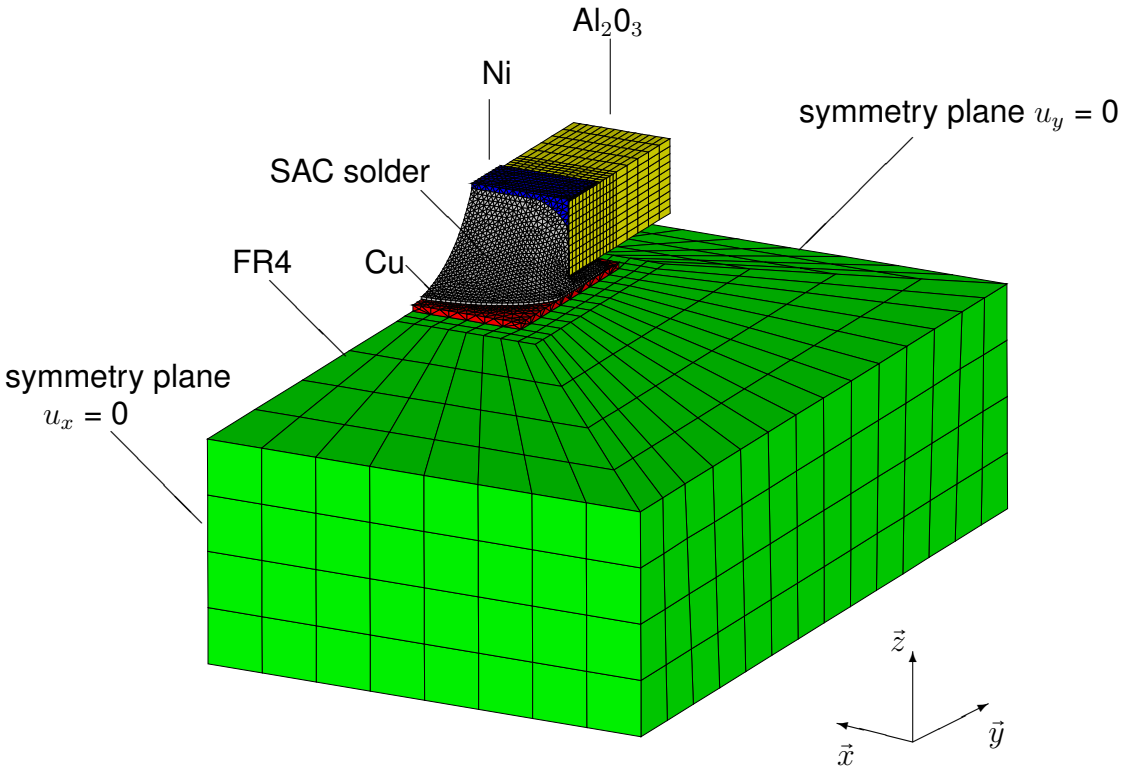

Fig. 5.3: $1/4^{th}$ FE model of a CR1206 mounted on a FR4 board

Material	E / MPa	ν / -	α_{CTE} $10^{-6}K^{-1}$ at 25°C	feature
Al_2O_3	340000	0.17	5.25	CTE temp. dependent
FR4	21093	0.35	13.7 (in $\vec{x}$ and $\vec{y}$) 32.5 in $\vec{z}$	visco-elastic temp. dependent
Cu	106000	0.34	16	linear elastic
Ni	206000	0.3	13	linear elastic

Tab. 5.2: Thermo-mechanical material parameters

In order to simplify the internal structure of the PCB, only the solder copper pad is designed such as the PCB is modeled by FR4 material only. Symmetry boundary conditions are applied on the two symmetry planes ensuring the free motion of the PCB, close to real testing conditions.

The solder material behavior is simulated using the developed viscoplastic damage law presented in the previous chapter together with the material parameters listed in Tab.4.7. Thermo-mechanical properties of the other materials involved are listed in Tab.5.2.

Prescribed temperature cycles are applied to the structure Fig.5.3. The stress-free temperature is defined at the soldering temperature T(soldering)=217°C in order to take into account the resulting internal stresses occurring after soldering. Thus,

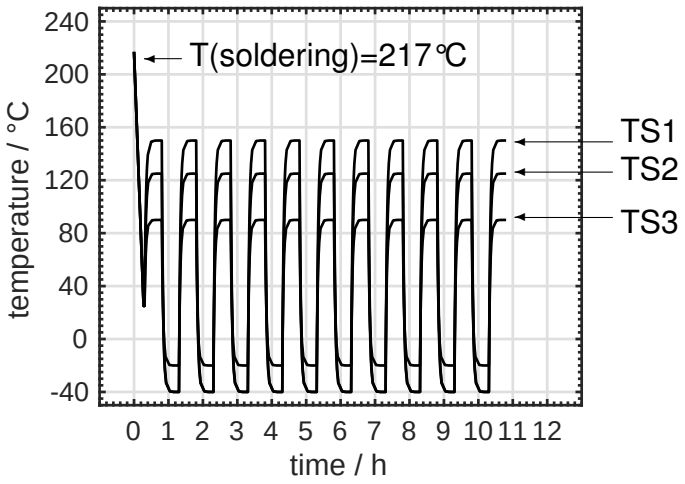

Fig. 5.4: Profiles of temperature applied to the FE-structure

the temperature swing is estimated being slow enough to neglect thermal gradients throughout the geometry, such as the same temperature is applied on every node of the structure within each time calculation step. Fig.5.4 shows the regime of temperature applied for 10 cycles which follows heating and cooling phases for a cycle duration of 60 minutes. Such a thermal profile is a reasonable estimation of the cooling and heating rates using typical testing-oven equipped with two separated temperature chambers [22].

The mismatch of the coefficient of thermal expansions of the neighboring components, e.g. Al2O3-chip and FR4-PCB (see Table 5.2), induces thermo-mechanical strains and stresses in the solder joint beyond its elastic limits. However, the mechanical loads are not homogeneously distributed throughout the solder volume, as it is suggested in Fig.5.5. First principal plastic strain and stress are evaluated in two positions, in the meniscus (Pos.1) and in the standoff region (Pos.2). A thin hysteresis is depicted in Pos.1, with plastic deformation below 0.15%. Besides, low stresses are evaluated at 125°C (under 1 MPa) at this position, indicating a rather low sensibility for creep damage. In contrast, larger hysteresis are observed at Pos.2 with higher stresses at both maximal and minimal temperature. In this case, the development of both creep and fatigue damage is expected. Although a strain drift is observed, stress and strain amplitudes remain nearly constant after the 6th cycle. Therefore, the 10th cycle can be assumed as stabilized and the related mechanical quantities calculated within this cycle can be used for lifetime prognosis purpose.

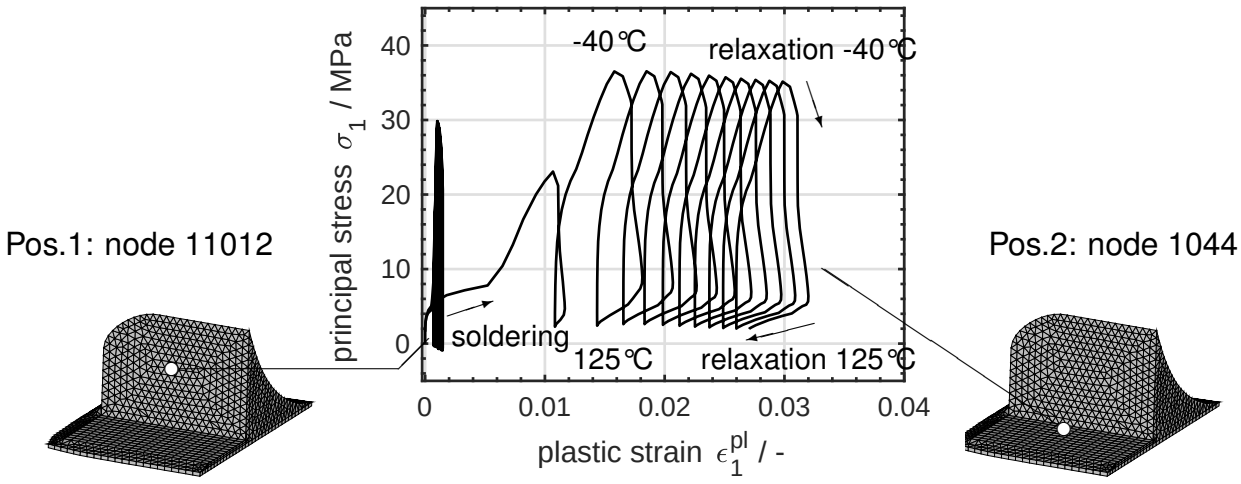

Fig. 5.5: Stress-strain hysteresis in two positions of the solder joint for the profile TS2

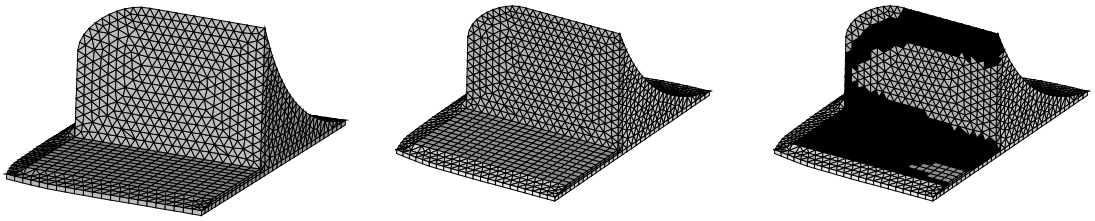

(a) total element volume of the solder joint

(b) selected critical volume for evaluation at the interface with the chip

(c) 50% most loaded element evaluated for TS1: -40/150°C

Fig. 5.6: Definition of solder volume for evaluation

Creep-fatigue partitioning lifetime concept

Because of the strong inhomogeneity of the mechanical loads on the solder joint, a volume averaging method is applied (see Fig.5.6(a)). It has the advantage to convert the mechanical quantities at every node into a global mean value representative for the solder joint. Besides, eventually appearing local singularities due to element shape and mesh topology are averaged out by weighting the element solution by the element volume. In this way, mesh dependency of the evaluation can be reduced. In correlation with the observed crack path in chip resistor solders, e.g. like in Fig.5.13, a critical volume at the interface solder/Chip is defined in Fig.5.6(b) which corresponds to the volume where cracks propagate when submitted to repeating temperature cycles.

The damage parameters are averaged over 50% of the most loaded elements

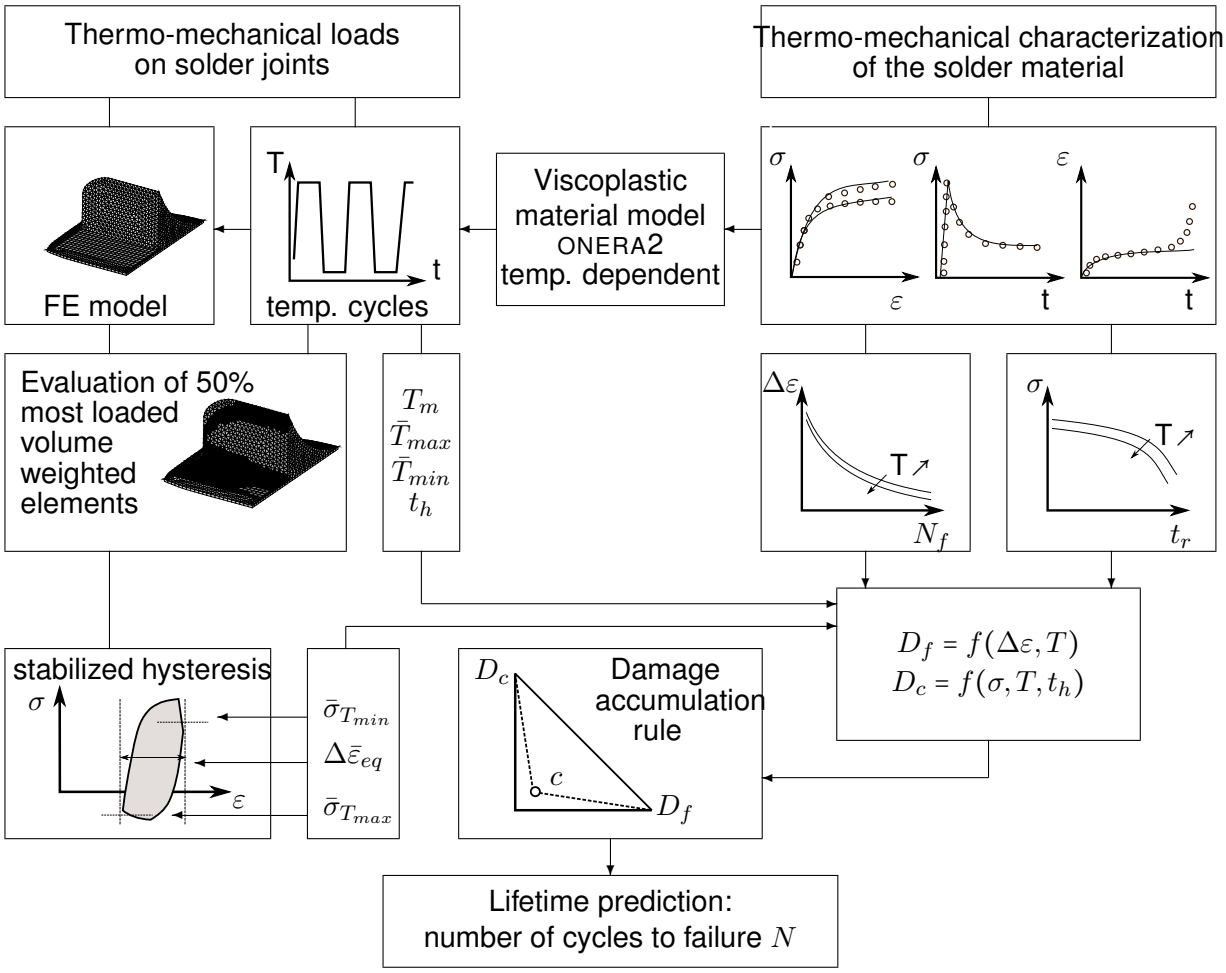

Fig. 5.7: Creep-fatigue partitioning lifetime concept for solder joints considering creep and fatigue loads under temperature cycles

within the critical volume. The ratio of 50% is related to the experimental shear force reduction of 50%, used as standard lifetime criterion for chip resistor solders tested within the LiVe project [1].The general equation for averaging a discretized field variable $F(i)$ over the volume V_{tot} discretized into element volumes i of infinitesimal volume $dV(i)$ is given by Eq.(5.1) Here, a ratio of 50% is defined.

$$\bar{F} = 0.5 \times \sum_{i=1}^{V=0.5V_{tot}} F(i)dV(i) \tag{5.1}$$

The total damage rate (per cycle) is calculated using Palmgren-Miner and Robinson accumulation rules, respectively, for fatigue and creep damage [65, 66] and [67].

The fatigue fraction life is derived from the strain range experienced during one cycle and obtained from the Coffin-Manson-Basquin Eq.(5.2). The creep fraction life

is derived from Larson-Miller time to rupture equation for a given stress and temperature and time exposition, see Eq.(5.6)-(5.7). However, the ASME method has to be adapted for thermo-mechanical loads in this case. On one hand, the temperature is constantly varying during the cycles, which raises the question at which temperature the fatigue damage has to be calculated, since the material parameters σ_f, E, b, ϵ_f, c are temperature dependent in the Eq.(5.2), (see Table 3.3 Chap.3). On the other hand, due to the viscoplastic behavior of the solder material, no constant stress is observed during the holding time periods but rather a stress relaxation occurs. Therefore, a constant stress cannot be determined and further used in the Larson-Miller equation, as it is originally proposed in the ASME guideline [61]. In order to deal with the viscoplastic behavior of the material and the resulting stress relaxation, a median equivalent stress is evaluated, as proposed by Rauch [27]. The lifetime concept is extended in order to take into account the temperature changes during the cycles. The mean temperature is evaluated as a reference temperature for the fatigue part. The median temperature in hot and cold phases is evaluated for the creep parts. The lifetime concept proposed in this work is depicted in a block diagram (see Fig.5.7). On the right side, the material characterization part is related to the mechanical and damage properties of the solder material. The viscoplastic properties are described using an ONERA2 material model implemented into user-routine for FE calculation. The damage properties are described by the damage functions of Coffin-Manson-Basquin and Larson-Miller, for fatigue and creep damage respectively. On the left side of Fig.5.7, a FE-thermo-mechanical simulation is performed. The mean and median temperatures are evaluated. The median stresses and strain amplitude of the hysteresis are averaged over 50% of the most loaded elements. Thus, a representative creep and fatigue damage D_c and D_f for one cycle is calculated, using the Coffin-Manson-Basquin fatigue life curves at T_{mean} (D_f) and the derived time to rupture curve from Larson-Miller creep parameter at $\bar{T}_{max}$ and $\bar{T}_{min}$ (D_c). Finally, the number of cycles to failure N of the component is calculated using a creep-fatigue damage accumulation rule. As far as the fatigue part is concerned, the von Mises equivalent strain range is evaluated within the 50% most loaded elements in the 10^{th} cycle. The material parameters of the fatigue life curve Eq.(5.2) are interpolated at the mean temperature of the test T_{mean} to calculate the number of cycles to failure N_f in case of pure fatigue loads.

$$\Delta\bar{\varepsilon}_{eq} = \frac{\sigma_f}{E}\left(N_f\right)^{-b} + \epsilon_f\left(N_f\right)^{-c} \tag{5.2}$$

The fatigue life curves in Fig.5.8(a) show a rather low sensibility to the temperature

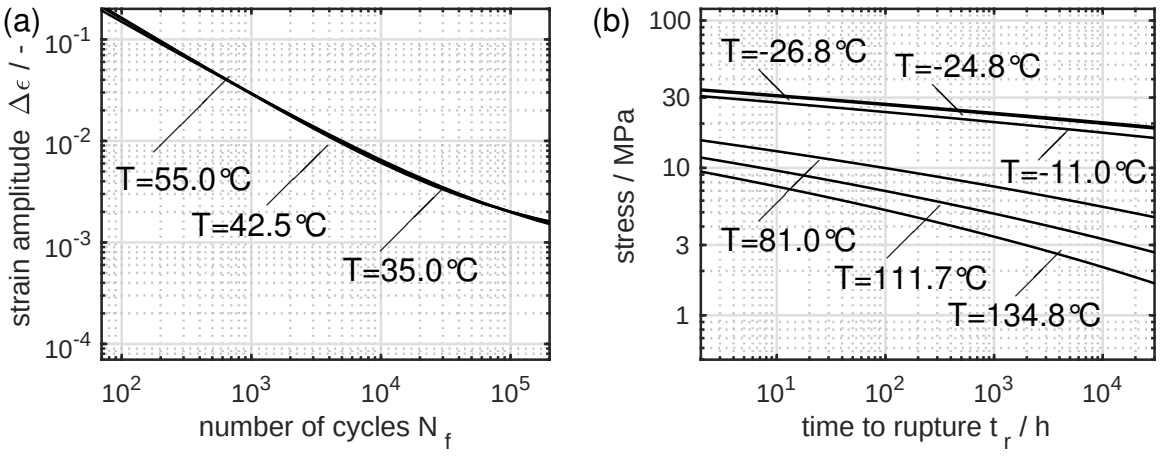

Fig. 5.8: (a) Coffin-Manson-Basquin fatigue curves at T_{mean} for SAC solder. (b) Larson-Miller derived time-to-rupture curves at $\bar{T}_{min,max}$ for SAC solder

in the range of the mean temperature T_{mean} investigated here. In contrast, the strain range has the main influence on the fatigue life N_f.

In order to calculate creep damage, the temperature is averaged during the hot and cold phases using Eq.(5.3)-(5.4). $\bar{T}_{min}$ and $\bar{T}_{max}$ represent the mean temperatures at which the solder is exposed during the holding time periods t_h. The time to rupture curves are evaluated at e.g. $\bar{T}_{min}$, $\bar{T}_{max}$, related to the median temperature in the experiments TS1, TS2 and TS3, see Fig.5.8(b).

$$\bar{T}_{min} = \frac{1}{t_h}\int_{t=t_1}^{t=t_1+t_h} T(t)dt \tag{5.3}$$

$$\bar{T}_{max} = \frac{1}{t_h}\int_{t=t_2}^{t=t_2+t_h} T(t)dt \tag{5.4}$$

The median first principal stress during the holding time is evaluated and defined as the equivalent stress leading to creep damage during stress relaxation. In order to take into account the multiaxial state of the stress, the hydrostatic stress σ_H is used to ensure that creep damage only accumulates under tensile situation ($\sigma_H > 0$), and avoids creep damage generation under compressed stress state.

$$\sigma_{1,med,\bar{T}_{min}/\bar{T}_{max}} = \frac{1}{t_h}\int_{t=t_{1,2}}^{t=t_{1,2}+t_h} \sigma_1(t)\frac{1}{2}\frac{\sigma_H(t)+|\sigma_H(t)|}{\sigma_H(t)}dt \tag{5.5}$$

The equivalent stress for 50% of the most damaged elements is the obtained by volume averaging using Eq.(5.1). The time to rupture t_r is calculated using the Larson-Miller equivalent creep damage parameter P_{LM}, which internal material pa-

test	$N_{f50,exp}$	T_{mean}	$\bar{T}_{max}$	$\bar{T}_{min}$	N_f cycles	$t_{r,\bar{T}_{min}}$ / h.	$t_{r,\bar{T}_{max}}$ / h.
TS1	231	55	134.8	-24.8	4229	556	52731
TS2	454	42.5	111.7	-26.8	5494	770	606060
TS3	3018	35	81.0	-11.0	14336	1108	9458100

Tab. 5.3: Creep and fatigue life damage parameters corresponding to the 3 Chip resistor experiments obtained by FE simulation and damage evaluation using Coffin-Manson-Basquin and Larson-Miller Eq.(5.1)-(5.6)-(5.7)

rameters have been determined by creep tests series in Chap.3.

$$t_{r,\bar{T}_{min}} = \exp\left(\frac{P_{LM}(\sigma_{1,med,\bar{T}_{min}})}{273+\bar{T}_{min}}+C\right) \tag{5.6}$$

$$t_{r,\bar{T}_{max}} = \exp\left(\frac{P_{LM}(\sigma_{1,med,\bar{T}_{max}})}{273+\bar{T}_{max}}+C\right) \tag{5.7}$$

The procedure for creep and fatigue evaluation is repeated for the LiVe experiments TS1, TS2 and TS3, see Tab.5.3.

For the 3 experiments TS1, TS2 and TS3, the main damage contribution results from creep accumulation at low temperature. At high temperature, large time to rupture are calculated, which is due to the fact that the meniscus region is under compression preventing any development of creep damage during the holding time period th. In contrast, tensile stresses at low temperature lead to creep damage and shorter time to rupture, see Fig.5.5. The life fraction consumed within one cycle regarding creep at low and high temperature is given by Eq.(5.8)-(5.9) and the life fraction consumed due to fatigue damage by Eq.(5.10).

$$D_{c,\bar{T}_{min}} = \frac{t_h}{t_{r,\bar{T}_{min}}} \tag{5.8}$$

$$D_{c,\bar{T}_{max}} = \frac{t_h}{t_{r,\bar{T}_{max}}} \tag{5.9}$$

$$D_f = \frac{1}{N_f} \tag{5.10}$$

Using a linear accumulation rule, the lifetime is determined by Eq.(5.10). The number of cycles obtained by simulation are listed in Tab.5.4. As expected, lifetime calculations obtained by linear accumulation rule are non-conservative, which is the case for the predictions of TS1 and TS2.

$$N = \frac{1}{D_f + D_{c,\bar{T}_{min}} + D_{c,\bar{T}_{max}}} \tag{5.11}$$

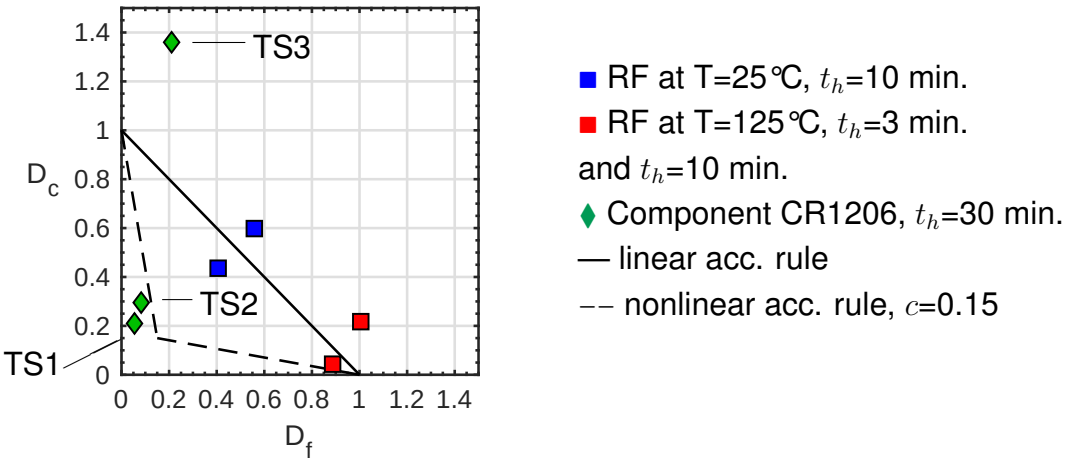

Fig. 5.9: Creep and fatigue damage fraction at $N_{f,exp}$ for the solder component CR1206 with 30 minutes dwell times.

In a second numerical study, a new lifetime calculation is performed, but instead of a linear rule, a nonlinear accumulation rule is employed. From the material characterization point of view, the Relaxation-Fatigue tests (RF) suggest a linear accumulation rule using Coffin-Manson and Larson-Miller damage parameters. On the opposite, a nonlinear rule gives a better match to the component experiments, using the same damage parameters, as illustrated in Fig.5.9. The diagram is constructed by evaluating the fraction of life consumed at $N_{f,exp}$ for the creep and fatigue parts, respectively. The experiments TS1 and TS2 are better predicted using a bilinear coefficient $c = 0.15$, giving in this case a larger accumulation of fatigue damage under creep dominated loads. The experiment TS3 has a creep life fraction $D_c > 1$, which means that creep damage alone would be responsible for failure without considering the accumulated fatigue life fraction. A nonlinear rule applied to TS3 predicts in this case an even more conservative lifetime in comparison with the experiment.

The number of cycles to failure N is calculated by Eq.(5.12)-(5.13) with nonlinear accumulation rule. For fatigue dominated loads, Eq.(5.12) is employed, and Eq.(5.13) for creep dominated loads. The parameter c refers to the inflection point in the bilinear rule Fig.5.9.

$$N = \frac{1}{D_f + \frac{1-c}{c}(D_{c,\bar{T}_{min}} + D_{c,\bar{T}_{max}})} \quad \text{if} \quad \frac{D_f}{D_c + D_f} > \frac{D_c}{D_c + D_f} \tag{5.12}$$

$$N = \frac{1}{\frac{1-c}{c}D_f + D_{c,\bar{T}_{min}} + D_{c,\bar{T}_{max}}} \quad \text{if} \quad \frac{D_f}{D_c + D_f} \leq \frac{D_c}{D_c + D_f} \tag{5.13}$$

test	$N_{f,50}$ from LiVe [1]	N pred. (linear rule)	N pred. (nonlinear rule) $c = 0.15$
TS1	231	873	444
TS2	454	1201	594
TS3	3018	1919	1181

Tab. 5.4: Predicted lifetimes of component solder joints using linear and nonlinear accumulation rule

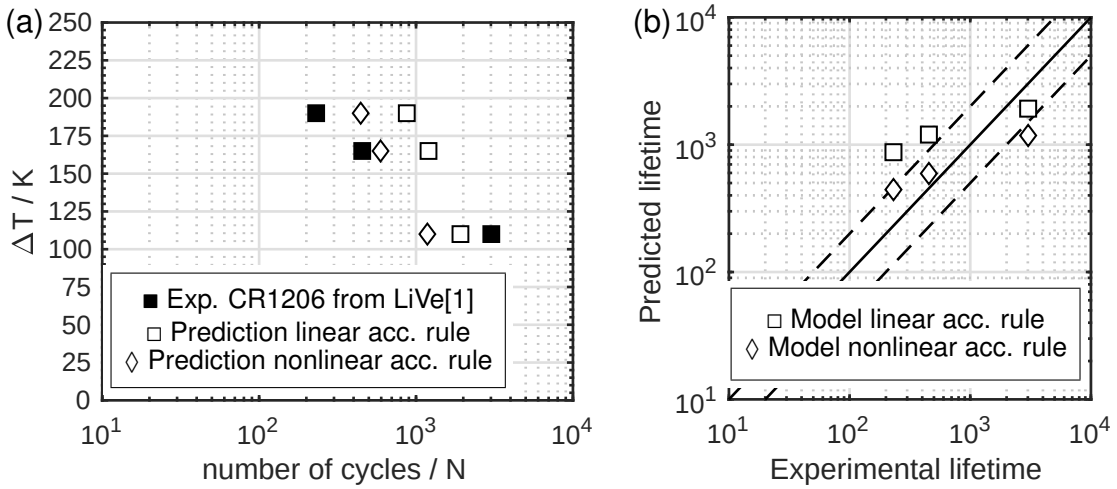

Fig. 5.10: (a) Lifetime prediction using linear and nonlinear (c=0.15) accumulation rule. (b) Quality of lifetime assessment with confidence intervals ($\times 2, \times 0.5$)

For the component experiments TS1, TS2 and TS3, N is calculated with Eq.(5.13) and the results listed in Tab.5.4.

Despite the nonlinear accumulation rule, still non-conservative lifetimes are calculated for TS1 and TS2, but closer to the experiments compared to the linear rule, see Fig.5.10(a). The nonlinear rule gives better results for the component lifetimes since TS1 and TS2 are inside the confidence intervals ($\times 2$, $\times 0.5$) and TS3 slightly outside this intervals ($\times 0.39$), see Fig.5.10(b). The deviation using the linear rule exceeds a factor of 3 for TS1. In the higher temperature amplitude regime, the deviation is rather non-conservative whereas a rather conservative prediction results for the lower temperature amplitude regime.

Assessment of the creep-fatigue partitioning lifetime concept

A lifetime concept has been worked out using a combination of FE simulations and failure predictions by superposition of creep and fatigue damage. The corresponding damage parameters are derived from the material characterization presented in Chap.3. The Coffin-Manson-Basquin curves at T_{mean} are used for evaluation of the

fatigue damage parameter D_f and a creep-rupture master curve derived from Larson-Miller equations serves for evaluation of the creep damage parameters $D_{c,\bar{T}_m in}$ and $D_{c,\bar{T}_{max}}$. In contrast, standard methods employed to diagnose the reliability of solder joint components make use of existing component lifetime data, which is used for a calibration of a lifetime model. Here, the joint-failure is calculated based on the creep and fatigue damage mechanisms resulting from the thermo-mechanical loads modeled in the FE-simulation. The concept remains independent on the component geometry and profile of temperature but depends only on the material properties of the solder alloy. For this, only standardized material testing data obtained under isothermal conditions has been used. The definition of most volume damaged element applied in this study corresponds to the failure criteria defined in the experimental tests. Creep and fatigue damage parameters are averaged over 50% of the most loaded volume weighted elements. The evaluation volume results at the interface chip-solder where typically cracks are experimentally observed and correlate well to the experimental shear force reduction of 50% defined as end-of-life criteria in the lifetime experiments [1]. However, further experimental and numerical investigations are necessary to completely understand the accumulation of creep-fatigue damages of solder joint materials. From the material point of view, the RF experiments on standardized samples and constant temperature indicate a rather linear accumulation. On the other hand, the component experiments are better predicted using a nonlinear rule, evaluated with the same damage parameters as in the RF experiments, but averaged on 50% of the most loaded elements. The overall strategy followed is based on a transfer from material level to component level evaluation, the latter including also a change in geometry and loading conditions. Here, material modeling and calibration are performed exclusively using mechanical tests at constant temperature (for the standardized samples) and later applied for components simulation under thermo-mechanical loads induced by temperature changes. Further, the ASME-lifetime concept is originally intended for crack initiation prediction only. Because solder joints reliability cannot be addressed by determination of crack initiation only, the original ASME concept had to be adapted for end-of-life prediction. Creep and fatigue damage parameters are not only evaluated onto the most critical element (which corresponds to crack initiation) whereas they are averaged on 50% of the most loaded elements, taking into account a global creep and fatigue damage parameters representative for solder joints end-of life. A different ratio can be related as well to the experimental 50% shear force reduction, which may not be valid for another solder geometry. Applying the methodology to other solder components

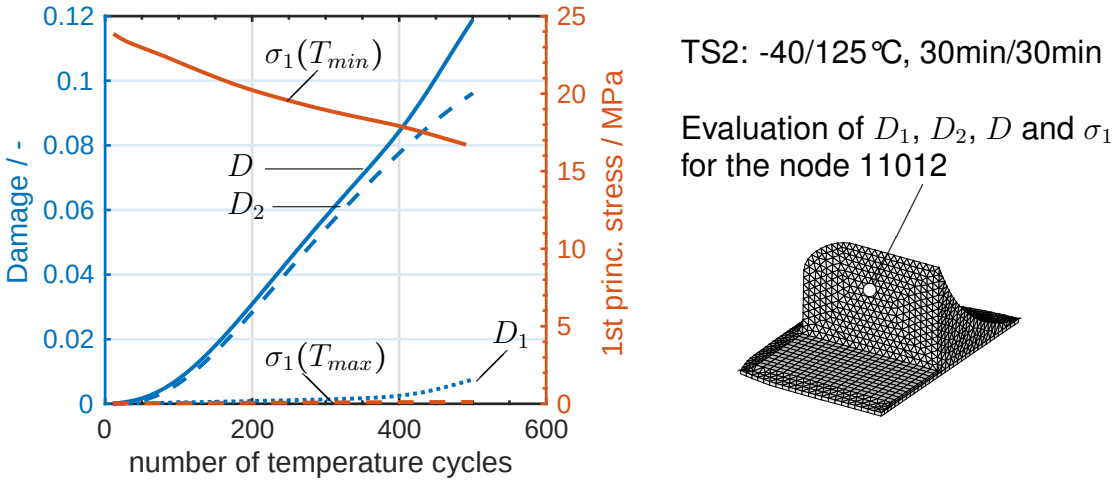

Fig. 5.11: Damage evolution and local stress softening for the node 11012 in the meniscus region

may validate the assumed evaluation strategy, and extend the universality of the proposed lifetime-concept. The volume definition should be transferable to any other solder geometry with respect to a common end-of-life criterion for the components. In the example provided within this work, the end-of-life criterion is established by 50% shear force reduction for the component CR1206.

5.2.2. Continuous Damage Mechanics (CDM) approach

The lifetime concept presented Fig.5.7 evaluates creep and fatigue damage parameters within a stabilized cycle and calculates the lifetime using Palmgren-Miner and Robinson's damage accumulation rule adapted for thermo-mechanical loads. However, the solder material shows a rather moderate softening behavior under repeating mechanical fatigue cycles but undergoes no stabilized stress-strain hysteresis in the temperature range investigated. An alternative strategy is proposed using the developed damage FE-material model in the present work which employs a simulation of all temperature cycles until end-of-Life. The experiment TS2 is taken as an example and 500 temperature cycles -40℃/125℃ of 30 minutes dwell time periods are repeatedly applied to the FE-structure represented on Fig.5.3. Fatigue and creep damage variables (D_1 and D_2) are continuously calculated during the simulation. The total damage D is locally determined in each time step, for all Gauss points of the solder joint material using a nonlinear accumulation rule. Damage and first principal stress are monitored and illustrated Fig.5.11 for a node in the center of the meniscus region.

The continuous decrease of the first principle stress at T_{min} (evaluated in each

cycle at the end of the relaxation) describes the softening behavior of the material occurring under thermo-mechanical loads. The stress decrease σ_1 results from the damage increase D due to the coupling of mechanical- and damage-equations of the material model. The stress decrease at T_{max} is hardly visible because of the stronger relaxation behavior at 125°C, such that the stress tends to 0 at the end of the dwell time period. The creep damage contributes at most to the total damage (90% creep ratio $D_2/(D_1 + D_2)$ after 500 cycles). The high stresses calculated during the low temperature regime are mainly responsible for D_2 steady evolution with the accumulation of temperature cycles which correlates with the results of the creep-fatigue lifetime concept described above. All over the cycles, D is larger than the sum of D_1 and D_2, illustrating the implicit nonlinear accumulation rule within the material model. Within the first 50 cycles, D shows a rather moderate increase and in the following stage from the 50^{th} up to the 400^{th} cycle a steady increase until it reaches $D = D_a = 0.09$. D_a represents the damage corresponding to crack initiation, and is defined as material parameter (see Chap.4). In the first 50 cycles, the damage rate is rather low, because the damage front concentrates in the standoff region and at the edge of the meniscus before reaching the center of the meniscus in Fig.5.12, where the evaluated node Fig.5.11 is located. After the crack initiation point for the node ($D = D_a$, N=400 cycles), the contribution of D_2 decreases as a consequence of the stress reduction. In parallel, the rate of D_1 increases indicating the effect of crack propagation. D_1-increase over-balances the D_2-decrease such that the total damage rate keeps increasing even after crack initiation. The creep and fatigue damage variables evolution indicates a complex interplay between the two damage mechanisms during the solder joint life. Before crack initiation, creep damage is preponderant under the influence of high stresses, suggesting damage development by formation of pores and growth of cavities. After crack initiation, the fatigue damage rate increases, describing a crack propagation facilitated by creep-pores previously formed in the already damaged microstructure. The damage evolution within the solder joint shows a concentration at the interface with the chip termination, as shown in Fig.5.12. This region correlates well to the most loaded volume elements used for evaluation in the creep-fatigue lifetime concept, see Fig.5.6. The simulation predicts a total degraded standoff before 100 cycles with a crack starting at the external edge of the standoff in (a). Under increasing cycles, the damage propagates through the standoff and concentrates at the interface with the chip-termination, and finally reaches the bottom corners at the inner plane in Fig.5.12 (b) and (c). Simultaneously, damage propagates towards the meniscus, parallel to the chip interface and reaches the top corner

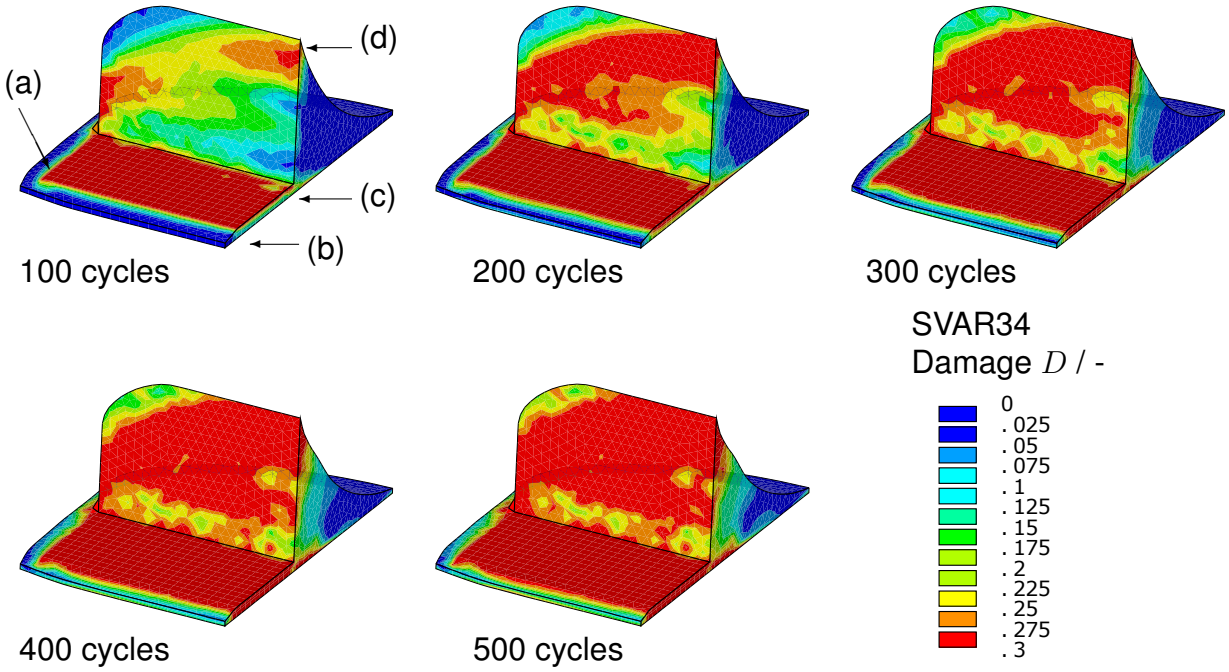

Fig. 5.12: Thermo-mechanical simulation of 500 temperature cycles -40/125 °C of solder joint chip-resistor soldered to a PCB (1/4-model). Distribution of damage variable D in the solder joint over the temperature cycles

of the meniscus inner-plane in (d). These regions correspond well to crack locations observed in real solder joints chip resistor 1206, as reported in [1] and by Dudek in [14], see Fig.5.13.

Typical failure mechanisms observed for solder joints chip resistors indicate two crack paths, as suggested in Fig.5.12. In a first stage, fast degradation is observed within the standoff region. Under progressing cycles number, cracks grow toward the meniscus region, from the top (d) to the bottom (c). These two crack paths correlate to the damage distribution and evolution depicted in Fig.5.12. In the simulation, the standoff completely cracks within the first 100 cycles whereas some damaged, but not fully cracked areas still remain in the meniscus region after 300 temperature cycles. The good correspondence between the damage variable evolution D (Fig.5.12) and observed degradation on real solder joints (Fig.5.13) shows the capability of the current phenomenological damage model to describe the failure mechanisms observed in a soldered chip resistor under thermo-mechanical cycles.

The Continuum Damage Mechanics (CDM) framework employed in the FE-simulation maps crack propagation by local damage evolution and softening of material regions. An explicit separation between mesh nodes and elements is not performed here since the mathematical equations remain only valid within a continuum

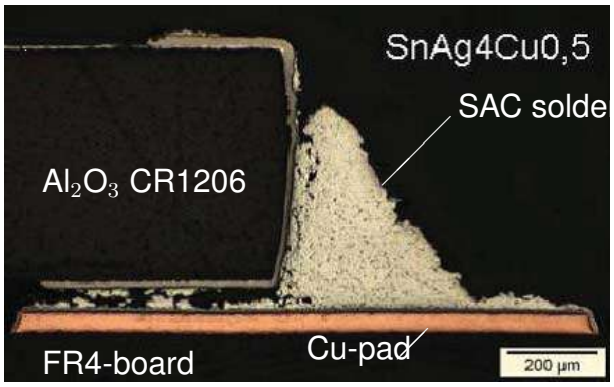

Fig. 5.13: Middle cross section of a solder joint chip resistor 1206 mounted on free FR4-board after 1000 temperature cycles $-40/125^{o}$C, from LiVe report [1]

environment. The degraded material regions obtain a local stiffness decrease over the element integration points p_i due to the accumulation of damage at these points $D(p_i)$. A local stiffness decrease of 50% for an individual integration point is obtained when the damage increases at this point up to $D(p_i) = D_c = 0.3$. The value for D_c results from the calibration on standardized LCF experiments like in Fig.5.1-5.2. The inhomogeneous damage distribution among the solder joint elements leads to an interaction and load transfer between damaged and undamaged elements. A three dimensional crack front can be interpreted as a volume composed by the elements, which have reached the critical damage $D(p_i) = D_c$. Selecting the same volume V_{tot} at the interface as in the lifetime concept (see Fig.5.6), the remaining crack-free normalized volume can be evaluated by Eq.(5.14) at the cycle N.

$$\bar{a}(N) = 1 - \frac{1}{V_{tot}} \sum dV_i(D = 0.3, N) \tag{5.14}$$

From the component experiments, the normalized shear force at the cycle N is obtained by Eq.(5.15) using the measurements reported in the LiVe-project [1].

$$\bar{F}(N) = \frac{F(N)}{F(N = 0)} \tag{5.15}$$

The Fig.5.14 compares the experimental shear force reduction and the remaining volume at the interface predicted by the simulation vs. the number of temperature cycles. The minimum and maximum values of shear forces centered on the mean value indicates an experimental scattering of ±-20% within the interval $0 \ldots 500$ cycles. The two quantities can be compared since they are normalized and by assuming an

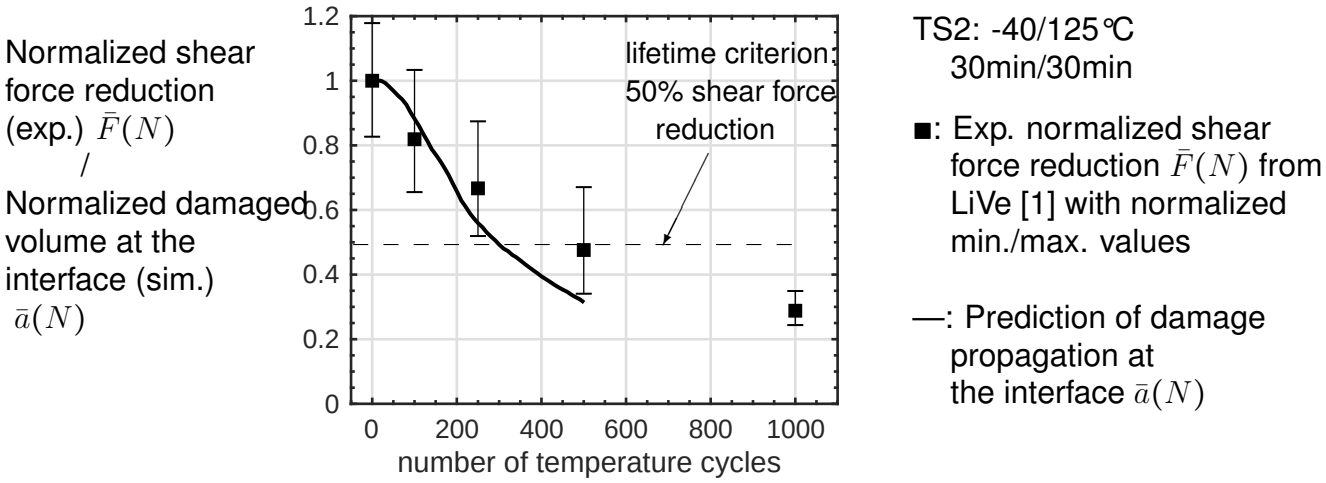

Fig. 5.14: Normalized experimental shear force reduction and predicted undamaged volume ratio at the interface obtained by FE-simulation

equal participation of the standoff and meniscus elements against the applied pull force during the shear tests of components.

The model follows not only the same trend as the experiments but also matches the normalized force reduction within the experimental scattering. The simulation deviates by 35% from the experimental mean value corresponding to the lifetime criterion of 50% shear force reduction. However, a better description is obtained during the first 200 cycles where the fastest shear force reduction is observed. The larger deviation from the experiments after 200 cycles can be explained by the 50% remaining stiffness of the cracked elements. The damage model enables a local stiffness decrease of 50% for the cracked elements whereas in reality a larger stiffness reduction might happen for the degraded regions. The elements of high damage variable values still contribute to some extend for a load transfer towards the solder geometry. Therefore, the surrounding less damaged elements might obtain higher local loads compared to reality, thus leading to faster damage propagation in the simulation. For the temperature profile TS2, a conservative end-of life of 295 cycles is simulated by the continuous damage model. The CDM approach shows not only the capability to resemble the most damaged region in solder joints but also to predict absolute number of cycles to failure close to the experimental end-of-life. The damage evolution is simulated throughout large number of temperature cycles, which gives insight to the specific crack propagation of the studied chip resistor solder geometry.

In summary, a lifetime concept and a CDM-method have been presented and applied to a chip resistor solder joint mounted onto a free PCB-board. The creep-fatigue partitioning approach calculates representative creep and fatigue damage parame-

ters based on a stabilized cycle, taking place in these examples between the 6^{th} and the 10^{th} simulated temperature cycle. The calculation of creep and fatigue damage parameters, which are the quantities used for lifetime prediction, is performed in a post-processing operation. The total computational cost of the simulation is rather low because it runs only until a stabilized cycle is reached. The method may be interesting for quick evaluation of solder joints reliability if no lifetime data for similar geometries are available. The prediction accuracy depends on the selected volume to be evaluated, which has to be chosen carefully according to the degradation stage of interest. The method enables a reliability engineer to pre-estimate the order of magnitude of temperature cycles leading to initial solder material degradation and plan accordingly the reliability tests on component level.

In order to overcome some of the issues mentioned above, a CDM-based simulation of large number of cycles has been performed. The evolution of damage within the solder joint during the temperature cycles is simulated by the damage material model. The results suggest crack propagation at the interface. The simulated damage locations correlate well to the cross section Fig.5.13 as well as the reported decrease of the experimental shear force (see Fig.5.14). The CDM approach presented in this thesis renders promising for calculations of absolute number of cycles to different degradation stages of solder joints. It should be noted, however, that the calculation of large number of temperature cycles of field loading conditions may pose a disadvantage in comparison to methods relying on extrapolation. In order to reduce time stepping influence and improve convergence, time and temperature increments have been kept low (eg. 250s or/and 8K) during the solution. Thus, the calculation of large cycle numbers becomes computationally intensive. However, the steady increase of computing capabilities could make the CDM approach attractive for industrial reliability analysis in the future, when complex geometry and loading conditions are involved.

6. Summary and outlook

In order to address reliability assessment of solder joints under temperature cycles, this work proposes a phenomenological approach developed on the basis of standardized isothermal creep and fatigue experiments. Under the well-defined loading conditions during material testing the deformation and degradation processes have been identified and quantitatively described in a constitutive FE-material model.

6.1. Mechanical-damage properties of SAC-solder alloy

Standardized experimental characterization has been realized using a testing setup for reversal cyclic tests and long-run creep tests, adapted to the requirements of solder materials. The mechanical properties of a SAC solder alloy are revealed by successive strain-rate variation sequences and stress relaxation experiments. The material exhibits complex viscoplastic behavior in the temperature range of -40 °C up to 125 °C under strain rates between 1×10^{-9} to 1×10^{-3} s^{-1}. The measurements are discussed in the context of the Ashby deformation maps describing the dependence of viscous exponents on different deformation mechanisms at the microstructure level [10]. In order to characterize the damage behavior, cyclic fatigue tests are conducted in the low and high cycle fatigue domains. The material shows a pronounced microstructure evolution of recrystallization processes identified on micrographs and supported by EBSD analysis. Fatigue testing at 125 °C results in a small granular structure and inter-crystalline crack propagation. In contrast, transcrystalline crack growth is observed at -40 °C, with no evidence of recrystallisation. Creep damage evolution during creep tests with large time to rupture ($t_r > 1000$ hours) under high temperatures reveal mixed-brittle fracture. EBSD analysis near the zone of fracture shows the presence of cavities with elongated shapes in the direction of loading, typical manifestation of creep damage in metals loaded under high homologous temperatures [49, 79]. Combined relaxation-fatigue tests show significant decrease of cyclic life when strain-controlled dwell-time periods are successively applied over the fatigue cycles. Finally, the last property of the material investigated within this work concerns the fatigue behavior under multiaxial loads. For this, tension-torsion cyclic

tests were realized until fatigue rupture, which indicate a moderate increase of lifetime under shear dominated fatigue loads. All tests serve to understand the mechanical behavior of the lead-free solder material and form the foundation for the formulation of a phenomenological material model, capable of describing the experimentally observed properties. Creep and fatigue damage are modeled using master-curve concepts. The analytic expressions of Larson and Miller as well as the Coffin-Manson-Basquin equations are employed to describe the creep time to rupture and number of cycles to failure under creep and fatigue conditions, respectively. Both models provide first indication of the material loading capability, if loaded under controlled testing conditions (e.g. constant temperature, strain amplitude, stress, etc...). The material behavior observed in the creep-viscoplasticity transition region suggests the need of two visco-functions to address the stress-strain and stress-time relations in the studied strain rate regime. The stress exponent varies from $m_1 = 0.095$ (viscoplastic) to $m_2 = 0.24$ (creep regime) at 25°C. Therefore, the ONERA2 model proposed originally by Chaboche [40] has been numerically implemented into FE-code and extended towards the continuum damage mechanics framework. The mathematical scheme for implementing the model within FE conformism is provided in detail, such as the reader has the possibility to implement FE-based ONERA2 model into similar FE-code. The material parameters are determined in a sequential manner beginning with those, which govern the deformation properties. The creep and fatigue damage properties are modeled by phenomenological formulations developed during this work. They map stress softening beyond crack initiation under fatigue conditions and include nonlinear damage accumulation under combined creep-fatigue. The simulations by the viscoplastic model achieves a very good description of the observed strain rate variations, secondary creep rate, stress relaxation, uniaxial and multiaxial shear fatigue within LCF regime, and tertiary creep stage. A good correspondence with the experiments is found with the provided set of parameters for 4 reference temperatures: -40°C, 25°C, 75°C and 125°C, which represents the relevant temperature range of operation of real solder joints for automotive applications. As a first real application of the model, a chip-resistor passive component attached to a FR4-substrate has been simulated under temperature cycles. The solder joint component lifetime is first estimated using a stabilized hysteresis. Damage parameters were derived from the master-curves established in Chapter 3 by using average mechanical stresses and strains over a defined volume. The creep-fatigue partitioning lifetime concept proposed in Chapter 5 constitutes an extension of the ASME-methodology, taking into account the thermally induced mechanical loads and by calculating sol-

der joints end-of-life instead of the number of cycles to crack initiation. The method is advantageous due to the low numerical effort necessary to estimate the solder component lifetimes. In contrast to the creep-fatigue partitioning method, the CDM-simulation worked out in this thesis gives direct access to the ongoing degradation of the solder joint throughout thermal cycling by means of a damage state variable. The simulated crack propagation paths correlate very well to observations of solder joint cross sections. By using the phenomenological CDM-approach, component lifetimes can be predicted by calculating specific material damage variables. This provides an a-priori lifetime prognosis without the usage of components lifetime data. The ability to predict the lifetime of a component based on the loading capability of its composed materials, in this case the solder material, under various external loading conditions constitutes the main advantage of the method. The model can be applied on different components and solder joint geometry types, for calculating the evolution of mechanical and damage properties on a local scale in the material. In this way, the degradation and mechanical softening of a specific solder joint can be simulated over a large number of thermal cycles which provides means to an absolute lifetime prediction. From an engineering point of view, the creep-fatigue partitioning approach provides a compromise between time calculation and accuracy, and would be interesting for preliminary design evaluation of new solder joint geometries. In the future, improvements of computer hardware could make the CDM approach even more attractive, by increasing the speed of calculation. Alternative methods e.g. cohesive zones or XFEM approaches are currently either not available in 3D FE-commercial codes or restricted to be used with linear elastic materials only, without taking into account viscoplasticity and creep effects. The CDM-approach can be realized in commercial FE codes, widely used in both research and industrial projects. It could position itself as a suitable method for simulation of degradation in ductile materials operating under high homologous temperatures, when creep and fatigue damage mechanisms are involved.

6.2. Further works and extension of the methodology

The experimental data analysis reveals moderate deviation over the samples tested. For the deformation properties, the deviation is estimated by 30% at 25 °C in the stress response, based on a statistic of three samples. For the creep experiments, only one sample has been tested for a given stress and temperature. The available creep data used to calibrate the damage model is not sufficient for quantitative calculation

of the experimental deviation in the time to rupture. Thus, further creep experiments are necessary in order to guarantee the correct description of creep damage within an experimentally derived confidence range. Additional creep experiments are particularly important since the model parameter analysis shows high sensitivity of the creep damage parameters which take part in the calculation of total damage. Further aspects in the modeling cover multiaxial loads, which have an impact on damage development as pointed out in [89]. Within this thesis, tension-torsion tests have been used to quantify the interaction for large coefficient q [88]. However, for smaller coefficients, where hydrostatic pressure prevails, no investigations have been reported yet. Future multiaxial experiments should further address pure cyclic torsion loads for large q coefficients, as well as combined tension and inner-pressure creep test, where $q < 1$ can be obtained [69], thus mapping the whole stress state domain in terms of multiaxiality.

Kuczynska et al. recently reported novel experimental procedure which aim to validate FE material models using combined thermo-mechanical fatigue tests (TMF) [90, 91], which realize loading conditions closer to real solder joint applications. This type of setup could provide an intermediate validation of the transferability of the methods from isothermal material samples to TMF-samples loaded by thermally induced mechanical loads. Furthermore, non-isothermal damage processes as creep-fatigue interaction could be observed by such TMF experiments, which are not accessible by an isothermal material characterization presented in this work. As far as the fatigue experiments are concerned, the HCF domain has not been extensively investigated except for 25°C. In power electronics modules soldered chips generate short current pulses, which induce local thermo-mechanical cyclic loads. In lab testing conditions, more than 100000 such power-cycles are needed to damage chip solder joints [5], which places the induced loads for solder joints in the HCF domain. The extension of both experiments and constitutive modeling to describe damage of the material towards the HCF domain may address reliability issues for chip solder joints under active power cycling. With a large number of lifetime thermal cycles involved, the question about computational efficiency is naturally raised. The current method has been applied on a simplified FE-geometry of 50000 elements and obtain the damage evolution throughout the first 500 cycles in a reasonable amount of calculation time. However, increasing both model size and number of cycles to be simulated before some damage occurs, would considerably increase the computational cost. This could potentially challenge the attractiveness of the proposed method. A short term alternative could be the utilization of extrapolation concepts within the damage

mechanics framework. Such methods have been proposed in [27] and later adapted for solder joints lifetime calculation in [77]. The FE calculation of the first cycles until steady state provides the accumulated cyclic damage rate. This quantity shows approximately a linear evolution over the cycles until crack initiation, enabling an extrapolation based approach in the lifetime evaluation. The technique would be as efficient as the creep-fatigue partitioning concept in terms of numerical effort, since the extrapolation is based on a stabilized cycle. The main advantages concern the temperature independency of the method and the ability to map the damage distribution throughout the complex geometry. The damage is calculated continuously during the temperature changes and over the structure which avoids the usage of the median stress or the assumption of a mean temperature for the estimation of the creep and fatigue damage parameters. Both are sources of approximations within the creep-fatigue partitioning concept presented in Chapter 5. Extrapolation techniques might need improvements to deal with numerical issues where cracks initiate in several locations as well as cases where crack propagation should be considered in order to calculate the component's end-of-life. A long term alternative and crucial step towards concerning end-of-life calculations can be achieved using the so called *Cycle-Jump* method in combination with the continuum damage mechanics framework. Basically, this technique makes it possible to calculate the damage state of a component without computing each individual cycle, which is supported by intermediate extrapolation steps [92]. Jump methods would shorten computation time of complex structures when large number of cycles are involved before failure occurs. Finally, numerical methods for reliability assessment of components are still under active research driven by industrial needs for acceleration of product development by FE-assisted lifetime calculations. The present work proposes a viscoplastic phenomenological damage model based on extended experimental characterization and contributes to the understanding of deformation and damage processes in solder materials. Nevertheless, improving the description of the material properties constitutes one aspect of a complete lifetime assessment methodology. For the application of the CDM- methods at large scale, numerical limitations have to be overcome in the future, in order to reduce calculation times of large structures. This could enable the complete end-of-life simulations even on system level, under both accelerated and field load conditions.

A. Appendix

A.1. EDX analysis, cross-section of SAC material

Spot (1)

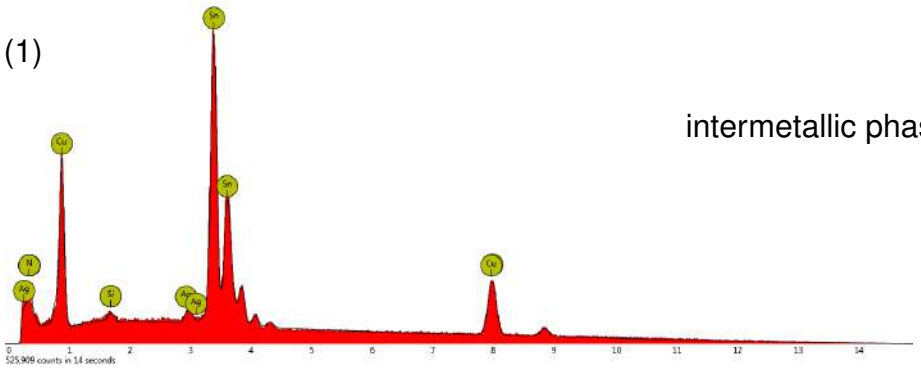

intermetallic phase Cu_6Sn_5

Spot (2)

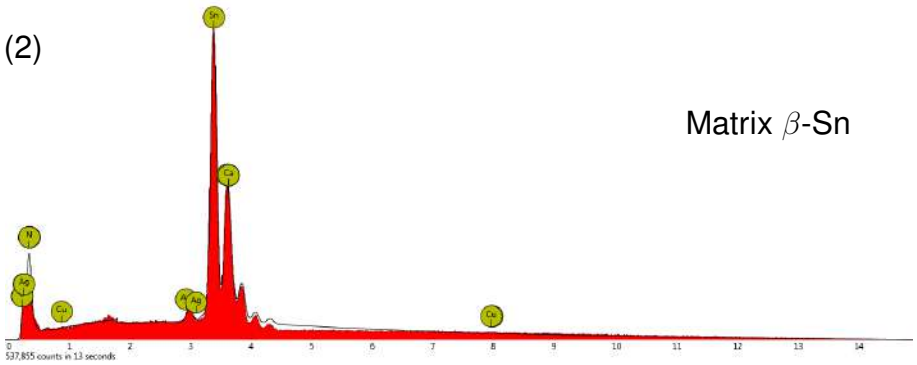

Matrix β-Sn

Spot (3)

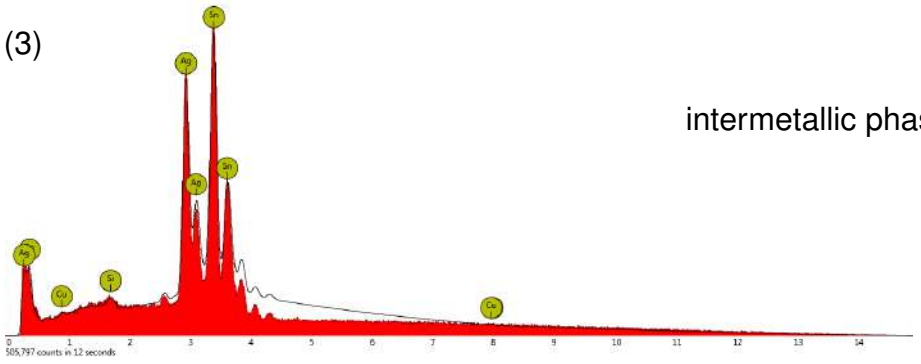

intermetallic phase Ag_3Sn

A.2. Experimental setup for tension-torsion (TT) tests

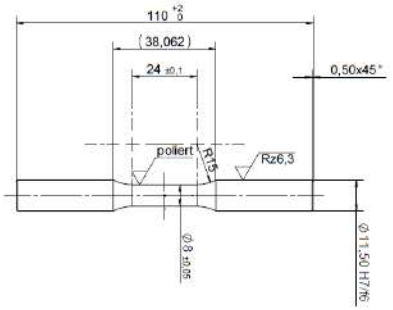

Sample geometry

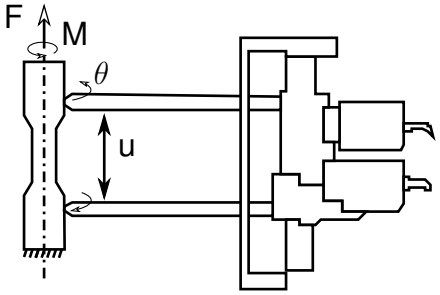

axial-tensorial extensometer

(a)
Fatigue test as reference
(b)
biaxial tension torsion test

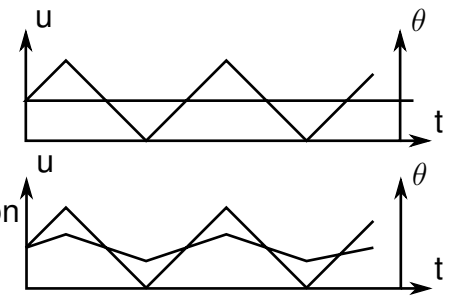

stress state in tension-torsion loads

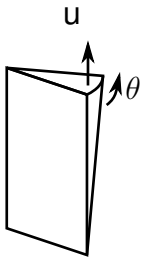

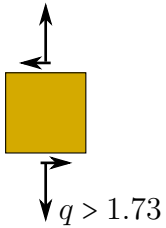

shape change dominated

triaxiality ratio q

$$q = \frac{1}{\sqrt{3}} \frac{\sigma_{eq}}{\sigma_H}$$

Expected distribution of q

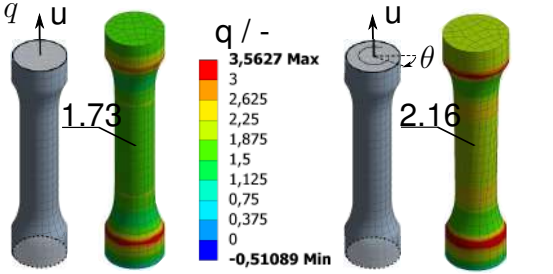

(a) u=24mm (b) u=20mm, θ=4°

for more details, see the corresponding publication [88]

A.3. J_2 operator [18], [81], [82], [83]

The material model respects the principle of incompressibility: any inelastic deformation induces an infinitesimal change of shape whereas no volume change is contracted. In other words, the plastic related variables are exclusively deviatorical. In consequence, the first invariant of these variables is equal to zero. For this reason, the second invariant is used to calculate the scalar associated variables of deviatorical quantities. Based on the second invariant, the algebra operator J_2 is used to transform the tensor variables into scalars which are equal to the tensor projection in the deviatoric plane. To put this definition within an equation, let us define X_{ij} and Y_{ij} two tensors, their scalar product is equal to

$$X_{ij} : Y_{ij} = X_{11}Y_{11} + X_{22}Y_{22} + X_{33}Y_{33} + 2 \times (X_{12}X_{12} + X_{23}X_{23} + X_{13}X_{13}) \tag{A.1}$$

Thus the deviatoric norm of this product is obtained by

$$\mathrm{J}_2(X_{ij} : Y_{ij}) = \sqrt{\frac{3}{2} X_{ij} : Y_{ij}} \tag{A.2}$$

As an example the von Mises stress σ_{eq} is calculated from the deviatoric stress S_{ij}

$$\sigma_{eq} = \mathrm{J}_2(S_{ij} : S_{ij}) \tag{A.3}$$

The mathematical formulation of the model and later its implementation refer to this operator with respect to the von Mises theory.

A.4. Intermediate calculation to obtain the local Newton-Raphson system of equations

The 5 equations for Newton-Raphson are

- equivalence through the deviatoric plane projection

$$f_1 = h + \alpha - Z_{eq} \tag{A.4}$$

- viscous stress

$$f_2 = \left(\frac{h - R}{K_1}\right)^{1/m_1} + \left(\frac{h - R}{K_2}\right)^{1/m_2} - \frac{\Delta \bar{\varepsilon}^p}{\Delta t} \tag{A.5}$$

- invariant 3 back stress terms

$$f_{i+2} = \mathrm{J}_2(X^{(i)}) - w_i M_i \qquad \text{for } i = 1 \dots 3 \tag{A.6}$$

Pivot variable starting values are for the 5 unknown:

- $\Delta\bar{\varepsilon}^p = \Delta\bar{\varepsilon}^{p,(0)}$: plastic strain increment
- $h = \sqrt{\frac{3}{2}(S^{tr} - X^{(n)}) : (S^{tr} - X^{(n)})}$: trial effective stress
- $J_2(X^{(i)}), i = 1 \dots 3$: second invariant for each back stress component

The trial deviatoric stress S^{tr} is obtained after the elastic predictor steps.f_2 results from the definition of viscous stress. In a similar way, f_3, f_4 and f_5 are obtained by definition of the second invariant of each back stress term. f_1 is obtained after reformulation of the back stresses:
back stress increment, $i = 1 \dots 3$, $X = \sum_{i=1}^{3} X^{(i)}$

$$\Delta X^{(i)} = c_i \Delta\bar{\varepsilon}^p \frac{S - X}{h} - \gamma_i \phi \Delta\bar{\varepsilon}^p X^{(i)} - \Delta t d_i \, \mathrm{J}_2(X^{(i)}) X^{(i)} \tag{A.7}$$

$$X^{(i)} = \Delta X^{(i)} + X^{(i),n} \qquad \text{and after factorisation} \tag{A.8}$$

$$X^i = w_i (c_i \Delta\bar{\varepsilon}^p \frac{S - X}{h} + X^{(i),n}) \qquad \text{for } w_i \text{ see Eq.A.16} \tag{A.9}$$

set-up consistency with plastic correction

$$S = S^{tr} - 3\mu \Delta\bar{\varepsilon}^p \frac{S - X}{h} \tag{A.10}$$

$$S - X = S^{tr} - \sum_{i=1}^{3} w_i X^{(i),n} - \Delta\bar{\varepsilon}^p \frac{S - X}{h} (3\mu + \sum_{i=1}^{3} w_i c_i) \tag{A.11}$$

after factorization with α defined in Eq.A.19 and Z in Eq.A.22

$$(S - X)(1 + \frac{\alpha}{h}) = Z \tag{A.12}$$

finally, applying J_2 on both side of Eq.A.12, f_1 is deduced

$$h + \alpha = Z_{eq} \tag{A.13}$$

for f_3, f_4 and f_5 one starts with Eq.A.9 and using the flow rule equality $\frac{S - X}{h} = \frac{Z}{Z_{eq}}$ for the other terms and their derivatives:

ϕ function

$$\phi = \phi_\infty + (1-\phi_\infty)\exp(-b_k(\varepsilon^p_{acc} + \Delta\bar{\varepsilon}^p) \tag{A.14}$$

$$\frac{d\phi}{d\Delta\bar{\varepsilon}^p} = -b_k(1-\phi_\infty)\exp(-b_k(\varepsilon^p_{acc} + \Delta\bar{\varepsilon}^p)) \tag{A.15}$$

back stress recovery, $i = 1\ldots3$

$$w_i = \frac{1}{1+\gamma_i\Delta\bar{\varepsilon}^p\phi + \Delta t d_i\,\mathrm{J}_2(X^{(i)})} \tag{A.16}$$

$$\frac{dw_i}{d\Delta\bar{\varepsilon}^p} = -(\gamma_i\phi + \gamma_i\Delta\bar{\varepsilon}^p\frac{d\phi}{d\Delta\bar{\varepsilon}^p})(w_i)^2 \tag{A.17}$$

$$\frac{dw_i}{d\,\mathrm{J}_2(X^{(i)})} = -\Delta t d_i (w_i)^2 \tag{A.18}$$

equivalent deviatoric part, first term

$$\alpha = (3\mu + \sum_{i=1}^{3} w_i c_i)\Delta\bar{\varepsilon}^p \tag{A.19}$$

$$\frac{d\alpha}{d\Delta\bar{\varepsilon}^p} = 3\mu + \sum_{i=1}^{3} w_i c_i + \Delta\bar{\varepsilon}^p \sum_{i=1}^{3}\frac{dw_i}{d\Delta\bar{\varepsilon}^p}c_i \tag{A.20}$$

$$\frac{d\alpha}{d\,\mathrm{J}_2(X^{(i)})} = \Delta\bar{\varepsilon}^p c_i \frac{dw_i}{d\,\mathrm{J}_2(X^{(i)})} \qquad \text{for } i = 1\ldots3 \tag{A.21}$$

vector deviatoric part

$$Z_{kl} = S^{tr}_{ij} - \sum_{i=1}^{3} w_i X^{(i),n} \tag{A.22}$$

$$\frac{dZ_{kl}}{d\Delta\bar{\varepsilon}^p} = -\sum_{i=1}^{3}\frac{dw_i}{d\Delta\bar{\varepsilon}^p}X^{(i),n} \tag{A.23}$$

$$\frac{dZ_{kl}}{d\,\mathrm{J}_2(X^{(i)})} = -\frac{dw_i}{d\,\mathrm{J}_2(X^{(i)})}X^{(i),n} \qquad \text{for } i = 1\ldots3 \tag{A.24}$$

equivalent deviatoric part, second term

$$Z_{eq} = \mathrm{J}_2(Z_{kl} : Z_{kl}) \tag{A.25}$$

$$\frac{dZ_{eq}}{d\Delta\bar{\varepsilon}^p} = \frac{3}{2}\frac{1}{Z_{eq}}Z_{kl} : \frac{dZ_{kl}}{d\Delta\bar{\varepsilon}^p} \tag{A.26}$$

$$\frac{dZ_{eq}}{d\,\mathrm{J}_2(X^{(i)})} = \frac{3}{2}\frac{1}{Z_{eq}}Z_{kl} : \frac{dZ_{kl}}{d\,\mathrm{J}_2(X^{(i)})} \qquad \text{for } i = 1\ldots3 \tag{A.27}$$

plastic flow rule direction $\vec{n}_{kl}$

$$\vec{n}_{kl} = \frac{Z_{kl}}{Z_{eq}} \tag{A.28}$$

$$\frac{d\vec{n}_{kl}}{d\Delta\bar{\varepsilon}^p} = \frac{Z_{eq}\dfrac{Z_{kl}}{d\Delta\bar{\varepsilon}^p} - Z_{kl}\dfrac{dZ_{eq}}{d\Delta\bar{\varepsilon}^p}}{(Z_{eq})^2} \tag{A.29}$$

$$\frac{d\vec{n}_{kl}}{d\,\mathrm{J}_2(X^{(i)})} = \frac{Z_{eq}\dfrac{Z_{kl}}{d\,\mathrm{J}_2(X^{(i)})} - Z_{kl}\dfrac{dZ_{eq}}{d\,\mathrm{J}_2(X^{(i)})}}{(Z_{eq})^2} \quad \text{for } i = 1\ldots3 \tag{A.30}$$

isotropic hardening

$$R = \sigma_0 + Q\left(1 - \exp(-b_q(\varepsilon^p_{acc} + \Delta\bar{\varepsilon}^p))\right) \tag{A.31}$$

$$\frac{dR}{d\Delta\bar{\varepsilon}^p} = b_q Q \exp(-b_q(\varepsilon^p_{acc} + \Delta\varepsilon^p)) \tag{A.32}$$

static recovery

$$M_i = \sqrt{\mathrm{J}_2(X^{(i),n})^2 + 3\Delta\bar{\varepsilon}^p X^{(i),n} : \vec{n} + (c_i\Delta\bar{\varepsilon}^p)^2} \quad \text{for } i = 1\ldots3 \tag{A.33}$$

$$\frac{dM_i}{d\Delta\bar{\varepsilon}^p} = \frac{1}{2M_i}\left(3c_i(X^{(i),n} : \vec{n} + \Delta\bar{\varepsilon}^p X^{(i),n} : \frac{d\vec{n}}{d\Delta\bar{\varepsilon}^p}) + 2\Delta\bar{\varepsilon}^p(c_i)^2\right) \quad \text{for } i = 1\ldots3 \tag{A.34}$$

$$\frac{dM_i}{d\,\mathrm{J}_2(X^{(j)})} = \frac{1}{2M_i}\left(3c_i\Delta\bar{\varepsilon}^p\frac{d\vec{n}}{d\,\mathrm{J}_2(X^{(j)})} : X^{(i),n}\right) \quad \text{for } i = 1\ldots3 \text{ and } j = 1\ldots3 \tag{A.35}$$

Derivatives of f_i functions needed for the Jacobian Matrix $\mathbb{J}$

Derivatives of f_1

$$\frac{df_1}{d\Delta\bar{\varepsilon}^p} = \frac{d\alpha}{d\Delta\bar{\varepsilon}^p} - \frac{dZ_{eq}}{d\Delta\bar{\varepsilon}^p} \tag{A.36}$$

$$\frac{df_1}{dh} = 1 \tag{A.37}$$

$$\frac{df_1}{d\,\mathrm{J}_2(X^{(i)})} = \frac{d\alpha}{d\,\mathrm{J}_2(X^{(i)})} - \frac{dZ_{eq}}{d\,\mathrm{J}_2(X^{(i)})} \quad \text{for } i = 1\ldots3 \tag{A.38}$$

Derivatives of f_2

$$\frac{df_2}{d\Delta\bar{\varepsilon}^p} = -\frac{1}{m_1K_1}\frac{dR}{d\Delta\bar{\varepsilon}^p}\left(\frac{h-R}{K_1}\right)^{1/m_1-1} - \frac{1}{m_2K_2}\frac{dR}{d\Delta\bar{\varepsilon}^p}\left(\frac{h-R}{K_2}\right)^{1/m_2-1} - \frac{1}{\Delta t} \tag{A.39}$$

$$\frac{df_2}{dh} = \frac{1}{m_1K_1}\left(\frac{h-R}{K_1}\right)^{1/m_1-1} + \frac{1}{m_2K_2}\left(\frac{h-R}{K_2}\right)^{1/m_2-1} \tag{A.40}$$

$$\frac{df_2}{d\,\mathrm{J}_2(X^{(i)})} = 0 \quad \text{for } i = 1\ldots3 \tag{A.41}$$

Derivatives of f_3

$$\frac{df_3}{d\Delta\bar{\varepsilon}^p} = -\frac{dw_1}{d\Delta\bar{\varepsilon}^p}M_1 - w_1\frac{dM_1}{d\Delta\bar{\varepsilon}^p} \tag{A.42}$$

$$\frac{df_3}{dh} = 0 \tag{A.43}$$

$$\frac{df_3}{d\,\mathrm{J}_2(X^{(1)})} = 1 - \frac{dw_1}{d\,\mathrm{J}_2(X^{(1)})}M_1 - w_1\frac{dM_1}{d\,\mathrm{J}_2(X^{(1)})} \tag{A.44}$$

$$\frac{df_3}{d\,\mathrm{J}_2(X^{(2)})} = -w_1\frac{dM_1}{d\,\mathrm{J}_2(X^{(2)})} \tag{A.45}$$

$$\frac{df_3}{d\,\mathrm{J}_2(X^{(3)})} = -w_1\frac{dM_1}{d\,\mathrm{J}_2(X^{(3)})} \tag{A.46}$$

Derivatives of f_4

$$\frac{df_4}{d\Delta\bar{\varepsilon}^p} = -\frac{dw_2}{d\Delta\bar{\varepsilon}^p}M_2 - w_2\frac{dM_2}{d\Delta\bar{\varepsilon}^p} \tag{A.47}$$

$$\frac{df_4}{dh} = 0 \tag{A.48}$$

$$\frac{df_4}{d\,\mathrm{J}_2(X^{(1)})} = -w_2\frac{dM_2}{d\,\mathrm{J}_2(X^{(1)})} \tag{A.49}$$

$$\frac{df_4}{d\,\mathrm{J}_2(X^{(2)})} = 1 - \frac{dw_2}{d\,\mathrm{J}_2(X^{(2)})}M_2 - w_2\frac{dM_2}{d\,\mathrm{J}_2(X^{(2)})} \tag{A.50}$$

$$\frac{df_4}{d\,\mathrm{J}_2(X^{(3)})} = -w_2\frac{dM_2}{d\,\mathrm{J}_2(X^{(3)})} \tag{A.51}$$

Derivatives of f_5

$$\frac{df_5}{d\Delta\bar{\varepsilon}^p} = -\frac{dw_3}{d\Delta\bar{\varepsilon}^p}M_3 - w_3\frac{dM_3}{d\Delta\bar{\varepsilon}^p} \tag{A.52}$$

$$\frac{df_5}{dh} = 0 \tag{A.53}$$

$$\frac{df_5}{d\,\mathrm{J}_2(X^{(1)})} = -w_3\frac{dM_3}{d\,\mathrm{J}_2(X^{(1)})} \tag{A.54}$$

$$\frac{df_5}{d\,\mathrm{J}_2(X^{(2)})} = -w_3\frac{dM_3}{d\,\mathrm{J}_2(X^{(2)})} \tag{A.55}$$

$$\frac{df_5}{d\,\mathrm{J}_2(X^{(3)})} = 1 - \frac{dw_3}{d\,\mathrm{J}_2(X^{(3)})}M_3 - w_3\frac{dM_3}{d\,\mathrm{J}_2(X^{(3)})} \tag{A.56}$$

Jacobian matrix $\mathbb{J}$ for N-R procedure, see Eq.4.29, chap.4.

$$\mathbb{J} = \begin{bmatrix} \frac{df_1}{d\Delta\bar{\varepsilon}^p} & \frac{df_1}{dh} & \frac{df_1}{d\,\mathrm{J}_2(X^{(1)})} & \frac{df_1}{d\,\mathrm{J}_2(X^{(2)})} & \frac{df_1}{d\,\mathrm{J}_2(X^{(3)})} \\ \frac{df_2}{d\Delta\bar{\varepsilon}^p} & \frac{df_2}{dh} & \frac{df_2}{d\,\mathrm{J}_2(X^{(1)})} & \frac{df_2}{d\,\mathrm{J}_2(X^{(2)})} & \frac{df_2}{d\,\mathrm{J}_2(X^{(3)})} \\ \frac{df_3}{d\Delta\bar{\varepsilon}^p} & \frac{df_3}{dh} & \frac{df_3}{d\,\mathrm{J}_2(X^{(1)})} & \frac{df_3}{d\,\mathrm{J}_2(X^{(2)})} & \frac{df_3}{d\,\mathrm{J}_2(X^{(3)})} \\ \frac{df_4}{d\Delta\bar{\varepsilon}^p} & \frac{df_4}{dh} & \frac{df_4}{d\,\mathrm{J}_2(X^{(1)})} & \frac{df_4}{d\,\mathrm{J}_2(X^{(2)})} & \frac{df_4}{d\,\mathrm{J}_2(X^{(3)})} \\ \frac{df_5}{d\Delta\bar{\varepsilon}^p} & \frac{df_5}{dh} & \frac{df_5}{d\,\mathrm{J}_2(X^{(1)})} & \frac{df_5}{d\,\mathrm{J}_2(X^{(2)})} & \frac{df_5}{d\,\mathrm{J}_2(X^{(3)})} \end{bmatrix} \tag{A.57}$$

A.5. Derivatives to obtain the tangent operator

The Tangent operator $\mathbb{C}^p$ is calculated using Eq.4.45. In this equation, the terms $\frac{d\Delta\bar{\varepsilon}^p}{d\varepsilon_{kl}}$ (vector $[1\times 6]$) and $\frac{d\vec{n}_{ij}}{d\varepsilon_{kl}}$ (matrix $[6\times 6]$) should be evaluated. The reduction of variables leads to the system of equation Eq.4.47. For this, the theorem of the total derivative (a particular case of the theorem of Lie) is referred:
The total derivative is the derivative with respect to t *of the function* $y = f(t, u_1, \ldots, u_n)$ *that depends on the variable* t *not only directly but also via the intermediate variables* $u_1 = u_1(t, u_1, \ldots, u_n) \ldots, \quad u_n = u_n(t, u_1, \ldots, u_n)$*. It can be calculated using*

$$\frac{\partial y}{\partial t} = \frac{\partial f}{\partial t} + \frac{\partial f}{\partial u_1}\frac{\partial u_1}{\partial t} + \cdots + \frac{\partial f}{\partial u_m}\frac{\partial u_m}{\partial t} \tag{A.58}$$

The partial derivative $\partial()$ are replaced by the Euler derivative $d()$ in the following.
Derivation left term in Eq.4.47: f_1

$$\frac{df_1}{dS^{tr}} = -\frac{3}{2}\frac{Z}{Z_{eq}} \tag{A.59}$$

$$\frac{dS^{tr}}{d\varepsilon_{kl}} = \mu(\delta_{ik}\delta_{jl} + \delta_{il}\delta_{jk}) - \frac{2}{3}\mu\delta_{ij}\delta_{kl} \tag{A.60}$$

$$\frac{df_1}{d\varepsilon_{kl}} = -3\mu\frac{Z_{kl}}{Z_{eq}} \tag{A.61}$$

Derivation f_2

$$\frac{df_2}{d\varepsilon_{kl}} = 0 \tag{A.62}$$

Derivation f_3

$$\frac{df_3}{dS^{tr}}\frac{dS^{tr}}{d\varepsilon_{kl}} = \frac{-3\mu w_1 c_1 \Delta\bar{\varepsilon}^p}{M_1(Z_{eq})^2}\left(Z_{eq}X^{(1),n} - \frac{3}{2}\frac{Z:X^{(1),n}}{Z_{eq}}Z\right) \tag{A.63}$$

Derivation f_4

$$\frac{df_4}{dS^{tr}}\frac{dS^{tr}}{d\varepsilon_{kl}} = \frac{-3\mu w_2 c_2 \Delta\bar{\varepsilon}^p}{M_2(Z_{eq})^2}\left(Z_{eq}X^{(2),n} - \frac{3}{2}\frac{Z:X^{(2),n}}{Z_{eq}}Z\right) \tag{A.64}$$

Derivation f_5

$$\frac{df_5}{dS^{tr}}\frac{dS^{tr}}{d\varepsilon_{kl}} = \frac{-3\mu w_3 c_3 \Delta\bar{\varepsilon}^p}{M_3(Z_{eq})^2}\left(Z_{eq}X^{(3),n} - \frac{3}{2}\frac{Z:X^{(3),n}}{Z_{eq}}Z\right) \tag{A.65}$$

Then the 5 unknown $\frac{\Delta\bar{\varepsilon}^p}{d\varepsilon_{kl}}$, $\frac{h}{d\varepsilon_{kl}}$, $\frac{\mathrm{J}_2(X^{(1)})}{d\varepsilon_{kl}}$, $\frac{\mathrm{J}_2(X^{(2)})}{d\varepsilon_{kl}}$ and $\frac{\mathrm{J}_2(X^{(3)})}{d\varepsilon_{kl}}$ are determined by multiplying the inverse of the Jacobian matrix $\mathbb{J}^{-1}$ by the pivot vector with the components Eq.A.60-A.65 solving the system Eq.4.47

Derivation of Z_{eq}

$$Z_{eq} = h + \alpha \tag{A.66}$$

$$\begin{aligned}\frac{dZ_{eq}}{d\varepsilon_{kl}} =& \frac{dh}{d\varepsilon_{kl}} + \frac{d\alpha}{d\Delta\bar{\varepsilon}^p}\frac{d\Delta\bar{\varepsilon}^p}{d\varepsilon_{kl}} + \frac{d\alpha}{d\,\mathrm{J}_2(X^{(1),n})}\frac{d\,\mathrm{J}_2(X^{(1),n})}{d\varepsilon_{kl}} + \\ & \frac{d\alpha}{d\,\mathrm{J}_2(X^{(2),n})}\frac{d\,\mathrm{J}_2(X^{(2),n})}{d\varepsilon_{kl}} + \frac{d\alpha}{d\,\mathrm{J}_2(X^{(3),n})}\frac{d\,\mathrm{J}_2(X^{(3),n})}{d\varepsilon_{kl}}\end{aligned} \tag{A.67}$$

Derivation of Z

$$Z = S^{tr} - \sum_{i=1}^{3} w_i X^{(i),n} \tag{A.68}$$

$$\begin{aligned}\frac{dZ}{d\varepsilon_{kl}} =& \mu(\delta_{ik}\delta_{jl} + \delta_{il}\delta_{jk}) - \frac{2}{3}\mu\delta_{ij}\delta_{kl} - \\ & \sum_{i=1}^{3}\left(\frac{dw_i}{d\Delta\bar{\varepsilon}^p}\frac{d\Delta\bar{\varepsilon}^p}{d\varepsilon_{kl}} + \frac{dw_i}{d\,\mathrm{J}_2(X^{(i),n})}\frac{d\,\mathrm{J}_2(X^{(i),n})}{d\varepsilon_{kl}}\right)X^{(i),n}\end{aligned} \tag{A.69}$$

Thus, the plastic flow direction and its derivative can be calculated Eq.4.48, which results in the tangent operator $\mathbb{C}^p$ Eq.4.45

A.6. Experiments and model prediction

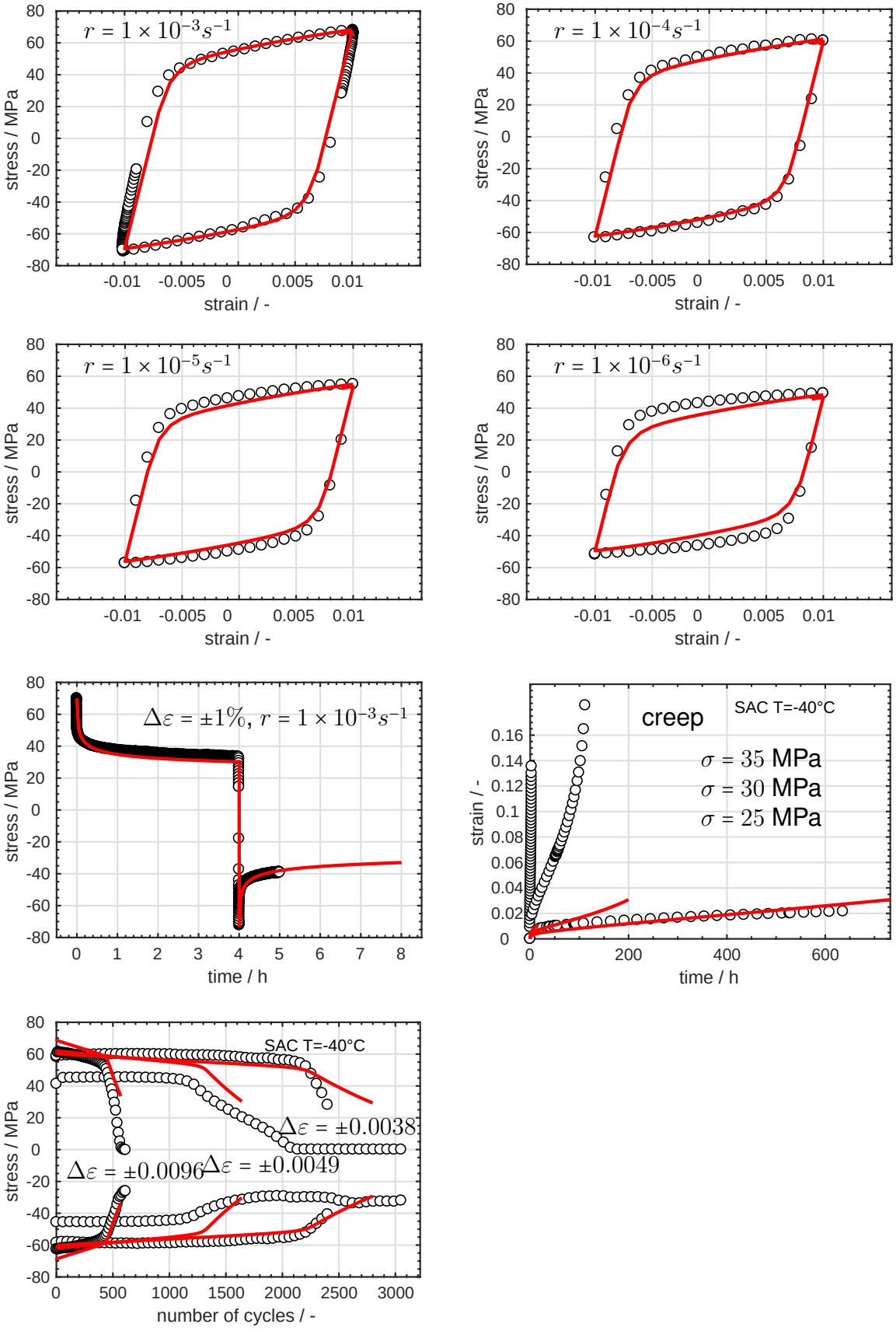

Fig. A.1: Experiments ◦ and model prediction — for T=-40 ℃

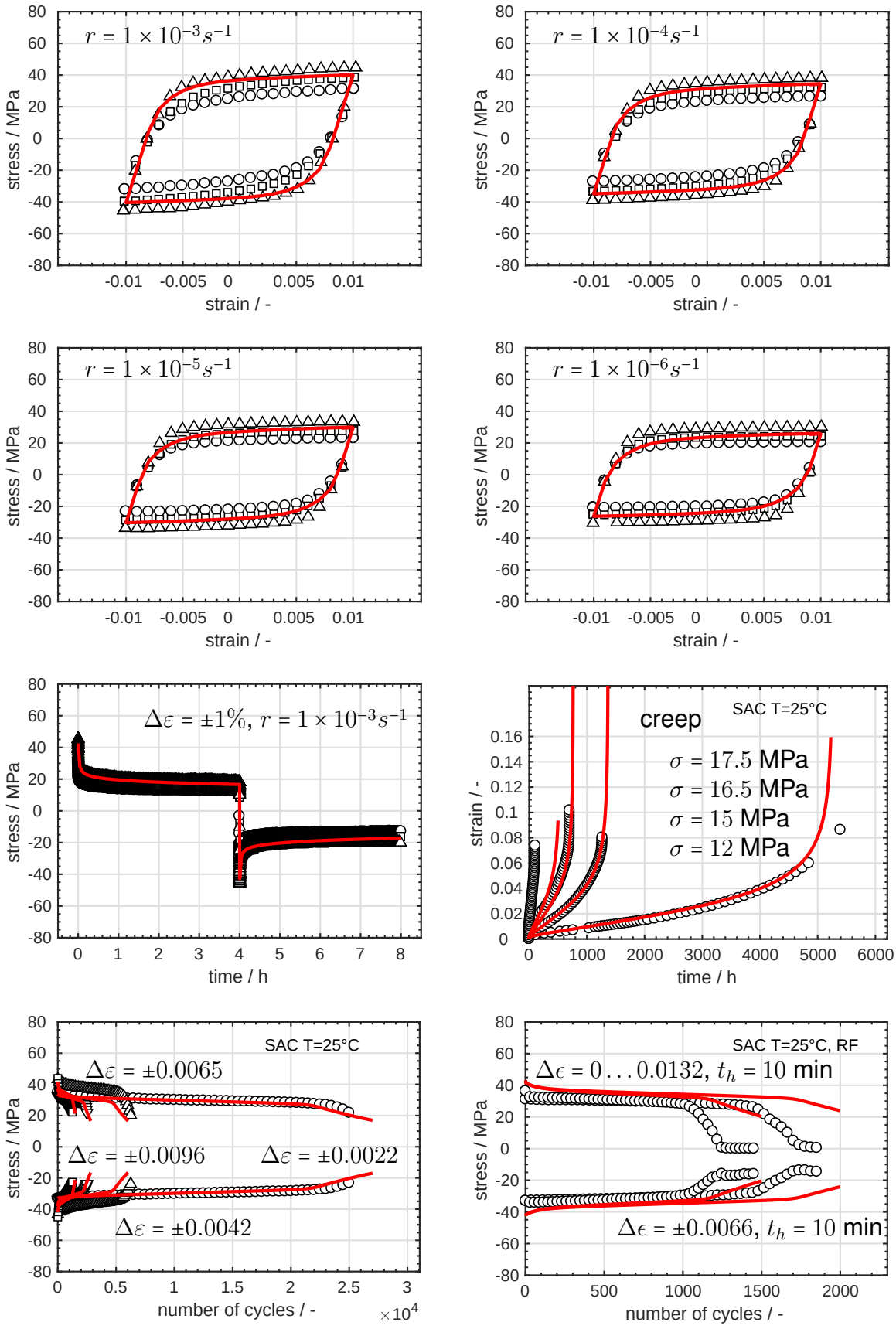

Fig. A.2: Experiments ∘ and model prediction — for T=25°C

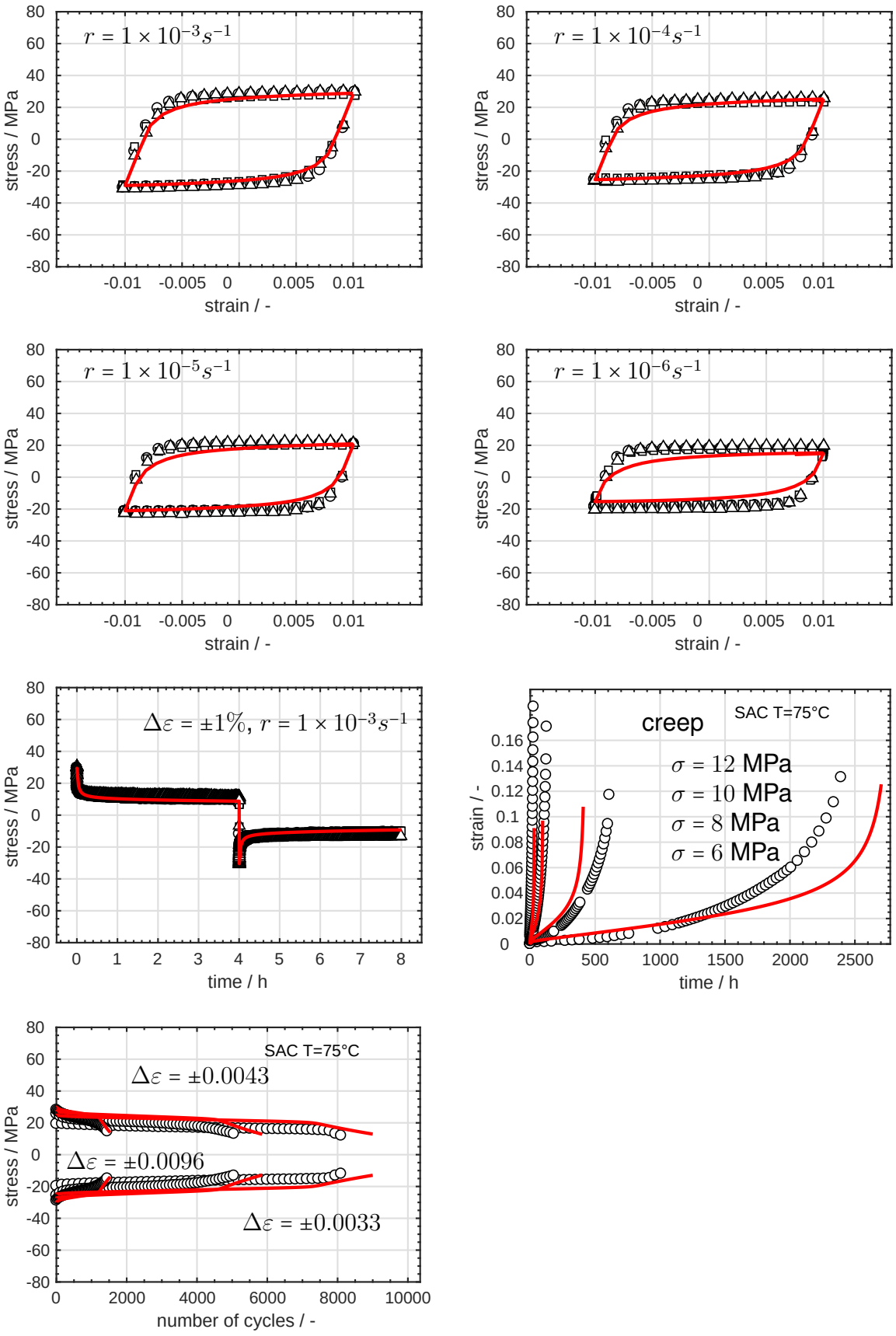

Fig. A.3: Experiments ◦ and model prediction — for T=75℃

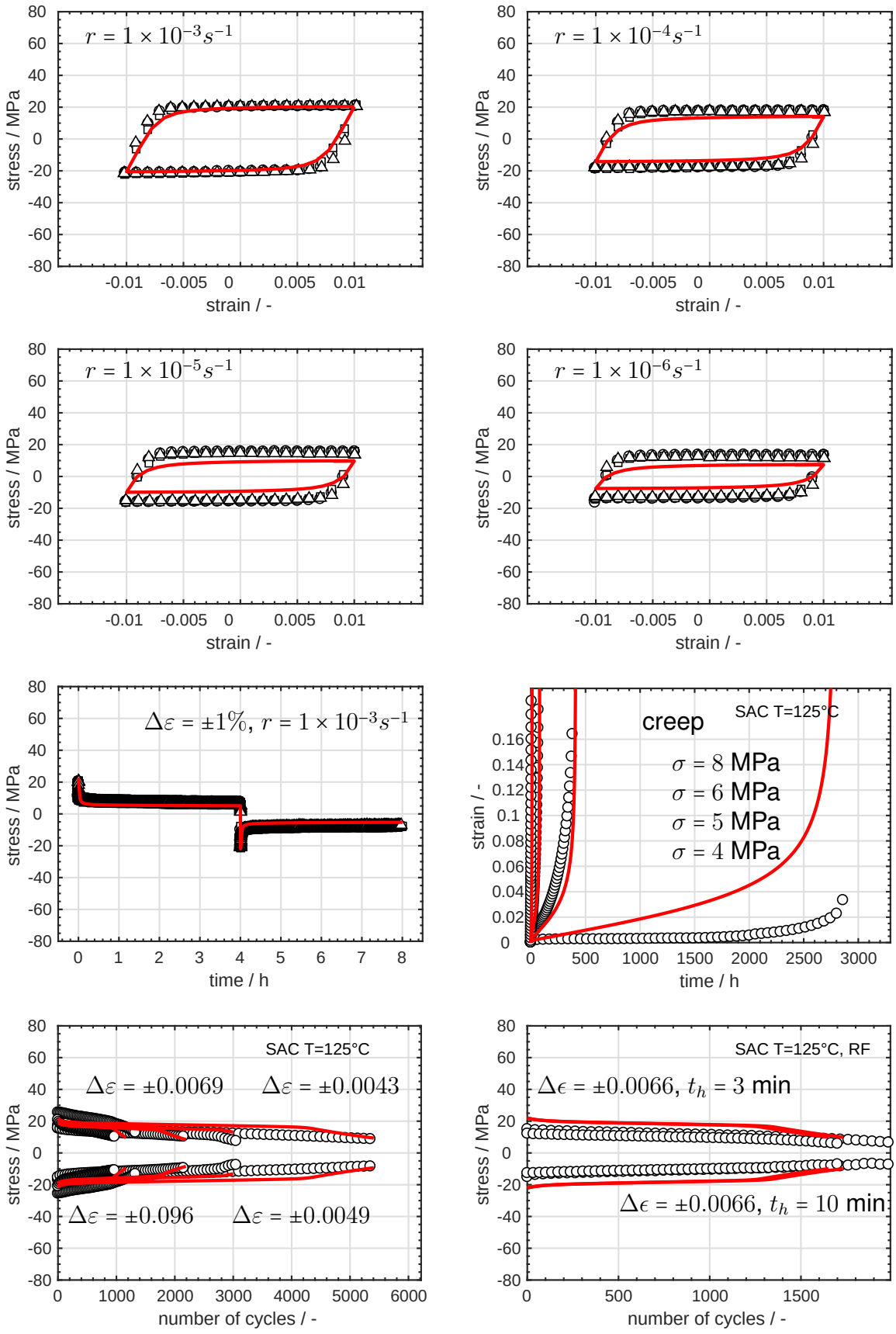

Fig. A.4: Experiments ◦ and model prediction — for T=125℃

Bibliography

[1] W. Scheel. *Materialmodifikation für geometrisch und stofflich limitierte Verbindungsstrukturen hochintegrierter Elektronikbaugruppen - LiVe*. Band 8 von Buchreihe Aufbau- und Verbindungstechnik in der Elektronik, Verlag Detert, Germany, 2009. ISBN: 9783934142572.

[2] Marko Kolbe and Stefan Di Bitonto. Electromibility in Germany: Vision 2020 and Beyond. In *Germany Trade and Invest*, issue 2013-2014. Gesellschaft für Außenwirtschaft und Standortmarketing mbH, Berlin, Germany, 2013.

[3] J. Wilde, M. Scheider-Ramelow, M. Petzold, and W. Scheel. *Methoden zur Zuverlässigkeitsqualifizierung neuer Technologien in der Aufbau- und Verbindungstechnik - Herausforderungen und Möglichkeiten -*. Buchreihe Aufbau- und Verbindungstechnik in der Elektronik - aktuelle Berichte, 3, Verlag Detert, Templin, Germany, 2006. ISBN: 3-934142-53-2.

[4] European Council and Parliament. Directive on the restriction of the use of certain hazardous substances in electrical and electronic equipment RoHs. *eur-lex.europa.eu L37, 13*, pages 19–23, 2006. Art. 95 EC.

[5] Camille Durand. *Thermo-mechanical study of a power module under Active Power Cycling by means of experiments and simulations*. PhD thesis, University of Valenciennes UVHC, France, 2015.

[6] Manfred Kuna and Stefan Wippler. A cyclic viscoplastic and creep damage model for lead free solder alloys. *Engineering Fracture Mechanics*, 77(18):3635–3647, 2010.

[7] Marco Güth. Schädigungsmechanismen in Zinn-Silber-Kupfer Legierungen. Master's thesis, University of Stuttgart, Institut für Metallkunde, Diplomarbeit, 2008.

[8] J. A. Rayne and B. S. Chandrasekhar. Elastic constants of β tin from 4.2°K to 300°K. *Phys. Rev.*, 120(5):1658–1663, 1960.

[9] L.P. Lehman, S.N Athavale, T.Z Fullem, A.C. Giamis, R.K. Kinyanjui, M. Lowenstein, K. Mather, R. Patel, D. Rae, J. Wang, Y. Xing, L. Zavalij, P. Borgesen,

and E.J. Cotts. Growth of Sn and intermetallic compounds in Sn-Ag-Cu solder. *Journal of Electronic Materials*, 33(12):1429–1439, 2004.

[10] H.J. Frost and Ashby M.F. *Deformation-Mechnism maps: the plasticity and creep of metals and ceramics*. Pergamon Press, Dartmouth College, USA and Cambridge University, UK, 1982. ISBN: 0080293379.

[11] S. Deplanque, W. Nuechter, M. Spraul, B. Wunderle, R. Dudek, and B. Michel. Relevance of primary creep in thermo-mechanical cycling for life-time prediction in Sn-based solders. In *EuroSimE 2005. Proceedings of the 6th International Conference on Thermal, Mechanial and Multi-Physics Simulation and Experiments in Micro-Electronics and Micro-Systems*, pages 71–78, Berlin, Germany, April 2005.

[12] S. Wiese, M. Roellig, and K.J. Wolter. Creep of eutectic SnAgCu in thermally treated solder joints. In *ECTC 2005. Proceedings of the 55th Electronic Components and Technology Conference*, volume 2, pages 1272–1281, Lake Buena Vista, FL, US, June 2005.

[13] Andreas Fix. *Auswirkungen von thermischen, mechanischen und thermomechanischen Belastungen auf die Mikrostruktur bei SMD-Lötstellen*. PhD thesis, Universität Freiburg, Germany, 2007.

[14] Rainer Dudek, M. Hildebrandt, S. Doering, R. Rzepka, H. Trageser, R. Kohl, and C.K. Wang. Solder fatigue acceleration prediction and testing results for different thermal test- and field cycling environments. In *ESTC 2014. Proceedings of the 5th Electronics System-integration Technology Conference*, pages 1–8, Helsinki, Finland, September 2014.

[15] K.C Norris and A.H. Landzberg. Reliability of controlled collapse interconnections. *IBM Journal of Research and Development*, 13(3):266–271, 1969.

[16] Werner Engelmaier. *Solder attachment reliability, accelerated testing, and result evaluation*, chapter 17, pages 545–587. in J.H. Lau, Ed., Solder Joint Reliability, Van Nostrand Reinhold, New York, US, 1991. ISBN: 978-1-4615-3910-0.

[17] Taoufiq Hannach. *Ermittlung von Lebensdauergleichungen vom Coffin-Manson- und Morrowtyp für bleihaltige und bleifreie Weichote durch Kombination von FE und Experiment*. PhD thesis, Technische Universität Berlin, 2010.

[18] Ansys Inc. Ansys Mechanical 18.0, Engineering simulation software, 2018. Canonsburg, Pennsylvania, USA.

[19] S. Wiese, M. Mueller, I. Panchenko, R. Metasch, and K-J. Wolter. The creep behaviour and microstructure of ultra small solder joints. In *EuroSimE 2011. Proceedings of the 12th Intl. Conf. on Thermal, Mechanical Multi-Physics Simulation and Experiments in Microelectronics and Microsystems*, pages 1/6–6/6, Linz, Austria, April 2011.

[20] F. Garofalo. *Fundamentals of creep and creep rupture in metals*. McMillan, New York, US, 1965.

[21] R. Metasch, J.C. Boareto, M. Roellig, S. Wiese, and K-J. Wolter. Primary and tertiary creep properties of eutectic SnAg3.8Cu0.7 in bulk specimens. In *EuroSimE 2009. Proceedings of the 10th International Conference on Thermal, Mechanical and Multi-Physics Simulation and Experiments in Microelectronics and Microsystems*, pages 1–8, Delft, Netherlands, April 2009.

[22] Manfred Spraul. *Lebensdauerprognosen für gelötete Bauteile mit Zinn-Blei und Zinn-Silber-Kupfer Lot für Temperaturewechselnprüfungen*. PhD thesis, Technische Universtität Berlin, Germany, 2006.

[23] Y. Kariya, T. Niimi, T. Suga, and M. Otsuka. Isothermal fatigue properties of Sn-Ag-Cu alloy evaluated by micro size specimen. *Japan Materials Transactions*, 46(11):2309–2315, 2005.

[24] Y. Kanda, Y Kariya, and Y. Mochizuki. Effect of hold time on low cycle fatigue life of micro solder joint. *Japan Materials Transactions*, 49(7):1524–1530, 2008.

[25] T. Yamamoto, T. Itoh, M. Sakane, and Y. Tsukada. Creep-fatigue life of Sn-8Zn-3Bi solder under multiaxial loading. *International Journal of Fatigue*, 43:235–241, 2012.

[26] R. Metasch, M. Roellig, A. Kabakchiev, B. Métais, R. Ratchev, K. Meier, and K-J. Wolter. Experimental investigation of the visco-plastic mechanical properties of a Sn-based solder alloy for material modelling in Finite Element calculations of automotive electronics. In *EuroSimE 2014. Proceedings of the 15th International Conference on Thermal, Mechanical and Multi-Physics Simulation and Experiments in Microelectronics and Microsystems*, pages 1–8, Gent, Belgium, April 2014.

[27] Markus Rauch. *Entwicklung eines Lebensdauerkonzeptes für Schaufel-Welle-Verbindungen stationärer Turbinen aus Nickelbasis- und 10 Chromlegierungen*. PhD thesis, Universität Stuttgart, 2006.

[28] J. Schemmel. *Beschreibung des Verformungs-, Festigkeits-, und Versagensverhaltens von Kompontenten im Kriechbereich unter instationärer Beanspruchung mit einem elastisch-viskoplastischen Werkstoffmodell*. PhD thesis, Universität Stuttgart, 2003.

[29] P. Buhl, A. Klenk, Schlesinger M., and T. Seifert. *Optimierung der numerischen Verformungs- und Schädigungsberechnung zur Lebensdauerbestimmung bei Kriechermüdungsbeanspruchung*. FVV Forschung Abschlussbericht, 2013. Deutsche Forschungsgemeinschaft (DFG) - Projektnummer 164675957.

[30] W.Z Wang, P. Buhl, and A. Klenk. A unified viscoplastic constitutive model for multi-axial creep fatigue loading. *International Journal of Damage Mechanics*, 24(3):363–382, 2014.

[31] E. Kullig and S. Wippler. Numerical integration and FEM-implementation of a viscoplastic Chaboche-model with static recovery. *Comptational Mechanics*, 38(6):491–503, 2006.

[32] Y. Yao, X. He, L.M. Keer, and M.E. Fine. A continuum damage mechanics-based unified creep and plasticity model for solder materials. *Acta Materialia*, 83:160–168, 2014.

[33] Stefan Wippler. *Entwicklung eines viskoplastischen schädigungsmechanischen Materialgesetzes für Lotwerkstoffe der Mikroelektronik*. PhD thesis, Technische Universität Freiberg, 2010.

[34] J.L. Chaboche. Viscoplastic constitutive equations for the description of cyclic and anisotropic behavior of metals. *Academie polonaise des sciences, serie Sciences et Techniques*, 25(1):33–42, 1977.

[35] A.D. Freed and K.P. Walker. Viscoplasticity with creep and plasticity bounds. *International Journal of Plasticity*, 9(2):213–243, 1993.

[36] J. Lemaitre and Chaboche J.L. *Mechanics of Solids Materials*. Cambridge University Press, 1990. ISBN: 9781107392984.

[37] F. C. Nix and D. MacNair. The Thermal Expansion of Pure Metals: Copper, Gold, Aluminum, Nickel, and Iron. *Phys. Rev.*, 60(8):597–605, 1941.

[38] E. Contesti and G. Cailletaud. Description of creep plasticity interaction with non-unified constitutive equations: application to an austenic stainless steel. *Nuclear Engineering and Design*, 116(3):265–280, 1989.

[39] G. Cailletaud and K. Sai. Study of plastic/viscoplastic models with various inelastic mechanisms. *International Journal of Plasticity*, 11(8):991–1005, 1995.

[40] J.L. Chaboche. Constitutive equations for cyclic plasticity and cyclic visoplasticity. *International Journal of Plasticity*, 5(3):247–302, 1989.

[41] B. Métais, A. Kabakchiev, Y. Maniar, M. Guyenot, R. Metasch, M. Roellig, P. Rettenmeier, P. Buhl, and S. Weihe. A viscoplastic fatigue creep damage model for tin-solder alloy. In *EuroSimE 2015. Proceedings of the 16th International Conference on Thermal, Mechanical and Multi-Physics Simulation and Experiments in Microelectronics and Microsystems*, pages 1–5, Budapest, Hungary, April 2015.

[42] D. Nouailhas. Unified modeling of cyclic of viscoplasticity: application to austentic stainless steels. *International Journal of Plasticity*, 5(5):501–520, 1989.

[43] P.J. Armstrong and C.O. Frederick. A mathematical representation of the multiaxial bauschinger effect. Technical report, Berkeley Nuclear Laboratories, 1966.

[44] W. Prager. Recent development in the mathematical theory of plasticity. *Journal of Applied Physics*, 20(3):235–241, 1949.

[45] D. Marquis. *Etude théorique et vérification expérimentale d'un modèle de plasticité cyclique*. PhD thesis, Université Paris VI, France, 1979.

[46] J.L. Chaboche. A review of some plasticity and viscoplasticity constitutive theories. *International Journal of Plasticity*, 24(10):1642–1693, 2008.

[47] Dassault system Simulia. Abaqus Inc. Engineering simulation software, 2016. Johnston, Rhode Island, US.

[48] R. Metasch, R. Schwerz, M. Roellig, A. Kabakchiev, B. Métais, R. Ratchev, and K.J. Wolter. Experimental investigation of the viscoplastic mechanical properties of a Sn-based solder alloy for material modeling in finite element calculations of automotive electronics. In *EuroSimE 2014. Proceedings of the 15th International Conference on Thermal, Mechanical and Multi-Physics Simulation and Experiments in Microelectronics and Microsystems*, Ghent, Belgium, April 2014.

[49] S.M. Arnold and S. Kruch. Differential continuum damage mechanics models for fatigue or unidirectional metal matrix composites. Technical report, Nasa Technical memorandum 105213, Lewis Research Center, Cleveland, OH, US, 1991.

[50] J.L. Chaboche and P.M. Lesne. A non-linear continuous fatigue damage model. *Fatigue Fracture of Engineering Material and Structure*, 11(1):1–17, 1988.

[51] J.L. Chaboche. Continuum damage mechanics: part I - general concepts. *Journal of Applied Mechanics*, 55(1):59–64, 1988.

[52] G. Rousselier. Ductile fracture models and their potential in local approach of fracture. *Nuclear Engineering and Design*, 105(1):99–101, 1987.

[53] J. Lemaitre and Chaboche J.L. A nonlinear model of creep-fatigue damage: cumulation and interaction. In *Proceedings IUTAM Smyp. of Mechanics of viscoelastic media and bodies*, Gothenburg, Sweden, 1974.

[54] J. Lemaitre and I. Doghri. Damage90: a post processor for crack initiation. *Computer Methods in Applied Mechanics and Engineering*, 115(3-4):197–232, 1994.

[55] J. Lemaitre and R. Desmorat. *Engineering Damage Mechanics: Ductile, Creep, Fatigue and Brittle Failures*. Springer Berlin Heidelberg, ENS Cachan, Université Paris 6, France, 2005. ISBN: 9783540272939.

[56] L.M. Kachanov. Time to the rupture process under creep conditions. *Izw. Akad. Nauk. SSR, Otd. Nauk (in Russian), in Int. J. of Fract. 1999*, no. 8:26–31, 1958.

[57] O.H. Basquin. The exponential law of endurance test. In *Proceeding of the 13th annual meeting of the American Society for Testing Materials*, volume 10, pages 625–630, Atlantic City, New Jersey, US, June 1910.

[58] L.F. Jr. Coffin. A study of the effect of cyclic thermal stresses on a ductile metal. In *a joint session of the Metals Engineering and Applied Mechanics Divisions at the Annual Meeting of the American Society of Mechanical Engineers*, pages 931–950, New York, US, December 1953.

[59] S.S. Manson. Behavior of materials under conditions of thermal stress. In *a lecture presented at Symposium on Heat Transfert*, University of Michigan, US, June 1952.

[60] ASM International. *Element of Metallurgy and Engineering Alloys*, chapter 14. ASM American Society for Metals, 2008. ISBN: 978-0-87170-867-0.

[61] American Society of Mechanical Engineers. *Boiler and Pressure Vessel Code: rule for construction of nuclear power plant components. Div. 1, Subsection NH, class 1, component at elevated temperature service*, chapter 12. ASME, New York, 1998.

[62] F.R. Larson and J. Miller. A time-temperature relationship for rupture and creep stresses. *Trans. ASME*, 74(5):1–11, 1952.

[63] Y.N. Rabotnov. *Creep Problems in Structural Members*. Applied Mathematics and Mechanics Series. Elsevier, 1969. ISBN: 0444102590.

[64] Geert Schellenberg. *Beschreibung des Risseinleitungsverhaltens von warmfesten Stählen unter Kriechermüdungsbeanspruchung*. PhD thesis, Universität Stuttgart, Germnay, 2002.

[65] M.A. Miner. Cumulative damage in fatigue. *Journal of Applied Mechanics*, 12(3):159–164, 1945.

[66] A. Palmgren. Die Lebensdauer von Kugellagern. *Zeitschrift des Vereins Deutscher Ingenieure*, 68(14):339–341, 1924.

[67] E.L. Robinson. Effect of temperature variation on the long-time to rupture strength of steels. *Transaction ASME*, 74:777–780, 1952.

[68] Clausmeyer. *Über die Versprödung von Stahl unter mehrachsiger Beanspruchung*. Habilitationnschrift D17, Darmstadt, Germany, 1967.

[69] M. Rauch, K. Maile, and M. Ringel. Numerical calculation and experimental validation of damage development in 9-Cr steels. In *Proceeding of the 30th MPA Seminar in conjonction with the 9th German-Japanese Seminar*, pages 1–19, Stuttgart, Germany, October 2004.

[70] A. Graham and K.F.A. Wailes. Relations between long and short time creep properties of a commercial alloy. *Journal of Iron and Steel Institute*, 179, 1955.

[71] A.L. Gurson. Continuum theory of ductile rupture by void nucleation and growth: Part I— yield criteria and flow rules for porous ductile media. *Journal of Engineering Materials and Technologies*, 99(1):2–15, 1977.

[72] V. Tvergaard and A. Needleman. Analysis of the cup-cone fracture in a round tensile bar. *Acta Metallurgica*, 32(1):157–169, 1984.

[73] European Commitee for Standardization. Aerospace series - metallic material - test methods. Technical report, EN-6072, 2011.

[74] Timo Herberholz. *Untersuchungen zu Möglichkeiten und Grenzen des Einsatzes von Zinn-Basislotlegierungen für Hochtemperaturelektronikanwendungen*. PhD thesis, Universität Rostock, Germany, 2015.

[75] Matecon GmbH. Machbarkeitsstudie thermisch-mechanische Ermüdungsversuche an Lotwerkstoffen. Technical report, Karlsruhe, Germany, 2007.

[76] Measure equipment Darmstadt, Germany. *Hottinger Baldwin Messtechnik GmbH*, 2014.

[77] B. Métais, A. Kabakchiev, M. Guyenot, R. Metasch, M. Roellig, P. Buhl, and S. Weihe. Entwicklung einer Pro-aktiven Löstellengeometrie-unabhängigen Lebensdauersimulation für bleifrei Lote. In *Elektronische Baugruppen und Leiterplatten (EBL), published in Mikroverbindungstechnik, Jahrbuch 2016/2017*, Stuttgart, Germany, February 2016.

[78] Steffen Wiese. *Verformung und Schädigung von Werkstoffen der Aufbau- und Verbindungstechnik, Das Verhalten im Mikrobereich*. Springer Heidelberg Dordrecht London New York, Halle, Germany, 2010. ISBN: 978-3-642-05462-4.

[79] K. Naumenko and H. Altenbach. *Foundation of Engineering Mechanics: Modeling of Creep for Structural Analysis*. Springer Berlin Heidelberg New York, Halle, Germany, 2007. ISBN: 3-540-70834-0.

[80] F.H. Norton. *The creep of steel at high temperature*. Mc Graw-Hill, New York, US, 1929.

[81] J.C. Simo. Numerical analysis and simulation of plasticity. In *Numerical Methods for Solids (Part 3) Numerical Methods for Fluids (Part 1)*, volume 6 of *Handbook of Numerical Analysis*, pages 183 – 499. Elsevier, 1998.

[82] J.C. Simo and T.J.R Hughes. Computational inelasticity. In *Interdisciplinary Applied Mathematics*, Mechanics and Material. Springer Verlag New York Inc., 1998. ISBN: 0-387-97520-9.

[83] E.A. de Souza Neto, D. Perić, and D.R.J. Owen. *Computational methods for plasticity, theory and applications*. John Willey and Sons Ltd. United Kingdom, 2004. ISBN: 978-0-470-69452-7.

[84] Vlado A. Lubarda and David J. Benson. On the numerical algorithm for isotropic–kinematic hardening with the Armstrong–Frederick evolution of the back stress. *Computer Methods in Applied Mechanics and Engineering*, 191(33):3583 – 3596, 2002.

[85] Guozheng Kang. A visco-plastic constitutive model for ratcheting of cyclically stable materials and its finite element implementation. *Mechanics of Materials*, 36(4):299 – 312, 2004.

[86] A. Kabakchiev, B. Métais, R. Ratchev, M. Guyenot, P. Buhl, M. Hossfeld, X. Schuler, R. Metasch, and M. Roellig. Description of the thermo-mechanical properties of a Sn-based solder alloy by a unified viscoplastic material model for Finite Element calculations. In *EuroSimE 2014. Proceedings of the 15th International Conference on Thermal, Mechanical and Multi-Physics Simulation and Experiments in Microelectronics and Microsystems*, Gent, Belgium, April 2014.

[87] J.H.L. Pang, B.S. Xiong, and T.H. Low. Comprehensive mechanics characterization of lead free 95.5Sn3.8Ag0.7Cu. *Micromaterials and Nanomaterials*, 3:87–93, 2004.

[88] B. Métais, M. Kuczynska, A. Kabakchiev, S. Wolfangel, P. Buhl, and S. Weihe. Experimental and numerical investigation of fatigue damage development under multiaxial loads in a lead-free Sn-based solder alloy. In *EuroSimE 2016. Proceedings of the 17th International Conference on Thermal, Mechanical and Multi-Physics Simulation and Experiments in Microelectronics and Microsystems*, Montpellier, France, April 2016.

[89] M. Kuczynska, N. Schafet, U. Becker, B. Métais, A. Kabakchiev, P. Buhl, and S. Weihe. The role of stress state and stress triaxiality in lifetime prediction of solder joints in different packages utilized in automotive electronics. In *EuroSimE 2016. Proceedings of the 17th International Conference on Thermal, Mechanical and Multi-Physics Simulation and Experiments in Microelectronics and Microsystems*, Montpellier, France, April 2016.

[90] M. Kuczynska, N. Schafet, U. Becker, R. Metasch, M. Roellig, A. Kabakchiev, and S. Weihe. Validation of different SAC material models calibrated on isother-

mal tests using in-situ TMF measurement of thermally induced shear load. In *EuroSimE 2017. Proceedings of the 18th International Conference on Thermal, Mechanical and Multi-Physics Simulation and Experiments in Microelectronics and Microsystems*, Dresden, Germany, April 2017.

[91] R. Metasch, M. Roellig, M. Kuczynska, M. Schafet, U. Becker, K. Meier, and I. Panchenko. Accelerated lifime measurement with in-situ force and displacement monitoring during thermal cycling on solder joints. In *EuroSimE 2017. Proceedings of the 18th International Conference on Thermal, Mechanical and Multi-Physics Simulation and Experiments in Microelectronics and Microsystems*, Dresden, Germany, April 2017.

[92] D. Cojocaru and A.M. Karlsson. A simple numerical method of cycle jumps for cyclically loaded structures. *International Journal of Fatigue*, 28(12):1677 – 1689, 2006.

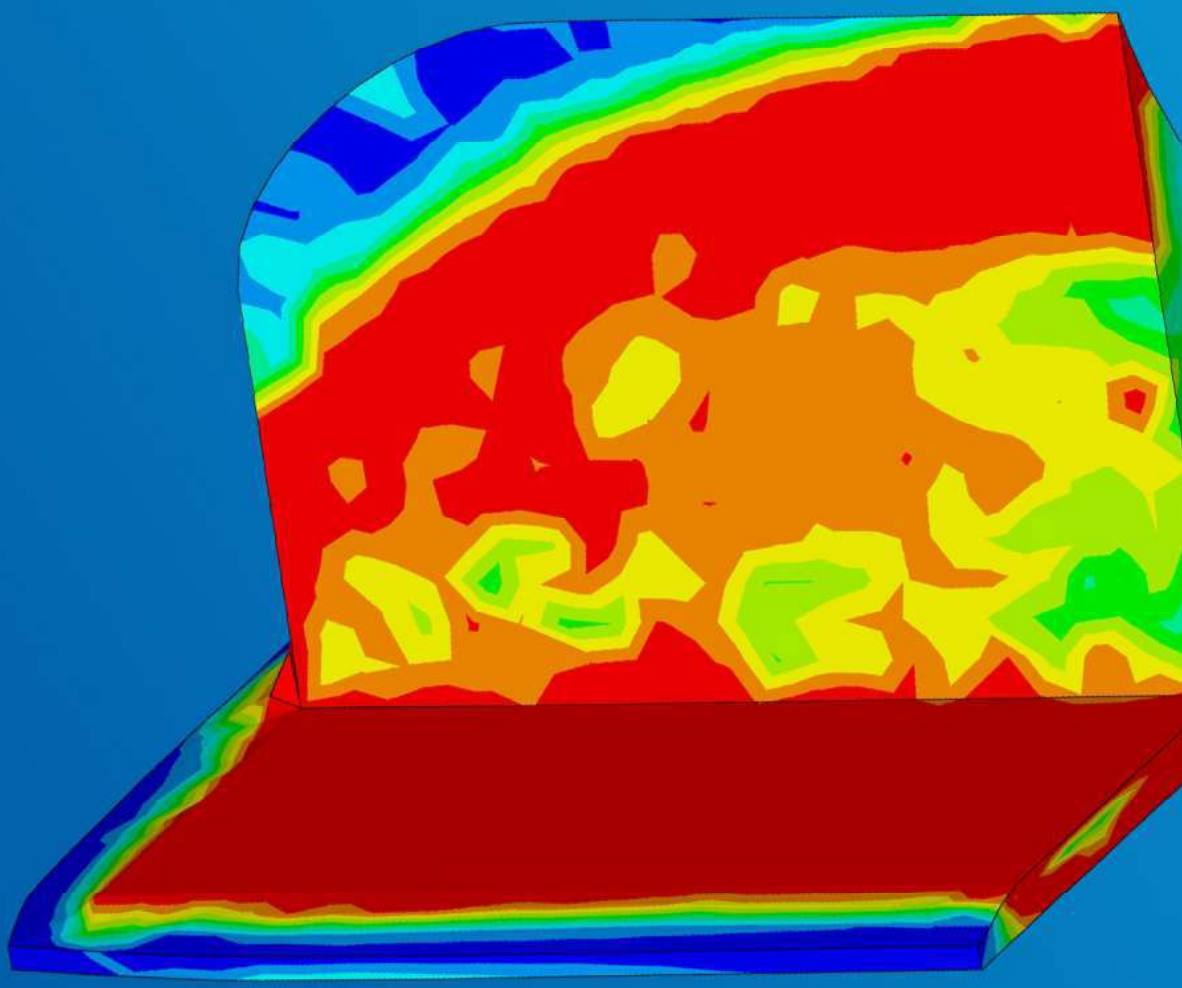

Universität Stuttgart

ISBN: 978-3-946789-03-1